



HAL
open science

Prediction of soot particles in Gas Turbine Combustors using Large Eddy Simulation

Lucien Gallen

► **To cite this version:**

Lucien Gallen. Prediction of soot particles in Gas Turbine Combustors using Large Eddy Simulation. Physics [physics]. Institut National Polytechnique de Toulouse - INPT, 2020. English. NNT : 2020INPT0058 . tel-04167267

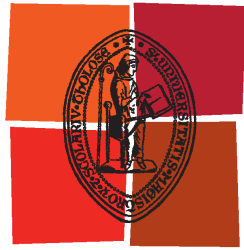
HAL Id: tel-04167267

<https://theses.hal.science/tel-04167267>

Submitted on 20 Jul 2023

HAL is a multi-disciplinary open access archive for the deposit and dissemination of scientific research documents, whether they are published or not. The documents may come from teaching and research institutions in France or abroad, or from public or private research centers.

L'archive ouverte pluridisciplinaire **HAL**, est destinée au dépôt et à la diffusion de documents scientifiques de niveau recherche, publiés ou non, émanant des établissements d'enseignement et de recherche français ou étrangers, des laboratoires publics ou privés.



Université
de Toulouse

THÈSE

En vue de l'obtention du

DOCTORAT DE L'UNIVERSITÉ DE TOULOUSE

Délivré par :

Institut National Polytechnique de Toulouse (Toulouse INP)

Discipline ou spécialité :

Energétique et Transferts

Présentée et soutenue par :

M. LUCIEN GALLEN

le mercredi 1 juillet 2020

Titre :

Prediction of soot particles in Gas Turbine Combustors using Large Eddy Simulation

Ecole doctorale :

Mécanique, Energétique, Génie civil, Procédés (MEGeP)

Unité de recherche :

Centre Européen de Recherche et Formation Avancées en Calcul Scientifique (CERFACS)

Directeur(s) de Thèse :

MME BENEDICTE CUENOT

MME ELEONORE RIBER

Rapporteurs :

M. BENOIT FIORINA, CENTRALESUPELEC GIF SUR YVETTE

M. HEINZ PITSCH, RHEINISCH-WESTFALISCHE TECH. HOCH.AACHEN

Membre(s) du jury :

M. BENOIT FIORINA, CENTRALESUPELEC GIF SUR YVETTE, Président

M. ABDERRAHMAN EL BAKALI, UNIVERSITE LILLE 1, Membre

M. KLAUS PETER GEIGLE, GERMAN AEROSPACE CENTER BERLIN, Membre

Mme BENEDICTE CUENOT, CERFACS, Membre

Mme ELEONORE RIBER, CERFACS, Invité

M. NICOLAS BERTIER, ONERA, Membre

ABSTRACT

Expected stringent legislation on particulate matter (PM) emission by gas turbine combustors is currently motivating considerable efforts to be better understand, model and predict soot formation. This complex phenomenon is very difficult to study in detail with experiment, and numerical simulation is an essential complementary tool. Considering that the chemistry of soot particles strongly depends on their size, the numerical prediction of soot formation requires the description of their size distribution. To do so, either Eulerian methods (sectional or moments) or stochastic Lagrangian approaches are reported in the literature. In the present work, a far more simple semi-deterministic Lagrangian approach is proposed. An accurate description of the gaseous phase including first Polycyclic Aromatic Hydrocarbons is also developed as a necessary input to detail soot model. This work aims to develop a viable methodology of soot description within the LES framework. The manuscript is organized into three parts. The first part introduces the context and presents a literature review of soot particles focusing on numerical soot modelling. Among the existing method, the Lagrangian soot tracking is retained where additional developments are required to describe the particle size distribution (PSD). Then, the second part deals with laminar sooting flames. The modelling of reactive flow is briefly described, and the choice of chemistry modelling is also discussed in details. The Analytically Reduced Chemistry (ARC) is retained for the chemical description. Several ARC including PAH chemistry are selected, derived and validated on canonical laminar flames for different fuels, targeting different PAH. Lagrangian soot tracking has been developed and validated on canonic flames compared to a well-established method from the literature for which excellent agreement is found. The combination of ARC chemistries with Lagrangian soot tracking has been applied to investigate a set of canonic laminar flames analyzing soot global quantities and PSD. Good predictions are obtained with the proposed methodology. Finally, the last part presents the soot prediction obtained with the proposed methodology in two complex configurations representative of an aeronautical combustors. The first one is the FIRST configuration, a gaseous confined pressurized swirled flame studied experimentally at DLR. Impact of precursors species and radiative transfers through the resolution of Radiative Transfer Equation (RTE). Good predictions are obtained compared to experiments for predicted temperature and soot volume fraction. The second target configuration is the UTIAS Jet A-1 burner and corresponds to a confined turbulent spray flame burning aviation jet fuel A-1 studied experimentally at UTIAS Toronto. LES of this configuration provides a qualitative and quantitative understanding of soot evolution in turbulent spray flames. Numerical predicted soot volume fraction using Lagrangian soot tracking and an ARC mechanism including pyrolysis method is compared to experimental measurements. Results show the ability of

the proposed methodology relying on ARC chemistry for Jet A-1 including pyrolysis method and Lagrangian soot tracking, to predict accurately soot compared to available measurements. In addition to an accurate soot model, the present work highlights the requirement of an accurate chemical description especially concerning soot inception as well as an accurate description of heat transfers for future investigation in turbulent flames.

RÉSUMÉ

Les futures réglementations en termes d'émission de polluants, notamment sur les particules fines (PM), qui s'appliquent aux chambres de combustion de nouvelle génération nécessitent de nouvelles approches de conception. Afin de réduire la formation des particules fines, ou particules de suies, la compréhension des processus de formation et de transports des particules est nécessaire. La chimie et la dynamique de ces particules de suies dépendent fortement de la taille et de la morphologie de celle-ci. La prédiction de ces polluants requière de prendre en compte la distribution en taille des particules tout au long du calcul. Pour cela, des méthodes Eulériennes sont utilisées (Moments, Sectionnels), ou des méthodes stochastiques Lagrangiennes sont proposées. Dans ce travail, une méthode semi-déterministique basée sur l'approche Lagrangienne est proposée. Parallèlement, une description précise de la chimie, notamment pour les précurseurs de suies nécessaire aux modèles détaillés de formation de suies est développée. Ce travail ambitionne de développer une méthodologie incluant la description des précurseurs de suies et le transport de celles-ci dans le cadre de la simulation aux grandes échelles. Le manuscrit est organisé en trois parties. La première partie introduit le contexte de l'étude ainsi qu'une revue détaillée de la littérature scientifique concernant les particules de suies et particulièrement leur modélisation. Parmi les méthodes existantes, le suivi lagrangien des particules de suies est retenu dans ce travail. Néanmoins de nombreux développements additionnels sont nécessaires afin de modéliser avec précision la distribution en taille des particules. Ensuite la deuxième partie s'intéresse à la modélisation des flammes laminaires et en particulier la prédiction des émissions de suies. La modélisation des écoulements réactifs est rapidement évoquée, le choix de la modélisation de la chimie de combustion est également discutée. Le choix de la chimie analytiquement réduite (ARC) est retenu dans ce travail. Le développement et la validation de schémas cinétiques réduits pour différents carburants ainsi que différents précurseurs de suies est détaillé. Enfin, la méthode du suivi Lagrangien des particules de suies est décrite en détails et validée par rapport à la littérature. La combinaison des chimies réduites ARC et du suivi Lagrangien des particules est utilisée sur plusieurs flammes canoniques pour lesquelles de bonnes prédictions de suies sont obtenues. Finalement, la dernière partie présente la prédiction des suies obtenue avec notre méthodologie dans deux configurations de type aéronautiques. La première est la configuration FIRST, il s'agit d'une flamme étudiée au DLR opérant à haute pression dans un milieu confiné et stabilisée à l'aide d'un swirlleur. L'impact du choix du précurseur de suies ainsi que la prise en compte des transferts radiatifs est évaluée. La température et la fraction volumique des suies sont en accord avec les mesures expérimentales. La seconde configuration est le brûleur UTIAS Jet A-1 où le Jet A-1 est un carburant aéronautique, il est caractérisé par une flamme swirlée

diphasique et étudié à l'université de Toronto au Canada. La simulation aux grandes échelles de cette configuration procure de nouvelles connaissances sur la formation des particules des suies dans les flammes turbulentes diphasiques. Un très bon accord avec les données expérimentales est observé pour cette configuration concernant les particules de suies. Le travail de cette thèse souligne la nécessité d'une description précise de la chimie, notamment celle des précurseurs de suies, ainsi qu'une description précise des transferts de chaleur pour la prédiction des particules de suies dans les brûleurs de type-aéronautiques.

Acknowledgements

I would like to thank Bénédicte Cuenot and Eleonore Riber for offering this PhD thesis opportunity within the European project SOPRANO. I also would like to thank all SOPRANO members, in particular Benedetta Franzelli and Klaus Peter Geigle for their help and discussions all along the PhD thesis as well as for SOPRANO PhD student like Livia, Kevin and Martin and the others for fruitful discussions. Moreover I would like to thank Heinz Pitsch and Benoît Fiorina for examining my work and the other members of the jury, Abderrahman El Bakali, Nicolas Bertier, Klaus Peter Geigle and Gorka Exilard for their positive and relevant comments.

Ce travail a été réalisé sous la direction de Bénédicte et Eleonore, qui m'ont guidé tout au long de mon travail. Je les remercie d'avoir eu confiance en moi et mon travail et de m'avoir permis de garder une grande autonomie. Merci aux séniors CERFACS qui ont contribué d'une façon ou une autre à ce travail, je pense en premier lieu à Antony qui a toujours pris le temps de m'expliquer en détails tout un tas de choses, un grand merci également à Gabriel et Olivier pour leur aide et leur savoir-faire que j'ai si souvent sollicité. C'est également le cas d'Isabelle et de tout l'équipe CSG. Je remercie surtout leur pédagogie sur la résolution de mes problèmes qui m'ont énormément appris. Merci également à l'équipe administrative, Michèle, Chantal, Marie, Nicole et Jade, pour leur efficacité et gentillesse. Merci à Thierry également pour l'énergie qu'il transmet à cette équipe (CFD).

Durant mon passage au CERFACS, j'ai eu la chance de rencontrer un grand nombre de collègues qui ont d'une manière ou d'une autre contribué à ce travail mais surtout à une bonne ambiance de travail. Merci à Jarjar, Bastien, Nico et Félix de m'avoir mis le pied à l'étrier dès le début. Merci à l'En Avant Cerfacs (EAC) et tous ces membres pour les bons moments partagés, à son capitaine emblématique Maxou et générosité extraordinaire (hors du terrain seulement), à Valou le goal/coach au top, aux anciens membres Majd le tricot, Dario le 9, Kelu le magnifique, Biolchi et Pedro avec leur tirs/dégagements hors norme jusqu'au nouveau avec l'équipe dirigeante douteuse menée par Christopher et David et tous ces membres qui en font un

centre d'excellence Cam', Nico, Vic', Marshall et beaucoup d'autres sans oublier l'ancien membre d'honneur doudou et l'unique supporter du club: Catchi. Et beaucoup d'autres en dehors de l'EAC, Bastien, Astoul, Gauthier, Flo' que l'on retrouve plutôt autour d'une mousse.

Plus récemment après avoir eu Félix comme exemple de bonne conduite et de rigueur, merci à mon nouveau co-bureau, le stagiaire, la male ou Maxicuisse d'avoir pris ma direction plutôt, merci pour les bons moments passés et d'avoir supporter mes fractures du mental en sortie récup' comme tu dis. Merci à tout l'étage: Charlélie, Fabien, Quegui, Juju, le bureau Arcane ! Et finalement merci à Etienne qui prend la suite et qui à la fin à contribué à ce travail grâce à son efficacité sur le code chimique et à nos diverses discussions.

Finalement un immense merci à ma grande et petite famille pour leur présence et leur soutien sans faille.

Contents

I	Context of the study	7
1	Introduction	9
1.1	Global context: combustion-generated pollutants	9
1.2	Effect of PM from aircraft engines on health and climate	12
1.3	Aeronautical burner design: status and constraints	14
1.4	Need and challenges for numerical simulations of pollutant emissions . .	16
1.5	Objectives and structure of the PhD thesis	18
2	Soot formation and its modeling	21
2.1	Soot morphology and internal structure	21
2.2	Soot formation and oxidation mechanism	28
2.3	Numerical methods for soot prediction	35
II	Numerical developments and validation for soot prediction in flames	49
3	Modeling of laminar reactive flows	51
3.1	Laminar flames	51
3.2	Conservative equations for gaseous reacting flow	57
3.3	Equations for reacting two-phase flow	66
4	Lagrangian soot tracking methodology	75
4.1	Lagrangian formalism for soot prediction	76
4.2	Numerical methods	77
4.3	Evaluation of LST efficiency	83
4.4	Conclusion	89
5	Analytically Reduced Chemistry with accurate soot precursors prediction	91
5.1	Chemical kinetics of ethylene-air flames with accurate PAH chemistry .	92
5.2	Derivation and validation of an ARC for ethylene-air flames with accurate PAH chemistry	98
5.3	Prediction of larger PAH for ethylene-air flames	104
5.4	Extension to aviation jet fuel chemistry	112
5.5	Conclusion	116

CONTENTS

6 Lagrangian Soot Tracking in laminar flames.	117
6.1 Detailed soot modeling	117
6.2 Bi-variate description of soot particles	123
6.3 Physical and numerical validation	125
6.4 Laminar flames: comparison with experiments	130
6.5 Conclusion	142
III LES of sooting flames	143
7 Modeling of turbulent reacting flows	145
7.1 Turbulent Flames	146
7.2 Large Eddy simulation	150
7.3 Turbulence - Chemistry interactions	153
7.4 Thermal radiation modeling in turbulent sooting flames	158
8 LES in a confined pressurized burner	167
8.1 The FIRST combustor	167
8.2 Numerical set-up	169
8.3 Results	172
8.4 Computational cost	205
8.5 Conclusion	208
9 LES in a turbulent spray flame	211
9.1 UTIAS Jet A-1 combustor	211
9.2 Numerical setup	212
9.3 Results	214
9.4 Computational cost	224
9.5 Conclusions	226
10 Conclusions and perspectives	227
Bibliography	231
Appendices	269
A Article on Lagrangian soot tracking methodology	271
B Gas spectral database	281

C Coupling procedure AVBP-PRISSMA	283
C.1 Coupling libraries	283
C.2 Coupling communications	283
C.3 Coupling time step	284
D Numerical set-up and FIRST flow validations	285

CONTENTS

List of symbols

Roman characters

Symbol	Description	Unit
a	Strain rate	$[\text{s}^{-1}]$
c	Flame progress variable	$[-]$
d_l	Liquid droplet diameter	$[\text{m}]$
D_k	Diffusion coefficient of species k	$[-]$
E	Gaseous total energy per unit mass	$[\text{J}/\text{kg}]$
ε	Efficiency function	$[-]$
$F_{d,i}$	Volumetric force vector of particle drag	$[\text{N}/\text{m}^3]$
$F_{p,i}$	Drag force vector of a Lagrangian particle	$[\text{N}]$
\mathcal{F}	Thickening factor	$[-]$
h_s	Sensible enthalpy	$[\text{J}/\text{kg}]$
HRR	Heat Release Rate	$[\text{W}/\text{m}^3]$
$J_{j,k}$	Diffusive flux vector of species k	$[\text{kg}/\text{m}^2/\text{s}]$
\mathcal{K}	Flame curvature	$[\text{m}^{-1}]$
L_v	Latent heat of evaporation	$[\text{J}/\text{kg}]$
m_p	Mass of a Lagrangian particle	$[\text{kg}]$
\dot{m}_p	Rate of change of droplet mass	$[\text{kg}/\text{s}]$
\dot{m}_p	Mass flux of gaseous fuel from a droplet	$[\text{kg}/\text{s}]$
\dot{m}	Mass flux	$[\text{kg}/\text{s}]$
$n_{\mathcal{F}}$	Number of points in the flame front	$[-]$
n_l	Number of droplet density	$[\text{m}^{-3}]$
P	Pressure	$[\text{Pa}]$
P	Probability density function	$[-]$
q	Momentum flux ratio	$[-]$
r	Mixture gas constant	$[\text{J}/\text{kg}/\text{K}]$
\dot{r}_j	Rate of reaction j	$[\text{mol s}^{-1}]$
\mathcal{R}	Universal gas constant (mass)	$[\text{J mol}^{-1}\text{K}^{-1}]$
S_{ij}	Strain rate tensor	$[\text{s}^{-1}]$
t	Time	$[\text{s}]$
T	Gaseous temperature	$[\text{K}]$
u_i	Gaseous velocity vector	$[\text{m}/\text{s}]$
u_l	Eulerian liquid phase velocity	$[\text{m}/\text{s}]$
$u_{p,i}$	Velocity vector of a Lagrangian particle	$[\text{m}/\text{s}]$
W	Molecular weight	$[\text{kg}/\text{mol}]$
x_i	Spatial coordinate (vector)	$[\text{m}]$
\mathbf{x}	Spatial coordinate (vector)	$[\text{m}]$
x	Spatial coordinate	$[\text{m}]$
$x_{p,i}$	Position vector of a Lagrangian particle	$[\text{m}]$
X_k	Molar fraction of species k	$[-]$
y	Spatial coordinate	$[\text{m}]$
Y_k	Mass fraction of species k	$[-]$
z	Spatial coordinate	$[\text{m}]$
Z	Mixture fraction	$[-]$

CONTENTS

Greek characters

Symbol	Description	Unit
α_l	Liquid volume fraction	[-]
χ	Scalar dissipation rate	[s ⁻¹]
δ_{ij}	Kronecker symbol	[-]
η_κ	Kolmogorov scale	[m]
Γ_l	Rate of change per unit volume of the liquid phase mass	[kg/m ³ /s]
Γ	Rate of mass change per unit vol. in the gas phase by evap.	[kg/m ³ /s]
$\Gamma_{u,i}$	Momentum exchange through mass exchange	[kg/m ² /s ²]
κ	Flame stretch	[s ⁻¹]
λ	Heat conduction coefficient	[W/m/K]
μ	Molecular viscosity	[Pa s]
μ_t	Turbulent viscosity	[Pa s]
ϕ	Equivalence ratio	[-]
Π_g	Sensible enth. rate of ch. per unit vol. in the gas phase by evap.	[W/m ³]
Π_l	Sensible enth. rate of ch. per unit vol. in the liq. phase by evap.	[W/m ³]
ρ	Gaseous density	[kg/m ³]
ρ_k	Density of the gaseous species k	[kg/m ³]
ρ_l	Liquid phase density	[kg/m ³]
τ_{ij}	Stress tensor	[N/m ²]
τ_{ij}^t	Turbulent stress tensor	[N/m ²]
τ_p	Particle relaxation timescale	[s]
Φ_g^c	Sensible enth. rate of change in the gas due to conduction	[W]
Φ_g^{ev}	Sensible enth. rate of change in the gas due to evaporation	[W]
Φ_l^{ev}	Sensible enth. rate of change in the liq. due to evaporation	[W]
Φ_l^c	Sensible enth. rate of change in the liq. due to conduction	[W]
Φ_l	Liquid volume flux	[m ³ /s/m ²]
$\dot{\omega}_k$	Species source term (in mass) of species k	[kg/m ³ /s]
$\dot{\omega}_{Y_k}$	Species source term (divided by density) of species k	[s ⁻¹]

Dimensionless numbers

Symbol	Description
B_M	Spalding number for mass transfer
B_T	Spalding number for heat transfer
Le	Lewis number
Nu	Nusselt number
Pr	Prandtl number
Pr_t	Turbulent Prandtl number
Re	Reynolds number
Re_t	Turbulent Reynolds number
Re_p	Particle Reynolds number
Sc	Schmidt number
Sh	Sherwood number
St	Stokes number
We	Weber number

Indices and superscripts

Symbol	Description
g	Index of a gaseous phase quantity
l	Index of a liquid phase quantity
p	Index of a solid phase quantity
F	Index of a fuel quantity
$glob$	Index of a quantity at global equivalence ratio
O	Index of an oxidiser quantity
st	Index of a quantity at stoichiometric equivalence ratio
tot	Superscript of an integrated quantity

CONTENTS

Acronyms

Acronym	Definition
ARC	Analytically Reduced Chemistry
CDSM	Chemical Discrete Sectional Method
CFD	Computational Fluid Dynamics
CFL	Courant-Friedrichs-Lewy
CMC	Conditional Moment Closure
CRZ	Central Recirculation Zone
DNS	Direct Numerical Simulation
DOM	Discrete Ordinate Method
DQ	Direct Quadrature Method Of Moments
DRG	Directed Relation Graph method
DRGEP	DRG with Error Propagation
DSM	Discrete Sectional Method
DTFLES	Dynamically Thickened Flame model for LES
FIM-UR	Fuel Injection Method by Upstream Reconstruction
FPI	Flame Prolongation of Intrinsic Low-Dimensional Manifold
GRC	Globally Reduced Chemistry
HACA	Hydrogen Abstraction Carbon Addition
HMOM	Hybrid Method Of Moments
IRZ	Inner Recirculation Zone
ISL	Inner Shear Layer
LES	Large Eddy Simulation
LST	Lagrangian Soot Tracking
LOI	Level Of Importance
LW	Lax-Wendroff
MOM	Method Of Moments
MOMIC	Method Of Moments with Interpolative Closure
NDF	Number Density Function
NSCBC	Navier-Stokes Characteristic Boundary Conditions
ORZ	Outer Recirculation Zone
PAH	Polycyclic Aromatic Hydrocarbons
PDF	Probability Distribution Function
PEA	Pre-Exponential Adjustment
PIV	Particle Image Velocimetry
PLIF	Planar Laser-Induced Fluorescence
PSD	Particle Size Distribution
PSDF	Particle Size Distribution Function
PSR	Perfectly Stirred Reactor
PVC	Precessing Vortex Core
QSS	Quasi-Steady State
QSSA	QSS Approximation
RANS	Reynolds Average Navier-Stokes
RMS	Root-Mean-Square
ROS	Reactive Oxygen species
RQL	Rich-burn, Quick-Quench, Lean-Burn
RSR	Resonantly-Stabilized Radicals
RTE	Radiative Transfer Equation
TF	Thickened Flame
TFLES	Thickened Flame model for LES
TTGC	Two-step Taylor-Galerkin scheme version C

CONTENTS

Part I

Context of the study

Chapter 1

Introduction

Contents

1.1	Global context: combustion-generated pollutants	9
1.2	Effect of PM from aircraft engines on health and climate	12
1.3	Aeronautical burner design: status and constraints	14
1.4	Need and challenges for numerical simulations of pollutant emissions	16
1.4.1	Soot prediction in aeronautical burners: the SOPRANO project	18
1.5	Objectives and structure of the PhD thesis	18
1.5.1	Organisation of the manuscript	19
1.5.2	Brief introduction of the target configurations	20

1.1 Global context: combustion-generated pollutants

The global demand in energy has been increasing continuously from decades driven by a robust global economy and higher heating and cooling needs in some parts of the world. In response to that high demand, the world's total energy supply which is almost exclusively based on combustion processes burning fossil resources, is still increasing as observed in Fig. [1.1a](#). Relying on practical combustion devices implies several policy dealing with energy independence, human health and environment. The exhaustion of fossil fuels and the environmental pollution thus generated by combustion is in itself a major preoccupation. This finding has been globally recognized for few years however fuel depletion, growing pollution and global warming still continue. Figure [1.1b](#) highlights the rising levels of CO₂ emissions for different fossil fuels which contribute to global warming. In 2017, transport accounted for nearly one quarter of direct CO₂ emissions from fuel combustion (Fig. [1.2](#)). Road vehicles were responsible for nearly three-quarters of transport CO₂ emissions followed by aviation and shipping sectors which both continue to rise. It can be observed on Fig. [1.3](#) that the world aviation annual traffic will double in just 15 years. In response to a significantly increase in air traffic, regulatory measures have been adopted by many countries to impose a drastic reduction of pollutant emissions and fuel consumption. For example, in 2017, it adopted CO₂ emissions standards were adopted for airplanes, to be enforced by national aviation authorities. These standards aim to limit the emissions of newly designed aircrafts.

1. INTRODUCTION

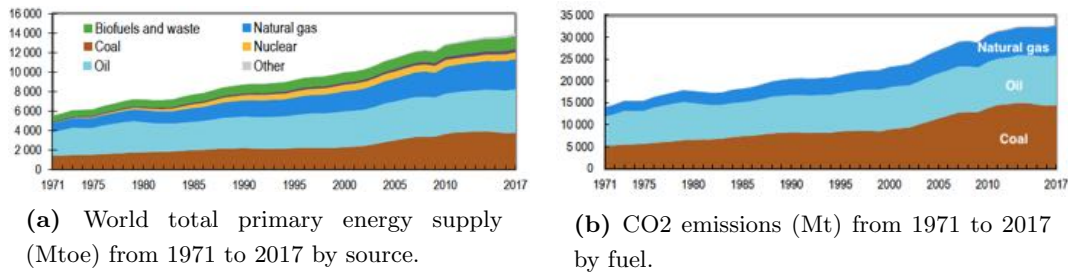


Figure 1.1: World total primary energy supply by source (a) and CO2 emissions by fuel (b) from 1971 to 2017 (Extracted from International Energy Agency (IEA) 2019)

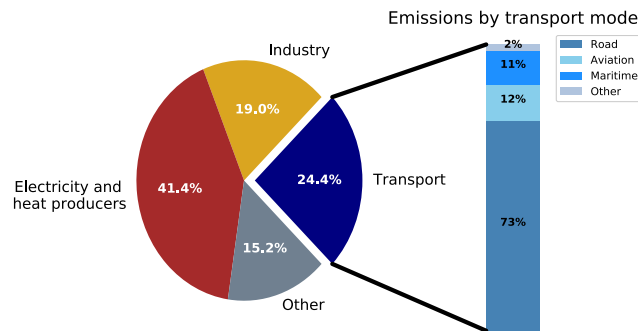


Figure 1.2: Rescaled direct CO₂ emissions by sector and by transport mode, data extracted from IEA 2019

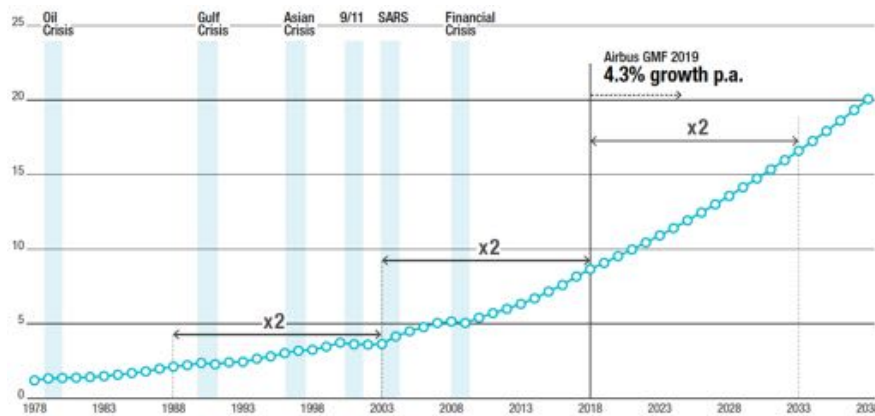


Figure 1.3: International Civil Aircraft Organization (ICAO) air traffic data and Airbus traffic forecast in revenue passenger kilometers (trillion unit). From [1].

1.1 Global context: combustion-generated pollutants

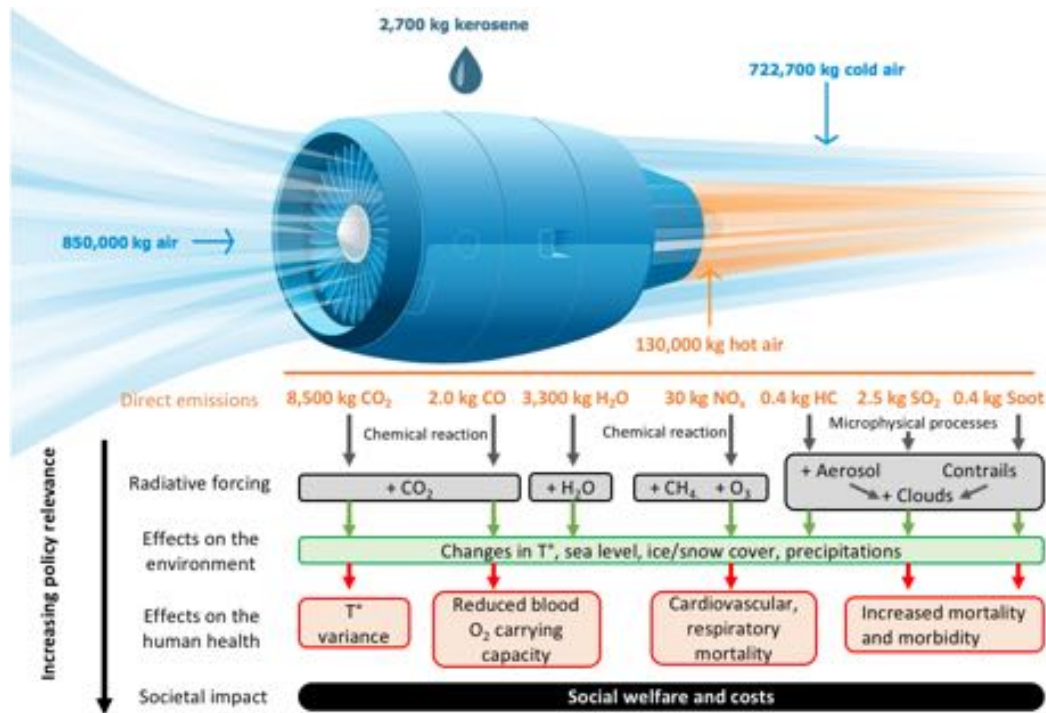


Figure 1.4: Emissions from a typical two-engine jet aircraft during 1-hour flight with 150 passengers (extracted from the *European Aviation Environmental Report 2019*), and their impact (adapted from the *European Aviation Environmental Report 2019*, Masiol *et al.* [3] and Lee *et al.* [4]).

Of course, CO₂ emission is not the only target of regulations. Incomplete combustion products such as carbon monoxide (CO), unburnt hydrocarbons (HC), sulfur dioxide (SO₂), nitrogen oxides (NO_x), or poly-cyclic aromatic hydrocarbons (PAHs), and soot particles also contribute significantly to global warming. These pollutants pose significant and growing threats to the environment and human health as depicted in Fig. 1.4 which quantifies the mean pollutant emissions for a typical two-engine jet aircraft during 1-hour flight with 150 passengers. Each of them affects both the environment and human health in their own way increasing the relevance to regulate all of them. Stringent regulations have already been adopted for CO₂, noise, CO and NO_x emissions and regulations for Particulate Matter (PM) and PAHs are expected for the coming years [2].

PAHs, depicted as HC in Fig. 1.4, are an important class of organic pollutants, because of their toxic effects on ecosystem and harmful effects for human health [5]. In addition to these negative effects, PAHs are soot precursors by means of radical addition reactions on double bonds, cyclization, and formation of resonantly stabilized radicals resulting in incipient soot [6]. Particulate matter (PM) and PAHs emissions from aircraft engines are produced as a result of incomplete combustion of organic materials in fuel-rich and high-temperature environments. As depicted in Fig. 1.4,

1. INTRODUCTION

these emissions affect global climate, local air quality, and public health in a direct or indirect way.

1.2 Effect of PM from aircraft engines on health and climate

PM are considered as aerosol and one of the most prominent groups of toxic air pollutants related to health effects, as being therefore of international concern today. PM are divided into two main classes of ambient air pollution particles depending on their diameter [7]. The first class is composed of coarse particles with diameter below $10\mu m$ (PM_{10}), defined as inhalable particles. The second class contains fine particles with diameter smaller than $2.5\mu m$ ($PM_{2.5}$), defined as respirable particles. However, recently another size class has been defined for ultra-fine particles smaller than $0.1\mu m$ ($PM_{0.1}$). Particle size is important for its lifetime in the atmosphere and its airways deposition. As a consequence PM classification is considered to be one of the best indicators for health effects from air pollution and will be used for further regulations [8]. As particle size decreases, deposition occurs deeper in the respiratory system. Particles affect both the pulmonary and cardiovascular systems. Soot particles contribute to numerous adverse health impacts including :

- airway inflammation
- asthma aggravation
- impairment of pulmonary defence mechanisms
- lung cancer
- heart arrhythmia

Recent epidemiological, human and animal model studies have shown that soot particles can trigger the formation of reactive oxygen species (ROS), which may cause oxidative stress, cell death, biological aging and diseases. Once formed into lungs, ROS cause damage to deoxyribonucleic acid (DNA), proteins, tissues, lipids; etc. [9]. They are of additional concern because of their ability to pass through cell walls and rapidly enter the blood stream due to their size close to virus size as shown in Fig. [1.5]. Immune responses can be affected by these particles, which drive pro-allergic inflammation through the generation of oxidative stress [10].

In addition to health concerns, aircraft also affects climate through CO_2 emissions (Fig. [1.4]) and a number of non- CO_2 climate forcing agents that are unique to this sector of transportation including soot particles and SO_2 . According to the Intergovernmental

1.2 Effect of PM from aircraft engines on health and climate

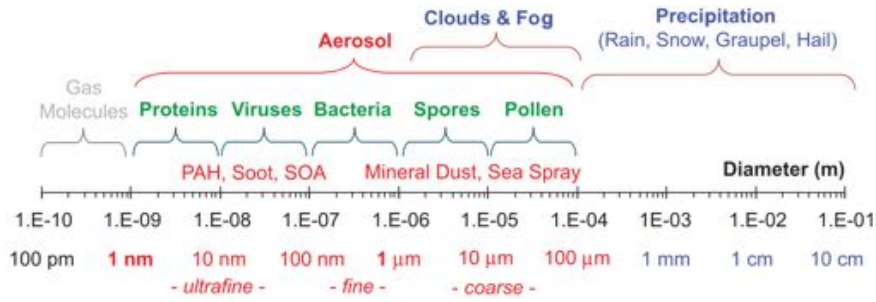


Figure 1.5: Size range of atmospheric aerosols and hydrometeors. (Extracted from [9])

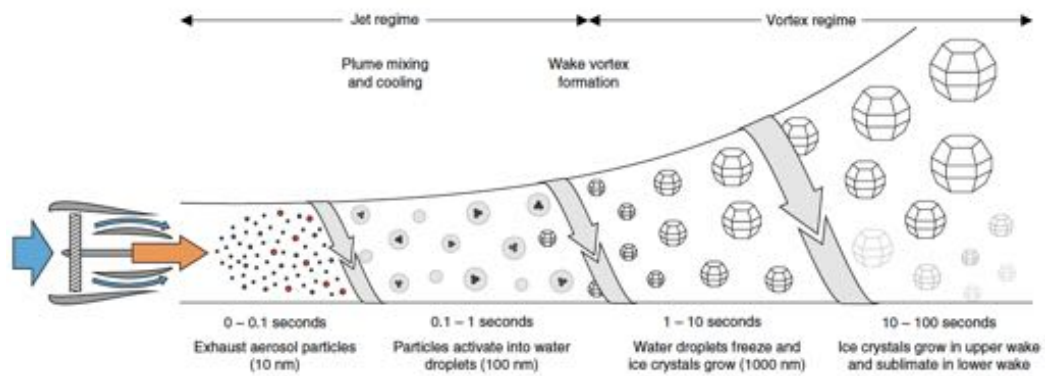


Figure 1.6: Processes influencing the contrail formation stage. (Extracted from [15])

Panel on Climate Change (IPCC) [11], these forcing agents accounted for nearly 4% of the global radiative forcing from all human activities in 2011, and represent the largest aviation radiative forcing component. PM emissions impact climate in three different ways. First, the black carbon component of PM is a strong light absorber, it directly contributes to climate forcing by absorbing solar radiation and increasing atmospheric temperatures [12]. Second, black carbon deposition on snow and ice accelerates melting [13]. Third, PM emissions alter the radiative properties and lifetime of clouds [14]. Additionally, the PM emitted from aircraft turbine engines at high altitudes act as vapor condensation nuclei initiating contrails and cirrus clouds [15]. While CO₂ emissions contribute to climate change on long time scales (about centuries), contrails affect environment on short time scale (about hours for long-lived contrails).

In Fig. 1.6, the aerosol particle types present in aircraft exhaust plumes are shown to comprise emitted soot particles, nanometre-sized aqueous aerosol particles formed within the plumes and particles mixed into the plumes from the ambient air. In the jet regime, these particles interact with condensable vapours (water vapour mainly) and ionised gas molecules. The different particle types compete for supersaturated vapour in water droplet formation, highlighted in grey. For aircraft emissions, soot particles figure most prominently in droplet formation. These droplets freeze and grow rapidly by uptake of water vapour forming a visible contrail. The contrail formation

1. INTRODUCTION

happens when the ambient temperature falls below the formation threshold determined by the Schmidt-Appleman criterion [16]. Plumes from multiple aircraft engines merge with two wing tip vortices, forming an inhomogeneous wake. The further evolution of ice crystals depends largely on fluid-dynamical processes, in the vortex regime. The downward motion of the vortex pair warms the air causing ice crystal sublimation in the lower wake. Ice crystals present in the upper wake continue to grow by uptake of entrained ice-supersaturated ambient water vapour. Few minutes past emission in the dissipation regime, the organised flow pattern collapses and mixes with ambient air.

Soot particles promote the formation of contrails and contrail cirrus which reflect solar radiation and trap outgoing terrestrial radiation resulting in a net positive radiative forcing [17]. The average effect of contrails on the earth's radiation budget, on radiative forcing and climate, depends on their global coverage and mean optical thickness. Both quantities are not well known and numerical modelisation is a valuable tool to reduce uncertainties about the global effect of contrails. Although the conditions for contrail formation can be fairly well predicted [16], the impact of contrails on radiative forcing strongly depends on the evolution of the number concentration, the size and the shape of ice crystals within the plume (see Fig. 1.6) which are not taken account in contrail formation models [18]. Soot particles provide a large number of potential ice nuclei that will influence contrails and induced cirrus clouds optical properties [15, 18]. Nowadays, uncertainties in soot particle emission indices in cruise regime which are sensitive to operating conditions, engine type, and even fuel composition [19] are one of the main problems to evaluate the radiative potential impact of contrails.

As a result, legislation is becoming more stringent for particulate emissions. The EU air quality directive defines the $\text{PM}_{2.5}$ concentration of $25\mu\text{g}/\text{m}^3$ on an annual basis and will lower a threshold to $20\mu\text{g}/\text{m}^3$ by 2020 [2].

1.3 Aeronautical burner design: status and constraints

Many practical combustion devices, especially aircraft engines, operate locally in non-ideal burning conditions that lead to incomplete combustion and result in the production of carbonaceous compounds. This is mainly due to local hot spots, insufficient mixing of fuel and oxidizer or liquid fuel atomizing of liquid fuels, or too short residence time at high temperatures. Of course, pollutants are formed in the propulsion system which is the most expensive part of the aircraft, representing up to 1/3 of the final aircraft cost. Moreover, the increasing cost of kerosene makes fuel consumption reduction another determinant challenge. Both aspects make the engine a key point of the current aeronautical challenge. Conventional double-flux gas turbines currently

1.3 Aeronautical burner design: status and constraints

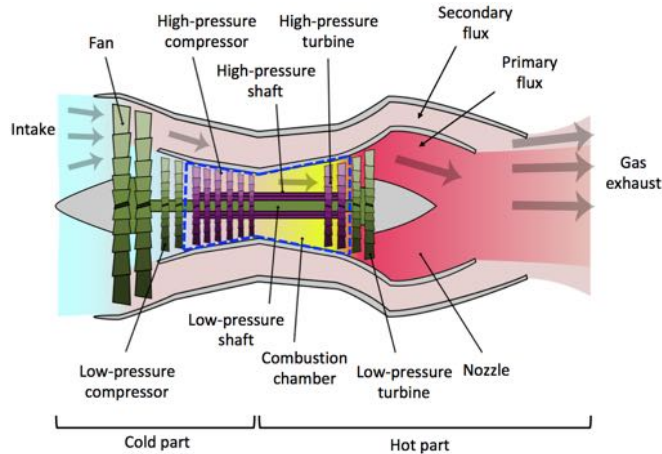


Figure 1.7: Sketch of a conventional double-flux gas turbine engine.

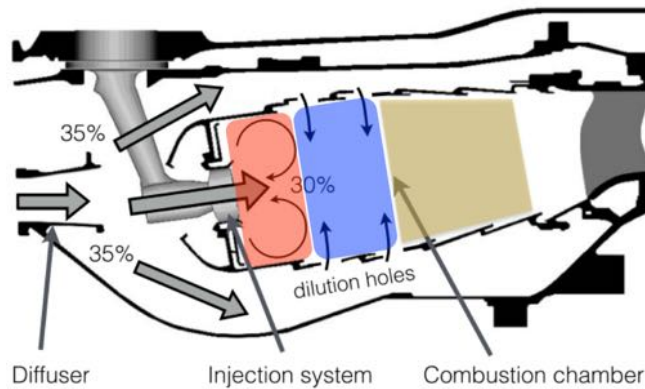


Figure 1.8: Sketch of a conventional RQL combustion chamber (Extracted from [20])

used in civil aircraft is illustrated in Fig. [1.7]. The air entering the primary flux by the fan is pressurized by the low and high pressure compressors to optimize the thermodynamic cycle. In the combustion chamber, air is rapidly mixed with liquid kerosene that evaporates and the fresh gas mixture burns, producing very hot combustion products at high velocity. These accelerated hot products then transfer their kinetic energy to high and low pressure turbines before being released through the nozzle. The turbine drives the compressor and the fan thanks to axial shafts, which is the main role of the primary flux. The major part of the engine thrust is produced by the action-reaction principle: the secondary flux is ejected at a much higher velocity than at intake thanks to the energy transfer from the fan to the secondary flux gases. A zoom of a conventional combustion chamber called Rich Burn, Quick-Mix, Lean Burn (RQL) system is proposed in Fig. [1.8]. It is generally divided in three zones: a primary zone (coloured in red in Fig. [1.8]), an intermediate zone (blue zone) and a dilution zone (yellow zone). Soot particle formation occurs mainly in the primary zone, close to the fuel spray, where fuel and air are not well mixed [21, 22]. The intermediate zone reduces gas temperature to an intermediate level by the addition of a small amount of air to promote the com-

1. INTRODUCTION

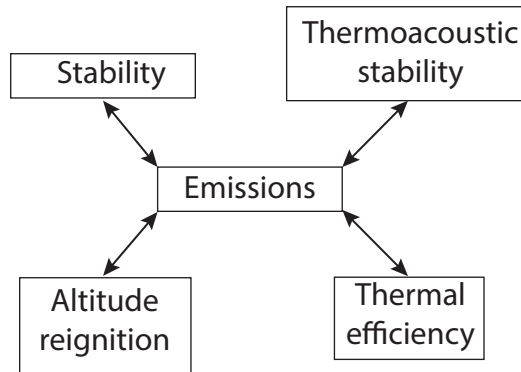


Figure 1.9: Design constraints applying to aeronautical burners.

plete oxidation of carbon monoxide and soot particles by oxidation. The dilution zone provides an outlet stream with a temperature distribution acceptable to the turbine, but encouraging NO_x formation.

From the combustor design point of view, the dual objectives of fuel efficiency and pollutant emissions are contradictory. Higher core engine thermal efficiency requires higher operating pressure and temperature of the combustor, which directly promotes soot emissions. As depicted in Fig. [1.9](#), the design of aeronautical combustion chambers is constrained by high safety and operability requirements over the whole flight envelope, as well as drastic weight and size constraints compared to land gas turbines. Thus the development of low emission innovative design must result from a global optimisation process.

The ICAO has also developed a regulatory standard for non-volatile Particulate Matter emissions from turbofan and turbojet aircraft engines with a rated thrust greater than 26.7 kN [\[8\]](#). Although the regulatory standard is based on soot number and mass emissions, these properties alone are not sufficient for evaluating the air-quality, health, and climate impacts of soot emissions. Regulatory standards will have to take into account particle size, reactivity and morphology to provide a more effective regulatory policy.

1.4 Need and challenges for numerical simulations of pollutant emissions

Given the expected stringent regulatory policies on aircraft engines and the constraints in terms of safety and operational requirements illustrated in Fig. [1.9](#), the combination of experimental campaigns and numerical tools like Large Eddy Simulation (LES) are of great help for a better understanding of the combustor behaviour and underlying mechanisms [\[23, 24\]](#).

1.4 Need and challenges for numerical simulations of pollutant emissions

In the last decade, LES have shown their capacity to correctly capture most unsteady features, such as fuel-air mixing, ignition and flame dynamics [24, 25, 26, 27] and has been able to accurately predict pollutants like CO and NO_x [28, 29, 30, 31]. Although the chemical processes for CO and NO_x are rather well understood and characterized (compared to soot), their accurate prediction in real aeronautical geometries remains a challenge due to the complex turbulent spray flame in the multiphase combustion, turbulence, air cooling and dilution, or radiative and wall heat transfer. To understand pollutant formation in real combustors, it is necessary to consider first academic configurations, well characterized by many measurement techniques. Indeed, in real systems at real operating conditions, no optical access is possible and measurements are often limited to exhaust gas composition.

Predicting soot emissions is even more ambitious since chemical and physical processes are only partly known and must be better understood. Current knowledge of soot formation has been derived from three types of work [6]:

- **Experimental** : Measurements of soot volume fraction f_v , soot number density N_s and particle size distribution (PSD) typically expressed as $dN/d\log(d_{soot})$.
- **Chemical** : Development of both detailed chemical mechanisms for the formation of soot precursors and detailed soot chemistry models.
- **Numerical** : Development of soot population dynamics models to describe the evolution of the particle ensemble.

All of them are required to predict accurately soot formation using LES. First, chemical mechanisms including accurate PAHs, which are highly reactive and difficult to detect (low levels) compared to classical pollutants, are of crucial importance in soot modeling as a necessary input. Then, a reliable soot chemistry model, where a lot of uncertainties remain, is used to compute soot evolution coupled with an adequate numerical methods to transport soot particles. Finally, thorough validations against experimental measurements are required before computing complex configurations.

Concerning soot prediction in complex configurations, most of the modeling effort relied for a long time on semi-empirical approach [32] by transporting only soot mass fraction and number density, these methods relied on many assumptions and correlations from experimental observations. Although efficient in terms of numerical cost, these methods only give access to a mean soot particle diameter and are however not able to describe soot formation from one configuration to the other with the same set of constants. An alternative to semi-empirical methods for soot prediction is to consider

1. INTRODUCTION

PSD, relying mainly on either complex mathematical methods to account for particle polydispersity or stochastic approaches where all soot processes are calculated by probability. These methods, more accurate, can be difficult to implement and can require considerable numerical resources in their execution.

1.4.1 Soot prediction in aeronautical burners: the SOPRANO project

This PhD has been supported by the H2020 project SOPRANO (SOot Processes and Radiation in Aeronautical inNOvative combustors) 2016-2020. This industrial and academic research project aims at providing new elements of knowledge, analysis and improved design tools, opening the way to alternative designs of combustion systems for future aircraft capable of simultaneously reducing gaseous pollutants and particles, and improve the liner lifetime. Therefore, the SOPRANO project will deliver more accurate experimental and numerical methodologies for predicting the soot emissions in academic or semi-technical combustion systems. This will contribute to enhance the comprehension of soot particle formation and their impact on heat transfer through radiation. In parallel, the durability of cooling liner materials, related to the wall air flow rate, is addressed by heat transfer measurements and predictions. Finally, the expected contribution of SOPRANO is to apply these developments in order to determine the main promising concepts, in the framework of current low-NO_x technologies, able to control the emitted soot particles in terms of mass and size over a large range of operating conditions without compromising combustor's liner durability and performance toward NO_x emissions.

To this purpose, a comprehensive numerical methodology for soot prediction has been developed, based on the solver AVBP developed by CERFACS. This methodology relies on detailed chemistry for the gaseous phase, a semi-deterministic Lagrangian approach to transport soot particles in complex configurations and the development of coupling strategy to solve Radiative Transfers Equation (RTE) in order to evaluate soot production in aeronautical burners.

1.5 Objectives and structure of the PhD thesis

Over the past decades, CERFACS has developed an expertise in Computational Fluid Dynamics (CFD) and more specifically in LES with the solver AVBP¹. AVBP has been continuously improved by students and senior researchers, and has been successfully employed to study a wide range of turbulent flow applications, in relatively complex geometries. Historically, semi-empirical models [32, 33, 34, 35] were used to evaluate soot production using AVBP. As said in Sec. 1.4, these models based on empirical

¹<http://www.cerfacs.fr/avbp7x/>

constants have shown their limits. There is a consensus however in the soot community that PSD must be taken into account to correctly capture soot evolution. Moreover, soot size is critical for associated health and environmental concerns and should be taken into account in future PM emissions regulations.

The available computational power is constantly increasing and the use of more accurate soot models is becoming affordable [36, 37, 38]. The main objective of this thesis is to investigate on the capabilities of a semi-deterministic Lagrangian approach for soot prediction in terms of accuracy; and to confront this approach to the existing techniques in terms of computational cost. Another objective is to combine a detailed soot model to an Analytically Reduced Chemistry (ARC) [39, 40], which ensures a good description of the flame structure and dynamics and species involved in the soot model considered.

1.5.1 Organisation of the manuscript

The manuscript is organised as follows:

- **Part I:** This part provides a brief overview of the pollutant emissions and some concerns regarding their negative effects in Chapter 1. In Chapter 2, mechanisms for soot particle formation and soot experimental characterization are discussed together with the soot modelling methods available in the literature.
- **Part II:** This part focuses on modeling of turbulent reactive flows as well as the numerical methods developed and implemented in this work. In Chapter 3, the theoretical concepts of combustion are described, and the sets of equations solved for both the gas and liquid phases are given. The Chapter 4 presents the Lagrangian Soot Tracking approach with a simple soot chemistry model and its evaluation in a complex geometry. Then Chapter 5 details the selection of the appropriate chemical schemes for the fuels considered in this PhD, from gaseous C_2H_4 to liquid aviation jet fuel Jet A1, with a special attention to soot precursors. Finally, the proposed Lagrangian Soot tracking approach with a more sophisticated soot chemistry model is detailed and validated in canonical flames configurations (Chapter 6).
- **Part III:** The third part focuses on performing, validating and analysing LES of turbulent sooting flames. LES and reactive models involved in such computations are defined in Chapter 7. Two turbulent sooting flames are then studied: a confined pressurized sooting ethylene-air swirled flame in Chapter 8 and an atmospheric Jet A-1-air sooting spray flame in Chapter 9. For both cases, soot formation and particles size distributions dynamics are analyzed.

1.5.2 Brief introduction of the target configurations

The operating conditions for two target configurations will be widely employed throughout the first chapters of the thesis to build and validate the different models. For the clarity of the reader, they are briefly introduced at this early stage:

- The **FIRST** configuration is a swirled pressurised combustor operated with ethylene. The combustor burns in a lean, non-premixed regime. The selected operating point operates under overall lean conditions ($\phi_{glob} = 0.86$), the primary combustion zone being characterized by an overall rich equivalence ratio ($\phi_{prim} = 1.2$). It operates under moderate pressure $P = 3$ bars with secondary air injection, fuel and air are supplied at $T_{in} = 300$ K.
- The **UTIAS jet A-1 burner** is a swirled turbulent spray flame configuration burning kerosene fuel. The combustor operates at ambient conditions $P = 1$ bars, $T_{in} = 300$ K.

Chapter 2

Soot formation and its modeling

In this chapter, generalities about soot formation and its modeling are discussed.

First soot particle is described in terms of morphology. Then the soot formation mechanisms and their impact on soot particles are detailed.

Second, the basis of numerical methods is introduced and the different modeling approaches are summarised. The selection of the retained soot model, the Lagrangian soot tracking approach, is discussed.

Contents

2.1	Soot morphology and internal structure	21
2.2	Soot formation and oxidation mechanism	28
2.2.1	Mechanisms involved in soot formation	28
2.2.2	Soot growth	31
2.2.3	Soot oxidation and fragmentation	34
2.3	Numerical methods for soot prediction	35
2.3.1	Governing Equations	36
2.3.2	Numerical approach	39
2.3.3	Choice of the numerical method	46

2.1 Soot morphology and internal structure

Soot differs from other pollutants in its composition. Contrary to CO_2 , CO or NO_x soot is a carbonaceous material containing thousands or millions of carbon atoms. The transition from fuel containing a few carbon atoms to a solid carbonaceous agglomerate is a complex physical and chemical process. A typical morphology of such a material from aircraft combustion devices is shown in Fig. 2.1. It is obtained from Transmission Electron Microscopy (TEM) analysis of soot particles which is the preferred method for direct characterization of aggregate structure. Soot aggregate is shown to be composed of primary particles with a chain-like structure [41]. The primary particles are near-spherical in shape with a diameter in the range of 10 nm to 80 nm [6, 42, 43, 44, 45]. The primary soot particles are made of about 10^4 numbers of crystallite structures, observed by High Resolution Transmission Electron Microscopy (HRTEM) [41, 46]. HRTEM images in Fig. 2.2 highlight the different levels of structure describing soot particles for two engine powers (low 4–7% and high 100% of the maximum thrust). First row shows

2. SOOT FORMATION AND ITS MODELING

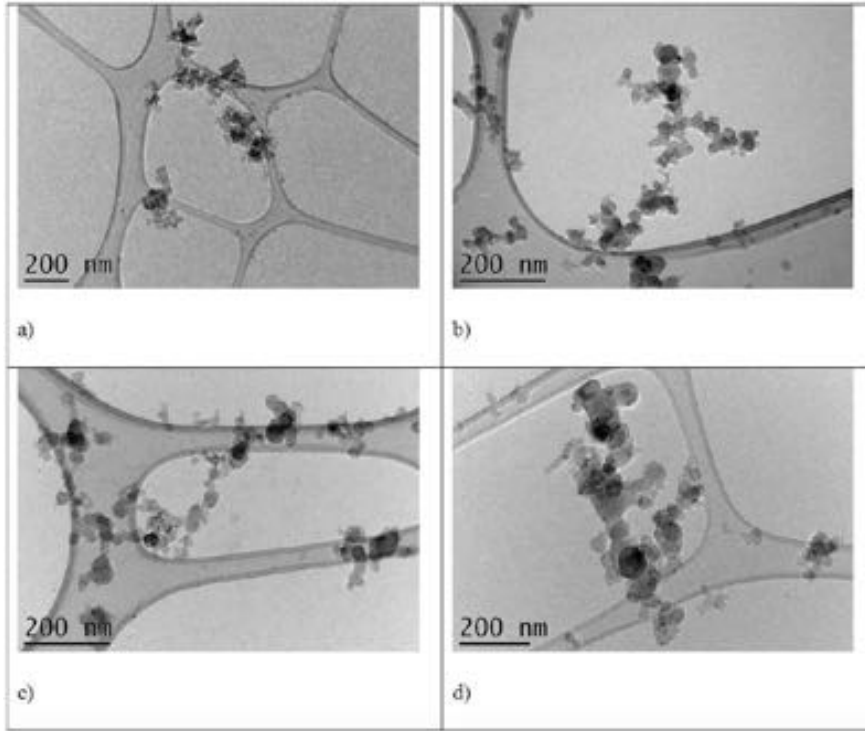


Figure 2.1: TEM images of soot aggregates emitted from a SaM146 engine at different thrust levels. a) 30% of the maximal thrust b) 70% of the maximal thrust c) 85% of the maximal thrust d) 100% of the maximal thrust. (Extracted from [18])

the aggregate size, the macro-structure. Second row displays the primary particle size, the micro-structure. The third row represents the nano-structure within the individual primary particle composed of crystallite structures. This crystallinity arises due to the stacking of planar PAH indicating that PAHs are soot precursors [41]. The bottom part of Fig. [2.2] shows a succession of hollow centers highlighting the presence of an amorphous structure using HRTEM. This amorphous structure arises from the random alignment of aromatic structures [46]. Figure [2.3] shows a schematic of the formation of such amorphous structures [47]. The clustering of PAHs (nanostructure) forms the incipient soot particle with a spherical shape forming a nucleation mode in terms of PSD (Mode-I in Fig. [2.3]). The incipient soot particle is a primary particle (microstructure), then aggregation promote the formation of soot fractal-like aggregates (macrostructure) that vary widely in size and shape. These soot aggregates are responsible for the second mode of the PSD. The presence of such soot aggregates and the persistent nucleation in rich flames both explain the bimodality of the soot PSD. In most cases soot particle is described at the macro-scale through its volume v and its surface area s . At micro-scale, soot particle is composed of n_p primary particles with the same primary particle diameter d_p [48]. The relation between macro and micro structures can be expressed

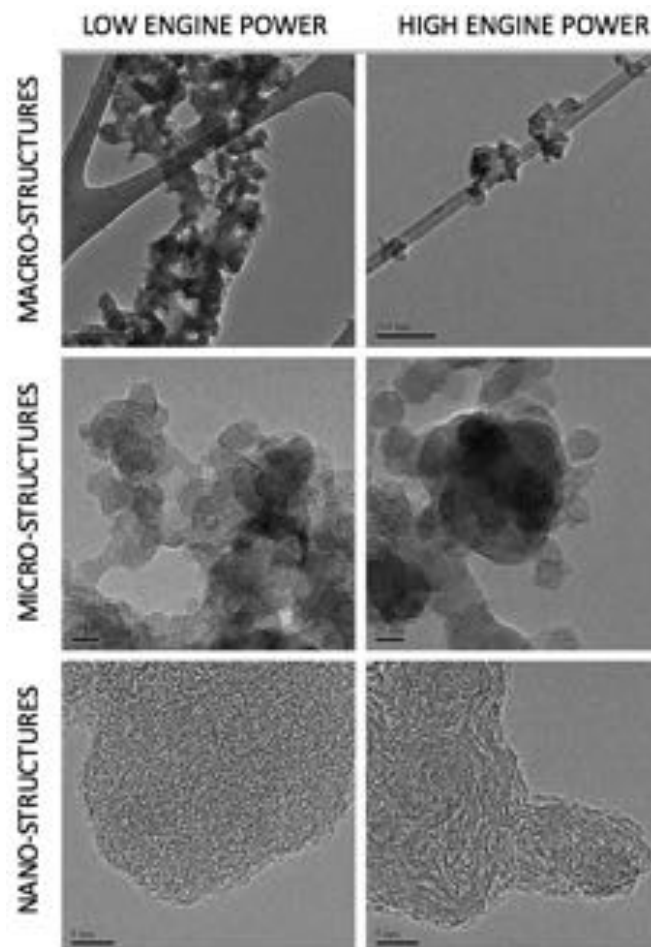


Figure 2.2: HRTEM images of derived soot macro - micro - and nano-structures; left column images are for low engine power level (4 – 7% of the maximum thrust) and right column images are for high (maximum thrust) engine power. (Extracted from [\[46\]](#))

2. SOOT FORMATION AND ITS MODELING

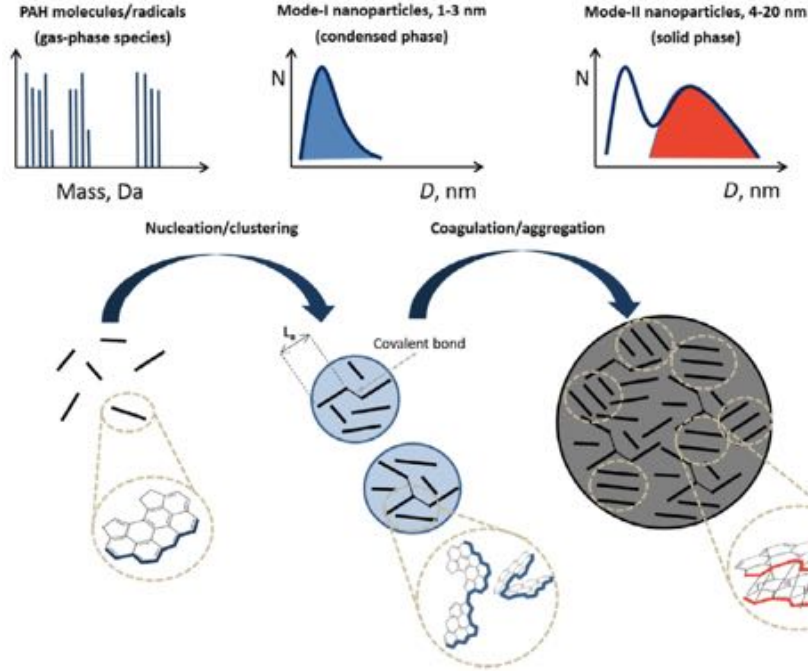


Figure 2.3: Schematic crystallite structure in soot nucleation and growth. (Extracted from [47])

as follows:

$$\begin{cases} d_p = \frac{6v}{s} \\ n_p = \frac{s^3}{36\pi v^2} \end{cases} \quad (2.1)$$

It can be noted that a spherical particle, such as an incipient particle can also be described as an aggregate with $n_p = 1$ and $d_p = d = (6v/\pi)^{1/3}$. However, these characteristics are not sufficient to describe soot aggregate structures. Those are typically characterized by a power law relationship, $n_p \propto (d_c/d_p)^{D_f}$, where the number of primary particles is proportional to the ratio of the collision diameter d_c of an aggregate to the primary soot particle diameter d_p and the fractal dimension D_f , which is about 1.8 for soot aggregate [49, 50, 51, 52]. The collisional diameter d_c , also called gyration diameter in the literature, is essential to describe collisional phenomena of soot aggregates. Following the definition of n_p , the collisional diameter reads :

$$d_c \propto d_p n_p^{1/D_f} \quad (2.2)$$

In addition to a complex internal structure, soot morphology is affected by many parameters that are listed below together with their impact on soot morphology.

- **Effect of pressure on soot morphology:** Pressure has been shown to significantly influence soot concentrations in diffusion flames [53]. Recently, Vargas et al. [54] have investigated pressure influence on soot PSDF and morphology, showing that the soot number density increases with increasing pressure. Measurements at elevated pressure indicate that the effect of pressure is to increase

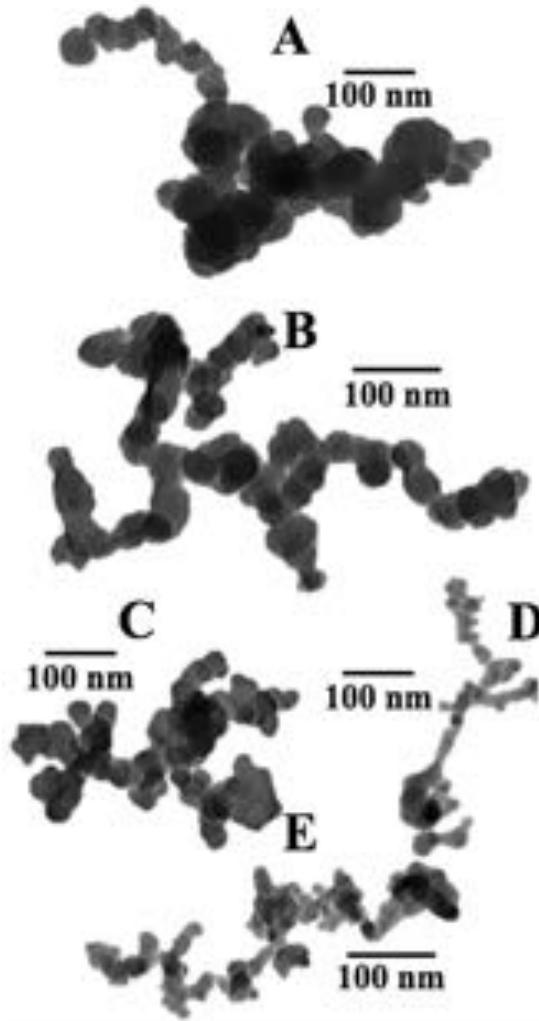


Figure 2.4: TEM images of soot aggregates at 2.3 atm (A), 4 atm (B), 5.4 atm (C), 7.1 atm (D), and 10 atm (E). (Extracted from [55])

the number of incipient soot particles, also called soot nuclei and to decrease the primary particle size as shown in Fig. [2.4]. The increase of soot number density can be explained by the reduction of particle collision rate with increasing pressure. The decrease of particle size is attributed to the reduction in the hydrogen radical concentration with increasing pressure leading to reduced soot surface growth, which will be detailed in Sec. [2.2].

- **Effect of temperature on soot morphology:** Temperature plays a crucial role in soot formation, especially high temperature environment which promotes soot formation. Experimental studies have shown that soot volume fractions from various fuels exhibit a "bell-shaped" curve as a function of temperature in both shock tubes and laminar premixed flames [56, 57, 58]. It has been highlighted that flames at low temperature favor soot bimodality with large soot aggregates [57],

2. SOOT FORMATION AND ITS MODELING

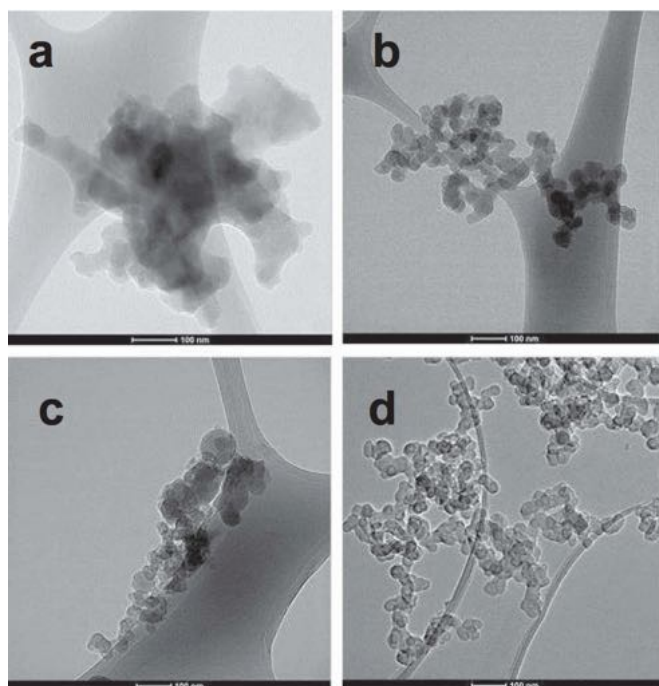


Figure 2.5: TEM images of soot incipient (a,c) and mature soot (b,d) for high flame temperature (top: a,b) and low flame temperature (bottom: c,d). (Extracted from [59])

while flames at high temperature favor unimodality of the soot PSD. Apicella et al. [59] investigated the soot properties in laminar premixed ethylene flames at different flame temperatures. TEM images of both incipient and mature soot for high and low flame temperature are shown in Fig. 2.5. For both high and low temperature flames, the nanostructure for mature soot is similar. However, it was found that nascent soot formed at low flame temperature is more hydrogenated, reactive and less aromatic while soot nuclei formed in the higher temperature flame undergoes enhanced dehydrogenation and aromatization processes.

- **Effect of fuel on soot morphology:** The fuel composition plays an important role in the nanostructure of soot. In laminar premixed flame, soot formed from aromatics (benzene) were found to have a core organized structure compared to ethylene [60], as shown in Fig. 2.6. This was explained by the flame environment containing a higher concentration of smaller PAHs including benzene, compared to aliphatic flames (ethylene). In addition, the small content of light hydrocarbons avoids their intrusion on the particle nuclei limiting the degree of disorder in the soot [61]. Recently, fuels of practical interest have been investigated in terms of soot properties. In a premixed flame [62], surrogate mixtures of m-xylene/n-dodecane and n-butanol/n-dodecane (oxygenated) have been studied. A similar structure has been observed for each fuel, however the mixture of n-butanol/n-dodecane presented a greater loss of structure and a much higher oxidation rate.

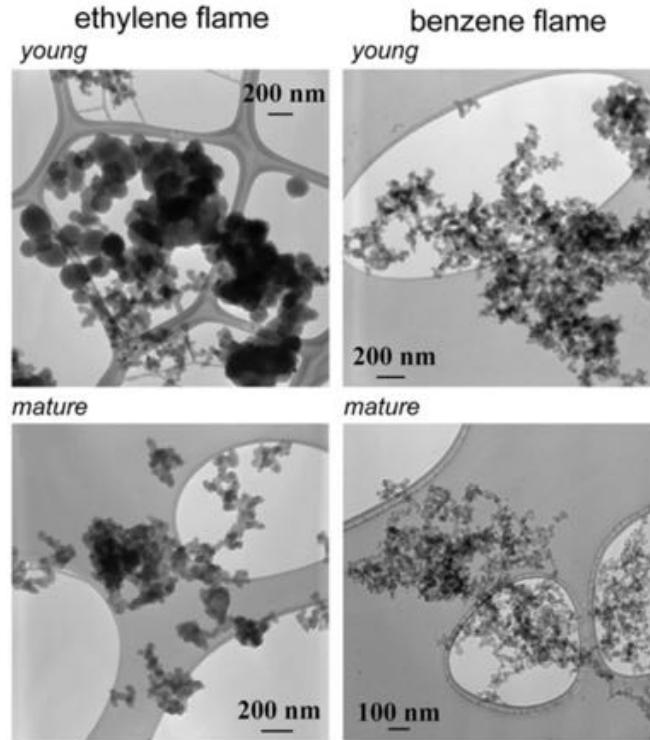


Figure 2.6: TEM images of young and mature soot for ethylene and benzene fuel. (Extracted from [60])

For a better understanding, Botero et al. [63] developed an image analysis code in order to quantify the structure of soot particles from HRTEM images. The morphology and nanostructure of soot particles were investigated in liquid-fuelled diffusion flames, varying the fuel: heptane, toluene, a commercial gasoline and an iso-volumetric heptane-toluene mixture. The main differences in the soot structure were the arrangement and the degree of order of the aromatic structures within each particle. For typical kerosene fuel, the impact of distillate fractions on soot was investigated showing a strong impact on premixed stretch-stabilized flames [64]. Indeed, the decomposition of such complex fuel via pyrolysis and evaporation process (for liquid fuel) affects directly the soot morphology. Information on the morphology and nanostructure of practical fuels or surrogates remain scarce and are of great importance to understand sooting phenomena.

Pressure, temperature and fuel characterize different structures and affect soot reactivities, which is crucial for determining its toxicity [65]. Practical combustion devices evolve typically under these conditions, i.e., high pressure, high temperature and burning kerosene (complex) fuel generating large macro-structures [18]. Actually, these conditions impact mainly soot processes, which must be identified, and then change the morphology evolution. Physical and chemical processes involved in soot morphological evolution are described in this chapter.

2. SOOT FORMATION AND ITS MODELING

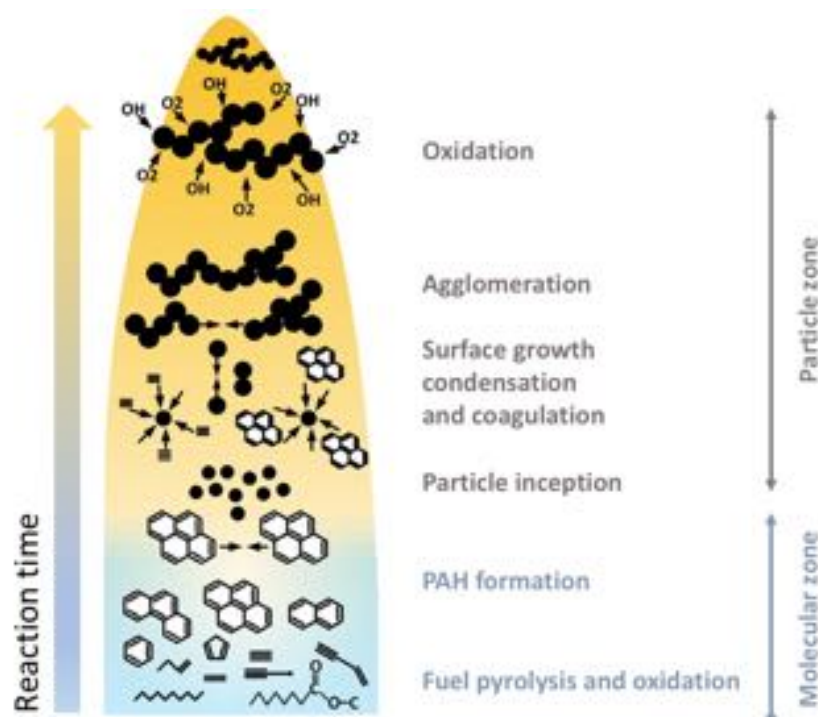


Figure 2.7: Schematic representation of soot evolution. (Adapted from [66])

2.2 Soot formation and oxidation mechanism

The formation and evolution of soot particles in flames are the result of complex mechanisms including both chemical and physical processes. These processes, illustrated in Fig. 2.7, include: initial gas-phase reactions, gas to condensed-phase transition corresponding to particle nucleation, particle mass and size growth through coagulation/coalescence, heterogeneous surface reactions and condensation of gaseous species and particle oxidation reactions, when oxygen is available in the flame. The whole mechanism takes place at high temperature and with a time scale of the order of a few milliseconds. Therefore, understanding the soot formation process in combustion is a great challenge.

2.2.1 Mechanisms involved in soot formation

2.2.1.1 Soot precursors formation

The soot formation process starts with the chemical decomposition reactions of fuel molecules. Successively, pyrolysis and then oxidation of the fuel lead to the formation of smaller carbon species, such as acetylene (C_2H_2). The contribution of C_2H_2 to aromatics formation via the H-Abstraction, Acetylene addition (HACA) mechanism was proposed in [67]. Then, the important contribution of resonantly-stabilized radicals (RSR) such as propargyl radical (C_3H_3) has been shown in the formation of the first

2.2 Soot formation and oxidation mechanism

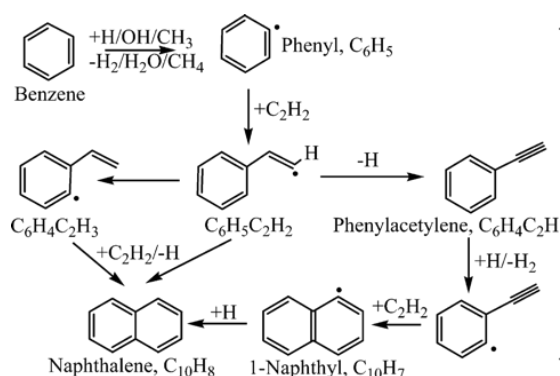


Figure 2.8: HACA mechanism between benzene and naphthalene. (Extracted from [70])

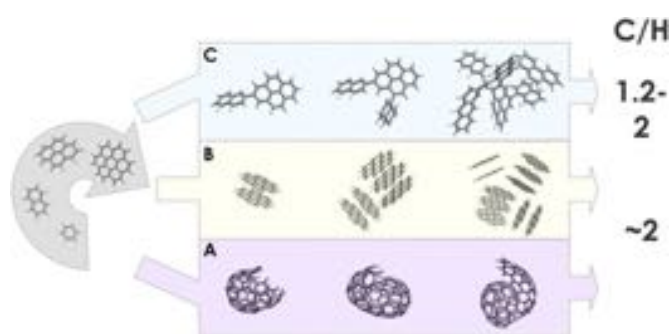


Figure 2.9: Conceptual mechanisms of soot particle nucleation: A) Fullerenic mechanism ; B) Dimerization process ; C) PAH addition (Extracted from [6])

aromatic, benzene ($C_6H_6 \equiv A1$) [68]. It is a key precursor since it is the first aromatic species and therefore the starting point of PAH and consequently of soot formation. Like for benzene formation, the HACA mechanism plays a key role in the formation of PAH [67, 69]. The HACA mechanism comprises two repetitive steps, which are first the abstraction of hydrogen atom forming a radical, and second the addition of acetylene on the radical site. This mechanism is illustrated in Fig. 2.8 for the naphthalene ($C_{10}H_8$) formation starting from benzene. Similar to benzene formation, RSR contribute to PAH formation, which has been confirmed experimentally [71, 72, 73] and theoretically [74, 75].

2.2.1.2 Soot nucleation

As discussed in Sec. 2.1, HRTEM reveals that soot are mainly composed of PAHs, which are then considered as the dominant class of precursors. Soot nucleation characterizing the transition from gaseous phase to solid phase is probably the less known process of soot formation. Various hypothetical pathways for soot nucleation have been suggested [6]. These conceptual pathways are depicted in Fig. 2.9 and discussed hereafter.

- **Fullerenic mechanism:** It concerns the evolution of stacked PAH together with presence of five-rings aromatics that can bend the structure into curved fullerene-

2. SOOT FORMATION AND ITS MODELING

like structures as illustrated in Fig. 2.9A. The consumption of such structures was observed [76] and attributed to their interactions with the abundant small carbon species to form soot. However, this hypothesis was discarded since almost no large molecules of fullerene-like can be found in the flame environment and this mechanism is too slow compared to soot inception.

- **PAH dimerization:** According to Frenklach and Wang [77], soot nucleation was explained to occur through physical colliding PAHs, leading to the formation of PAH dimers. This dimerization process is a pathway explaining soot inception in high-temperatures regions as shown in Fig. 2.9B. Schuetz and Frenklach [78] attempted to understand the non-equilibrium dynamics of dimerization process performing molecular dynamics simulation on the collision of pyrene under flame conditions. Their work has confirmed the dimerization compatibility as soot formation pathway in terms of chemical timescale.
- **PAH addition:** This nucleation process, shown in Fig. 2.9C), is linked to the chemical growth of nascent soot from PAH species. This growth mechanism proposed by D’Anna and coworkers [79], also involves PAH coalescence as the dimerization process. The continuous mass and size growth of three-dimensional, cross-linked, ring-ring aromatic structures leads to the properties of nascent soot. The repetitive reaction sequences involved in this pathway can be depicted by :



where A_i and A_{i^-} represent the PAH species and its radical respectively. Subscript i , j or $i + j$ refers to the size of PAHs. This mechanism explains a variety of chemical structures as a result of collisions with different PAHs. However, this mechanism cannot explain the persistent particle nucleation into the post-flame region [57], where the presence of H atoms, is not sufficient to trigger soot formation.

These conceptual pathways, often used for soot modeling (especially the PAH dimerization), still cannot explain the transition from gas phase to solid phase. In addition to these conceptual pathways, Johansson and coworkers [80] proposed a new mechanism called the clustering of hydrocarbons by radical-chain reactions (CHRCR) mechanism that involves a sequential reaction of RSR, involved in benzene and PAH formation. Each sequence in this mechanism forms a more stable RSR and further sustains the mechanism. It initiates with repetitive additions of C_2H_2 , C_2H_3 leading to small resonant species, such as C_3H_3 or C_5H_5 . The growth reaction generates new

RSR with increasingly higher molecular weights. And this mechanism does not require H-abstraction, it is independent of the presence of H atoms and may explain soot formation in post-flame regions [57] contrary to previous conceptual pathways. However, this mechanism is not yet available and to test this hypothetical mechanism, there is a need to establish detailed reaction rates for the many reactions between RSR and other radical and stable hydrocarbon species as well as, the formation of an initial cluster of soot particles and the growth [81].

Meanwhile, *PAH* dimerization is widely used to model soot nucleation and accepted by the soot community.

2.2.2 Soot growth

Once soot particles have been formed by nucleation, the total amount of soot is mainly due to soot growth [82] occurring via several processes:

- **Surface growth:** surface growth by acetylene
- **Condensation:** chemical growth by PAHs
- **Coagulation:** collision of soot particles

Surface growth and condensation increase the total soot mass while coagulation controls the number of soot particles and the particle size.

Surface growth

Surface growth consists in the incorporation of gaseous species to the surface of pre-existing soot particles [83]. It implies an increase of primary particle diameter d_p and then of soot volume fraction without any change in soot particle number. It acts through carbon addition at the surface of soot particles, and C_2H_2 is considered as the main species involved in this carbon addition. The analogy between chemical reactions taking place at PAH surface and those occurring at soot surface has been proposed by Frenklach and Wang [69]. Similarly to benzene and PAH formation, the HACA mechanism is characterized by the following reaction:



where S_c and S_c^* refer to a soot particle with c carbon atoms and its associated radical respectively. Reaction [R2.3] represents the function of S_c^* from S_c by the abstraction of a hydrogen atom at the soot surface. Reaction [R2.4] is the associated deactivation

2. SOOT FORMATION AND ITS MODELING

reaction. Finally, C_2H_2 addition occurs in Reaction [R2.5](#) where C_2H_2 reacts with S_c^* surface at high temperatures [\[69\]](#). However the initial HACA mechanism is known to have different limiting regimes [\[84\]](#).

However the initial HACA mechanism is known to have different limiting regimes [\[84\]](#). A numerous extension to HACA mechanism have been proposed to extend its validity range with different set of Arrhenius parameters [\[85, 86, 87\]](#) or with additional reactions [\[88, 89, 90\]](#) or to add species to contribute to H-abstraction [\[91, 92, 93, 94\]](#).

Zhang et coworkers [\[95\]](#) proposed an alternative to HACA mechanism in the low-temperature regime based on C_2H_2 addition to a hydrogenated aromatic site followed by H Migration (CAHM) that should be more favorable below 1500K in the fuel rich post-flame region. Recently, the progress of quantum and reaction-rate theories enables to improve kinetics and thermodynamics of the HACA reaction step [\[87\]](#) to reproduce the experimental observations. A major concern in the surface growth mechanism is to take into account the soot S_c surface reactivity. Harris and Weiner observed that the rate of surface growth is highly correlated to the particle surface area [\[96\]](#). Surface growth processes can be understood in terms of elementary chemical reactions of surface active sites. As the number of active sites decreases, Frenklach and Wang [\[77\]](#) observed that soot particle reactivity, also called soot particle aging, decreases proportionally. It was explained by the the graphitization of soot particles, corresponding to carbon atoms rearrangement in order to form a more ordered structure. These structure implies a decrease of the number of active sites where carbon addition occurs. The particle aging is typically modeled by a constant correction factor α introduced by Frenklach and Wang [\[77\]](#) and investigated in numerous modeling studies [\[97, 98, 99, 100\]](#). It corresponds to the ratio of active sites to the total number of sites found on the surface of a soot particle proportion of active sites on the surface area, and was originally fitted as a function of the flame temperature. Appel et al. [\[101\]](#) considered the dependence of this parameter α to the flame properties. A similar way to reduce surface growth rate at high temperatures was done introducing additional chemical reaction [\[89, 102\]](#) as stated previously. Blanquart and Pitsch [\[85\]](#) introduced an additional independent parameter to describe the reactivity of soot particle. It is the number of active sites H found on the surface of soot particle, and enables to predict accurately soot formation [\[85, 103\]](#). However, the use of this approach remains limited. Indeed, from a modeling point of view an additionnal parameter to solve involves a significant computational cost.

Condensation

PAH condensation is the process by which gas phase PAHs can condense onto the surface of a soot particle. It corresponds to the collision of a soot particle with a PAH (or dimer), while soot nucleation can be described by the collision of two dimers. Nucleation enables to generate new soot particles, while condensation enables to increase the size of existing soot particles. In the literature, soot nucleation and condensation which are collisional phenomena rely on collisional efficiencies of dimers. Saffaripour and coworkers [104] have observed that the collisional efficiency of nucleation versus condensation heavily influences soot primary particle diameter predictions. Lower nucleation efficiencies compared to condensation ones result in larger predicted primary particle diameter, while the opposite produces particles with smaller predicted primary particle. The collisional efficiencies can be constants to adjust in soot formation models, or functional expressions based on theoretical assumptions [105]. An alternative to predict accurately soot formation and condensation without relying on these collisional efficiencies has been proposed. Following the work of Sabbah et al. [106] who showed that at flame temperatures, the dimerization of two pyrene PAH [78] was not thermodynamically favored, it was determined that dimerization must be highly reversible. Then the reversibility of the dimerization has been investigated and developed while reducing the need for arbitrary fitted constants [107]. Although the large contribution of PAH condensation to soot particles has been observed [66, 108], a better understanding of the process involved in PAH condensation is still needed.

Coagulation

Once soot particles are formed, they collide with each other forming larger particles. This is the coagulation process, that conserves the total mass of soot formed, but changes the particle size and number density and thus the PSD. Soot morphology is largely influenced by particle-particle interactions. Indeed, coagulation between particles can be generally classified into two distinct types of coagulation, the coalescent growth and the agglomeration into fractal-like aggregates.

The coalescent growth or coalescence occurs when two soot particles collide and merge to form a single larger particle following a spherical shape [6]. Coalescence indicates the disappearance of the boundary between two particles, resulting in a reduction of the total surface area. It is similar to the collision of liquid droplets, indeed coalescence occurs typically for nascent particles with liquid-like behavior [109, 110, 111]. Therefore, coalescence impacts especially young and small particles.

As described in Sec. 2.1, numerous TEM images show that young particles exhibit a spherical shape, while mature soot particles are aggregates where primary soot parti-

2. SOOT FORMATION AND ITS MODELING

cles stick to each other forming fractal-like structures. It is called agglomeration, where particles collide and stick to each other by point-contact without impacting their properties. PSD measurements have shown that the contribution of small and nascent soot to agglomerates is much smaller than larger particles [112, 113, 114]. Additional investigations confirmed that the coagulation efficiency depends on both particle size and temperature [115]. It was found that the coagulation rate of small particles, already low at ambient temperature, decreases with increased temperature. However, large particles do not show an important sensitivity to temperature.

Finally, these observations indicate that the transition between coalescence and agglomeration is size and temperature dependent. Nascent soot particles grow successively by surface growth, condensation and by coagulation, coalescence at least in flame regions. Then the mature soot resulting from these processes evolves in the post-flame region where conditions for agglomeration are favorable. It explains the presence of soot aggregates and thus the bimodality of soot encountered in post-flame regions.

2.2.3 Soot oxidation and fragmentation

The process of soot particle oxidation is a competitive reaction to surface growth and is also the primary mechanism for soot removal from combustion exhausts. Therefore, a mechanistic understanding of soot oxidation is of both fundamental and practical importance. There is a unanimous consensus that oxidizing agents in flames are primarily O_2 and OH with minor contributions of O, H_2O , CO_2 , NO_2 , ... [116, 117]. Early studies of soot oxidation focused on O_2 as oxidizing agent. However, it was found that at high temperature flame conditions, OH radicals are particularly efficient in oxidizing soot [118, 119, 120]. In addition, OH concentration is abundant in near stoichiometric and fuel-rich conditions, while O_2 is abundant only in fuel-lean conditions.

Soot oxidation models by OH express the oxidation process through collision efficiency of OH with the particle surface [119]. Soot oxidation by O_2 are expressed by an empirically-derived rate expression, typically Nagle and Strickland-Constable (NSC) [121], or by physically-based model [101]. Then oxidation is typically described by processes competitive to the HACA mechanism: a single reaction step of O_2 with a soot surface radical and the OH collision with active sites on soot surface.

Recently, Frenklach and co-workers reviewed the oxidation chemistry highlighting a more complex behavior [122]. Theoretical studies show that the reaction of $OH + S_c^*$ does not lead to CO expulsion, and thus is not considered to be a relevant soot oxidation pathway. Instead, OH reacts with soot surface radical site to form various oxy-radicals, which once decomposed lead to CO expulsion. In addition, soot oxidation by O_2 was investigated using TEM analysis [123]. This investigation highlights the role of O as

the most effective oxidizer [122] even if oxidation is dominated by OH and O₂ in terms of oxidation fluxes.

In addition, TEM analysis have shown that the structure of soot particles changes during oxidation [123]. As discussed in Sec. 2.1, nascent soot exhibits a disordered and less graphitic structure than mature soot. The differences in morphology between young and mature soot lead to different oxidation processes. The study of nascent soot oxidation with O₂ indicates that the oxidation rate has a first-order dependency to O₂ concentration, much more than the classical NSC correlation. Further TEM analysis [123] observed that nascent soot showed the oxygen permeation into the core of primary soot particles causing the internal oxidation associated with surface oxidation simultaneously while mature soot tends to oxidize only at soot surface. Concerning soot aggregates, it was observed that the effect of surface oxidation causes structural changes. Successive surface oxidations at the bridge between primary particles lead to the particles break up, the so-called fragmentation. Primary soot particles resulting from the soot fragmentation tend to coalesce. The resulting spherical-like soot particle is more exposed to total oxidation since its graphitic layer has burnt in the oxidation process facilitating complete oxidation: soot is completely burned. The fragmentation was first observed with rising in soot particle number under fuel-lean conditions in a two-stage burner [119]. It was concluded that soot aggregate breakdown was caused by soot oxidation process. O₂ is responsible for weakening the soot structure and promotes soot fragmentation, while OH tends to burn only the outer soot surface before reaching the soot core structure [105]. These conclusions are shared by Echevarria et al. [124, 125], who studied soot fragmentation in a two-stage burner as well. The evolution of the particle size distribution indicates a reduction in particle mean diameter in the leanest condition followed by an increase of nanometric ($< 10nm$) soot particles corresponding to the primary particle diameter. These observations suggest that oxidation occurs at the bridges of soot aggregates, which was confirmed recently by TEM investigation [123].

Soot oxidation consists in complex phenomena depending on the local conditions and soot structure, much more complicated than the actual consensus from a modeling point of view. The appropriate identification of mechanisms involved in soot oxidation is still a big challenge for future studies.

2.3 Numerical methods for soot prediction

In Sec. 2.2, the chemical and physical processes governing soot formation and evolution has been described. Fundamental understandings about soot mechanisms are still required [6]. To go further, extensive experimental and numerical studies have been

2. SOOT FORMATION AND ITS MODELING

conducted. Various numerical methodologies have been developed to describe soot evolution: empirical/semi-empirical models, kinetic models, sectional methods, methods of moments, stochastic methods or Lagrangian soot tracking method. To accurately predict the soot evolution, the PSD is required since all soot processes are strongly linked to the size of soot particles.

Therefore, most of detailed methods are based on solving the Population Balance Equation (PBE), typically employed to model aerosol dynamics. PBE governing equations for soot population are described in Sec. 2.3.1. The general principle as well as the different pros and cons of these methodologies are discussed. Finally, the choice of the Lagrangian Soot Tracking method used in this work is explained.

2.3.1 Governing Equations

Smoluchowski equation

The introduction of the PBE is usually attributed simultaneously to Hulburt and Katz [126] and Randolph [127]. However, PBE was first used for polydispersed particle dynamics in the work of Smoluchowski [128] in 1916 [129]. At that time, a set of nonlinear differential equations for coagulation were introduced and are still used to solve collisional phenomena: the Smoluchowski equation is still applied to describe the three collisional phenomena involved in soot evolution:

- **Nucleation:** Collision of two dimers [78] (gaseous phase) in numerous soot model [6]
- **Condensation:** Collision between a solid particle and a dimer (gaseous phase)
- **Coagulation:** Collision between solid particles

The Smoluchowski equation expresses the gain $\dot{n}^c(v)$ of distribution of the number density function (NDF) due to particle collisions. The particles NDF $n(v)$ is the number of soot particles over the volume space v described by soot particles and illustrated in Fig. 2.10. For a particle of size v , the gain source term $\dot{n}^c(v)$ can be expressed as:

$$\dot{n}^c(v) = \underbrace{\frac{1}{2} \int_0^v \beta_{v-u,u} n(u) n(v-u) du}_{\text{gain of particles with size } v} - \underbrace{\int_0^\infty \beta_{u,v} n(u) n(v) du}_{\text{loss of particles with size } v} . \quad (2.3)$$

The gain source term is function of the collision frequencies $\beta_{u,v}$ of the particle of size v with all other particles of any size u , and the collision frequencies $\beta_{v-u,u}$ of all particles of size u with all other particles of size $v-u$. These collision frequencies, and then the gain source term, depend almost exclusively on the size of the different particles

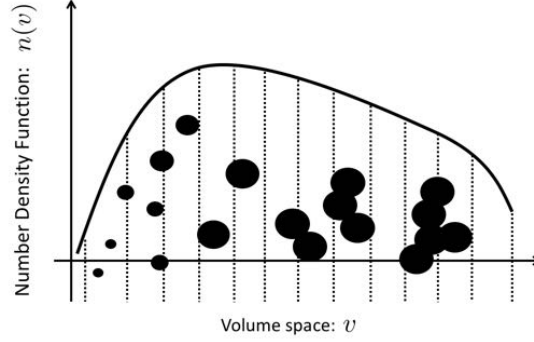


Figure 2.10: Soot number density function (NDF) over the volume described by soot particles.

involved. The collision frequency $\beta_{u,v}$ between a particle of size u and a particle of size v depends on the value of their Knudsen number (Kn_v) defined for a particle v by:

$$Kn_v = \frac{2\lambda_{gas}}{d_{c,v}} \quad (2.4)$$

where $d_{c,u}$ corresponds to the collision diameter defined in Eq. 2.2 (Sec. 2.1). λ_{gas} is the mean free path expressed as:

$$\lambda_{gas} = \frac{R T}{\pi\sqrt{2} d_{gas}^2 N_A P} \quad (2.5)$$

with R the perfect gas constant, T the temperature, d_{gas} the diameter of a gas molecule (constant and equal to $0.2nm$), N_A the Avogadro number and P the pressure. Particle collision is classified into three different physical regimes on the basis of the Knudsen number [130] :

- **Molecular regime** ($Kn \gg 1$): If the pressure is sufficiently low or if thermal agitation is low or if particles are small enough, the collision regime is the free molecular regime (superscript fm). The associated collision frequency $\beta_{u,v}^{fm}$ is expressed as:

$$\beta_{u,v}^{fm} = \epsilon_{u,v} \sqrt{\frac{\pi T k_b}{2\rho_s}} (d_{c,u} + d_{c,v})^2 \sqrt{\frac{1}{u} + \frac{1}{v}} \quad (2.6)$$

where $\epsilon_{u,v}$ corresponds to the van der Waals factor [131], which is still subject to understanding as mentioned in Sec. 2.2. k_b refers to the Boltzmann constant and ρ_s is the soot particle density which is assumed constant and equal to $\rho_s = 1860kg/m^3$.

- **Continuum regime** ($Kn \ll 1$) : If the pressure is sufficiently high or if the particles are large enough or if thermal agitation is important, the collision regime is the continuous regime (superscript $cont$), or the so-called continuum regime.

2. SOOT FORMATION AND ITS MODELING

The associated collision frequency $\beta_{u,v}^{cont}$ is expressed as:

$$\beta_{u,v}^{cont} = \frac{2k_bT}{3\mu} (d_{c,u} + d_{c,v}) \left(\frac{Cu_u}{d_{c,u}} + \frac{Cu_v}{d_{c,v}} \right) \quad (2.7)$$

with μ the dynamic gas viscosity, Cu_v the corrective Cunningham coefficient for a particle of size v defined as follows:

$$Cu_v = 1 + 1.257Kn_v \quad (2.8)$$

- **Transition regime** ($0.1 < Kn < 10$): If the thermodynamic conditions or the PSD lead to an average Knudsen number neither too high (molecular regime) nor too low (continuum regime), the collision regime corresponds to the intermediate or the transition regime (superscript tr). The associated collision frequency $\beta_{u,v}^{tr}$ is expressed as:

$$\beta_{u,v}^{tr} = \frac{\beta_{u,v}^{fm} \beta_{u,v}^{cont}}{\beta_{u,v}^{fm} + \beta_{u,v}^{cont}} \quad (2.9)$$

Population Balance Equation

Starting from the work of Smoluchowski [128], Müller proposed a continuous integro-differential equation in 1928 [132]. It leads to the PBE which is used in many branches of engineering and science involving liquid or solid particles. The processes modeled by the PBE are characterized by the presence of both continuous phase and dispersed phase composed of entities with a distribution of properties as size, composition, porosity, etc. When considering soot particles, the volume distribution $n(v)$ of the particles number density is considered, and the PBE governs the temporal and spatial evolution of $n(v)$:

$$\frac{\partial n}{\partial t} + \nabla \cdot ((\mathbf{u} + \mathbf{v}_T) n) = \nabla \cdot (D_s \nabla n) + \dot{n}_s \quad (2.10)$$

where :

- \mathbf{v}_T is the thermophoretic velocity,
- D_s is the particle diffusion coefficient,
- \dot{n}_s is the source term of the volume distribution $n(v)$. It accounts for collision with $\dot{n}^c(v)$ defined in Eq. 2.3 (nucleation, condensation and coagulation) and particle surface reactions with the gaseous phase (surface growth and oxidation).

Transport properties

Thermophoresis

The expression of the thermophoretic velocity \mathbf{v}_T comes from the works of Waldmann and Schmitt [133] and Dejarguin et al. [134] and reads:

$$\mathbf{v}_T = -C_{th}\nu\frac{\nabla T}{T} \quad (2.11)$$

where ν is the gas kinematic viscosity and C_{th} is the thermophoretic constant equal to $C_{th} \approx 0.554$. The thermophoretic effect refers to the drift of particles in a direction from high to low temperature regions. The thermophoresis phenomenon is then not negligible in a flame environment showing important temperature gradient.

Molecular diffusion

The molecular diffusion coefficient of soot particles D_s has been studied by Epstein [135]. Spherical particles were considered as a perfect thermal conductor and the corresponding diffusion force was expressed, depending strongly to particle diameter d . The associated molecular diffusion coefficient can be expressed as:

$$D_s = \frac{2C_{th}}{\rho} \frac{1}{d^2} \sqrt{\frac{W_{gas}k_bT}{2\pi N_A}} \quad (2.12)$$

with W_{gas} the gas molar weight. Although the Epstein equation has been developed for spherical particles, it works also for fractal-like soot aggregates [136].

2.3.2 Numerical approach

The development of reliable and predictive soot models requires a consistent description of the gas-phase chemistry including an accurate description of the flame and PAHs to capture soot inception. As mentioned in Sec. 2.2, soot inception was typically modelled as the physical collision of large PAH such as pyrene [98, 99, 137, 138], or an ensemble of larger aromatics up to coronene [139, 140, 141]. The associated nucleation reactions were assumed to be irreversible [77], however recent works stated the reversibility of these reactions [107, 142, 143, 144], the corresponding equilibrium constants and reverse rate coefficients can be evaluated using statistical mechanics. The transition from gas-phase to nanoparticles was successively modeled as a purely growth process [145, 146, 147, 148, 149, 150] using the Atomistic Model for Particle Inception (AMPI) model [148, 149] or the Stochastic Nanoparticle Simulator (SNAPS) [145, 146, 147, 150]. These numerical models enable to correctly predict the order of magnitude of the nascent soot particle, a crucial input for detailed soot model. Once formed, nascent soot particles will experience surface reactions and particle-particle interactions, and their size and morphology will change. To model these processes, several

2. SOOT FORMATION AND ITS MODELING

different numerical methodologies with increasing complexity, cost and applicability to real systems have been developed [151].

Monodisperse soot models

Empirical/semi-empirical models: These methods are generally based on empirical and ad-hoc formulation of soot formation processes and simple transport equations [152, 153, 154, 155, 156]. Generally, a maximum of two transport equations are considered in order to describe soot particles evolution in terms of mass and/or number density. The main advantage of such methods is their very low cost. However, they present many drawbacks:

- Transport equation source terms are generally based on unphysical-based expressions,
- They are not universal: case-dependent fitted parameters are used in the transport equation source terms,
- They do not provide access to the soot PSD or NDF evolution, but only to a mean soot diameter,
- They are not enable to describe the morphology of soot particles in terms of surface/volume ratio evolution.

Three-equation model: *Franzelli et al.* [157] developed a 3-equation model that accounts for soot fractality and provides a reasonable prediction of soot global quantities and an estimation of the NDF at a small CPU cost. It is based on the transport of three global variables: N_s , S_s and $Y_s = \rho_s f_v / \rho$, respectively the soot number density, the soot surface and the soot mass fraction, following the PBE equation. The associated source terms are derived from a sectional method [37] by assuming a mono-disperse distribution. The evolution of the surface is derived from the work of *Mueller et al.* [158]. The main advantages of this method are:

- The additional surface equation guarantees a better description of surface reactions compared to the semi-empirical method,
- The source terms are based on detailed description of the different physical and chemical phenomena guaranteeing a large validity,
- It is easy to implement in CFD solvers,
- The soot NDF can be estimated at low computational cost.

The main drawbacks of this method are:

- The NDF reconstruction to estimate soot NDF proposed by the authors still requires more validation
- The accuracy of the 3-eq model is expected to be reduced when the NDF is highly polydisperse.

Monte-Carlo Method (MC)

In order to avoid any assumption on the PSD shape, Monte-Carlo (MC) techniques have been applied to the solution of soot population balances [159, 160, 161]. MC based models provided accurate results by tracking the evolution of number density through an assemble of particles governed by stochastic processes. However, due to its extremely high computational cost and the large number of shots needed to guarantee convergence, this methodology is not affordable in practical complex configurations. Although MC applicability has so far been limited to simple configurations, this method has been recently used as a post-processing tool to compute the PSD in a turbulent diffusion flame [38]. This method is generally independent from the gas-phase, the gas-phase being an input of the stochastic soot solver. To couple the stochastic MC approach to predict soot particles evolution with the gas-phase, an operator splitting technique has been first introduced [161]. Nevertheless, the Monte-Carlo approach is generally employed in order to validate the development of other models for PSD prediction, such as the sectional methods or methods of moments in academic configurations. The main advantages of this method are:

- No assumption is made on the PSD or NDF shape,
- Detailed description of physical and chemical soot processes can be taken into account,
- Bi-variate volume-surface description of PSD or NDF can be considered,
- The corresponding solutions can be considered as reference solutions of the soot population balance equation.

Its main drawbacks are:

- Its coupling with gas phase chemical kinetics description requires specific numerical methods [161],
- Its expensive computational cost due to the large number of shots required for numerical convergence.

2. SOOT FORMATION AND ITS MODELING

Method of Moments (MOM)

For the method of moments (MOM), the detailed description of particle dynamics described by Eq. 2.10 is reformulated in terms of the moments of the PSD or NDF [103, 137, 162, 163, 164, 165, 166, 167, 168, 169, 170]. Moments can be uni-variate (in the particles volume or surface space) or multi-variate. For a uni-variate description of the PSD (in the particles volume space), the moment M_x of order x is generally formulated as:

$$M_x = \int_{v=0}^{+\infty} n(v)v^x dv \quad (2.13)$$

For a bi-variate volume-surface description of the PSD, the moment of order x in the volume space and y in the surface space can be formulated as:

$$M_{x,y} = \int_{v=0}^{+\infty} \int_{s=0}^{+\infty} v^x s^y dv ds \quad (2.14)$$

It can then be observed that the first moments $M_{0,0}$, $M_{1,0}$ and $M_{0,1}$ characterize respectively the particle number density, the total soot volume (and therefore the soot volume fraction) and the total soot surface. In principle, knowing all the moments for $(x, y) \in [0, +\infty[\times [0, +\infty[$ is equivalent to knowing of the PSDF [84]. In practice, only the first moments are considered. Transport equations are solved for each of the selected moments. The source terms depend on the different moment weights, gas phase parameters, the transported moments. However, numerical scheme such as the interpolative close (MOMIC) [162, 163, 169] or variants of the quadrature method [137, 164, 166, 167, 168, 170] or the combination of the latter methods [165] is necessary to close the system of equations for the moments. Finally, the method of moments can provide many expected soot properties keeping a relatively low computational cost compared to MC. Therefore, it has been widely employed to compute soot particle dynamic in both laminar and turbulent flames [171] and has also been used in real aircraft combustor [172]. The main advantages of this method are:

- It is based on a detailed description of the different physical and chemical phenomena,
- Mono-variate (in the particle volume or surface space) or bi-variate volume-surface descriptions of the PSD can be considered enabling to describe the soot particle morphology.

Its main drawbacks are:

- Its high mathematical complexity. Indeed, the different moment source terms are generally function of non-transported moments, and closure problems need to be solved,

- Most of the methods of moments do not provide direct access to the PSD (or NDF). The PSD can be reconstructed based on the values of the transported moments but the reconstruction is generally expensive.

Discrete Sectional Method (DSM)

Discrete sectional method [37, 98, 99, 143, 144, 173, 174, 175, 176, 177] is another widely used method to solve the PBE. It is based on the discretization of the entire particle domain into a finite number of classes or sections with neighboring size [178]. Although the discretization can be done either by particle volume or molar weight, the first one is preferred in the literature. To delimit the volume space occupied by these sections, different solutions are possible. The one proposed by *Netzell et al.* [179] describes a power law for the volume space occupied by each section i . For a discretization with N_{sect} sections, the maximum volume v_i^{max} of a particle size of the section i verifies the following relation:

$$v_i^{max} = v^{MIN} \left(\frac{v^{MAX}}{v^{MIN}} \right)^{i/N_{sect}} \quad (2.15)$$

where v^{MIN} and v^{MAX} correspond to the smallest and biggest soot particle respectively. The properties of particles within each section are averaged. Then, a mono-variate description of the soot PSD is solved by solving one or several moments of the soot PSD inside each section i . There, this method can accurately provide the PSD if the proper set of sections is chosen. Since the sectional approach can be solved simultaneously with the gas-phase chemistry and the flow field, this method is able to follow the transition from gas to particle phase [143]. The main advantages of this method are:

- It is based on a detailed description of the different physical and chemical phenomena,
- Mono-variate (in the particle volume or surface space) or bi-variate volume-surface description of the PSD can be considered enabling to describe the soot particles morphology. For mono-variate description of the PSD, the morphology can be accounted for by imposing a surface-volume relationship depending on the soot particles size.

Its main drawbacks are:

- The method is expensive and is generally considered as unaffordable when bi-variate surface-volume description of the PSD or NDF is considered.
- The numerical accuracy depends on the number of sections used for the PSD or NDF discretization. More than 20 sections are generally required in order to have a correct numerical accuracy for a mono-variate description.

2. SOOT FORMATION AND ITS MODELING

Chemical Discrete Sectional Method (CDSM)

Kinetic models correspond to the discrete sectional approach within a chemical mechanism. It was introduced by *Pope and Howard* [180], they converted the aerosol dynamics modeling of the discrete sectional approach into equivalent Arrhenius-like reactions where particles are gathered in classes, generally called "BINs". These BINs are considered as chemical species and their evolution are solved together with the other chemical species of the kinetic scheme. *Richter et al.* [181] proposed a detailed kinetic mechanism, it contains 295 species including 20 sections of BINs representing both large lumped PAH and soot particles. Each BINs has only one single and decreasing H/C ratio (hydrogen over carbon atoms) from 0.5 in the first section to 0.125 in the last section. Later, *D'Anna and Kent* [182] followed the same approach considering 26 BINs with a constant H/C ratio about 0.8. Further developments have been done to consider different H/C ratio ranges [183] and an additional dimension to account different morphologies [105]. Another research group who has been actively working on a kinetic soot modeling is the CRECK modeling group at Politecnico di Milano. *Saggese et al.* [108] developed a discrete sectional soot model considering different H/C ratio of soot particles and coupled it to the gas-phase. It includes 20 BINs, the first BINs correspond to large lumped PAH species, the following BINs are spherical soot particles while the last ones are assumed to be soot aggregates. Recently, *Pejpichestakul et al.* [66] proposed an updated version of the detailed kinetic mechanism extending the H/C discretization and combining approaches from the previous mentioned studies [105, 108]. The main advantages of this method are:

- It provides access to the PSD particles evolution,
- This is based on detailed description of the chemical and physical processes and interactions with the gaseous phase can be easily handled.

Its main drawbacks are:

- The method is expensive as it requires the combined resolution of the global kinetic scheme which generally involves, accounting for the soot particles classes, more than 200 species and 1000 reactions for *C1-C4* fuel,
- The NDF is generally mono-variate and is considered only as a function of the soot particle volume. However, morphology can be accounted for by imposing a surface-volume relationship depending on the soot particle size [105, 108] or using a post-processing tool to predict primary soot particle size [184].

Lagrangian Soot Tracking Method (LST)

The soot distribution observed in the flame results from the effect of all the individual soot particles interacting with one another and the surrounding gaseous phase. The Eulerian detailed methods do not provide specific information for each of these particles, while stochastic approaches do require large computational cost, still unaffordable for complex configurations. An alternative and simple way to access individual information of soot particles is to employ a Lagrangian approach, the so-called Lagrangian Soot Tracking (LST) method. Soot particles are treated as fictitious point source Lagrangian particles and are tracked individually. It is similar to droplets in two-phase flow computations. LST has already been used to investigate soot transport [185, 186, 187, 188, 189, 190] in various combustion applications and non-combustion applications. In laminar diffusion flames, *Katta et al.* [187] or *Fuentes et al.* [188] tracked the history of soot particles. Note that these methods did not include surface reactions, condensation and coagulation considering then a constant size. Later, *Katta et al.* improved their soot tracking model to consider the effect of soot oxidation by introducing a soot burnout model in oxidation regions, which would delete the fictitious soot particles [190, 191]. First, the LST method focused on the history of soot particles and their transport inside the flame. Then *Mahmood et al.* proposed to predict both soot trajectories and particle size evolution within diesel engine application [185, 186, 192]. Actually, soot particles were tracked from starting locations based on the soot mass concentration in the engine, then particles are tracked inside the engine computing the evolution of soot via surface growth and oxidation, both based on empirical model. This approximations and assumptions make it difficult to differentiate young and mature particles and to predict accurately their size evolution neglecting several soot processes. To go further, *Cai Ong et al.* implemented a LST model [193] combining the tracking capability of a Lagrangian method and the ability to predict primary soot particle sizing. The particle inception and oxidation processes relied on the semi-empirical *Brookes and Moss* model [156], the particle ageing is also investigated. Although several processes are neglected and the simplicity of the based soot model, the associated PSD showed encouraging results. In this work, the LST approach is extended to consider collisional phenomena and to optimize the computational cost [194] detailed in Chap. 6. Simultaneously, *Dellinger et al.* [195] have proposed in parallel additional numerical and physical methods to improve the LST approach. The main advantages of this method are:

- No assumption is realized on the PSD or NDF shape,
- The source terms are based on a detailed description of the different physical and chemical phenomena guaranteeing a large validity,

2. SOOT FORMATION AND ITS MODELING

Method	Soot processes description	PSD/NDF description	Morphology description	Mathematical complexity	Cost
(Semi-)empirical	–	-	-	++	++
CDSM	+	+	+	+	–
MOM	+	-	++	–	+
DSM	+	+	+	+	-
MC	+	++	++	-	—
Three-equations	+	-	+	++	++
LST	+	+/-	++	++	+

Table 2.1: Comparison between the different mentioned numerical methods. Crosses correspond to advantages and dashes correspond to drawbacks (Extracted and adapted from [196]).

- Uni-variate like volume-surface-hydrogen description of PSD or NDF can be considered without impacting the computational cost,

The main drawbacks of this method are:

- The parallelization of the Lagrangian solver
- The statistical convergence of Lagrangian particles population

2.3.3 Choice of the numerical method

Following the work initiated by P. Rodrigues [196] the different categories of numerical methods just introduced in Sec. 2.3.1 are compared in terms of soot evolution process description, PSD/NDF description, soot particle morphology description, mathematical complexity and computational cost in Tab. 2.1. In this PhD, the main goal is to describe the PSD evolution in 3-D complex turbulent flame configurations. Although empirical and semi-empirical models are still widely used at the design stage of practical combustion devices, they present a lot of drawbacks. One can predict that these methods, with their tuned parameters to capture mass and number of soot, will be insufficient at the design stage to follow the expected future regulations in terms of PSD. For such reason, investments in detailed methods are preferred attempting to keep a relative reasonable computational cost. Then MC and CDSM based approaches are neglected due to their high computational resources demand limiting these method to canonical flames. MOM present a low computational cost, however they generally presume the PSD rather than providing it and they need serious implementation developments. A direct access of the PSD can be obtained using DSM, requiring at least 20 additional equations to solve with a significant computational cost. Although the

2.3 Numerical methods for soot prediction

three-equations model is monodisperse, its surface equation and the associated NDF reconstruction make it a suitable candidate for our purpose. However, this method came too late for this thesis work. The LST approach based on the Lagrangian formalism remains still too little known and its ability to describe accurately the PSD has to be proved. In two-phase flow, Lagrangian formalism is an incredible tool to model polydisperse particles population like fuel droplets. Based on the experience of two-phase flow, the LST approach can be considered as a suitable candidate to describe the PSD at low computational cost. Compared to two-phase flow combustion soot simulation involves a large number of nanometric particles and their collision, the main challenges are in this thesis to propose an adequate numerical and physical solution to handle such particle population.

2. SOOT FORMATION AND ITS MODELING

Part II

Numerical developments and validation for soot prediction in flames

Chapter 3

Modeling of laminar reactive flows

The goal of this chapter is to introduce basic theoretical concepts of reactive flow. General aspects of premixed and non-premixed combustion are first given. Then both gaseous and two-phase equations are introduced as well as the different techniques to account for flame chemistry. In this chapter, only laminar flames are considered.

Contents

3.1	Laminar flames	51
3.1.1	Laminar premixed flames	51
3.1.2	Laminar non-premixed flames	55
3.2	Conservative equations for gaseous reacting flow	57
3.2.1	Navier-Stokes equations	57
3.2.2	Flux description	58
3.2.3	Transport modeling	58
3.2.4	Chemical kinetics	59
3.3	Equations for reacting two-phase flow	66
3.3.1	Euler-Lagrange modeling	66
3.3.2	System of equations	66
3.3.3	Exchange terms	67
3.3.4	Coupling with the gaseous phase	72
3.3.5	Droplet injection	73

3.1 Laminar flames

3.1.1 Laminar premixed flames

Flame structure

A premixed flame can appear when fuel and oxidiser are mixed before being heated. The simplest structure of laminar unstretched premixed flame is represented in Fig. [3.1](#). The fresh and burnt gases are separated by the flame. Three layers can be seen:

- The pre-flame zone essentially made of fresh gases. When getting closer to the flame, fresh gases are heated due to thermal diffusion.

3. MODELING OF LAMINAR REACTIVE FLOWS

- When the temperature is high enough, first chemical reactions are triggered consuming the fuel and the oxidiser. Highly reacting radical species (O , OH , C_2H_2 , ...) are produced and consumed due to hundreds of elementary reactions. This reaction zone is very thin, of the order of few hundreds of microns.
- When final stable products (H_2O , CO_2 , CO) are produced, the overall reactivity decreases, which corresponds to the post-flame region. Some slow reactions can still occur, for example producing NO_x products.

The flame structure can also be analysed as a function of c , the progress variable which evaluates the advancement of the combustion process. It can be defined using the temperature:

$$c = \frac{T - T_f}{T_b - T_f} \quad (3.1)$$

with T_f and T_b respectively the fresh gases and burnt gases temperatures, or based on the mixture composition:

$$c = \frac{Y_c}{Y_c^{eq}} \quad (3.2)$$

with Y_c a composition index bounded between 0 in fresh gases and Y_c^{eq} in the mixture at equilibrium. Typically, combustion products are used for instance $Y_c = Y_{CO} + Y_{CO_2} + Y_{H_2O}$. Based on either temperature or composition, the progress variable evolves from 0 in the fresh gases to 1 in the burnt gases. It allows to compare flames independently of their thickness. An iso- c line can be used to localize the flame front and the gradient of c can be used to determine the local normal direction of the flame towards fresh gases:

$$\mathbf{n} = -\frac{\nabla c}{|\nabla c|}. \quad (3.3)$$

Flame properties

Parameters driving the flame properties are essentially the fresh gas state: pressure P_f , temperature T_f , and composition often described by the equivalence ratio ϕ relating the fuel mass fraction Y_F and the oxidiser mass fraction Y_O :

$$\phi = s \frac{Y_F}{Y_O}. \quad (3.4)$$

The parameter introduced s is the mass stoichiometric ratio defined as:

$$s = \left(\frac{Y_O}{Y_F} \right)_{st} = \frac{\nu'_O W_O}{\nu'_F W_F}. \quad (3.5)$$

where ν'_F and ν'_O are the fuel and oxidiser stoichiometric coefficients of the global oxidation reaction and W_F and W_O are the molecular weights of the fuel and oxidiser. When burning a mixture with exactly s times more oxidiser than fuel (in mass), all the oxidiser and the fuel are consumed. This situation corresponds to a stoichiometric

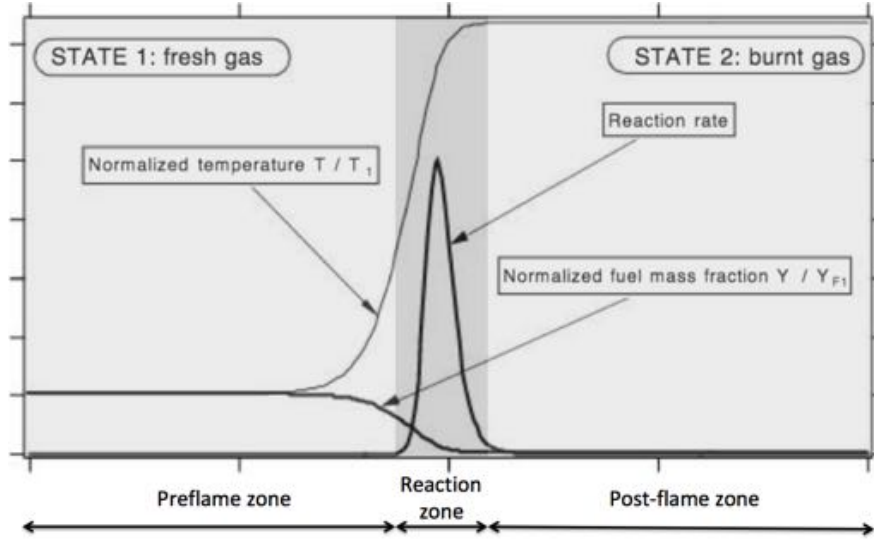


Figure 3.1: Laminar premixed flame structure. Extracted from Poinot & Veynante [197].

case: $\phi = 1$. When decreasing the initial amount of fuel, oxidiser remains in the burnt gases. This is called lean combustion: $\phi < 1$. Finally, if fuel is provided in excess, rich combustion occur: $\phi > 1$ and fuel remains in the burnt gases.

P_f, T_f, ϕ influence the two main global properties of the flame: its laminar speed s_l^0 and thickness δ_l^0 . Different definitions of the flame thickness exist. The most common one uses the temperature profile of the flame:

$$\delta_l^0 = \frac{T_b - T_f}{\max\left(\left|\frac{\partial T}{\partial x}\right|\right)}. \quad (3.6)$$

Assuming a global one-step chemistry, one can show that:

$$\delta_l^0 \propto \sqrt{\frac{D_{th}}{A}} \quad (3.7)$$

with the thermal diffusivity $D_{th} = \lambda/\rho_f C_p$, λ the thermal conductivity, ρ_f the fresh gases density, C_p the heat capacity at constant pressure of the mixture and A the Arrhenius pre-exponential constant of the global reaction. Equivalently,

$$s_l^0 \propto \sqrt{D_{th} A}. \quad (3.8)$$

The flame speed s_l^0 is actually a concept that can have various definitions depending on the reference frame. With notations introduced in Fig. 3.2:

- The absolute flame velocity $S_a = \mathbf{w} \cdot \mathbf{n}$ is the flame front speed relative to a fixed reference frame.
- The displacement flame speed $S_d = (\mathbf{w} - \mathbf{u}) \cdot \mathbf{n} = S_a - \mathbf{u} \cdot \mathbf{n}$ is the flame front speed relative to the local flow. A density weighted displacement speed is also often used defined as $S_d^* = \rho_b/\rho_f S_d$ in order to take into account the gases dilatation created.

3. MODELING OF LAMINAR REACTIVE FLOWS

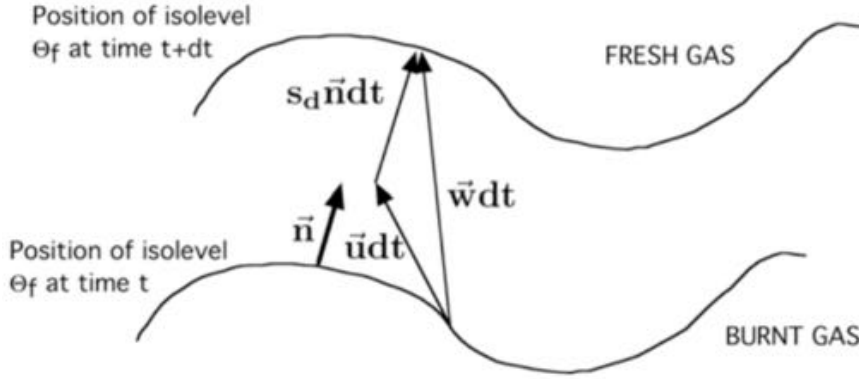


Figure 3.2: Flame speed definitions. Extracted from Poinso & Veynante [197].

- The consumption speed S_c is the speed at which reactants are consumed.

Contrary to S_a and S_d that are local, the consumption speed is a global quantity expressed as:

$$S_c = -\frac{1}{\rho_f Y_F^f} \int_{-\infty}^{+\infty} \dot{\omega}_F d\mathbf{n} \quad (3.9)$$

with $\dot{\omega}_F$ the fuel consumption rate. S_c represents the fuel consumption integrated in the normal direction of the flame.

Stretch effect

In a non-uniform flows, the flame surface may change due to the flame stretch κ :

$$\kappa = \frac{1}{A} \frac{dA}{dt} \quad (3.10)$$

with A the flame surface. κ can be splitted in two components [198]:

$$\kappa = \underbrace{(\delta_{ij} - n_i n_j) \frac{\partial u_i}{\partial x_j}}_{\text{Tangential strain rate}} + \underbrace{S_d \frac{\partial n_i}{\partial x_i}}_{\text{Curvature effect}} = a_t + 2S_d \mathcal{K}. \quad (3.11)$$

Two terms are revealed: a_t the tangential strain rate, and \mathcal{K} the flame front curvature. Strain and curvature can modify the flame speed depending on the fuel Lewis number $Le_F = D_{th}/D_F$ comparing the thermal and fuel diffusion coefficients. For fuels with $Le_F < 1$, the consumption speed increases with stretch. A linear dependence is even found for small stretches. On the contrary, for fuels with $Le_F > 1$, S_c decreases when the stretch increases, and can even lead to flame extinction for too high stretch levels. Figure 3.3 shows two archetypes of premixed flame subjected to stretch. In Fig. 3.3a in the counterflow configuration, the flame is subjected to strain only, without curvature effect. In Fig. 3.3b, an expanding spherical flame is subjected to curvature only. These

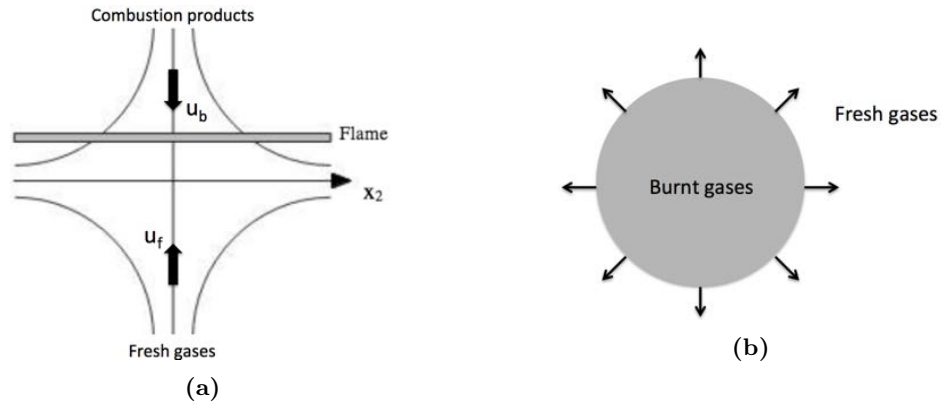


Figure 3.3: Canonical stretched premixed flame: (a) Strained flame, (b) Curved flame.

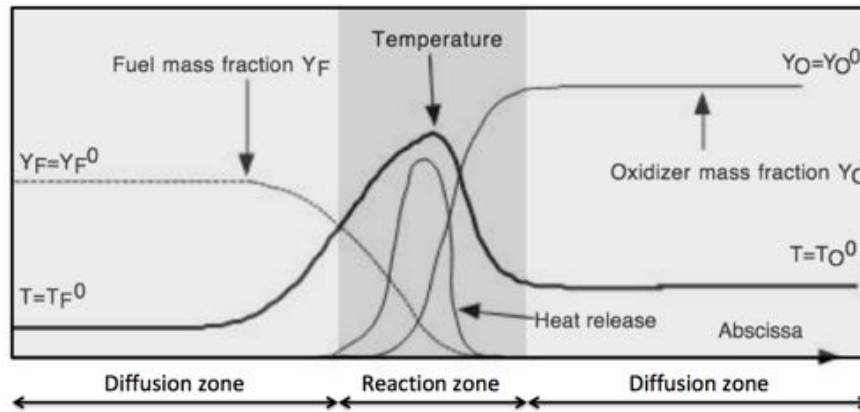


Figure 3.4: Laminar diffusion flame structure. Extracted from Poinot & Veynante [197].

simple configurations are useful to isolate strain and curvature effects on the flame response. For the strained flame, a strain rate

$$a = \frac{u_f + u_b}{L} \quad (3.12)$$

is generally defined with u_f , u_b the fresh gases and burnt gases inlet velocities and L the distance between the two inlets.

3.1.2 Laminar non-premixed flames

Contrary to a premixed flame, a non-premixed flame (also called diffusion flame) appears when fuel and oxidiser are not mixed. The flame actually separates the fresh pure fuel on one side and the fresh pure oxidiser on the other side as sketched in Fig. 3.4. In the reaction zone, fuel and oxidiser burn around stoichiometry. Heat is diffused to both sides. Contrary to premixed flames, diffusion flames do not have intrinsic propagation speed and thickness. The rate of reaction is mainly controlled by the mixing of fuel and oxidiser along the flame that is driven by the inlet fuel and oxidiser flow rates. A typical diffusion flame is the strained flame shown in Fig. 3.5. Considering

3. MODELING OF LAMINAR REACTIVE FLOWS

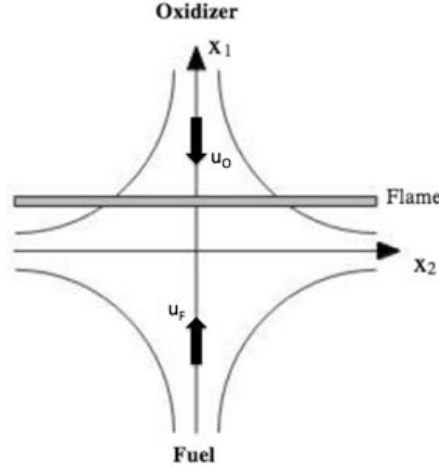


Figure 3.5: Canonical laminar stretched flame. Extracted from Poinot & Veynante [197].

infinitely fast chemistry, and supposing that all species diffusivities are equal to the thermal diffusivity ($D_k = D_{th} = D$), the flame consumption speed can be evaluated as

$$S_c \propto \sqrt{aD}. \quad (3.13)$$

This expression shows that the fuel consumption is controlled by the local flow condition for diffusion flames. The burning rate is increased when reactants are brought faster to the reaction zone and when their mixing is faster. When considering real finite rate chemistry, a competition between mixing and chemical times arises and the fuel consumption rate may also be limited by chemistry.

An essential quantity to study diffusion flames is the mixture fraction z , adequately defined by Bilger [199]:

$$z = \frac{\beta - \beta_O}{\beta_F - \beta_O} \quad (3.14)$$

with the function:

$$\beta = \sum_{i=1}^{n_{spec}} \gamma_i \sum_{j=1}^{N_a} n_{ij} \frac{W_i Y_j}{W_j}. \quad (3.15)$$

Here, n_{ij} is the number of atoms of the i^{th} element in the j^{th} species and N_a is the total number of atoms. γ_i are weighting factors, with values $\gamma_C = 2/W_C$, $\gamma_H = 1/(2W_H)$ and $\gamma_O = -1/W_O$. β_F and β_O are the values obtained in the incoming fuel stream and incoming oxidiser stream. The quantities ϕ and z are related as:

$$\phi = \frac{z}{1-z} \frac{1-z_{st}}{z_{st}}. \quad (3.16)$$

3.2 Conservative equations for gaseous reacting flow

3.2.1 Navier-Stokes equations

The Navier-Stokes equations for multi-species reacting flows arise from conservation laws for mass, momentum and energy. They are recalled here in their conservative form:

- Mass conservation

$$\frac{\partial \rho}{\partial t} + \frac{\partial}{\partial x_j} (\rho u_j) = 0 \quad (3.17)$$

with ρ the density and u_j the j^{th} velocity component.

- Species conservation

$$\frac{\partial \rho Y_k}{\partial t} + \frac{\partial \rho Y_k u_j}{\partial x_j} = - \frac{\partial}{\partial x_j} J_{jk} + \dot{\omega}_k, \quad \text{for } k = 1, n_{spec} \quad (3.18)$$

with Y_k the mass fraction of species k , J_{jk} the species diffusive flux and $\dot{\omega}_k$ the chemical source term.

- Momentum conservation

$$\frac{\partial \rho u_i}{\partial t} + \frac{\partial \rho u_i u_j}{\partial x_j} = - \frac{\partial}{\partial x_j} (P \delta_{ij} - \tau_{ij}), \quad \text{for } i = 1, 2, 3 \quad (3.19)$$

with $P \delta_{ij}$ the pressure flux tensor and τ_{ij} the viscous momentum flux tensor. δ_{ij} is the Kronecker symbol, equal to 1 if $i = j$ and 0 otherwise.

- Energy conservation

$$\frac{\partial \rho E}{\partial t} + \frac{\partial}{\partial x_j} (\rho E u_j) = - \frac{\partial}{\partial x_j} (u_i (P \delta_{ij} - \tau_{ij}) + q_j) + \dot{\omega}_T \quad (3.20)$$

with E the total energy, q_j the energy flux, and $\dot{\omega}_T$ the chemical source term.

The equation of state for perfect gases is used to close this set of equations:

$$P = \rho r T \quad (3.21)$$

with $r = \mathcal{R}/W$. $\mathcal{R} = 8.314 \text{ J.mol}^{-1}.\text{K}^{-1}$ is the universal gas constant, and W is the mean molecular weight:

$$\frac{1}{W} = \sum_{k=1}^{n_{spec}} \frac{Y_k}{W_k} \quad (3.22)$$

with W_k the molecular weight of the k^{th} species.

3. MODELING OF LAMINAR REACTIVE FLOWS

3.2.2 Flux description

3.2.2.1 Species diffusion flux

The species diffusion flux is found using the Hirschfelder Curtis approximation:

$$J_{jk} = -\rho \left(D_k \frac{W_k}{W} \frac{\partial X_k}{\partial x_j} - Y_k V_j^c \right). \quad (3.23)$$

D_k is the diffusivity of the k^{th} species and $X_k = Y_k W / W_k$ is the mole fraction of the k^{th} species. The velocity V_j^c ensures mass conservation:

$$V_j^c = \sum_{k=1}^N D_k \frac{W_k}{W} \frac{\partial X_k}{\partial x_j}. \quad (3.24)$$

3.2.2.2 Viscous momentum flux

The viscous momentum flux tensor writes:

$$\tau_{ij} = 2\mu \left(S_{ij} - \frac{1}{3} \delta_{ij} S_{ll} \right) \quad (3.25)$$

with μ the molecular viscosity and S_{ij} the strain rate tensor:

$$S_{ij} = \frac{1}{2} \left(\frac{\partial u_i}{\partial x_j} + \frac{\partial u_j}{\partial x_i} \right) \quad (3.26)$$

3.2.2.3 Energy flux

The energy flux is made of two parts. A term for heat diffusion and a second term for species diffusion:

$$q_j = -\lambda \frac{\partial T}{\partial x_j} + \sum_{k=1}^N J_{jk} h_{s,k}. \quad (3.27)$$

λ is the heat conduction coefficient and $h_{s,k} = \int_{T_0}^T C_{p,k} dT$ is the sensible enthalpy of the k^{th} species and $C_{p,k}$ the constant pressure mass heat capacity of the k^{th} species.

3.2.3 Transport modeling

In the flux expressions given above, three transport coefficients need to be determined: D_k , μ and λ . In kinetics solvers, D_k is calculated as a function of the binary coefficients D_{ij} obtained from kinetic theory (Hirschfelder et al. [200]). The strategy in this work is to simplify this estimation by assuming a constant Schmidt number $S_{c,k}$ for each species so that:

$$D_k = \frac{\mu}{\rho S_{c,k}}. \quad (3.28)$$

Similarly, λ is computed assuming a constant Prandtl number Pr of the mixture:

$$\lambda = \frac{\mu C_p}{Pr} \quad (3.29)$$

with $C_p = \sum_{k=1}^{n_{spec}} C_{p,k} Y_k$ the heat capacity of the mixture.

Finally, the dynamic viscosity μ is obtained using a simple power law:

$$\mu = \mu_0 \left(\frac{T}{T_0} \right)^b \quad (3.30)$$

with b a parameter to calibrate. This simple modelling is used throughout this work, unless explicitly mentioned for some parts when a more complex strategy is used.

3.2.4 Chemical kinetics

The description of combustion chemistry is of critical importance for simulation oriented towards pollutant prediction, and results from a compromise between cost and accuracy. To correctly describe the flame structure and pollutant formation, the retained model should be able to capture all flame regimes previously described and to correctly handle multiple chemical time scales, while keeping the numerical cost and stiffness reasonable for 3-D computations of realistic configurations. The main approaches available in the literature are presented in the next subsections.

Detailed chemistry

The most direct approach is to employ detailed chemistry, containing a thorough description of the chemical system, with up to hundreds of species and thousands of elementary reactions. Such mechanisms are constructed to reproduce experimental data for a large variety of phenomena: auto-ignition, extinction, shock tube experiments, premixed and non-premixed flames, spray flames, etc. They are available for small hydrocarbons (e.g. USCII mechanism for H₂/CO/C₁-C₄ [201]) to large hydrocarbon chains (e.g. the Dagaut mechanism for aviation jet fuel [202]). Detailed mechanisms are oriented for high-temperature (HT), low-temperature (LT) or both, it may include sub-mechanisms for soot (using the CDSM method previously introduced) and NO_x [203, 204]. The mechanisms contain a large set of elementary reactions, generally involving two or three species that represent from a mesoscopic point of view the interactions occurring at the molecular level. The reaction rate of a given reaction i of the form:



involving species A , B , C and D is expressed in an Arrhenius form as

$$\dot{r}_i = k_i [A][B] T^{\beta_i} \exp\left(\frac{-E_{a,i}}{RT}\right) \quad (3.31)$$

with:

- $[X] = \frac{\rho Y_X}{W_X}$ is the molar concentration of the species X ,

3. MODELING OF LAMINAR REACTIVE FLOWS

- k_i is the pre-exponential factor of the reaction [s^{-1} or $m^3.mol^{-1}.s^{-1}$],
- $E_{a,i}$ is the activation energy of the reaction [$kJ.mol^{-1}$],
- β_i is the Fudge factor [-].

Detailed mechanisms are generally applied only to 1-D laminar flames for two essential reasons:

- These mechanisms contain highly reacting radicals essential to describe the fuel oxidation. These highly reacting radicals have a life-span of the order 10^{-10} – $10^{-8}s$ and are associated with very small length scales as well. Therefore, their correct prediction requires a tremendous grid resolution and a costly implicit temporal integration of the stiff source terms might be required [205].
- The number of transported species rapidly becomes higher than one hundred for mechanism including PAH chemistry, which strongly increases the computational, memory and storage cost.

Therefore, for 3-D computations of realistic configurations including soot precursors chemistry alternative approaches have to be considered.

Skeletal chemistry

Skeletal mechanisms constitute the first level of reduction of a detailed mechanism, with a more limited validity range. However, in practical combustion applications, the operating conditions are known and the chemical description validity can be restricted to these conditions. Then, species and reactions that are not relevant to the target can be removed from the detailed mechanism.

Skeletal mechanism derivation

Numerous techniques are available to identify species and reactions that can be removed from a detailed mechanism without altering its prediction capability. Graph methods, such as Directed Relation Graph method (DRG) [206] and Directed Relation Graph method with Error Propagation (DRGEP) [39] are commonly used. The last one relies on a graph where the degree of coupling between species is mapped. It aims to identify easily the dependency between species, which are connected when they participate in at least one common reaction. The strength of the direct connection between a species A and a species B is quantified and weak connection can be removed from the mechanism.

Skeletal mechanism limitations

Although the number of species and reactions can be significantly lower than the detailed mechanism, highly reactive intermediates involved in the fuel oxidation can not be removed. This raises some limitations a use in CFD solver:

- The number of species in the mechanism and then the number of conservation equations to solve remains high.
- The resulting skeletal mechanism generally contains short time-scales species which are temporally and spatially stiff. The resolution of such intermediate species involves a space and time resolution that can be too restrictive for CFD solver.

Analytically Reduced Chemistry (ARC)

Skeletal mechanisms can be further optimized by removing highly reactive intermediates. For this purpose two strategies are reported in the literature:

- **Partial-Equilibrium Approximation (PEA):** This approach aims at reducing the stiffness of intermediate species by assuming associated reactions at equilibrium:

$$\dot{r}_i = 0 \quad (3.32)$$

For a reaction i , the equilibrium condition between reactant and product concentrations writes:

$$\prod_{k=1}^{n_{spec}} c_k^{\nu_{ik}} = K_i^{eq} \quad (3.33)$$

- **Quasi-Steady State Approximation (QSSA):** This approach assumes that some fast species, called QSS species featuring very low concentration are in an equilibrium state. This means that their net chemical source term is zero, and leads to a set of algebraic relations that has to be solved to determine the concentration of the QSS.

ARC derivation

Several methods are available in the literature to select the appropriate QSS candidates. They rely on the study of species production rates, time-scale analysis and optimization algorithms [207, 208, 209]. The method used in this work is the time-scale analysis using the Level of Importance (LOI) criterion [208, 210]. This method considers a species k as QSS if:

$$LOI_k = [X_k] \tau_k S_k^Q < \varepsilon \quad (3.34)$$

with:

- τ_k : the lifetime of species k , defined as $\tau_k = Y_k^{max} / \dot{\omega}_k^{max}$,
- S_k^Q : the species sensitivity of the relevant variable Q on species k ,
- ε : the tolerance parameter discriminating fast species.

3. MODELING OF LAMINAR REACTIVE FLOWS

Therefore, a species is suitable for QSSA if it remains the property of remaining in a small concentration while being highly reactive.

ARC limitations

The use of such methods can lead to an important reduction of the computational time but encounters some limitations:

- Although ARC has been successfully applied to the prediction of pollutants such as CO, NO_x or C_2H_2 for soot semi-empirical models [30, 31, 35, 211, 212, 213], its extension to complex soot modeling involving PAH or to multi-component fuel is difficult and leads to only moderate reductions.

Tabulated chemistry

Tabulated chemistry model relies on the flamelet concept: the chemical timescales compared to the flow time scales, are short so that the local structure of the reaction zone remains close to a canonical laminar flame. Flamelet models were introduced by *Peters* [214], where the flame structure is parametrized by a reduced set of control parameters [215, 216, 217]. First developed for non-premixed combustion, it can also be employed for partially-premixed and premixed combustion regimes.

Tabulation for non-premixed flames

Laminar counterflow diffusion flames introduced in Sec. 3.1.2 are generally chosen as the reference case. Flames are written as function of the mixture fraction z and parametrized with the scalar dissipation rate χ_z [218]. Unsteady flamelet modelling can be used to better describe slow processes such as the formation of pollutants and radiative heat transfer [28].

Tabulation for premixed and partially-premixed flames

In this case, laminar premixed flame are typically preferred as the reference flame for the table generation. The flame is written as a function of the progress variable c , and parametrized with the equivalence ratio. Similar to non-premixed flames, additional variables might be considered to include heat transfer or multi-stream problems [219]. Once reference flame identified, the chemical response of the reference case is stored in a look-up table as:

$$\dot{\omega} = \dot{\omega}_{\chi_z}(z) \quad \text{or} \quad \dot{\omega} = \dot{\omega}_\phi(c) \quad (3.35)$$

Tabulated models present a low computational cost thanks to the small number of scalars to transport and thus have been applied in numerous turbulent reactive flow simulations [28, 218, 219].

Tabulation limitations

However, these methods suffer some limitations when applied to practical combustion systems.

- To promote mixing and stabilization, practical combustion systems are generally swirled, leading to high turbulence intensity. This results in strong interactions through strain and curvature effects, along with dilution by burnt gases that are generally not taken into account in a tabulated approach.
- Multiple combustion regimes like stratified or partially-premixed flames are generally found in practical combustion systems. Therefore, there might be no proper reference flame suitable or identified to build the look-up table [220].
- In addition to flamelet hypothesis, strong modelling assumptions are generally needed to generate the look-up table to include spray description, pollutant formation and heat loss [28, 218, 219, 221]

Globally Reduced Chemistry (GRC)

The simpler approach to account for kinetic effects relies on Globally reduced chemistries (GRCs), which do not reproduce the details of chemistry, but are calibrated to reproduce essential properties of the flame, especially laminar flame speed and burnt gas temperature. They contain typically about 10 species and reaction steps, making their implementation in CFD solvers straightforward with a low computational cost. These mechanisms have been extensively used for small [222] and large hydrocarbons [223].

GRC derivation

Franzelli et al. [223] developed an empirical method to derive two-step mechanisms valid on a wide range of operating conditions. It is based on a fit of pre-exponential factors to reproduce the flame speed function of ϕ . For example using two reactions: one for the fuel oxidation and one for the CO - CO_2 equilibrium:



the constants of each reaction progress rate are fitted to match specified targets (laminar flame speed and thickness) in a large range of pressure-temperature-equivalence ratio conditions. A modified Arrhenius-like expression is built, for example for the fuel oxidation reaction:

$$\mathcal{Q}_1 = f_1(\phi)k_1[F]^{n_1} [O_2]^{n_2} T^{\beta_1} \exp\left(\frac{-E_{a,1}}{RT}\right) \quad (3.38)$$

with $f_1(\phi)$, k_1 , n_1 , n_2 , β_1 , $E_{a,1}$ adjustable parameters. Other general optimisation methods [224, 225] such as genetic algorithm [226] may also be used.

3. MODELING OF LAMINAR REACTIVE FLOWS

GRC limitations

Being much simplified, this type of approach has several limitations:

- GRC derivation is based on a given canonical case (laminar premixed flame) and not on physical grounds. Then, there is no guarantee about its capability to capture complex flame structures.
- No or wrong information about intermediate species is available, therefore GRC are not suitable to predict complex chemistry effect or pollutant formation.

Virtual chemistry

Recently, *Cailler et al.* [227] proposed an alternative method to address combustion chemistry. The so-called virtual chemistry is based on virtual optimized mechanisms to account for multiple combustion regimes at a reduced computational cost. The resulting virtual mechanism is composed of virtual reactions and virtual species, both reaction parameters and species thermodynamic properties are calibrated to describe the user-defined targets. First validated on 1-D laminar flames [227], and then CO prediction has been evaluated in methane turbulent flames [228, 229]. The extension of the method to large hydrocarbon fuel has been investigated successfully on laminar flames [229] as well as the prediction of soot using CDSM [108] on laminar ethylene-air flames [230].

Virtual chemistry methodology

First step is to define the quantities of interest and an ensemble of flame configurations representative of the target configuration. The virtual optimized mechanisms methodology is schematized in Fig. 3.6. Starting with an user-defined detailed chemistry, flame properties and reference flames are identified. Then, the mechanism is reduced and optimized to capture flame properties, the main virtual mechanism and another reduced sub-mechanism for each pollutant species considered in the reduction process. Since the main virtual mechanism is only trained to recover the flame structure, it does not give any information about individual species, the sub-mechanism are introduced to have access to the species of interest, typically the pollutants.

Virtual chemistry limitations

Virtual chemistry has shown its ability to reproduce complex flames, however the methodology presents some limitations waiting for further developments:

- The sub-mechanism methodology to have access to species of interest fails with complex chemical processes such as NO_x , where different chemical time scales are involved.

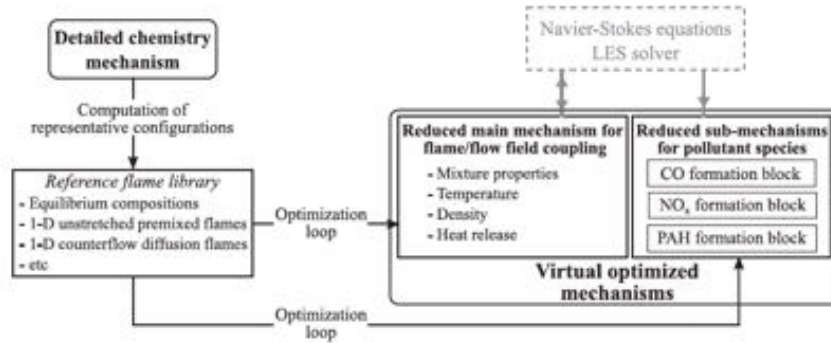


Figure 3.6: Virtual optimized methodology. Extracted from Cailler et al. [227].

- Spray flames are not taken into account. Since the thermodynamic properties are virtual as well, neglecting droplets-flame interactions can lead to significant errors.
- The target computation case must be clearly identified for the virtual optimization process (combustion regimes for example) and virtual chemistry can fail to predict some unexpected phenomena at the design stage.

Conclusion on chemical description

Recently, the analytically reduced chemistry (ARC) has been successfully applied to many complex phenomena. It addresses complex flame structures for simple gaseous fuels [30, 35, 143, 211, 231] as well as more complex fuels like aviation jet fuel [212, 213]. It has been retained to investigate ignition of liquid n-heptane [24] or the flame-wall interaction in a LO₂/LCH₄ cryogenic flame [232].

In this work, the capability of the ARC to describe species involved in soot formation like C₂H₂, PAH and other intermediate species, while keeping an affordable computational cost is investigated for both simple fuel (C₂H₄) and aviation jet fuel (Jet A-1). In the literature on the prediction of sooting flames, tabulation methods are typically preferred for the gaseous chemical description while the solid phase is usually modeled by sectional or moments method [36, 37]. Recently, virtual chemistry applied to soot prediction through the optimization of detailed mechanism with Chemical Discrete Sectional Method (CDSM) [230] represents also a promising method to predict soot formation at an affordable computational cost in complex configuration.

3.3 Equations for reacting two-phase flow

3.3.1 Euler-Lagrange modeling

In order to account for the spray in the LES equations, two main methodologies are available:

- In the Eulerian (EE) formalism, the liquid phase is considered as a continuous phase, that is resolved on the same grid than the gaseous phase.
- In the Lagrangian (EL) formalism, the spray is viewed as a discrete phase, composed of an ensemble of droplets that are tracked individually.

The main advantage of the EE formalism is to be very scalable in a parallel solver as the liquid and gaseous phases are solved on the same grid. This method has therefore been used in many applications including aeronautical configurations. In its mono-dispersed version, at each grid point and at each time, only a statistically averaged droplet diameter is known. The poly-dispersion of the spray can be recovered using sectional methods that involve multiple liquid phases and implies an important numerical cost. In order to take into account at a reasonable cost the poly-dispersion of the spray that must be considered in aeronautical engines, the Lagrangian formalism implemented in the AVBP code [233, 234, 235, 236, 237, 238, 239] is retained in this work.

This chapter starts by describing in Sec. 3.3.2 the set of equations solved for the dispersed phase. Exchange terms between phases are presented in Sec. 3.3.3, along with the coupling with the gaseous phase in Sec. 3.3.4. Finally, the injection model used in this work is explained in Sec. 3.3.5.

3.3.2 System of equations

3.3.2.1 Assumptions

In the EL formalism, different levels of coupling between the gaseous and liquid phases depend on the dispersed phase number density.

- For very dilute sprays ($\alpha_l < 1e^{-6}$), the liquid phase is not dense enough to have any impact on the gas phase. However, the droplets dynamics are influenced by the gas. This is called a **one-way coupling**.
- For moderately dense sprays, ($1e^{-6} < \alpha_l < 1e^{-3}$), the liquid phase acts on the gas dynamics by a retro-coupling force (fuel evaporation and drag force for instance). Thus, it is called a **two-way coupling**.
- Finally, for very dense sprays, ($\alpha_l > 1e^{-3}$), droplets are so close from each other that they interact. This level of coupling is named **four-way coupling**.

Two-way coupling is the relevant regime in aeronautical applications, where the fuel is injected by spray atomizer creating a mist of small droplets. Collisions between droplets are neglected as the spray is sufficiently diluted. The evolution of the spray is then described by resolving the evolution of each single droplet individually. Droplets are seen as simple material points that are tracked, with their inherent properties (temperature, size, etc). Considering the small size of droplets, they are also considered as spherical due the high surface tension forces.

3.3.2.2 Equations

With the assumptions previously given, the droplet evolution and motion is described with the following equation:

$$\frac{\mathcal{D}X_{p,i}}{\mathcal{D}t} = u_{p,i}, \text{ for } i = 1, 2, 3 \quad (3.39)$$

$$\frac{\mathcal{D}m_p u_{p,i}}{\mathcal{D}t} = F_{p,i}^{ext}, \text{ for } i = 1, 2, 3 \quad (3.40)$$

$$\frac{\mathcal{D}m_p}{\mathcal{D}t} = \dot{m}_p \quad (3.41)$$

$$\frac{\mathcal{D}m_p h_{s,p}}{\mathcal{D}t} = \dot{\Phi}_p \quad (3.42)$$

with X_p , u_p , m_p , $h_{s,p}$ respectively the position, velocity, mass, and sensible enthalpy of particle p , and F_p^{ext} , \dot{m}_p , and $\dot{\Phi}_p$ respectively the forces acting on it, its variation of mass and sensible enthalpy. These three last terms are explicitly derived in Sec. [3.3.3](#).

3.3.3 Exchange terms

3.3.3.1 Drag force

Single droplet dynamics have been studied widely and are well documented now. Forces acting on a droplet (F_p^{ext} in Eq. [3.40](#)) are buoyancy and gravity forces:

$$\vec{F}_G = \rho_l V_p \vec{g} \left(1 - \frac{\rho_g}{\rho_l} \right) \quad (3.43)$$

with ρ_l and ρ_g the liquid and gaseous densities, V_p the volume of the particle, and \vec{g} the gravity. Considering the liquid/gas ratio of densities, the buoyancy force can be neglected.

The unsteady virtual mass effect and Basset force, created by a change of the relative velocity between the droplet and the gas are also easily neglected [\[240\]](#) considering the density ratio in our application.

The most important force is the drag force \vec{F}_D applied on a droplet having a velocity \vec{u}_p in a gaseous environment at velocity \vec{u}_g . The general formulation of this force is:

$$\vec{F}_D = \frac{1}{2} \rho_g C_D A \|\vec{u}_g - \vec{u}_p\| (\vec{u}_g - \vec{u}_p) \quad (3.44)$$

3. MODELING OF LAMINAR REACTIVE FLOWS

with $A = \Pi d_p^2/4$ the projected area of the spherical droplet and \mathcal{C}_D the drag coefficient. This drag coefficient is very dependent on the relative velocity between the droplet and the gas as shown in Fig. 3.7 showing the evolution of \mathcal{C}_D as function of the Reynolds number based on the particle defined as:

$$\mathcal{R}e_p = \frac{\rho_g d_p \|\vec{u}_g - \vec{u}_p\|}{\mu_g} \quad (3.45)$$

with d_p the diameter of the particle and μ_g the gaseous dynamic viscosity. In typical aeronautical applications, Re_p stays below 500. Correlations describing $\mathcal{C}_D(Re_p)$ have been derived early in the literature starting from [Stokes,1851]. In 1927, Oseen [241] proposed:

$$\mathcal{C}_D = \frac{24}{Re_p} \left(1 + \frac{3}{16} Re_p \right) \quad (3.46)$$

but this law is valid only for $Re_p < 5$. In 1935, Schiller & Naumann [242] extended this law to $Re_p < 800$ with an empirical formulation:

$$\mathcal{C}_D(Re_p) = \frac{24}{Re_p} f(Re_p) \quad (3.47)$$

$$f(Re_p) = (1 + 0,15 Re_p^{0,687}). \quad (3.48)$$

This law is one of the most used in aeronautical applications and is used in the present work. Equation 3.40 finally writes:

$$\frac{\mathcal{D}u_{p,i}}{\mathcal{D}t} = \frac{1}{\tau_p} (u_{g,i} - u_{p,i}). \quad (3.49)$$

In this form, a characteristic droplet time τ_p is evidenced:

$$\tau_p = \frac{\rho_l d_p^2}{18 \mu_g f(Re_p)}. \quad (3.50)$$

τ_p can be compared to a characteristic gaseous time τ_g via the Stokes number $S_t = \tau_p/\tau_g$. For low S_t numbers, the droplet behaves like a tracer, which means that the velocity of the droplet is similar to the gaseous one. On the contrary, for high S_t number, the particle is little affected by the gaseous dynamics and its trajectory is dictated by its own inertia.

3.3.3.2 Evaporation

Spalding model

Evaporation is responsible for exchange terms of mass and energy \dot{m}_p and $\dot{\Phi}_p$. The analytical Spalding model [243] for isolated spherical droplet evaporation is recalled here as it is the basis of the evaporation model that is used in this work. Some hypotheses are required: the temperature inside the droplet is considered homogeneous (the thermal conductivity is infinite), and the gas and the droplet are considered at rest, so that

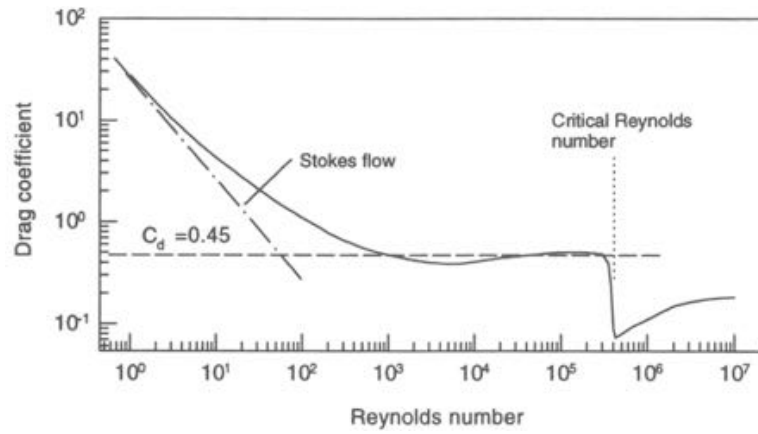


Figure 3.7: Drag coefficient C_D as function of the particle Reynolds number Re_p . Extracted from Crowe et al [240].

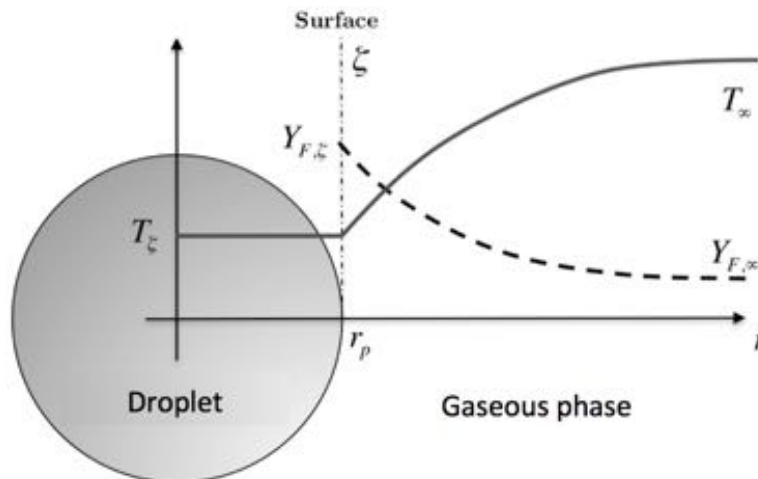


Figure 3.8: Radial profile of temperature T and fuel mass fraction Y_F around a droplet.

3. MODELING OF LAMINAR REACTIVE FLOWS

the gas has a quasi-static evolution. These hypotheses allow to solve the mass and thermal evolution of the droplet in its spherical reference frame and to only consider radial variations as illustrated in Fig. 3.8. Momentum, species and energy conservation is written between the surface of the droplet, denoted ζ , and the infinite ∞ , in steady conditions:

$$\rho_g u_g r^2 = \text{constant} = \frac{\dot{m}_F}{4\pi} \quad (3.51)$$

$$\rho_g u_g r^2 \frac{dY_F}{dr} = \frac{d}{dr} \left(r^2 [\rho_g D_F] \frac{dY_F}{dr} \right) \quad (3.52)$$

$$\rho_g u_g r^2 \frac{dC_P T}{dr} = \frac{d}{dr} \left(r^2 \frac{\lambda}{C_P} \frac{dC_P T}{dr} \right). \quad (3.53)$$

In the above conservation equations, r is the radial coordinate, \dot{m}_F is the gaseous fuel flux leaving the surface, Y_F the fuel mass fraction, D_F the fuel diffusivity, C_p the heat capacity of the mixture, T the gas temperature, and λ the thermal diffusivity. In the simplest formulation $[\rho_g D_F]$ and λ/C_P are evaluated at infinity (for $Y_{F,\infty}$ and T_∞) and are supposed constant along the radial profile. To improve the model Miller et al. [244] proposed a 1/3 – 2/3 rule: the reference temperature T_R and fuel mass fraction $Y_{F,R}$ at which transport and thermodynamic properties are evaluated and defined as:

$$T_R = T_\zeta + \frac{1}{3} (T_\infty - T_\zeta) \quad (3.54)$$

$$Y_{F,R} = Y_{F,\zeta} + \frac{1}{3} (Y_{F,\infty} - Y_{F,\zeta}). \quad (3.55)$$

If the constant Schmidt number Sc_F and Prandtl number Pr approximation is made, the transport coefficients finally write:

$$\rho_g D_F = \frac{\mu(T_R)}{Sc_F} \quad (3.56)$$

$$\frac{\lambda}{C_P} = \frac{\mu(T_R)}{Pr}. \quad (3.57)$$

The Schmidt and Prandtl numbers of the gaseous mixture can be used but it has been found by Sierra et al. [236] that these values may significantly differ from the values around the droplet: following Wilke's formulation [245] more accurate values may be used.

Droplet mass and temperature evolution

The integration of Eq. 3.52 between the infinite and the droplet surface leads to the expression of the evaporation rate of Eq. 3.41:

$$\dot{m}_p = -2\pi d_p [\rho \mathcal{D}_F] \ln(B_M + 1) \quad (3.58)$$

with B_M the mass Spalding transfer number:

$$B_M = \frac{Y_{F,\zeta} - Y_{F,\infty}}{1 - Y_{F,\zeta}}. \quad (3.59)$$

$Y_{F,\zeta}$ is obtained from the Clausius-Clapeyron equation considering that the droplet interface is in thermodynamic equilibrium. The evolution of the droplet diameter is easily recovered:

$$d_p^2 = d_{p,0}^2 - \frac{8\rho_g \mathcal{D}_F}{\rho_l} \ln(B_M + 1) \times t \quad (3.60)$$

with $d_{p,0}$ the initial droplet diameter. The classic d^2 evaporation law is found when the droplet temperature T_p is constant. A characteristic evaporation time τ_{ev} can then be defined:

$$\tau_{ev} = \frac{\rho_l d_{p,0}^2}{8\rho_g \mathcal{D}_F \ln(B_M + 1)}. \quad (3.61)$$

The evolution of the droplet temperature is calculated from the energy conservation equation (Eq. [3.42](#)):

$$\frac{\mathcal{D}m_p h_{s,p}}{\mathcal{D}t} = \dot{\Phi}_p. \quad (3.62)$$

By combining this thermal balance at the droplet interface where no energy is stored with the integration of Eq. [3.53](#), the evolution of T_p is found:

$$\frac{dC_{p,l}T_p}{dt} = \frac{1}{m_p} \left(\dot{m}_p L_v(T_p) - 4\pi r_p \frac{\lambda}{C_P} (C_P(T_p)T_p - C_P(T_\infty)T_\infty) \frac{\ln(B_T + 1)}{B_T} \right). \quad (3.63)$$

In the above expression, $L_v(T_p) = h_{s,g}(T_p) - h_{s,l}(T_p)$ is the latent heat of evaporation, r_p is the droplet radius, and $B_T = (1 + B_M)^{\frac{1}{\zeta_{eF}}} - 1$ is the temperature Spalding transfer number. The simultaneous integration of Eq. [3.58](#) and [3.63](#) allows to describe the temporal evolution of the evaporating droplet.

3.3.3.3 Abramzon & Sirignano correction

One of the hypotheses of the Spalding evaporation model described above is that the droplet and the gas are at rest. However in practical applications, an important relative velocity between the gas and the droplet can be found, leading to particle Reynolds number up to $Re_p \approx 500$. This flow enhances the evaporation process and must be included to better model the mass and thermal transfers between phases. Ranz & Marshall [\[246\]](#) introduced a Sherwood number and a Nusselt number as:

$$Sh = 2 + 0.55 Re_p^{1/2} (Sc_F)^{1/3} \quad (3.64)$$

$$Nu = 2 + 0.55 Re_p^{1/2} Pr^{1/3} \quad (3.65)$$

3. MODELING OF LAMINAR REACTIVE FLOWS

to take into account the local Re_p value. Eq. 3.58 and 3.63 are modified as follows:

$$\dot{m}_p = -Sh\pi d_p [\rho \mathcal{D}_F] \ln(B_M + 1) \quad (3.66)$$

$$\frac{dC_{p,i}T_p}{dt} = \frac{1}{m_p} \left(\dot{m}_p L_v(T_p) - 2Nu\pi r_p \frac{\lambda}{C_P} (C_P(T_p)T_p - C_P(T_\infty)T_\infty) \frac{\ln(B_T + 1)}{B_T} \right). \quad (3.67)$$

Finally, Abramzon & Sirignano [247] again modified the Sh and Nu numbers to take into account the boundary layer around the droplet allowing to estimate more accurately mass and thermal fluxes:

$$Sh^* = 2 + (Sh - 2) / F_M \quad (3.68)$$

$$Nu^* = 2 + (Nu - 2) / F_T \quad (3.69)$$

with

$$F_M = (1 + B_M)^{0,7} \frac{\ln(1 + B_M)}{B_M} \quad (3.70)$$

$$F_T = (1 + B_T)^{0,7} \frac{\ln(1 + B_T)}{B_T}. \quad (3.71)$$

3.3.4 Coupling with the gaseous phase

The coupling between the liquid and gaseous phases is simply done by transferring conservatively F_p^{ext} , \dot{m}_p , and $\dot{\Phi}_p$ for all droplets to the gaseous phase thanks to source terms in the gaseous conservation equations.

- Source term for mass conservation **and** fuel species conservation:

$$S_m^{l \rightarrow g} = \frac{1}{\Delta V} \sum_{p=1}^N \Psi_p \dot{m}_p. \quad (3.72)$$

- Source term for momentum:

$$S_{qdm,i}^{l \rightarrow g} = \frac{1}{\Delta V} \sum_{p=1}^N \Psi_p (-m_p F_{p,i}^{ext} + \dot{m}_p u_{p,i}). \quad (3.73)$$

- Source term for energy:

$$S_E^{l \rightarrow g} = \frac{1}{\Delta V} \sum_{p=1}^N \Psi_p \left(-m_p \vec{F}_p^{ext} \cdot \vec{u}_p + \frac{1}{2} \dot{m}_p \|\vec{u}_p\|^2 - \dot{\Phi}_p \right). \quad (3.74)$$

ΔV is the control volume of the considered grid node and N is the total number of droplets in this control volume. Ψ_p is the interpolation function on the grid. In this work, an inverse distance interpolation, illustrated in Fig. 3.9 is used.

$$\Psi_{p,j} = \frac{1/d_j}{\sum_{k=1}^{N_v} 1/d_k} \quad (3.75)$$

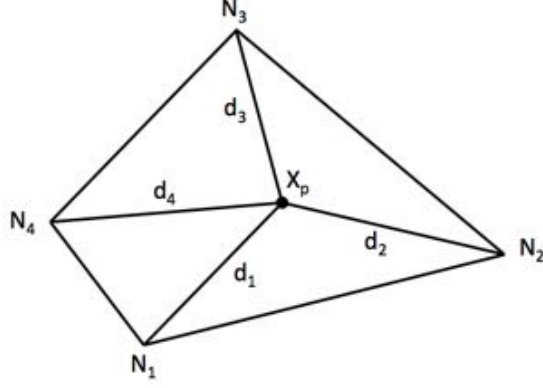


Figure 3.9: Particle source term projection on the nodes of the grid.

$\Psi_{p,j}$ is the particle weight associated to the vertex j of the element containing the droplet. d_j is the distance between the particle and the vertex j , and N_v is the number of vertices of the element. Note that when gaseous properties at the particle position are required, the same inverse distance interpolation is used.

3.3.5 Droplet injection

In order to accurately simulate pressurized liquid injectors that are often used in aeronautical combustors, primary and secondary breakup phenomena should be taken into account. However, these steps are not resolved with the Euler-Lagrange formalism used here. Sanjosé et al. [248] proposed a method imposing velocity and grain size profiles at the injector outlet without resolving atomisation. This FIM-UR (Fuel Injection Model by Upstream Reconstruction) model needs the liquid flow and injector geometry properties as inputs. In Fig. 3.10, θ_s is the mean half angle made by particles after their injection. R_a and R_0 are respectively the inner and outer radius of the liquid injection ring. Indeed, due to the swirling motion, an air core is formed in the center of the injector, and the liquid is pushed against the outer surface. A ratio variable is defined:

$$X = \frac{R_a^2}{R_0^2} = \frac{\sin^2 \theta_s}{1 + \cos^2 \theta_s} \quad (3.76)$$

In the Lagrangian formalism, only the injector parameters R_a , R_0 , the liquid mass flow rate \dot{m}_l and the spray characteristic θ_s are needed to determine the velocity imposed at the injection outlet ($x = x_0$). For one particle injected randomly in the injection ring :

$$u_{l,x}^0(\theta, r_0) = \frac{\dot{m}_l}{\rho_l \pi R_0^2 (1 - X)} \quad (3.77)$$

$$u_{l,r}^0(\theta, r_0) = 0 \quad (3.78)$$

$$u_{l,\theta}^0(\theta, r_0) = \tan(\theta) u_{l,x}^0(\theta, r_0) \quad (3.79)$$

3. MODELING OF LAMINAR REACTIVE FLOWS

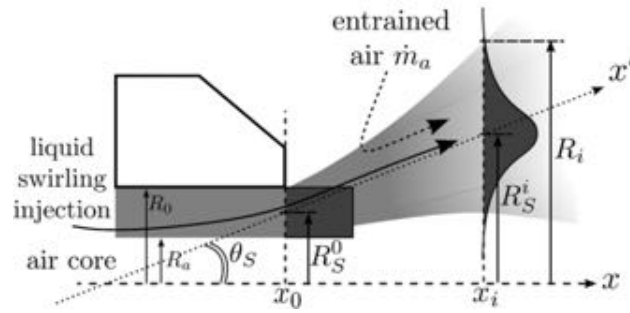


Figure 3.10: Scheme of the FIM-UR injection.

where θ is the half angle of the trajectory of the considered particle. The axial component is derived thanks to conservation laws. The radial component is null initially while the tangential one is set to respect the mean half angle of the injector. Finally, the grain size distribution is given by the user.

Chapter 4

Lagrangian soot tracking methodology

Various approaches are available in the literature to describe the formation and evolution of soot as well as their convective transport. They can be classified in two major classes:

- In the Eulerian (EE) formalism, the soot population is considered as a continuous phase, which is resolved on the same grid than the gaseous phase.
- In the Lagrangian (EL) formalism, the soot population is viewed as a discrete phase, composed of an ensemble of particles which are tracked individually.

The main advantage of the EL formalism is the direct description of a polydisperse particle population while Eulerian methods imply complex modeling. However depending on the number of particles, EL may lead to extremely high computational cost. In this work, the Lagrangian formalism implemented in the AVBP code is used [233, 234, 235, 236, 237, 238]. Its adaptation to soot modeling, named Lagrangian Soot Tracking (LST) is detailed here.

First, Lagrangian formalism applied to soot particles is introduced. Then, the development of efficient numerical methods to manage the computational cost of the method and the particle collisions is described. A simple soot chemistry model is first considered and implemented to evaluate LST approach. This evaluation is performed on both canonical and turbulent flames in terms of computational cost and soot predictions.

Contents

4.1	Lagrangian formalism for soot prediction	76
4.2	Numerical methods	77
4.2.1	Control of the number of particles	77
4.2.2	Physical particle collisions	80
4.2.3	Computational efficiency	82
4.3	Evaluation of LST efficiency	83
4.3.1	A semi-empirical soot model	84
4.3.2	Soot prediction	86
4.3.3	Computational efficiency	87
4.4	Conclusion	89

4.1 Lagrangian formalism for soot prediction

The prohibitive computational cost of the Lagrangian tracking of all physical particles in a 3D complex configuration explains why this method is barely used for soot. Most Lagrangian calculations are restricted to the resolution of realizability issues in MOM [249]. An attempt of deterministic Lagrangian calculation of soot has been made very recently by *Ong et al.* [193] where however the interactions between particles were neglected. This considerably simplified the implementation of the approach but also significantly reduced the accuracy as particle interactions are essential for soot. In the same time, *Lucchesi et al.* [38] proposed a MC-based (stochastic) [160] approach to simulate the evolution of an ensemble of soot particles where coagulation is simulated stochastically, while the other processes are treated in a deterministic manner. They used it to compute Lagrangian trajectories in a post-processing step of a previously computed simulation, i.e., without direct two-way coupling with the gas flow. In the present work, it is proposed to compute soot with a fully coupled semi-deterministic Lagrangian approach, overcoming the computational cost issue, with optimized algorithms. In particular, this requires maximum parallel efficiency, as well as a careful control of statistical convergence.

The LST methodology is based on the Discrete Particle Simulation (DPS) concept, similar to what is used for example for spray computations. However, contrary to dilute sprays, soot particle populations are dense, so that collisions have a high probability and must be accounted for. In addition, soot particles are nanometric with a very small Stokes number (defined in Sec. 3.3.3.1), leading to the following assumptions:

- **Dynamics:** Due to their small size soot particles may be considered as tracers. This means that drag is neglected in Eq. 3.44 and that particle velocity is always equal to the local gas velocity.
- **Molecular and thermal diffusion:** Soot transport is characterized by a high Schmidt number and diffusive mass fluxes are therefore neglected [250]. Thermophoretic effects are negligible in sooting turbulent non-premixed jet flames [231, 251] and are not considered in this work focusing on highly turbulent aeronautical-like combustors. However, thermophoresis may become significant in laminar flames.
- **Thermal state:** Due to their size, soot particles are assumed to thermal equilibrium with the gas, so that their temperature is homogeneous and equal to the local gas temperature.

Following the DPS approach, soot particles are handled as point sources, with the following properties for each particle p :

- X_p : position,
- u_p : velocity,
- r_p : radius,
- T_p : temperature.

In addition, as only a subset of physical particles are computed in the semi-deterministic concept (see Section 3.3), each particle also has a weight ω_p (also denoted *rparcel*) representing the number of physical particles having the same properties at the same location and time. To preserve statistical convergence at each location, this *rparcel* is not a user-defined parameter, but varies in space and time (see Section 4.2.1).

4.2 Numerical methods

The Lagrangian tracking of individual soot particle motion is standard and straightforward. The challenge lies in the computation of particle interactions and the control of the computational cost.

The latter is managed by introducing the concept of numerical particles, and controlling their number.

4.2.1 Control of the number of particles

The inception of nascent soot particles implies the constant creation of new particles, increasing their number in an uncontrolled way. In MC simulations, dynamic (also called resizing) [252] or constant-number approaches [253] are applied to nucleation [254]. To avoid resolving all physical particles in LST, the concept of numerical particle is introduced. The idea is to group all particles with similar properties in one particle representing them all. This numerical particle is then associated to a weight (ω_p or *rparcel*), proportional to the number of physical particles it represents [57]. To ensure statistical convergence while controlling the number of such particles, this weight may evolve in time and space, following a set of rules which are described below.

- **Particle creation:** The nascent particles are created with a weight dictated by both the control volume and the numerical timestep (see Sec. 4.3.1)
- **Maximum number of particles:** The number of particles in a control volume cannot exceed a maximum value N_{soot}^{max} , defined by the user.
- **Merging:** If the number of particles exceeds N_{soot}^{max} , merging is applied. Different merging mass-conservative techniques are investigated in the present work with different levels of accuracy on statistics. More accurate techniques require more

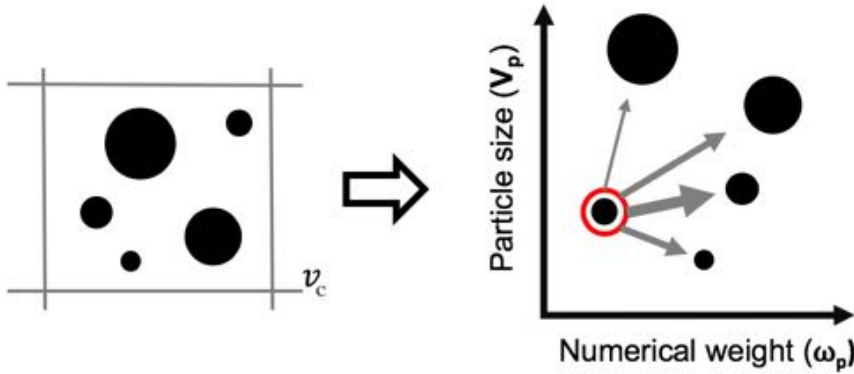


Figure 4.1: Schematic representation of MGNS merging procedure in a control volume.

computations, and the choice of the merging procedure is a trade-off between computational efficiency and accuracy on the predicted particle size distribution.

Various merging procedures, available in the literature, have been tested and are described below.

Constant-number approach

The Constant-number approach is quite popular as it enables to control and fix the computational cost of the simulation. To keep the number of particles per cell constant, each inception of a nascent soot implies the merging of one pair of particles or the removal of one selected particle and the redistribution of its mass over the remaining ones. Although it is the fastest method, random particle removal [254, 255, 256] is more detrimental to statistical convergence than the merging of particles with close properties or the selected removal of low-weighted particles.

An efficient method, as fast as random removal but more accurate, is the Garg, Narayanan, and Subramaniam (GNS) method [257]. The minimum weight particle is selected and its mass is redistributed equally to the remaining soot particles in the control volume. Targeting minimum-weighted particles enables to significantly reduce the impact on statistics [257]. Typically, nascent soot particles or particles that lost numerical weight by multiple collisions are most targeted by the removal procedure. Recently, *Tofighian et al.* [258] proposed a Modified version of GNS, so-called MGNS, where the properties of the removed particle are not equally distributed over all remaining particles, but proportionally to the proximity of their properties to the removed particle. The MGNS approach is schematized in Fig. 4.1

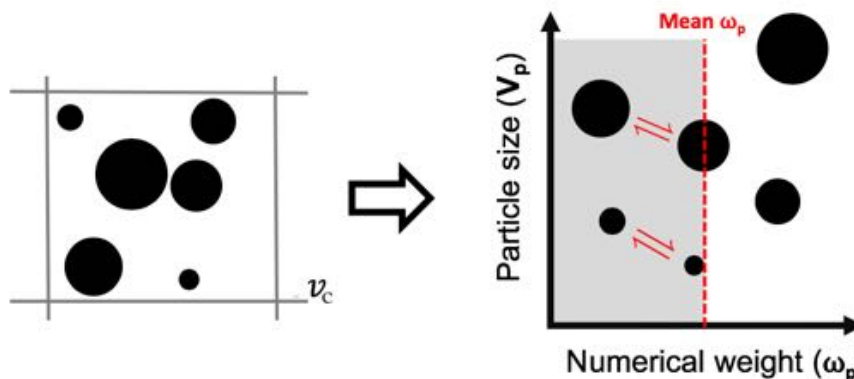


Figure 4.2: Schematic representation of low-weight merging in a control volume.

Low-weighted merging

The low-weighted merging approach follows the work of *Kotalczyk et al.* [259], where the merging of particles with low numerical weight is preferred. Particles having a numerical weight below the mean numerical weight of all particles in control volume are identified, and pairs with similar properties (size here) are merged. This procedure is schematized in Fig. 4.2. Note that this is not a constant-number approach, as the number of merged particles varies depending on the local particle size distribution. It is an enhanced version of MGNS approach, in which redistribution has been replaced by true-size pairing and merging. Computationally, this method is more efficient because it treats more than one particle at a time. However, it does not account for particle spatial location in the control volume, so that merging may considerably modify the spatial distribution of soot. Therefore, in this work the MGNS approach is preferred.

Statistical merging

The statistical approach is widely used in rarefied plasma flows, particle-based simulations (Particle In Cell PIC simulations) [260, 261]. This method implies a high computational cost as it evaluates each pair of particles in the control volume. All pairs of particles that are sufficiently close in terms of size and location are merged, according to two tolerance parameters given by the user:

- τ_V : the size tolerance [%]
- τ_X : the location tolerance [%]

The statistical procedure is illustrated in Fig. 4.3. τ_V and τ_X set to 33%. The shaded area corresponds, in the left figure to a zone where particles are merged. These two parameters drive the number of numerical particles. Low values limit the number of merges and then lead to a high number of numerical particles. Although this method

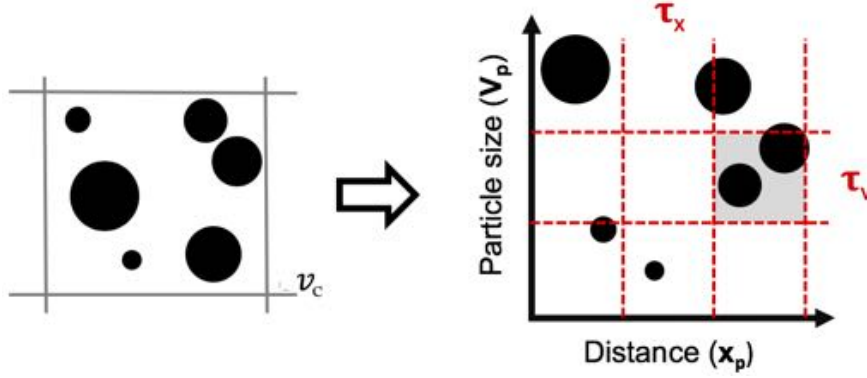


Figure 4.3: Schematic representation of statistical merging procedure in a control volume.

is very accurate for the particle size distribution, the number of numerical particles usually stays high and the gain in computational cost is too small for the application targeted in this work.

4.2.2 Physical particle collisions

In this work, soot particle collisions are involved in the coagulation process. For a monodisperse size distribution of soot particles, the coagulation source term reduces to a source term that is common to all particles. Coagulation in a polydisperse population is more complex, and requires to describe the collision between each pair of particles. This would lead to an extremely high computational cost in the LST approach. Stochastic approaches are therefore preferred, and were used for many applications, including atmospheric aerosols [255, 262, 263], rarefied gases [264], or particle-particle collisions in turbulent flows [265] and fluidized bed [266].

Stochastic coagulation

The coagulation of weighted particles has been defined in *Kotalczyk and Kruijs* [259]. Following *Kruijs et al.* [267], only binary collisions are retained. Considering a particle pair (i, j) with $i \neq j$, the collision frequency $\beta_{i,j}$ describes the collision rate between both particles. For symmetry reasons $\beta_{i,j} = \beta_{j,i}$ and the total coagulation rate between all particles represented by the pair (i, j) in the control volume v_c is expressed:

$$\beta_{i,j}^* = \max(\omega_i, \omega_j) \beta_{i,j} / v_c \quad (4.1)$$

where (ω_i, ω_j) are the weights of the numerical particles. The coagulation frequency (β) is calculated using the molecular regime defined in Eq 2.6. The probability of coagulation for each pair of particles (i, j) is then given by:

$$P_{i,j} = \frac{\beta_{i,j}^*}{\sum_{k,l \neq i,j} \beta_{k,l}^*} \quad (4.2)$$

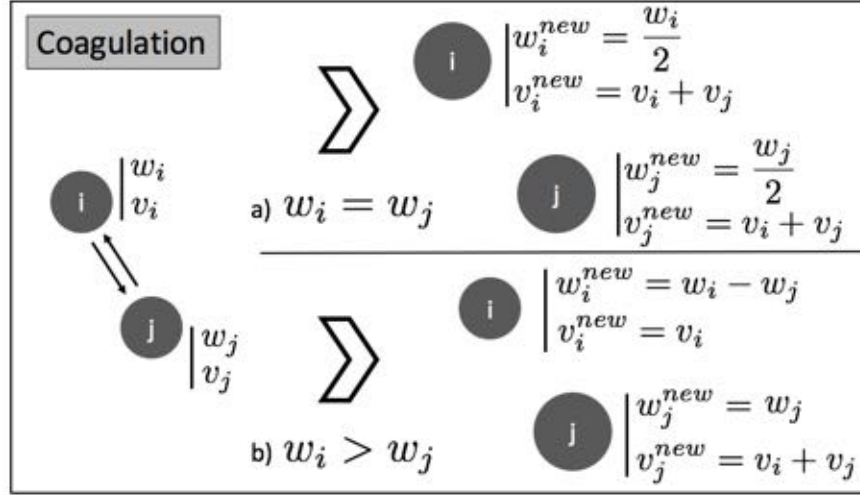


Figure 4.4: Description of a coagulation event between two numerical (weighted) particles.

This probability is used in the LST approach as follows:

- 1 At the cell level, $\beta_{i,j}^*$ is computed for each pair of particles (i, j) , and the maximum coagulation rate in the cell, β_{max}^* is determined.
- 2 The acceptance-rejection method [262] is applied: selecting a pair of soot particles (i, j) , a random number $r \in [0, 1]$ is computed and coagulation occurs if $r \leq \beta_{i,j}^*/\beta_{max}^*$. If the selected pair does not coagulate, the operation is repeated until one coagulation pair is found [263].
- 3 The selected coagulation event is realized accordingly to the constant-number method [263].
- 4 The coagulation time is computed as the inverse of the sum of all coagulation rates in the cell : $\tau_{coag} = 1/\sum_{i \neq j}^{N_{pair}} \beta_{i,j}^*$ [255, 267]. After an event-driven coagulation takes place, a time τ_{coag} is waited before the next coagulation event.

The above coagulation model assumes that the particles in the control volume are sufficiently numerous, and describe a sufficient number of discrete states of particles to fully describe coagulation statistics.

A coagulation event for a pair of particle (i, j) characterized by their volume (v_i, v_j) and their numerical weight (w_i, w_j) is described in Fig. 4.4. Two cases are considered depending on the numerical weights of the colliding particles:

- a) **Same numerical weight** ($w_i = w_j$): It is assumed that half of the physical particles represented by each colliding numerical particle effectively collide: for both colliding particles, the coagulation event induces a loss of numerical weight (divided by 2) and a gain in mass (sum of the mass of the colliding particles).

4. LAGRANGIAN SOOT TRACKING METHODOLOGY

- b) **Different numerical weight** ($\omega_i \neq \omega_j$): It is assumed that all physical particles described by the numerical particle with the smaller weight collide. Therefore, after collision, only $\omega_i - \omega_j$ are left to the particle i and particle j has increased in mass.

This coagulation process follows the constant-number approach: the number of numerical particles remains unchanged, and only the size and numerical weight of the considered particles are changed. In that way, the coagulation process is very efficient in terms of computational cost as it does not modify the number density of the soot population.

Limitations of the proposed stochastic coagulation

Although the proposed stochastic approach seems to be a suitable method to handle soot coagulation, it presents some limitations in its use in a CFD solver, and raises three issues:

- **Spatial and temporal discretization:** if the control volume and the numerical timestep are too big, collision rates may be underestimated. Fortunately, the simulation of turbulent sooting flames requires a fine mesh discretization, which induces in compressible flow a very small acoustically-driven timestep.
- **Soot intermittency:** in highly turbulent flames, especially flames considered in this work, soot intermittency is very high and the use of a coagulation timestep τ_{coag} may not be relevant: if evaluated at a time where soot concentration is very low, it induces no coagulation for a period which may be too long. To avoid this, soot coagulation is calculated only when soot population is sufficiently dense, preventing too long τ_{coag} . *Dellinger et al.* [195] proposed a coagulation method based on the work of *Fede et al.* [268], where coagulation is performed at each timestep. This could be considered for future developments.
- **Physical coagulation:** In this approach, there is no distinction between coalescence and agglomeration. This is addressed with a bi-variate description of soot particles presented in Chapter 6.

4.2.3 Computational efficiency

4.2.3.1 Increasing the time step

As particle motion is driven by a convective scale or chemical time usually larger than the acoustic timescale of the compressible flow, Lagrangian integrations are performed

with a convective time step, for each NS flow integrations. A soot frequency f_s is introduced, depending on the case and the numerical setup, and estimated as:

$$f_s = \alpha \tau_{min}/\tau_f \quad (4.3)$$

where τ_f is the flow time scale and τ_{min} corresponds to the minimum characteristic time of soot processes. The coefficient α allows to filter out some unsteadiness of the flow and depends on the application. In the present case $\alpha = 2$. Note that the soot frequency has to be chosen carefully to guarantee a minimum error.

The impact of soot frequency and gain in computing time are discussed in Section [4.3](#).

4.2.3.2 Soot parallelism

For a parallel application, the whole domain is partitioned into subdomains, with each subdomain assigned to a unique processor in such a way that each processor has about the same amount of computation and the communication cost between processors is minimized, it is the load-balancing. Similarly to mesh cells, Lagrangian particles are partitioned into the same subdomains. Lagrangian transport algorithm aims to localize in the mesh each moving particles at each iterations, even if a particle crosses a subdomain requiring parallel communications between processors. These communications are responsible about 80% of the Lagrangian computational cost [\[238\]](#).

Usually, the partitioning is done at the beginning of the computation, based only on mesh cells. However, a double partitioning pre-processing tool, imposing constraints on both mesh and particles, is available, the resulting partitioning can be used directly in AVBP and used in this work.

In addition, in each subdomains particles are sorted by their cell number in order to significantly reduce the computational cost of particles interactions.

4.3 Evaluation of LST efficiency

The efficiency of the proposed LST approach in complex configuration is evaluated here with a simplified soot model [\[155\]](#). The evaluation is done in 1D flame and in the FIRST configuration detailed in Chapter [8](#) following exactly the same numerical set-up employed by *Felden et al.* [\[35\]](#). Both the EE and EL formulations are evaluated and compared. starting from the same initial solution.

The EE approach has been validated in [\[35\]](#). The gas-phase chemistry was described by an Analytically Reduced Chemistry including 29 species, among which 11 were set in Quasi Steady State [\[213\]](#). The reaction rate constants of the Leung model have been calibrated in order to improve soot prediction. This is a standard procedure for such

4. LAGRANGIAN SOOT TRACKING METHODOLOGY

simple model, that has anyway a limited accuracy. It is however not the objective here to demonstrate the validity of the Leung model, but rather to demonstrate the validity and efficiency of LST. Compared to EE, for the same soot model. These guarantee a correct behavior before focusing on the soot numerical formalism. These results have been published in [194].

4.3.1 A semi-empirical soot model

First a simple, semi-empirical soot model is considered to evaluate the LST method. It is the semi-empirical, two-equations Leung model [155], employed in many previous studies [33, 35]. The model describes soot as a spherical monodisperse particle size distribution population, and was written in both EE and LST formulations. Although this model is too simple to be quantitatively accurate, this choice was made to ease the comparison between Eulerian and Lagrangian approaches.

In the Leung model, the soot particle mass evolves as:

$$\dot{m}_p = \frac{\dot{\omega}_s}{N} - \frac{m_p}{N} \dot{\omega}_n N_A \left[\frac{kg}{s} \right] \quad (4.4)$$

where N is the soot particle number density per volume, N_A is the Avogadro number and m_p is the particle mass. $\dot{\omega}_n$ and $\dot{\omega}_s$ refer to soot number density and mass fraction source terms, and are detailed below. Note that condensation is not taken into account.

//

In a monodisperse LST approach, soot particles are injected in the control volume with the local mean soot diameter, all these particles evolve in the same way following Eq. 4.4. This monodisperse LST approach should reproduce exactly the monodisperse EE approach and is used only as a validation step, it does not account for individual particle collisions but a mean coagulation source terms considering monodisperse particles in Eq. 4.4. However this chapter aims to apply the simple soot chemistry model used in [35, 155] in a polydisperse LST approach, different than monodisperse EE approach but with the same soot source terms.

Nucleation

Nucleation, which leads to the inception of nascent soot particles (nuclei), is expressed with the following source term:

$$\dot{\omega}_{n,nu} = \frac{R_{nu}}{N} \left(M_s - m_{p,nu} N_A \frac{2}{C_{min}} \right) \quad (4.5)$$

where $\dot{\omega}_{n,nu}$ is the nucleation part of the source term $\dot{\omega}_n$, M_s is the soot molecular weight, C_{min} is a constant, and R_{nu} is the nucleation reaction rate defined by Leung

et al. [155]:

$$R_{nu} = k_{nu}(T) [C_2H_2] \quad (4.6)$$

where k refers to the reaction rate (from [213]), T is the gas temperature, and $[-]$ stands for molar concentration. As the Lagrangian formalism is based on discrete particles, a new particle is created only after the nucleation source term is found sufficiently large. The new particle then has an initial weight equal to the number of generated nuclei, and is injected at a random position in the control volume with a given initial diameter. This initial diameter can be retrieved analytically from Eq. 4.5, considering that nuclei are formed at the end of the nucleation process, i.e., $\dot{\omega}_{n,nu} = 0$. This gives here an initial value of 0.98 nm.

In the current model, nucleation contributes only to the inception of soot particles and does not modify their properties. Therefore it does not contribute to the source term $\dot{\omega}_s$.

Surface reactions

Surface reactions act on the soot mass fraction source term $\dot{\omega}_s$ in Eq. 4.4 with two contributions:

$$\dot{\omega}_s = \dot{\omega}_{s,sg} - \dot{\omega}_{s,ox} \quad \left[\frac{kg}{m^3s} \right] \quad (4.7)$$

where subscripts sg and ox refer to surface growth and oxidation, and respectively read:

$$\dot{\omega}_{s,sg} = k_{sg}(T) [C_2H_2] S^{1/2} M_s \quad (4.8)$$

$$\dot{\omega}_{s,ox} = (k_{ox,O_2}(T) [O_2] + k_{ox,OH}(T) X_{OH}) S M_s \quad (4.9)$$

where X_{OH} refers to the molar fraction of OH species. Surface reactions are directly linked to the soot surface area per unit volume $S = \pi/4 d_p^2 N$, if spherical particles of diameter d_p are assumed.

Coagulation

The coagulation kernel for a particle pair i, j is calculated in the free molecular regime (see Sec. 2.3.1) as in the original Leung model [155]:

$$\beta_{i,j}^{fm} = C_a \sqrt{\frac{\pi \kappa T}{2 \rho_s}} \left(\frac{1}{v_i} + \frac{1}{v_j} \right)^{\frac{1}{2}} (d_{p,i} + d_{p,j})^2 \quad \left[\frac{m^3}{s} \right] \quad (4.10)$$

where C_a is the agglomeration rate constant equal to 9.0 higher than the commonly used value around 2.0 [37], κ is the Boltzmann constant, and ρ_s is different, following Leung model and equal to 2000 $[kg \cdot m^{-3}]$.

4. LAGRANGIAN SOOT TRACKING METHODOLOGY

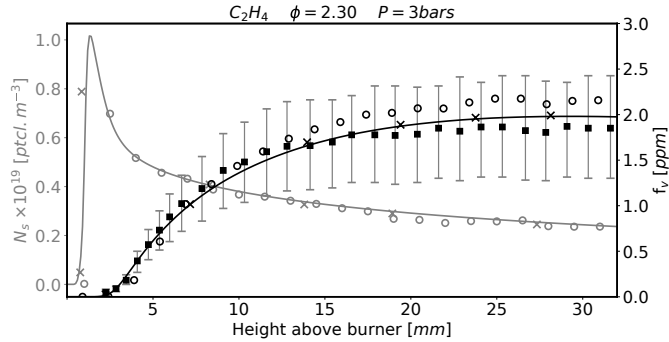


Figure 4.5: Soot number density (left axis, grey line) and soot volume fraction (right axis, black line) in the ISF Target Flame 4 (Laminar Premixed Pressurised 2). Comparison between experiment [269] (squares), EE (lines), monodisperse LST (crosses) and LST (circles).

4.3.2 Soot prediction

To assess the quality of the proposed method, results obtained in a 1D laminar sooting flame (ISF4) and the FIRST burner are presented below.

1D sooting flame ISF4

The pressurised 1D premixed ethylene-air sooting flame from the International Sooting Flame workshop (ISF Target Flame 4: Laminar Premixed Pressurised 2 [269]) is studied here. The equivalence ratio is high $\phi = 2.3$ ($C/O = 0.766$), and the pressure is 3 bars. For this case N_{soot}^{max} is set to 20 per control volume. Soot has been computed with both the EE and LST approaches. An additional case using monodisperse LST is also computed as a validation step only. Results are compared in Fig. 4.5.

As expected both monodisperse approaches, Eulerian and Lagrangian, are strictly identical and reproduce well the experiment as in [35]. The LST approach gives the same soot number density, but a slightly higher soot volume fraction downstream the flame.

To go further, the same 1D sooting flame is computed without surface reactions, in order to focus on coagulation. As the LST approach for coagulation is stochastic, several computations have been performed. Results are compared to the monodisperse Eulerian approach in Fig. 4.6. LST introduces a slight stochastic noise on soot volume fraction directly linked to N_{soot}^{max} . As expected, higher N_{soot}^{max} reduces the stochastic noise. Near the exit the statistical average of soot volume fraction is slightly higher in LST while the average soot number density is slightly lower. This is due to polydispersity which promotes coagulation of the largest particles: the number of particles is negatively impacted whereas the soot diameter increases.

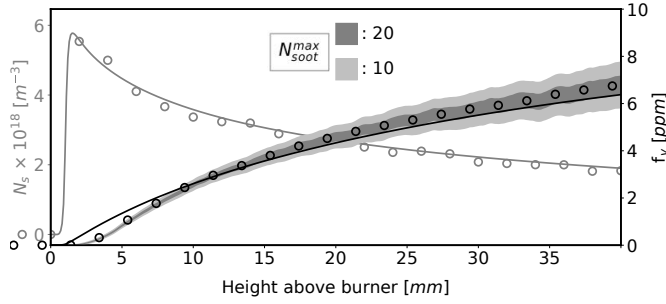


Figure 4.6: Soot number density (left) and soot volume fraction (right axis) for coagulation in the ISF Target Flame 4 (Laminar Premixed Pressurised 2). Comparison between EE (lines) and LST (symbols), shaded area indicate the stochastic noise of LST for two values of N_{soot}^{max} .

3D sooting burner: FIRST configuration

Figure 4.7 presents a qualitative comparison of time-averaged soot mass fraction fields obtained with both formalisms (EE and LST) and the experimental results. In both simulations a good order of magnitude and distribution of soot volume fraction is retrieved. The EE and LST descriptions lead to very similar results, confirming the validity of our LST approach. The two formalisms however lead to slight differences for oxidation. This is due to the removal of particles with a diameter lower than the nuclei in the LST approach, in order to avoid computing small diameter residual particles, whereas all particles are kept in the EE approach. A white isocontour of diameter at the nuclei value in Fig. 4.7b confirms that results for EE and LST are very similar for soot particles larger than nuclei.

The main difference between both approaches lies in the PSD [194], which is reduced to a Dirac function in the monodisperse EE. Results are available in Appendix A. The access to the PSD is critical to improve soot modeling as discussed in Chapter 2.

4.3.3 Computational efficiency

Test have been performed with varying soot frequencies (Section 4.2.3) and maximum number of soot particles per cell (Section 4.2.1). Results are reported in Tab. 4.1 for the laminar flame case. The soot frequency parameter leads to a significant gain of computational time without losing accuracy. The error is found negligible for $f_s \leq 10$ while the gain in computational time is significant. Higher values lead to significant errors since the resulting timestep can not solve properly the soot processes especially coagulation with characteristic time τ_{coag} .

The computing times required to compute 1 ms physical time of FIRST configuration with EE and LST are reported in Tab. 4.2. The computational time of the LST

4. LAGRANGIAN SOOT TRACKING METHODOLOGY

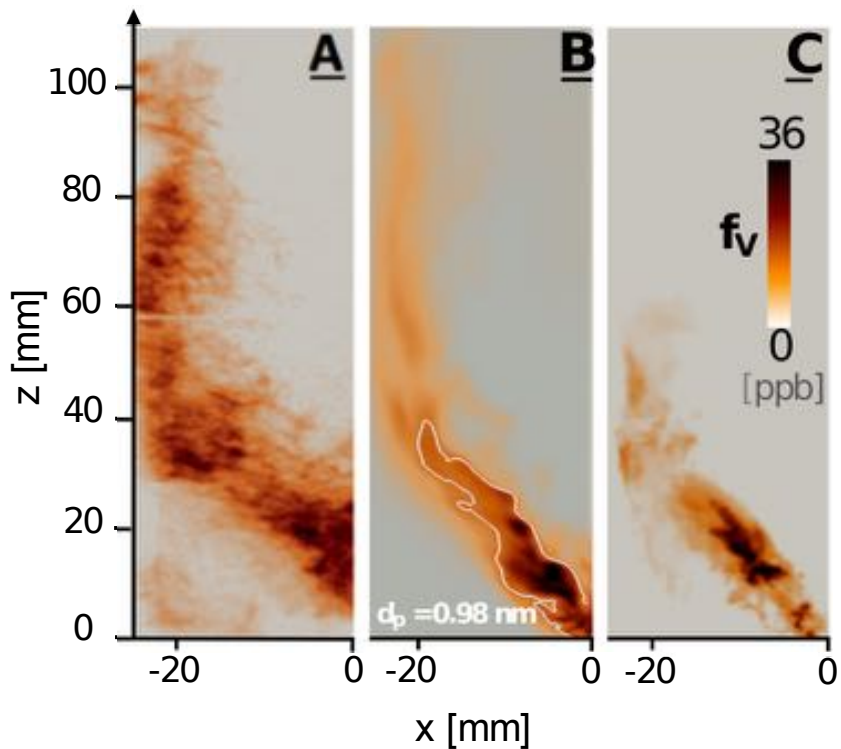


Figure 4.7: FIRST configuration: Comparison of time-averaged LII soot measurements with time-averaged soot volume fraction from LES using (B) the EE and (C) the LST approaches. Soot diameter isocontour $d_p = 0.98$ nm is shown in white.

Soot frequency, f_s	1	2	10	20	50
Lagrangian solver, %	23	8	4	3	2
Mean Error on f_v , %	0	1.3	4	13	19
Mean Error on PSD, %	0	1.5	7	16	25
Maximum Error on f_v , %	0	2.8	8	17	26
Maximum Error on PSD, %	0	3.7	11	23	34

Table 4.1: Contribution of the LST algorithm to the computational time for different values of f_s and maximum relative error on soot prediction and PSD for a laminar premixed flame.

	EE		LST		
f_s	-	1	5	1	5
N_{soot}^{max}	-	10	10	20	20
CPUh	12500	20250	13600	26650	14675

Table 4.2: Summary of computational requirements for the computation of 1 *ms* physical time of the FIRST configuration.

approach is of the same order of magnitude than the monodisperse EE approach, with the gain of an accurate PSD..

4.4 Conclusion

In this Chapter, an efficient Lagrangian method (LST) method has been proposed for soot prediction. The method is deterministic in the sense that individual physical particles are tracked, contrary to MC methods dealing with stochastic particles. It however includes a stochastic process for collisions. To limit the computational time, only a subset of particles is computed, representative of all particles possibly present in a control volume. With this strategy, LST becomes affordable in real complex geometries such as aircraft or internal combustion engines.

It has been found on a realistic geometry that LST gives access to the PSD at the same computational cost as a monodisperse EE approach, and then allows to envisage sophisticated soot chemistry models in real complex geometries. Note that detailed soot chemistry models may involve additional properties like surface or H/C ratio. If adding such properties is easier with Lagrangian than Eulerian methods [160], it may require more numerical particles to reach sufficient accuracy and then increase the computational cost. This will be discussed further in Chapter 8. However it was shown that increasing the number of particles impacts the computational cost to a reasonable extent.

4. LAGRANGIAN SOOT TRACKING METHODOLOGY

Chapter 5

Analytically Reduced Chemistry with accurate soot precursors prediction

Numerical models to describe soot particle chemistry has been described with various levels of accuracy and computational cost. However, the performance of these models is strictly related to the accuracy of the selected gas phase chemistry for soot precursors and other species participating to the soot surface reactivity.

The objective of this chapter is to select an appropriate gaseous chemistry including PAH species for the different fuels considered in this work: **ethylene** (C_2H_4) and **aviation jet fuel** (Jet A-1). The reduction of the retained mechanism is evaluated in terms of computational cost, e.g. the number of species associated.

First, the choice of an appropriate mechanism for ethylene-air mixture including PAH is explained. Then the derivation of an ARC with accurate PAHs prediction for ethylene-air mixture is detailed, and validated on laminar canonical cases. An attempt to consider larger PAHs in the resulting ARC mechanism is proposed. Finally, a methodology to predict PAH from the oxidation of an aviation jet fuel is presented.

Contents

5.1	Chemical kinetics of ethylene-air flames with accurate PAH chemistry	92
5.1.1	Ethylene combustion in sooting flames	92
5.1.2	Flame description	93
5.1.3	PAH description	93
5.2	Derivation and validation of an ARC for ethylene-air flames with accurate PAH chemistry	98
5.2.1	The YARC tool	98
5.2.2	Derivation of the reduced mechanisms	99
5.2.3	Validation of the ARC on laminar unstretched premixed flame	102
5.2.4	Comparison of spatial profiles	102
5.2.5	Global flame quantities	103
5.2.6	Preliminary conclusions about ARC for ethylene-air combustion with PAHs	103
5.3	Prediction of larger PAH for ethylene-air flames	104

5. ANALYTICALLY REDUCED CHEMISTRY WITH ACCURATE SOOT PRECURSORS PREDICTION

5.3.1	PAH modeling in the literature	104
5.3.2	Chemical sub-mechanism for large PAH	105
5.3.3	Validation on laminar premixed flames	109
5.3.4	Final reduction of PAH sub-mechanisms	110
5.4	Extension to aviation jet fuel chemistry	112
5.4.1	The HyChem methodology	113
5.4.2	Combining aviation jet fuel chemistry and PAH description	115
5.5	Conclusion	116

5.1 Chemical kinetics of ethylene-air flames with accurate PAH chemistry

5.1.1 Ethylene combustion in sooting flames

For an accurate description of soot particles in flames, not only gaseous combustion quantities must be retrieved but also soot precursors and other species participating to the soot surface reactions. In [270], several kinetic schemes were studied for the prediction of ethylene-air flame properties (laminar flame speed, adiabatic temperature) and PAH formation and the KM2 [94] was retained. In the present work additional mechanisms are studied :

- The Bisetti mechanism is based on the detailed chemical mechanism developed by Blanquart et al. [271]. This detailed mechanism accounts for all major pathways of PAH up to cyclopentapyrene $C_{18}H_{10}$. It has been validated extensively for a large set of fuels ranging from methane to iso-octane and one-ring aromatic species using different configurations. In the scope of using this detailed mechanism in DNS, the original detailed mechanism was reduced by *Bisetti et al.* [231] to a smaller mechanism, following a multi-step approach [39].
- The Slavinskaya mechanism [272] is an updated version of the Slavinskaya mechanism [273] and Chernov mechanism [274].
- The Polimi mechanism is an updated mechanism from POLIMI with a detailed soot kinetic description [275] using Chemical Discrete Sectional Method (CDSM). This mechanism takes into account the consumption of precursors to form the solid phase.

Details of all of the studied mechanisms are given in Tab. 5.1. According to the work of P. Rodrigues et al. [270], three mechanisms were adequate for the prediction of both flame properties and PAHs : KM2 , Slavinskaya and Polimi mechanism. The last two of them have been updated in the present work. Since the final application is to include

5.1 Chemical kinetics of ethylene-air flames with accurate PAH chemistry

Name	Nb. of species	Nb. of reactions	Largest hydrocarbon	Reference
KM2	202	1351	$C_{24}H_{12}$	[94]
BLANQUART	149	1651	$C_{18}H_{10}$	[271]
BISETTI	47	290	$C_{10}H_8$	[231]
SLAVINSKAYA	94	719	$C_{20}H_{12}$	[272]
POLIMI	451	23480	Large soot	[66]

Table 5.1: Studied mechanisms

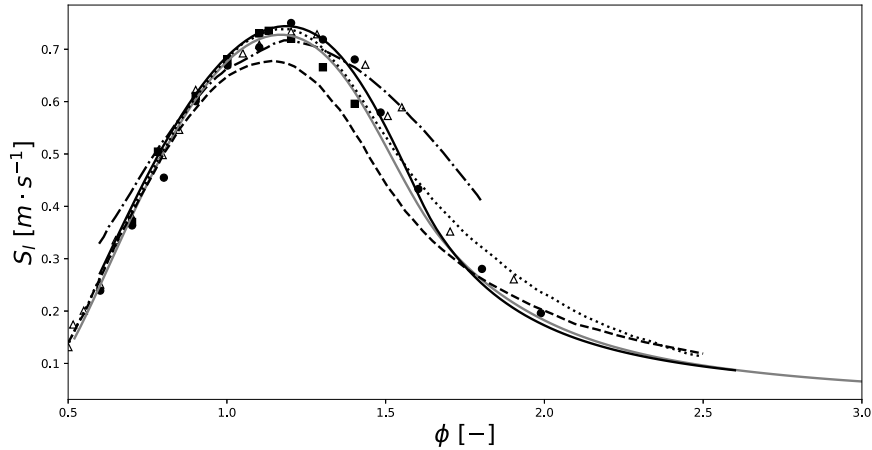


Figure 5.1: Comparison of ethylene laminar flame speed for different mechanisms (Bisetti et al. [231] : (—), Blanquart et al. [271] : (---), Slavinskaya et al. [272] : (- · - ·), KM2 [94] : (- - -), POLIMI [275] : (····), Hassan et al. [276] : (■), Egolfopoulos et al. [277] : (●), Jomaas et al. [278] : (△))

directly analytical chemistry in the LES solver, the objective is to assess the validity of the reduced BISETTI mechanism compared to these three more detailed mechanisms, currently considered as the state of the art.

5.1.2 Flame description

The prediction of the laminar flame speed of ethylene-air premixed unstrained flames at atmospheric conditions for different equivalence ratios are presented in Fig. 5.1. Results are compared to experimental data. It can be observed that all mechanisms predict well the laminar flame speed. As expected BLANQUART and BISETTI mechanisms are close and in perfect agreement with experiment. In terms of flame properties, the choice of BISETTI mechanism is a good compromise with only 47 species.

5.1.3 PAH description

The prediction of PAH in canonical flames is still an active field of research. PAH starts from one-ring aromatics like benzene (C_6H_6) to first nuclei including few hundred

5. ANALYTICALLY REDUCED CHEMISTRY WITH ACCURATE SOOT PRECURSORS PREDICTION

Case	phi	U [cm/s]	P [atm]	T [K]	Ref.
CASTALDI	3.06	2.0	1	298	[279].
ISF 5	2.4	2.0	1	298	[280, 281]
Nucleation Flames	1.95	2.3	0.263158	298	[282, 283, 284, 285]
	2.05	2.3			
	2.32	2.2			

Table 5.2: Target configurations to validate PAH predictions.

molecules and radicals. This complexity explains the difficulty of measurements, which still have high uncertainties, moreover increasing with the size of PAH. In an effort to provide reliable data to the community, the International Sooting Flame database (ISF¹) has been proposed and is available today. This database tends to minimize uncertainties linked to soot and PAH measurements since a lot of researchers from around the world with different techniques are involved. In this section three configurations are considered and listed in Tab. 5.2

First the flame experimentally studied by Castaldi et al. [279] corresponds to a burner stabilized C_2H_4 (21%) / O_2 (20.9%) / Ar (57.8%) premixed flame. A comparison of the prediction of several species for this burner is presented in Fig. 5.2. Soot production is not considered in this part. Since PAHs are consumed for soot production, it is expected that PAHs are slightly overestimated by the different mechanisms except for POLIMI mechanism where soot production is accounted for. A good agreement is obtained for the different mechanisms. Both CO molar fraction and PAHs are well captured by the different mechanisms. It should be noted that the reduced mechanism from Bisetti et al. [231] reproduces correctly the Naphthalene (A2), slightly overestimated as expected.

Figure 5.3 presents a comparison of the prediction of several PAHs for the flame experimentally studied by Ciajolo et al. [280], [281]. It corresponds to a burner-stabilized C_2H_4 (44.4%) / O_2 (55.6%) premixed flame known as the ISF-4 Premixed Flames 5. In this configuration, better agreement on large PAHs is found for the KM2 kinetic scheme compared to the other mechanisms. The prediction of Naphthalene (A2) is still in good agreement for both BLANQUART and BISETTI mechanisms.

In the next, only two mechanisms will be considered : KM2 and BISETTI mechanisms. These two reduced mechanisms have the capability to retrieve both flame properties and PAH, especially KM2 mechanism. Recently, the soot and PAH formation process has been investigated in three low pressure premixed methane flames [282, 283, 284, 285] :

¹www.adelaide.edu.au/cet/isfworkshop

5.1 Chemical kinetics of ethylene-air flames with accurate PAH chemistry

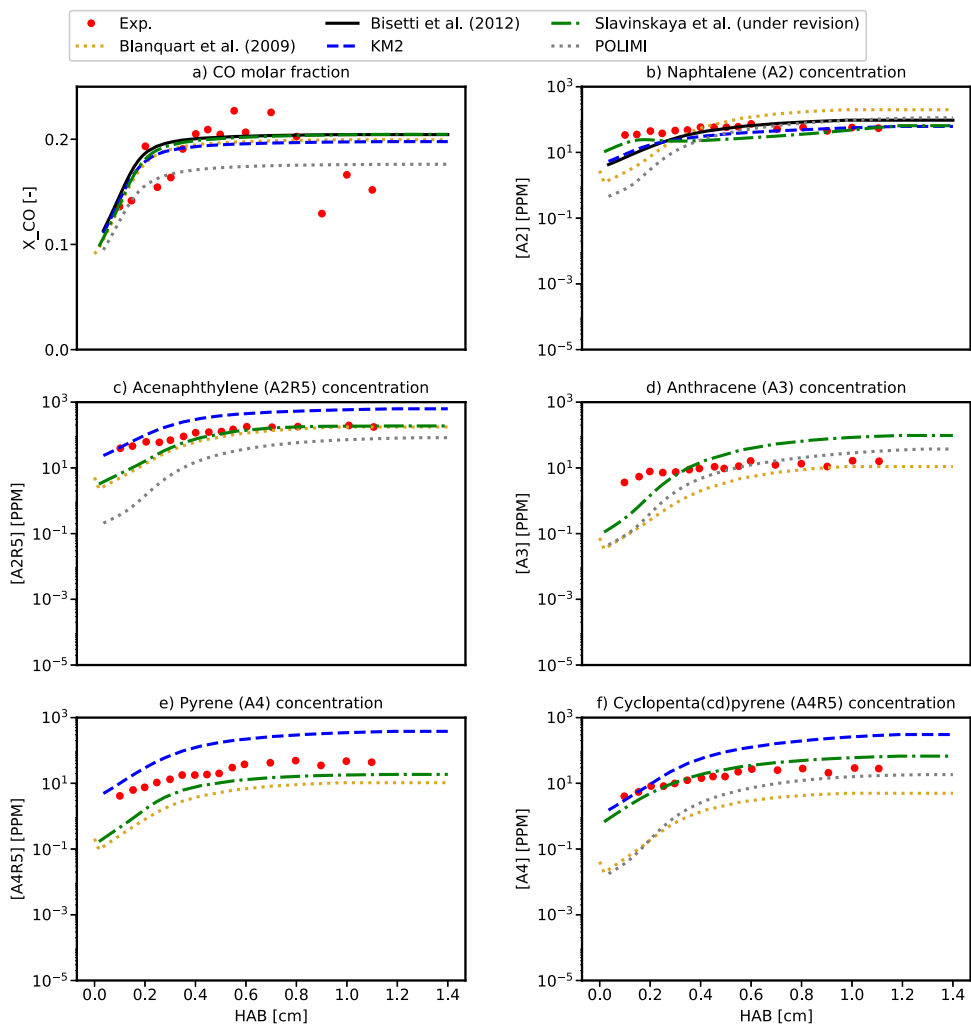


Figure 5.2: Numerical species profiles obtained on the burner stabilized $C_2H_4/O_2/Ar$ premixed flame for different mechanisms compared with experiment from *Castaldi et al.* [279]

5. ANALYTICALLY REDUCED CHEMISTRY WITH ACCURATE SOOT PRECURSORS PREDICTION

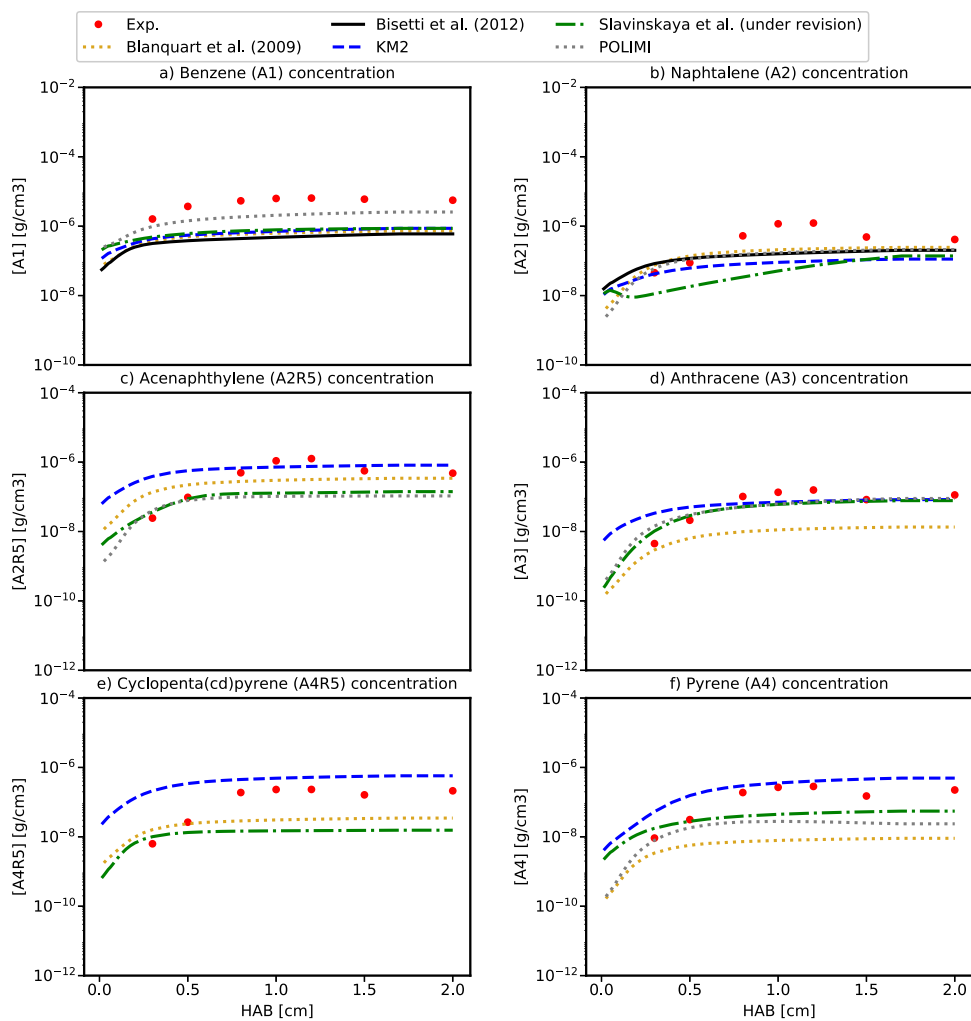


Figure 5.3: PAHs numerical predictions obtained on the burner stabilized C_2H_4/O_2 premixed flame for different mechanisms compared with experiment from *Ciajolo et al.* [280, 281]

5.1 Chemical kinetics of ethylene-air flames with accurate PAH chemistry

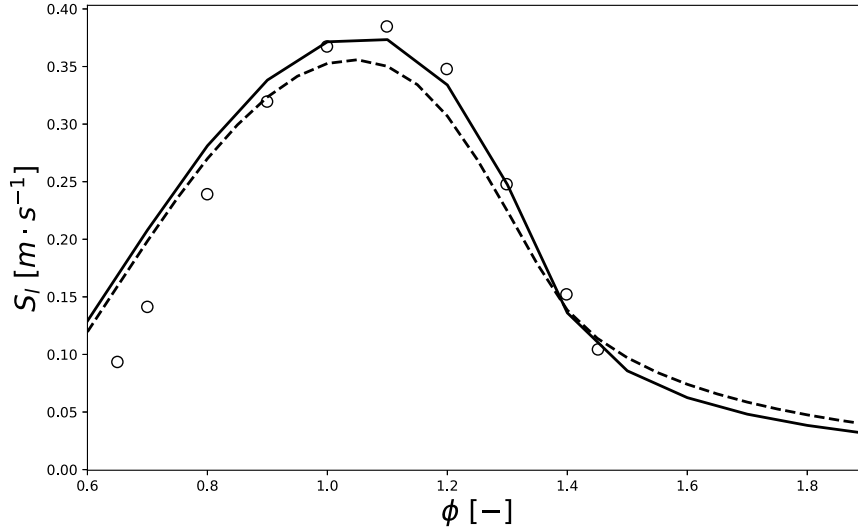


Figure 5.4: Laminar flame speed of methane-air flames for different mechanisms (BISETTI [231]: (—), KM2 [94]: (- - -). Circles (○) correspond to measurements by Van Maaren *et al.* [286]

- a so-called nucleation flame with equivalence ratio 1.95. In the nucleation flame no measurable soot growth after soot inception occurs, and the soot mass increases only by nucleation from the gas phase.
- a reference sooting flame with equivalence ratio 2.32.
- an intermediate flame with equivalence ratio 2.05.

In these flames, particular attention is devoted to soot gaseous precursors like polycyclic aromatic hydrocarbons. The low-pressure condition (200 Torr) enables to perform high fidelity measurements of both gaseous and solid phases. These flames are suitable to evaluate PAHs prediction and to assess the nucleation model (precursors choice, retro-coupling, etc..).

First, the prediction of laminar flame speed by the two mechanisms for methane-air mixtures is compared to experiment [286] in Fig. 5.4. Both mechanisms are able to describe CH₄-air oxidation process and can be considered to simulate low-pressure methane flames [285]. As suggested by Aubagnac-Karkar *et al.* [144], the temperature profile from El Bakali *et al.* [287] is imposed. Figure 5.5 compares the A₂ molar fraction for BISETTI and KM2 mechanisms at three equivalence ratio.

As expected, both mechanisms overestimate X_{A_2} since PAH consumption is neglected at this stage. With that in mind, A₂ is fairly predicted by both mechanisms. The final level of A₂ is better predict with KM2 mechanism, again. However, the shape of X_{A_2} profile of BISETTI mechanism is closest to the measurements. In addition, despite close equivalence ratio of Flame 1.95 and Flame 2.05 a significant difference is observed

5. ANALYTICALLY REDUCED CHEMISTRY WITH ACCURATE SOOT PRECURSORS PREDICTION

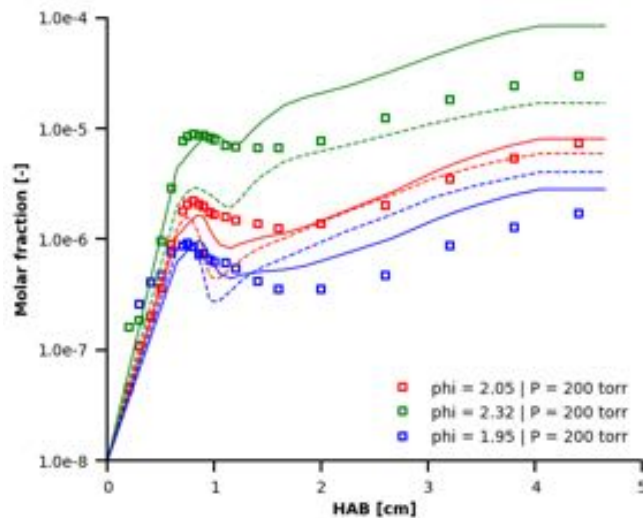


Figure 5.5: A_2 numerical predictions for BISETTI (solid lines) and KM2 (dashed lines) mechanisms for different equivalence ratio compared with experiment of *Desgroux et al.* [285] (symbols)

on X_{A_2} , only retrieved with BISETTI mechanism. The KM2 mechanism seems to be a suitable candidate for the present work for the following reasons :

- It contains large PAHs up to coronene (A_7).
- It captures well the level of first PAHs up to pyrene (A_4) in burner stabilized premixed flames.
- Its predicts well the PAHs evolution in C_2H_4 /Air counterflow diffusion flames (see [94]).

However it is far too big for the final application using 3D LES. On the other hand, the BISETTI reduced scheme is able to predict naphthalene (A_2) in two burner stabilized premixed flames (this work), in counterflow diffusion flames [231] and in nucleation flames (this work). In addition, it correctly predicts the laminar flame speed of ethylene at different pressures (Fig. 5.6) in particular is conditions considered in Chapter 8 for the FIRST configuration is computed as well before to go further. For these reasons, the BISETTI mechanism is retained for all simulations presented in this work.

5.2 Derivation and validation of an ARC for ethylene-air flames with accurate PAH chemistry

5.2.1 The YARC tool

The YARC reduction tool was developed by *Pepiot-Desjardins* [39]. It is employed throughout this thesis to derive ARCs from detailed mechanisms. The tool incor-

5.2 Derivation and validation of an ARC for ethylene-air flames with accurate PAH chemistry

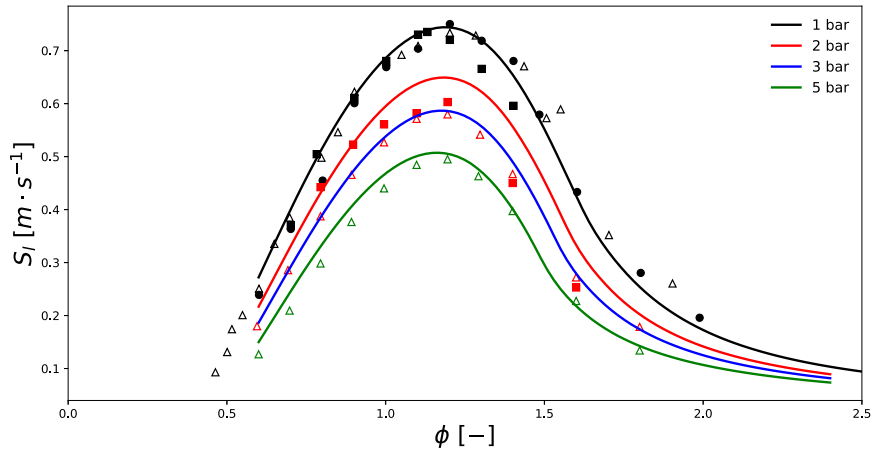


Figure 5.6: Flame speed of ethylene flames at various pressures: *Bisetti et al.* mechanism [231] (lines), *Hassan et al.* [276] (■), *Egolfopoulos et al.* [277] (△), *Jomaas et al.* [278] (●)

porates the DRGEP and LOI reduction techniques introduced. The flame solutions needed as sampled applications for the reduction techniques are computed using the software FlameMaster¹. Interfacing between FlameMaster and the reduction algorithms is automatically handled by YARC. The canonical cases that can be considered and combined for the reduction process are: auto-ignition, one-dimensional premixed flames and diffusion flames. The ranges of pressure, temperature and equivalence ratio are also defined by the user. However, to keep the computational cost of the reduction process moderate, the sampled applications consist in practice of a limited number of pertinent cases that are sufficient to involve all the relevant chemical pathways to be preserved in the reduced mechanism.

5.2.2 Derivation of the reduced mechanisms

Objective of the reduction process

In the present section, the objective is to derive ARCs suitable for ethylene-air combustion application in the conditions of the ISF-4 Target Flame 4. The reduction process is oriented towards preserving essential properties of interest: flame temperature, consumption speed, as well as correct prediction of C_2H_2 and PAH formation.

Reference mechanism

As stated in Sec. 5.1, the reference mechanism retained for ethylene-air oxidation is the BISETTI mechanism [231], which is already a skeletal mechanism built from the BLANQUART mechanism [271] following a multi-step approach [39]. This mechanism predicts all species involved in the HACA mechanism and PAH up to naphthalene (A2). Naphthalene plays an important role as a key intermediate in the formation of

¹www.itv.rwth-aachen.de/downloads/flamemaster

5. ANALYTICALLY REDUCED CHEMISTRY WITH ACCURATE SOOT PRECURSORS PREDICTION

larger aromatic species commonly used as soot precursors. The formation of naphthalene is believed to be the rate limiting step in the formation of large PAH [288]. Naphthalene is also considered to be the smallest aromatic species susceptible to forming dimers of significant lifetimes [289], making it a suitable candidate for nucleating species. This candidate has been successfully used [85, 182, 290, 291]. For all these reasons, BISETTI mechanism and its nucleating species, the naphthalene (A_2) has been used in the present work.

Existing reduced mechanisms in the literature

Existing reduced mechanisms with accurate PAH chemistry up to naphthalene A_2 [143, 231] are still rare and include about fifty species. They focused first on flame temperature and consumption speed [292, 293], later on pollutants like NO, CO [31] and C_2H_2 used in semi-empirical soot modeling [35]. In the work of *Dellinger et al.* [195], the reduced mechanism was derived from the skeletal mechanism from *Eberle et al.* [143] using QSSA.

Choice of the target canonical application

In the work of *Bisetti et al.*, emphasis was placed on accurately predicting the combustion characteristics of both n-heptane (C_7H_{16}) and toluene (C_7H_8). Ethylene (C_2H_4) was considered also as an important target during the reduction since a lot validation studies of soot models are performed with ethylene flames. The automatic reduction was performed for counterflow diffusion flames of C_7H_{16} -air and C_7H_8 -air at various scalar dissipation rates. As the targeted ISF-4 Target Flame 4 features both non-premixed and premixed local combustion, these two regimes have been investigated in this work.

5.2.2.1 From skeletal to ARC: the QSSA

First note that considering the targeted application, the species strictly involved only in n-heptane oxidation were removed: C_7H_{16} , C_7H_{15} , C_5H_{11} , C_5H_{10} and C_4H_8 . At the end the final skeletal mechanism contains 42 species and 276 reactions.

The appropriate QSS species are identified using the LOI criterion [210] using YARC tool and a chemical time scale analysis. The chemical time scale for each species can be estimated from the species source term and mass fraction as:

$$\tau_k = \frac{Y_k^{max}}{\dot{\omega}_{Y_k}^{max}} \quad (5.1)$$

where the superscript max denotes the maximum value over the domain. This estimation can be refined by decomposing the net formation rate of a species into production and destruction contributions [294]:

$$\dot{\omega}_{Y_k} = \dot{\omega}_{Y_k}^+ - \dot{\omega}_{Y_k}^-, \quad (5.2)$$

5.2 Derivation and validation of an ARC for ethylene-air flames with accurate PAH chemistry

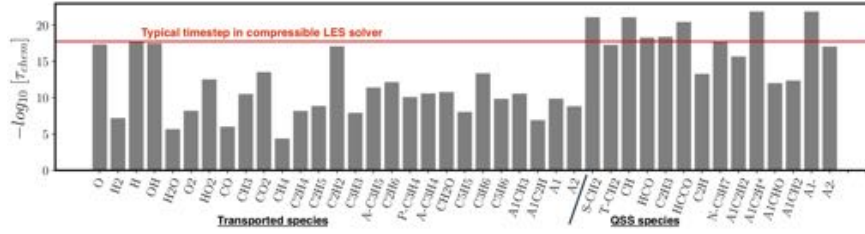


Figure 5.7: Chemical timescales of the skeletal mechanism of Bisetti compared to typical flow timescale in the ISF-4 Target Flame 4 condition.

where the superscripts $+$ and $-$ denote production and destruction respectively. Two time scales, respectively associated to production and destruction are then deduced

$$\tau_k^+ = \frac{Y_k^{max}}{\dot{\omega}_{Y_k}^{+,max}}, \quad (5.3)$$

$$\tau_k^- = \frac{Y_k^{max}}{\dot{\omega}_{Y_k}^{-,max}}. \quad (5.4)$$

This definition is of interest for species exhibiting a strong disparity in time scales between production and destruction, which is typical for CO: the production occurring in the flame region is generally much faster than the oxidation into CO₂ in the flame and post-flame regions.

Stiff species are identified by comparison of their time scale with the time scale of the flow. Species with very short time scales may lead to numerical instabilities if they are integrated with the flow timestep.

Numerical strategies exist to improve the stability of the temporal integration, as detailed in Jaravel and Felden thesis [295, 296]. An alternative is to consider stiff species as good candidates. Although this might deteriorate the prediction capability of the ARC, it leads to a robust chemical description.

Figure. 5.7 reports the time scales in the target application conditions. Keeping targeted species and highly coupled species as transported species, 14 species, namely S-CH₂, T-CH₂, CH, HCO, C₂H₃, HCCO, C₂H, N-C₃H₇, C₅H₁₁, A1C₂H₂, C₅H₁₀, A1C₂H*, A1CHO, A1CH₂, A1- and A2- are retained for QSS approximation.

Direct analytical expressions are derived for the concentrations of QSS species from the algebraic QSS system. Finally, 28 non-QSS species remain in the resulting Analytically Reduced Chemistry (ARC) named C2H4_A2_28_205_14_LG in the following.

5. ANALYTICALLY REDUCED CHEMISTRY WITH ACCURATE SOOT PRECURSORS PREDICTION

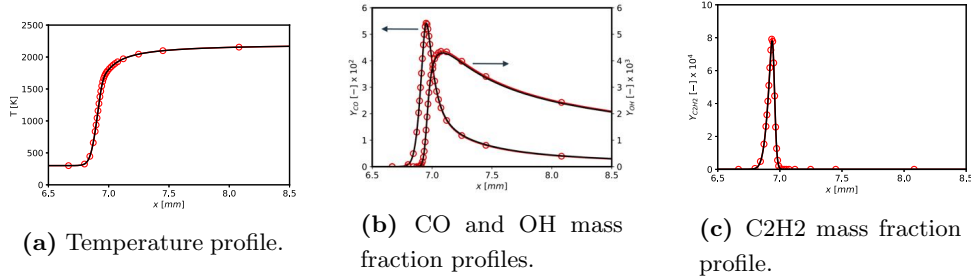


Figure 5.8: One-dimensional premixed unstrained ethylene-air laminar flame at $P = 3 \text{ bars}$ and equivalence ratio $\phi = 0.8$. Comparison between BISETTI (—), C2H4_A2.28.205.14_LG (\circ), of T (a), CO and OH (b) and C_2H_2 (c).

5.2.3 Validation of the ARC on laminar unstretched premixed flame

The objective of this subsection is to assess the C2H4_A2.28.205.14_LG mechanism on canonical laminar flames, covering the full range of equivalence ratio.

5.2.4 Comparison of spatial profiles

Three examples have been selected to illustrate the behaviour of the reduced scheme, corresponding to a lean case with $\phi = 0.8$ (Fig. 5.9), a rich case at $\phi = 1.2$ (Fig. 5.9) and a very rich case at $\phi = 2.0$ (Fig. 5.10). All cases are at $P = 3 \text{ bars}$ as in the target application FIRST.

In the **lean case** ($\phi = 0.8$), the skeletal mechanism from *Bisetti et al.* and the reduced mechanism exhibit the same temperature, CO, OH evolutions and C_2H_2 evolution (Fig. 5.8). In particular, the peak of each species shown (CO/OH/ C_2H_2) is well captured by the reduced mechanism. In this example, there is not enough A2 to compare both mechanisms. The C2H4_A2.28.205.14_LG matches perfectly the *Bisetti et al.* mechanism for all other quantities (not shown).

In the **rich case** ($\phi = 1.2$) shown in Fig. 5.9, the flame structure is again well reproduced by the reduced mechanism compared to the reference. The CO and C_2H_2 profile increase with the equivalence ratio but A2 is still too low to allow a comparison.

In the **very rich case** ($\phi = 2.0$) shown in Fig. 5.10, a relevant level of naphthalene (A2) is found and is representative of the locally rich mixture found in the target configuration where soot particles appear. The peak and the level in the post-flame of C_2H_2 and A2 mass fractions are well captured by the reduced mechanism. The agreement is here again very good between the reduced mechanism and the reference mechanism.

5.2 Derivation and validation of an ARC for ethylene-air flames with accurate PAH chemistry

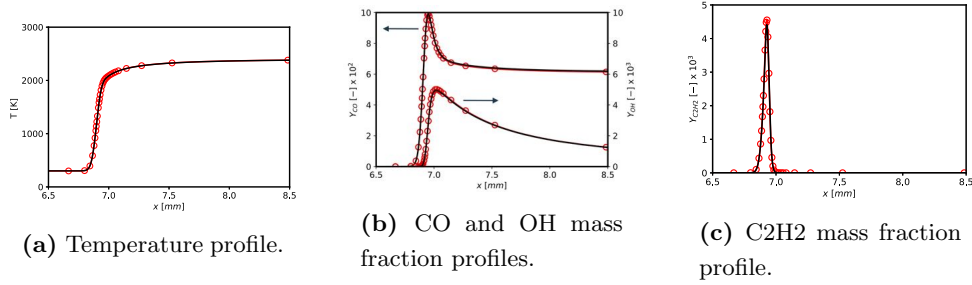


Figure 5.9: One-dimensional premixed unstrained ethylene-air laminar flame at $P = 3$ bars and equivalence ratio $\phi = 1.2$. Comparison between BISETTI (—), C2H4_A2_28_205_14_LG (○). of T (a), CO and OH (b) and C_2H_2 (c).

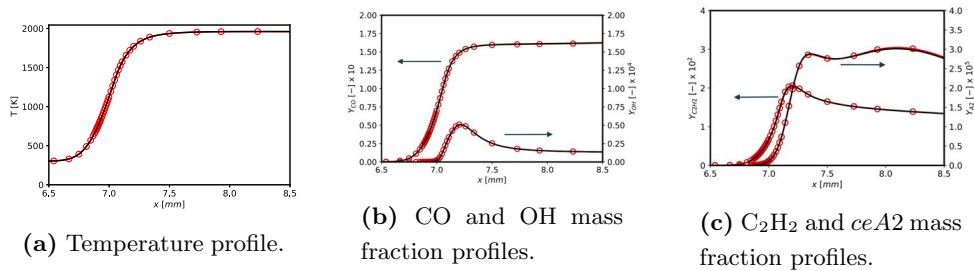


Figure 5.10: One-dimensional premixed unstrained ethylene-air laminar flame at $P = 3$ bars and equivalence ratio $\phi = 2.0$. Comparison between BISETTI (—), C2H4_A2_28_205_14_LG (○). of T (a), CO and OH (b) and C_2H_2 (c).

5.2.5 Global flame quantities

To continue the validation of the reduced mechanism, the laminar flame speed, adiabatic temperature, CO and A2 formation rate integrated through the flame (i.e. total production rate in the flame) are shown as functions of the equivalence ratio ($\phi = 0.5 - 2.5$) in Fig. 5.11. To focus on the flame zone, CO and A2 total production rates are integrated up to $c = 0.98$, where $c = (Y_{CO} + Y_{CO_2} + Y_{H_2O}) / (Y_{CO}^{eq} + Y_{CO_2}^{eq} + Y_{H_2O}^{eq})$ is the progress variable, with the superscript eq denoting equilibrium values:

$$\dot{\omega}_{CO,A2}^{tot} = \int_{c < 0.98} \dot{\omega}_{CO,A2} dx. \quad (5.5)$$

The value $c = 0.98$ is sufficiently high to capture CO and A2 formation in the flame front and sufficiently low to exclude slow post-flame chemical processes. The ARCs recover very well the laminar flame speed, A2 and CO flame production rates for the whole range of equivalence ratio considered.

5.2.6 Preliminary conclusions about ARC for ethylene-air combustion with PAHs

The laminar validation cases illustrate the capability of ARCs to accurately describe the flame structure and PAH evolution. However, it should be noted that all these

5. ANALYTICALLY REDUCED CHEMISTRY WITH ACCURATE SOOT PRECURSORS PREDICTION

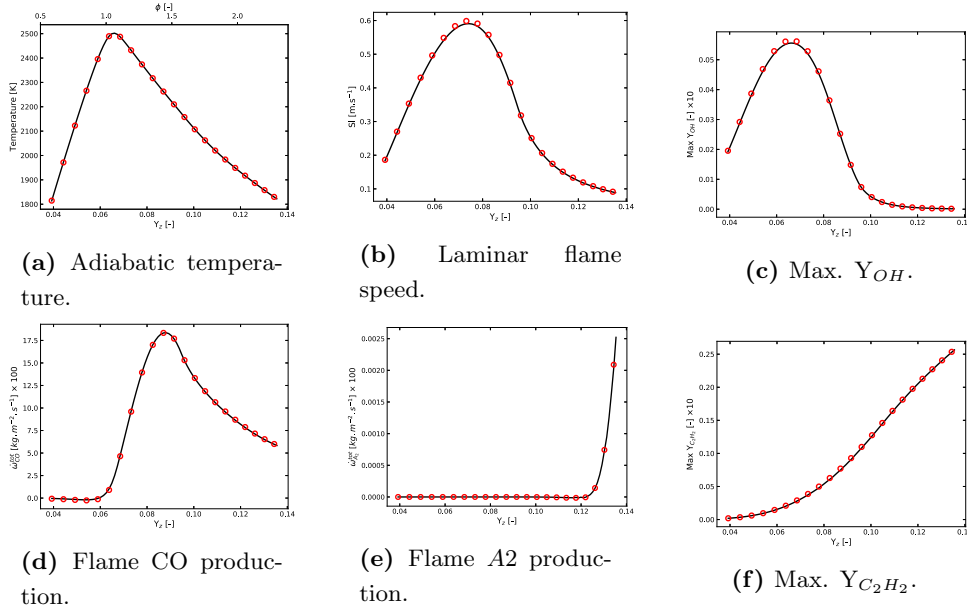


Figure 5.11: One-dimensional premixed unstrained ethylene-air laminar flame at $P = 3$ bars. Comparison between BISETTI (—), C2H4_A2_28_205_14_LG (○). ; Adiabatic temperature, laminar flame speed, OH and C₂H₂ mass fraction, CO and A2 flame production.

results were obtained using Cantera, which includes detailed transport models and is restricted to laminar cases.

5.3 Prediction of larger PAH for ethylene-air flames

5.3.1 PAH modeling in the literature

The ARC C2H4_A2_28_205_14_LG mechanism describes PAH evolution up to naphthalene (A2) only. The next step is to model larger PAHs. A common approach is to initiate soot by collision between two pyrene (A4) molecules, which gives credible results [78, 99, 137, 181, 290, 297, 298], although it has been proven that the dimer of pyrenes is not thermodynamically stable at flame temperature [6, 106, 299]. Many other approaches have been proposed to model larger PAHs:

- Large PAHs (A5) with reversible dimerization reaction [142, 300],
- lumped PAHs from naphthalene (A2) to cyclo[cd]pyrene (A4R5) [85] or from pyrene (A4) to coronene (A7) [36, 270] including respectively 8 and 7 PAH,
- fictitious PAHs linking the gas phase to the solid phase [143, 177, 195, 301] using sectional methods similarly to soot particles as illustrated in Fig. 5.12.

5.3 Prediction of larger PAH for ethylene-air flames

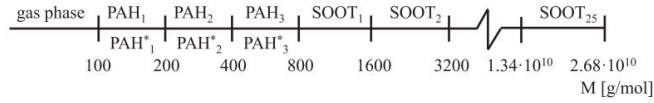


Figure 5.12: Definition of the PAH, PAH* and soot sections (Extracted from *Eberle et al.* [143]).

Name	PAH ₂	PAH ₂ *	PAH ₃	PAH ₃ *
Composition	C ₂₀ H ₁₀	C ₂₀ H ₉	C ₄₀ H ₂₀	C ₄₀ H ₁₉
Diameter (nm)	0.75		0.95	

Table 5.3: List of fictitious PAH species

- lumped or fictitious PAH species and soot particles gathered into classes called "BINS" in kinetic models or Chemical Discrete Sectional Method (CDSM) [66, 108, 181, 302] introduced in Sec. 2.3.1

In the following, starting from the ARC C2H4_A2.28_205.14_LG , two strategies to have access to larger PAHs are evaluated and the associated effect on soot prediction is investigated. The first strategy relies on fictitious PAHs, as developed by *Eberle et al.* [143], applying SPAMM methodology [180] to convert sectional sections into chemical lumped species. In this approach, naphthalene (A2) acts as the first PAH (PAH₁ in Fig. 5.12). The second strategy is to identify and reduce the main reaction pathways leading to pyrene (A4), to give access to large PAH, at low computational cost, e.g., with the minimum number of additional species.

5.3.2 Chemical sub-mechanism for large PAH

Two strategies are detailed for the description of large PAH sub-mechanism.

Fictitious PAHs

The sectional description of PAHs proposed by *Eberle et al.* [143] involves three sections, where each section represents a range of molecular PAH and its radicals PAH*. In this work, the first PAH₁ and its radical are A2 and A2* available in the BISETTI mechanism. Then four additional species are required, defined in Tab. 5.3. Following the work of *Eberle et al.* [143], PAH₂ results from the collision of two radicals PAH₁*, where PAH₁* is C₁₀H₇ i.e., the radical associated to naphthalene C₁₀H₈. Then the number of PAH₂ carbon atoms is $n_{C_{PAH_2}} = 2n_{C_{PAH_1}}$, in the same way the number of PAH₂ carbon atoms is two times higher than $n_{C_{PAH_2}}$. Their H/C ratio is fixed to 0.5 similarly to nascent soot particles [6]. The set of reaction is defined in Tab. 5.4. The collision rates \dot{r}_c of PAH_i and PAH_j are defined as:

$$\dot{r}_c = 2.2N_A\gamma_{i,j}\beta_{i,j} \quad (5.6)$$

5. ANALYTICALLY REDUCED CHEMISTRY WITH ACCURATE SOOT PRECURSORS PREDICTION

PAH gaseous chemistry		$K = AT^n \exp\left(\frac{-E_a}{RT}\right)$		
PAH dehydrogenation ($1 \leq i \leq 3$)		A	n	E_a
$\text{PAH}_i + \text{OH}$	$= \text{PAH}_i^* + \text{H}_2\text{O}$	$2.1E^{13}$	0.0	4570.5
$\text{PAH}_i + \text{H}$	$= \text{PAH}_i^* + \text{H}_2$	$2.5E^{14}$	0.0	15900.0
$\text{PAH}_i + \text{O}$	$= \text{PAH}_i^* + \text{OH}$	$2.0E^{13}$	0.0	14705.0
$\text{PAH}_i^* + \text{H}$	$= \text{PAH}_i$	$1.0E^{14}$	0.0	0
PAH growth ($1 \leq i \leq 3$)		A	n	E_a
$\text{PAH}_i^* + \text{C}_2\text{H}_2$	$\rightarrow \nu_1\text{PAH}_i + \nu_2\text{PAH}_{i+1} + \nu_3\text{H}$	$1.2E^{26}$	-3.4	30005.0
$\text{PAH}_i + \text{H}$	$\rightarrow \nu_1\text{PAH}_{i-1}^* + \nu_2\text{PAH}_i^* + \nu_3\text{H}_2 + \text{C}_2\text{H}_2$	$3.6E^{30}$	-4.3	39091.5
PAH oxidation ($1 \leq i \leq 3$)		A	n	E_a
$\text{PAH}_i + \text{O}$	$\rightarrow \nu_1\text{PAH}_{i-1}^* + \nu_2\text{PAH}_i^* + \nu_3\text{H}_2 + \text{HCCO}$	$2.0E^{13}$	0.0	4173.0
$\text{PAH}_i^* + \text{O}$	$\rightarrow \nu_1\text{PAH}_{i-1}^* + \nu_2\text{PAH}_i^* + \nu_3\text{H}_2 + \text{CO}$	$1.0E^{14}$	0.0	0
$\text{PAH}_i + \text{OH}$	$\rightarrow \nu_1\text{PAH}_{i-1}^* + \nu_2\text{PAH}_i^* + \nu_3\text{H}_2 + \text{CH}_2\text{CO}$	$1.3E^{13}$	0.0	10532.0
$\text{PAH}_i^* + \text{O}_2$	$\rightarrow \nu_1\text{PAH}_{i-1}^* + \nu_2\text{PAH}_i^* + \nu_3\text{H}_2 + 2\text{CO}$	$2.0E^{12}$	0.0	7352.5
PAH collisions ($i, j \in 1, 3$ and $k = \max(i, j)$)		A	n	E_a
$\text{PAH}_i^* + \text{PAH}_j^*$	$\rightarrow \nu_1\text{PAH}_k + \nu_2\text{PAH}_{k+1} + \nu_3\text{H}_2$	$2.2N_A\gamma_{i,j}\beta_{i,j}$	0.5	0
$\text{PAH}_i^* + \text{PAH}_j$	$\rightarrow \nu_1\text{PAH}_k + \nu_2\text{PAH}_{k+1} + \nu_3\text{H}_2 + \text{H}$	$2.2N_A\gamma_{i,j}\beta_{i,j}$	0.5	0

Table 5.4: Summary of PAH chemistry and collisions. Reaction rates are in Arrhenius form: $K = AT^n \exp\left(\frac{-E_a}{RT}\right)$. Units are mol, s, and cal/mole.

These collision rates can be expressed in the Arrhenius form:

$$\dot{r}_c = \underbrace{2.2N_A\gamma_{i,j} \left(\frac{\pi k_B(m_i + m_j)}{2m_i m_j}\right)^{0.5}}_A (d_i + d_j)^2 \underbrace{T^{0.5}}_{T^n} \exp\left(\frac{0}{RT}\right) \quad (5.7)$$

with:

- 2.2 is the van der Waals enhancement factor,
- $\gamma_{i,j}$ is the collision efficiency assumed equal to 1 [182],
- $\beta_{i,j}$ is the collision frequency defined in Sec. 2.3.1,
- $m_{i,j}$ and $d_{i,j}$ refers to the PAH mass and diameter respectively, defined in Tab. 5.3.

The associated thermodynamics for these fictitious PAH are taken from the equivalent *BIN* species in the work of Saggese et al. [108].

Reduced scheme to produce A4

Pang et al. [303] used sensitivity analysis of rate of production (ROP) to reduce PAH over a wide range of operating conditions.

With this approach, reactions with normalized ROP value less than a specified threshold

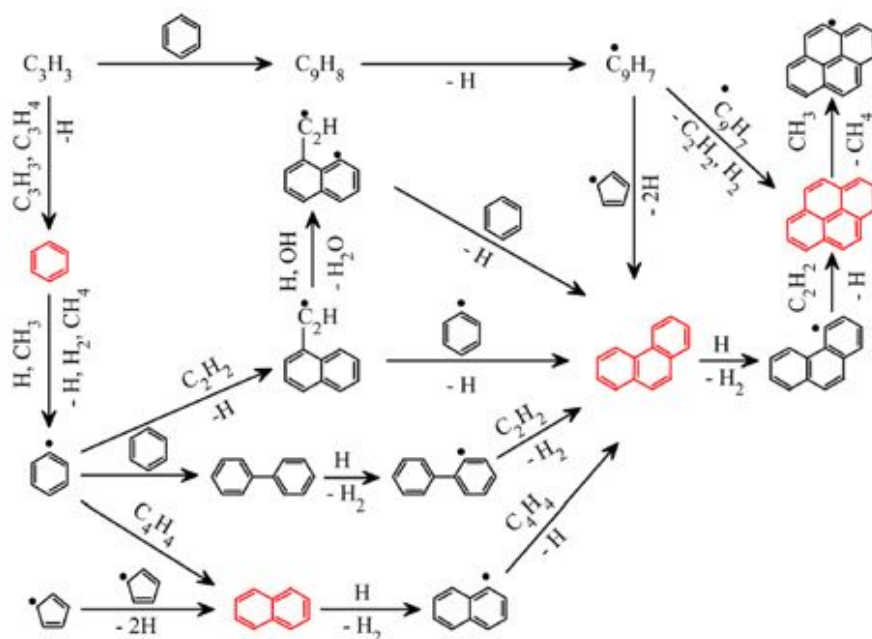


Figure 5.13: Major reaction pathways for formation of PAH (Extracted from *Pang et al.* [304]).

value (0.2 in the work of *Pang et al.* [304]) are simply removed. First, the normalized ROP approach is applied in premixed flames [305, 306, 307] based on a detailed soot mechanism [308], a previous version of KM2 mechanism [94]. Then the constants of the resulting PAH sub-mechanism are fitted to match experimental data. This procedure can be summarized in three steps:

- 1 Fitting of reaction rate constants to match PAH concentrations measurements in premixed flames for different operating conditions [305, 306, 307].
- 2 Fitting of reaction rate constants by comparing the PAH concentrations with the initial detailed mechanism [308] in shock tubes.
- 3 Repeat steps 1 and 2 until an accurate prediction of PAHs in both premixed flames and shock tubes is determined.

Important reaction pathways retained in the reduced PAH mechanism are schematized in Fig. 5.13: 12 species and 26 reactions are finally retained. In this work, only the sub-mechanism pathway to pyrene (A4) from naphthalene (A2) is considered and described in Tab. 5.5. This sub-mechanism involves 7 species and 11 reactions, and is combined with the BISETTI mechanism as illustrated in Fig. 5.14. Note that, in order to combine BISETTI skeletal mechanism with the PANG sub-mechanism reaction involving C_4H_4 has been neglected since mechanisms do not share this species.

5. ANALYTICALLY REDUCED CHEMISTRY WITH ACCURATE SOOT PRECURSORS PREDICTION

PAH sub-mechanism	$K = AT^n \exp\left(\frac{-E_a}{RT}\right)$			Ref.
	A	n	E_a	
$A1 + C_3H_3 = C_9H_8 + H$	$6.26E^9$	2.6	56500.0	[308]
$A1C_2H^* + A1 = A3 + H$	$1.1E^{24}$	-2.9	15890.0	[309]
$A1^* + A1C_2H = A3 + H$	$1.1E^{24}$	-2.9	15890.0	[309]
$A1^* + A1 = C_{12}H_{10} + H$	$1.1E^{23}$	-2.9	15890.0	[309]
$C_{12}H_{10} + H = C_{12}H_{10}^* + H_2$	$2.5E^{14}$	0.0	16000.0	[310]
$C_{12}H_{10}^* + C_2H_2 = A3 + H$	$4.6E^6$	2.0	7300.0	[310]
$A3 + H \rightarrow A3^* + H_2$	$5.0E^8$	1.9	9829.5	[304]
$A3^* + C_2H_2 = A4 + H$	$1.4E^{29}$	-3.4	17800.0	[311]
$C_9H_8 = C_9H_7 + H$	$1.73E^{68}$	-15.2	116371.9	[271]
$C_9H_7 + C_5H_5 \rightarrow A3 + 2H$	$6.39E^{29}$	-4.0	35205.5	[271]
$C_9H_7 + C_9H_7 \rightarrow A4 + C_2H_2 + H_2$	$6.39E^{29}$	-4.0	35205.5	[139]

Table 5.5: PAH formation sub-mechanism from A2 to A4 (Adapted from *Pang et al.* [304]).

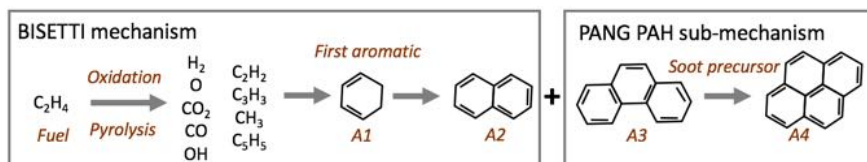


Figure 5.14: Schematic combination of BISETTI and PANG PAH sub-mechanism.

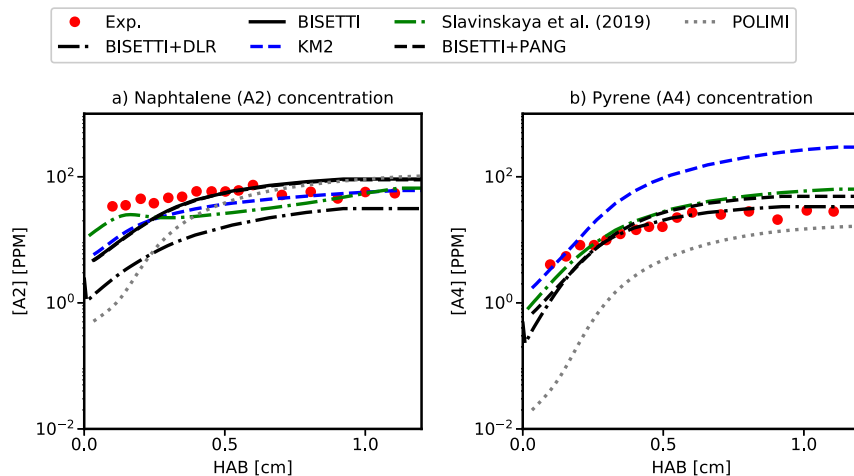


Figure 5.15: Numerical $A2$ and $A4$ profiles in a burner stabilized $C_2H_4/O_2/Ar$ premixed flame for different mechanisms compared with experiment from *Castaldi et al.* [279]

5.3.3 Validation on laminar premixed flames

Both PAH sub-mechanisms have been validated independently [143, 304]. Here the combination of these sub-mechanisms with C2H4_A2_28_205_14_LG is evaluated. In the following BISETTI-DLR and BISETTI-PANG refer respectively to the first and the second methodology. The same laminar premixed flames defined in Tab. 5.2 are used for validations focusing on $A2$ and $A4$ predictions. In addition to experiments, PAH is also compared to KM2, SLAVINSKAYA, POLIMI and the skeletal BISETTI mechanism. In BISETTI-DLR, PAH_2 ($= C_{20}H_{10}$) is compared to $A4$ [143]. First, results for the CASTALDI burner are shown in Fig. 5.15. The prediction of $A2$ is similar between skeletal BISETTI and BISETTI-PANG mechanisms, while in BISETTI-DLR the consumption of $A2$ to form larger PAHs can be observed in Fig. 5.15. Indeed, the chemical pathways leading to larger PAH are very different in both methodologies. As shown in Tab. 5.4 for BISETTI-DLR, the main route to form PAH_2 is the C_2H_2 addition to $PAH_1(=A2)$ or the collision of $A2^*$ radicals. The $A4$ formation in BISETTI-PANG is rather controlled by Indene (C_9H_8) and its radical or by Anthracene ($A3$), and does not directly involve $A2$ as suggested by Tab. 5.5. Both mechanisms predict well $A4$, as well as SLAVINSKAYA lead about similar $A4$ concentration.

Results for ISF 5 burner are shown in Fig. 5.16, similar conclusions than in the Castaldi flame. Here BISETTI-DLR mechanism is closest to SLAVINSKAYA mechanism. Remember that the DLR PAH sub-mechanism has been derived from the Slavinskaya mechanism [139, 274]. In addition, Tab. 5.5 shows the presence of SLAVINSKAYA mechanism in its derivation as well.

Finally, results for the nucleation flames of Tab. 5.2 are shown in Fig. 5.17. If $A2$ is correctly predicted by both mechanisms, especially for BISETTI-PANG, only

5. ANALYTICALLY REDUCED CHEMISTRY WITH ACCURATE SOOT PRECURSORS PREDICTION

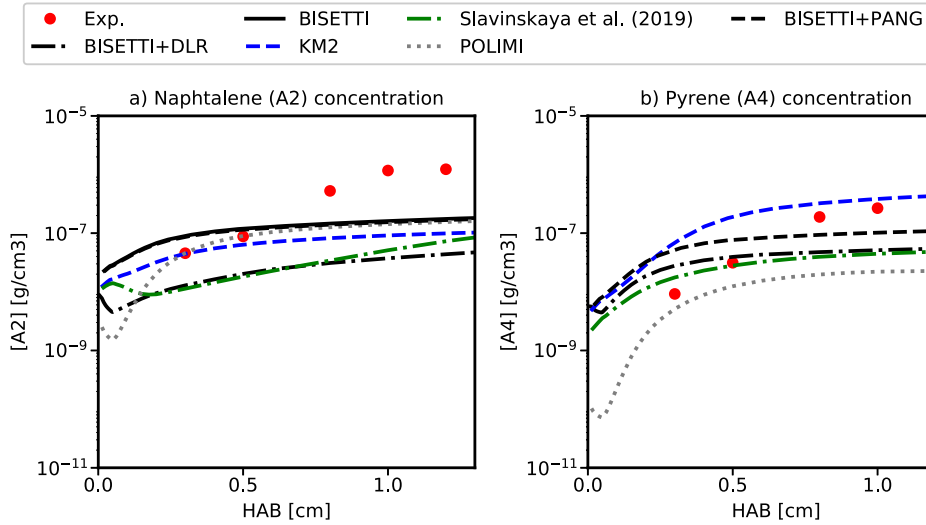


Figure 5.16: A2 and A4 numerical predictions in a burner stabilized C_2H_4/O_2 premixed flame for different mechanism compared with experiments from *Ciajolo et al.* [280, 281]

BISETTI-DLR gives a correct prediction of A4 prediction, BISETTI-PANG overestimating it by more than 1–2 order of magnitude. Nevertheless, in these flames the PAH consumption by soot formation is expected to be significant. Therefore, soot formation should be taken into account before concluding about the ability of the mechanisms to predict PAH accurately.

5.3.4 Final reduction of PAH sub-mechanisms

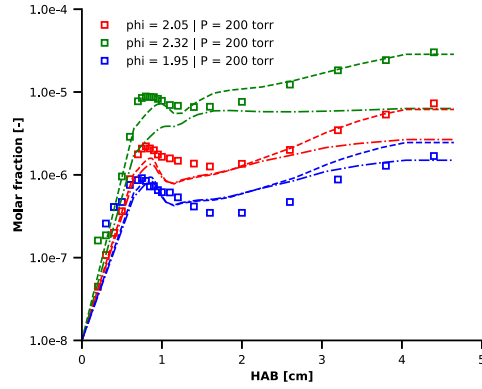
Both methodologies have shown their ability to reproduce correctly large PAH. However both are still too demanding in terms of computational cost and a final reduction using QSSA is applied. Following the method described in Sec. 5.2, a timescale analysis and LOI criteria have been performed to select QSS species.

A significant issue raised in the reduction of BISETTI-DLR mechanism. The highly reactive PAH_i^* radicals are involved in quadratic reactions, e.g. they react together to form PAH_{i+1} . This means that the QSS assumption can not be applied to PAH_i^* , although they are stiff and impossible to integrate in CFD solver with a reasonable timestep.

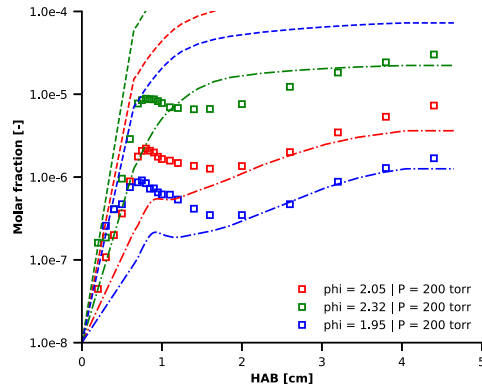
On the contrary, BISETTI-PANG mechanism has been reduced without any difficulty. The reduced BISETTI-PANG mechanism has been therefore retained in this work. The associated transported and QSS species are listed in Tab. 5.6. The QSSA was found to have absolutely no impact on the prediction of quantities of interest as well as on A4 prediction.

The C2H4.A4.32_233.13.LG refers to the mechanism resulting from the combination of C2H4.A2.28_205.14.LG and BISETTI-PANG. Its validation in terms of adia-

5.3 Prediction of larger PAH for ethylene-air flames



(a) A2 molar fraction.



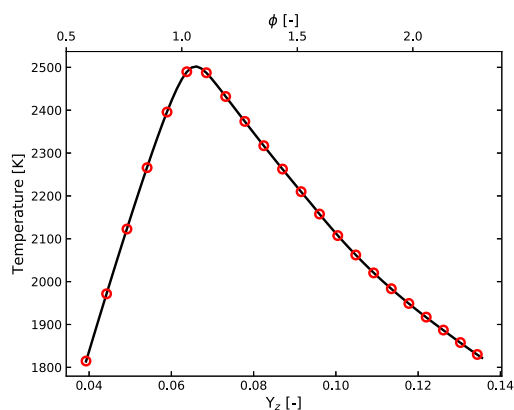
(b) A4 molar fraction.

Figure 5.17: A2 and A4 numerical predictions for BISETTI-PANG (dashed lines) and BISETTI-DLR (dash-dot lines) mechanisms for different equivalence ratios, compared with experiment from *Desgroux et al.* [285] (symbols)

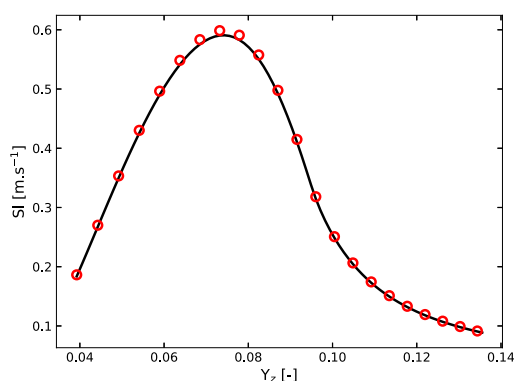
Transported species				QSS species		
C ₉ H ₇	C ₁₂ H ₁₀	A3	A4	C ₉ H ₈	C ₁₂ H ₉	A3*

Table 5.6: List of species of the reduced BISETTI-PANG mechanism.

5. ANALYTICALLY REDUCED CHEMISTRY WITH ACCURATE SOOT PRECURSORS PREDICTION



(a) Adiabatic temperature.



(b) Laminar flame speed.

Figure 5.18: One-dimensional premixed unstrained ethylene-air laminar flame at $P = 3$ bars. Comparison between BISETTI-PANG (—), C2H4_A4.32_233.13.LG (○). in terms of Adiabatic temperature and laminar flame speed.

batic flame temperature and laminar flame speeds is shown in Fig. 5.18

5.4 Extension to aviation jet fuel chemistry

The composition of aviation fuel Jet A-1 is described in Fig. 5.19. It contains paraffins, naphthenes and aromatics typically found in commercial kerosenes. The average chemical formula ranges from $C_{10.9}H_{20.9}$ to $C_{12}H_{23}$ [202]. Jet A is commonly described through surrogates. Ideally, both physical (density, molecular weight, H/C ratio, viscosity, distillation curve) and chemical (ignition delay, flame speed, sooting tendency) properties should be correctly retrieved with the surrogate [312]. However, this implies



Figure 5.19: Jet A-1 chemical composition.

a high number of surrogate components which may not be affordable [313, 314]. Many other attempts employing different targets for the formulation of the surrogate are reported by Dagaut and Cathonnet [202]. Recent work limits the number of components to four at the most with selected targets [315, 316, 317]. Associated reaction mechanisms are then usually compiled from those of each component. Unfortunately, the interaction of various pathways associated with each fuel component make it difficult to reduce the mechanism with the methods described in Sec. 5.2. As an example, *Keita et al.* [317] proposed a detailed mechanism for the combustion of liquid transportation fuels (gasoline, Jet A-1 and diesel) with accurate PAH description, ignition delay times and flame speeds over a wide range of operating conditions. Such mechanism involves 1014 species and 4550 reactions and its reduction is still the object of numerous studies. To have a chance to reduce the chemical mechanism, the surrogate is reduced to one component. The Luche skeletal mechanism derives from *El Bakali-Ristori* detailed mechanism [318] with 91 species and 991 reactions, it is widely employed in CFD [223]. Skeletal mechanisms based on n-dodecane ($nC_{12}H_{26}$) only are also extensively used [202]. Recently, two reduced mechanisms have been derived from the JetSurf 1.0-1 scheme [319] with a reasonable number of transported species (< 30) [295, 320]

An alternative approach to the surrogate fuel model has been recently proposed by Wang and coworkers [321, 322, 323]. This approach relies on the assumption that any fuel first decomposes into a handful of small molecules via pyrolysis reactions, followed by an oxidation process of the pyrolysis products. The so-called HyChem methodology is detailed below.

5.4.1 The HyChem methodology

The HYbrid CHEMistry (HyChem) approach has been developed to mimic the behavior of real fuels using a pyrolysis model. It is derived from shock-tube and flow-reactor experiments to capture important features such as ignition delay times and laminar flame speeds. It is based on the decomposition of the combustion process into a fuel pyrolysis step and a subsequent oxidation step of the pyrolysis products. The kinetic model for a particular fuel can thus be obtained by merging the fuel specific pyrolysis model, comprised of a few lumped reactions and yielding the primary pyrolysis products, with a detailed generic oxidation model of C1-C4 species. In this approach, the fuel is modeled as a lumped species. The HyChem methodology is schematized in Fig. 5.20.

The fuel POSF10425 breakdown is described by a few lumped reactions expressed as:

5. ANALYTICALLY REDUCED CHEMISTRY WITH ACCURATE SOOT PRECURSORS PREDICTION

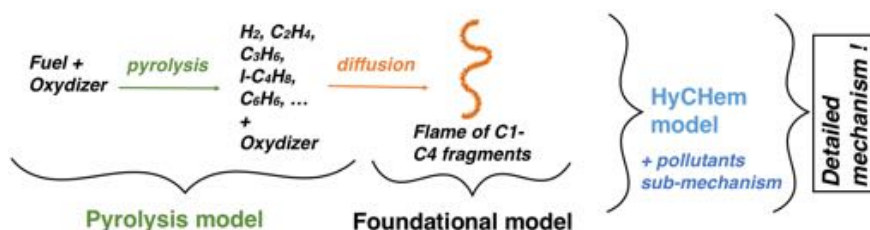
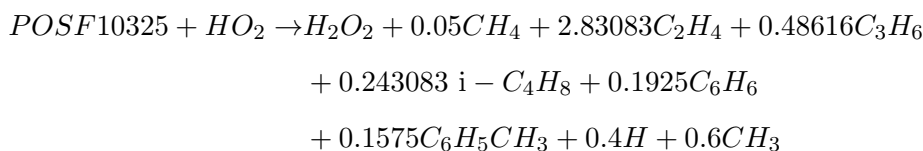
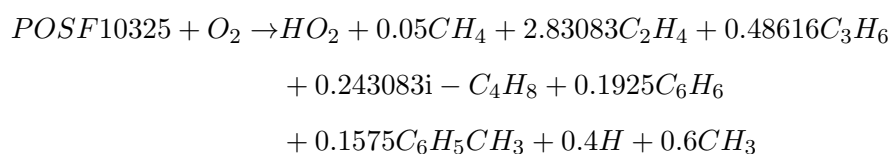
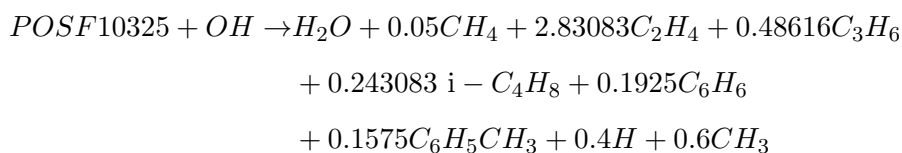
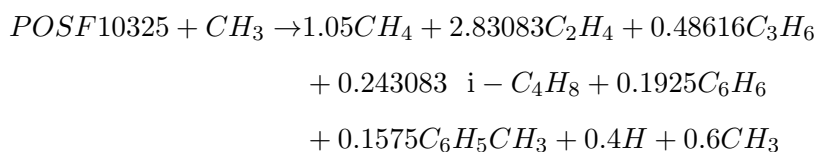
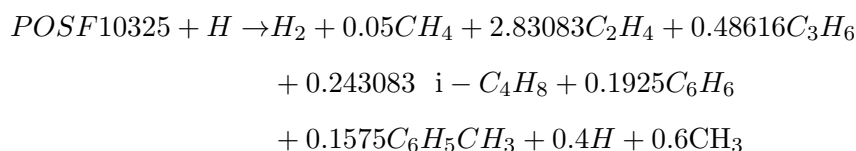
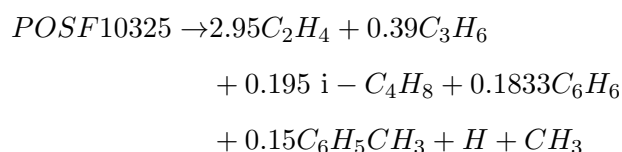


Figure 5.20: Schematic HyChem methodology.



The pyrolysis intermediates are dominated by ethylene (C_2H_4), methane (CH_4), hydrogen (H_2), propene (C_3H_6), iso-butene ($i-C_4H_8$), l-butene ($l-C_4H_8$), benzene ($A1$ or C_6H_6) and toluene (C_7H_8).

HyChem method combined with USCII mechanism [201] has been recently validated for soot propensity of the Jet A fuel [64] or applied to pollutant formation [324] as well as for soot prediction in counterflow flame [300] using KM2 mechanism [94] (also based on USCII) for large PAHs description. HyChem model combined with ARC has been successfully applied to spray combustion in a complex configuration [213].

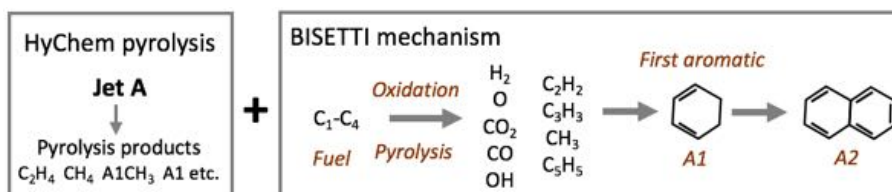


Figure 5.21: Schematic combination of BISETTI and HyChem.

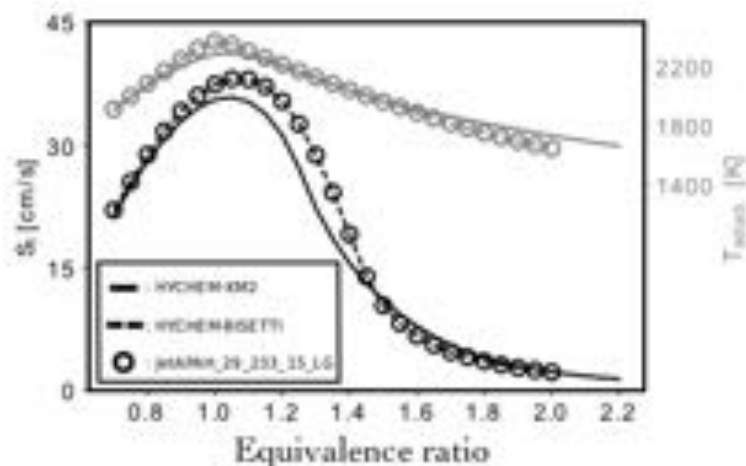


Figure 5.22: One-dimensional unstrained premixed laminar flames in the UTIAS Jet A-1 burner conditions [22]. Comparison of three chemical mechanisms in terms of laminar flame speed and adiabatic flame temperature.

5.4.2 Combining aviation jet fuel chemistry and PAH description

The HyChem methodology is here combined with the BISETTI mechanism as illustrated in Fig. 5.21 and then reduced to obtain an ARC scheme. Note that, in order to combine BISETTI skeletal mechanism with HyChem, reaction involving H_2O_2 has been neglected since BISETTI and HyChem do not share this species. A_2 and all species included in soot chemistry are retained as target quantities in laminar flames in the equivalence ratio range $\phi = 0.8 - 2.0$. The resulting *JetAPAH_29_233_15_LG* mechanism comprises 29 transported species and 15 species in QSS. *JetAPAH_29_233_15_LG* is compared in Fig. 5.22 to the skeletal HYCHEM-BISETTI and the detailed HYCHEM-KM2 on a series of laminar unstrained premixed flames at atmospheric pressure. The HYCHEM-KM2, successfully used for detailed soot prediction [300], is taken as a reference. The reduced mechanism *JetAPAH_29_233_15_LG* and the skeletal mechanism HYCHEM-BISETTI are in quasi-perfect agreement. Some discrepancies can be observed with HYCHEM-KM2 which seems however reasonable considering the Jet A-1 complexity.

5.5 Conclusion

In this chapter, three ARC mechanisms have been proposed to describe PAH formation in flames, all based on the skeletal mechanism developed by *Bisetti et al.* [231]:

- The C2H4_A2.28.205.14_LG scheme contains 14 QSS species and 28 transported species, with an accurate description of naphthalene (A2) for C_2H_4 -air combustion. It is validated in a wide range of equivalence ratio and for different pressure from 1 to 5 bars.
- The C2H4_A4.32.233.13_LG scheme is built to predict higher PAH by combining C2H4_A2.28.205.14_LG with a PAH submechanism. The final reduced mechanism contains 32 transported species and 13 QSS species including pyrene chemistry (A4).
- The JetAPAH.29.233.15_LG scheme describes the combustion of Jet A-1 including PAH formation. It relies on a pyrolysis sub-mechanism for Jet A-1 using the HyChem methodology, and has been combined with the skeletal mechanism BISETTI to describe the combustion of pyrolysis products. The resulting reduced mechanism contains 29 transported species and 15 QSS species including naphthalene (A2).

Validation over a wide range of equivalence ratio and different pressures for C_2H_4 and Jet A-1 flames, has been performed. All these mechanisms allow the computation of sooting flame in a CFD solver with a PAH description at a reasonable computational cost (about 30 transported species). They are retained for all simulations in this work.

Chapter 6

Lagrangian Soot Tracking in laminar flames.

The objective of this Chapter is to validate the retained strategy which is the combination of LST (introduced in Chapter 4) and ARCs (described in Chapter 5) on canonical laminar flames. This chapter starts implementing a detailed soot model, followed by the extension of LST towards a bi-variate description. LST and sectional methods with similar soot chemistry model are compared to validate the implementation. Then, the soot model is applied to canonic flames in Sec. 6.4, in order to evaluate the reduced chemistry as well as the description of the soot particle population, including its Particle Size Distribution (PSD).

Contents

6.1 Detailed soot modeling	117
6.1.1 Soot inception	118
6.1.2 Evolution of soot particles	119
6.2 Bi-variate description of soot particles	123
6.2.1 Empirical morphological description	123
6.2.2 Bi-variate soot description: Surface transport	123
6.3 Physical and numerical validation	125
6.3.1 Validation of physical models	125
6.3.2 Validation of numerical algorithms	126
6.4 Laminar flames: comparison with experiments	130
6.4.1 Impact of soot precursors on soot evolution	135
6.4.2 Bi-variate description of soot particles	138
6.5 Conclusion	142

6.1 Detailed soot modeling

The detailed soot model used in this work is taken from *Rodrigues et al.* [196]. Contrary to the semi-empirical model, previously introduced in Section 4.3.1, soot formation relies on PAH accounting for condensation. This change induces new soot source terms, but does not impact the developed LST approach nor its computational cost. The new source terms are successively described below.

6.1.1 Soot inception

Nucleation processes characterize the inception of nascent soot particles (nuclei). As stated by *Blanquart and Pitsch* [103], nuclei are assumed to form from the collision of two dimers, which themselves form from PAH.

Dimerization process

The dimerization process corresponds to the coalescence of two PAH molecules, resulting in a dimer (subscript dim). Here contrary to the work of *Rodrigues et al.* [270], dimerization is based on only one PAH, either A2 or A4, and not on a sum of high PAHs. The overall dimerization rate \dot{r}_{dim} considering one PAH writes :

$$\dot{r}_{dim} = \frac{1}{\rho} C_n W_{PAH}^4 \sqrt{\frac{4\pi k_b T}{N_A}} n_c^{PAH} [PAH]^2 d_{PAH}^2 N_A \quad (6.1)$$

with:

- k_b : the Boltzmann constant
- N_A : the Avogadro's number
- $[PAH]$: the considered PAH molar concentration
- n_c^{PAH} : the carbon atoms number of the considered PAH
- W_{PAH} : the considered PAH molecular weight
- d_{PAH} : the considered PAH diameter
- $C_n = 7.5 \cdot 10^{-12} mol^4 \cdot g^{-4}$: a constant to compute PAH collision efficiency [85].

The consumption of PAH by the dimerization process is expressed as:

$$\dot{\omega}_{PAH} = -2 \dot{r}_{dim} \rho \quad (6.2)$$

Indeed, the collision of two moles of PAH leads to the formation of one mole of dimer, explaining the factor two in Eq. 6.2

Nucleation

Nucleation is the inception of a spherical primary soot particle by the coalescence of two dimers. The corresponding source term for soot number density N_p reads:

$$\frac{dN_p}{dt} = \frac{1}{2} \beta_{dim,dim}^{fm} N_{dim}^2 \quad (6.3)$$

where $\beta_{dim,dim}^{fm}$ is the collision frequency of dimers in the free molecular regime (Eq. 2.6) with a van der Waals factor $\epsilon_{dim,dim} = 2.5$, and N_{dim} is the dimer number density which is computed using a QSS assumption:

$$\frac{dN_{dim}}{dt} = \dot{r}_{dim} - \beta_{dim,dim}^{fm} N_{dim}^2 \sim 0 \quad (6.4)$$

This leads to:

$$N_{dim} = \sqrt{\frac{\dot{r}_{dim}}{\beta_{dim,dim}^{fm}}} \quad (6.5)$$

As the Lagrangian formalism is based on discrete particles, a new particle is created only after the nucleation source term dN_p/dt is found sufficiently large ($N_p > 1$). It assumes that all n particles formed in a small control volume v_c at the time t can be represented by only one numerical particle with numerical weight $\omega_p = n$. This means that all physical particles follow the same trajectory [187] and size evolution as the numerical particle.

The properties of the nuclei particles depend directly on the selected soot precursor and are then:

$$\omega_p = \frac{dN_p}{dt} v_c \delta t \quad ; \quad r_p^3 = 2r_{dim}^3 = r_{PAH}^3 \quad (6.6)$$

where r_p , r_{dim} and r_{PAH} are respectively the radius of nuclei, dimer and PAH molecule. A similar inception process in Lagrangian formulation has been proposed recently by Ong *et al.* [193]. In other previous studies inception of Lagrangian soot particles relied on pre-defined soot particles (location and properties) [185, 186, 325].

Note that in the present model, nucleation contributes only to the inception of soot particles and conserves mass and enthalpy. Therefore it does not contribute to the particle mass and energy source terms.

6.1.2 Evolution of soot particles

The newly formed Lagrangian particles undergo mass addition and size increase through surface growth as well as PAH condensation. In the same time, oxidation may occur, counteracting the previous phenomena. These processes are expressed as soot particle mass source terms.

Surface reactions

Surface chemistry corresponds to gaseous reactions occurring at the particle surface. It can be divided in two types of processes: surface growth and oxidation. Both involve complex chemical reaction networks described respectively in Section 2.2.2 and Section 2.2.3. Surface growth is modeled by the HACA-Ring Closure (HACA-RC) [89, 90] mechanism as in the work of Rodrigues *et al.* [270]. Compared to HACA [67],

6. LAGRANGIAN SOOT TRACKING IN LAMINAR FLAMES.

HACA-RC [89, 90]		$k = A T^n \exp(-E_a/RT)$			
No.	Reaction	A	β	E_a [kJ/mol]	
1	$S_c + H \rightleftharpoons S_c^* + H_2$	k_{1f}	$1.000 \cdot 10^{14}$	0	0.0
		k_{1b}	$1.439 \cdot 10^{13}$		-37.63
2	$S_c + OH \rightleftharpoons S_c^* + H_2O$	k_{2f}	$1.630 \cdot 10^8$	1.4	6.10
		k_{2b}	$1.101 \cdot 10^8$	1.4	31.14
3	$S_c^* + H \rightleftharpoons S_c$	k_{3f}	$1.000 \cdot 10^{13}$	0	0.0
		k_{3b}	0.000		0.0
4	$S_c^* + C_2H_2 \rightleftharpoons S_c^*C_2H_2$	k_{4f}	$3.500 \cdot 10^{13}$	0	0.0
		k_{4b}	$3.225 \cdot 10^{14}$		181.69
5	$S_c^*C_2H_2 \rightleftharpoons S_{c+2} + H$	k_{5f}	$1.000 \cdot 10^{10}$	0	20.0
		k_{5b}	$8.770 \cdot 10^{11}$		74.44
6	$S_c^*C_2H_2 + O_2 \rightleftharpoons S_{c-2} + 2CO$	k_{6f}	$1.000 \cdot 10^{10}$	0	20.0
6'	$S_c^*C_2H_2 + O_2 \rightleftharpoons S_c^* + 2HCO$	$k_{6'f}$	$1.000 \cdot 10^{10}$	0	20.0
7	$S_c + OH \rightleftharpoons S_{c-2}^* + CH + HCO$	k_{7f}	Efficiency $\gamma = 0.13$		

Table 6.1: HACA-RC sub-mechanism: Reactions and reaction rate constants.

it accounts for additional reactions to mimic the effect of temperature on soot surface reactions as detailed in Chapter 2, as well as oxidation reactions. The set of reactions is presented in Tab. 6.1 with the reaction rate constants.

The oxidation reaction by OH (R7 in Tab. 6.1) is based on the works of [326, 327, 328] and is detailed in *Rodrigues* [196].

Surface growth corresponds to the addition of C_2H_2 to a soot particle by surface reactions (R4 in Tab. 6.1). This growth is counter-balanced by oxidation by O_2 (R6 and R6' in Tab. 6.1) which leads to the removal of C_2H_2 molecule at the soot particle surface.

The global reaction rates corresponding to surface growth and oxidation can be expressed as combinations of Arrhenius laws corresponding to the reaction presented in Tab. 6.1:

$$\dot{r}_{sg} = k_{4f}[S_c^*][C_2H_2] - k_{4b}[S_c^*C_2H_2] \quad (6.7)$$

$$\dot{r}_{ox} = \underbrace{k_{7f}[S_c][OH]}_{\text{oxidation by } OH} + \underbrace{k_{6f}[O_2][S_c^*] + k_{6'f}[O_2][S_c^*C_2H_2]}_{\text{oxidation by } O_2} \quad (6.8)$$

These source terms require the prediction of species involved in the HACA-RC mechanism, as well as concentration of radical sites at the surface of the soot particles: S_c^* , S_c and $S_c^*C_2H_2$. *Rodrigues* [196] proposed to consider the QSS assumption for these

three species allowing to write Eqs. 6.7 & 6.8 as:

$$\dot{r}_{sg,p} = k_{sg}[S_c]_p \quad (6.9)$$

$$\dot{r}_{ox,p} = k_{ox}[S_c]_p \quad (6.10)$$

where $[S_c]$ corresponds to the concentration of active sites at the surface of a soot particle and is expressed as:

$$[S_c] = \frac{\alpha \lambda_s s_p}{N_A} \quad (6.11)$$

with:

- λ_s : the number of active sites per unit surface area of soot particle. It assumes that each active site occupies a surface equivalent to the surface of the C_2H_2 molecule [179], then $\lambda_s s_{C_2H_2} = 1$,
- α : the proportion of these sites which are active (set to $\alpha = 1$ according to Rodrigues [196]),
- s_p : the surface of the soot particle p .

As a result, the associated mass source terms for a particle p are:

$$\dot{m}_p^{sg} = \rho_s V_{C_2H_2} N_A \dot{r}_{sg,p} = \rho_s V_{C_2H_2} \lambda_s s_p k_{sg} \quad (6.12)$$

$$\dot{m}_p^{ox} = \rho_s V_{C_2H_2} N_A \dot{r}_{ox,p} = \rho_s V_{C_2H_2} \lambda_s s_p k_{ox} \quad (6.13)$$

where $V_{C_2H_2}$ refers to the volume of the C_2H_2 molecule and is equal to $V_{C_2H_2} = W_{C_2H_2}/(\rho_s * N_A) \sim 2.14 \cdot 10^{-26} \text{ m}^3$

Condensation

Condensation, as defined in Sec. 2.2.2, is here assumed to be the collision between a dimer and a soot particle. The dimer condensates on the soot particle, thus increasing its mass and volume.

For a particle with numerical weight ω_p , the collision source term with a dimer writes:

$$k_p^{cn} = \beta_{p,dim}^{fm} * \omega_p \quad (6.14)$$

where $\beta_{p,dim}^{fm}$ has been defined in Eq. 2.6, with the van der Waals factor set to $\epsilon_{p,dim} = 1$. PAH condensation induces dimer consumption similarly to the nucleation process. The overall condensation source term k_{cn} is computed as the sum of each particle source term k_p^{cn} :

$$k_{cn} = \sum_{p=1}^{N_p} k_p^{cn} \quad (6.15)$$

6. LAGRANGIAN SOOT TRACKING IN LAMINAR FLAMES.

The dimer number density (defined in Eq. [6.5](#)) must be corrected accounting for condensation, using again the QSS assumption:

$$\frac{dN_{dim}}{dt} = \dot{r}_{dim} - \beta_{dim,dim}^{fm} N_{dim}^2 - k_{cn} N_{dim} \sim 0 \quad (6.16)$$

The resulting N_{dim} is expressed as:

$$N_{dim} = -\frac{k_{cn}}{2\beta_{dim,dim}^{fm}} + \sqrt{\frac{r_{dim}}{\beta_{dim,dim}^{fm}} + \left(\frac{k_{cn}}{2\beta_{dim,dim}^{fm}}\right)^2} \quad (6.17)$$

With the correct N_{dim} , the particle condensation source term corresponds simply to the addition of mass, corresponding to the mass of available dimers multiplied by the condensation collision frequency (Eq. [2.9](#)):

$$\dot{m}_p^{cn} = \rho_s V_{dim} \beta_{p,dim}^{tr} N_{dim} \quad (6.18)$$

Coagulation

Coagulation, defined Sec. [2.2.2](#), is the collision between two particles. Here, the collision frequency used in the coagulation algorithm (see Sec. [4.2.2](#)) is calculated in the transition regime over a wide range of Knudsen number and defined in Eq. [2.9](#) proportional to the collisional diameter.

Computation of new soot diameter

The net mass added to a soot particle is computed from the surface growth, condensation and oxidation models:

$$\dot{m}_p = \dot{m}_p^{sg} - \dot{m}_p^{ox} + \dot{m}_p^{cn} \quad (6.19)$$

Both surface growth and PAH condensation increase the particle mass, while oxidation by OH and O₂ decreases it. Relating the soot particle mass m_p to its diameter d_p :

$$m_p = \frac{\pi}{6} d_p^3 \rho_s \quad (6.20)$$

the diameter evolves as:

$$\frac{dd_p^3}{dt} = \frac{6}{\pi \rho_s} \dot{m}_p \quad (6.21)$$

Any soot particle with a size below a threshold value is removed from the computation and considered fully oxidized. The threshold value is set to the dimer diameter d_{dim} .

6.2 Bi-variate description of soot particles

As mentioned in Sec. 2.1, nascent soot can be considered as spherical while larger soot particles present a complex fractal-like morphology. A soot aggregate is characterized by its number of primary particles defined in Eq. 2.1, and its surface to volume ratio. Soot surface has a key role in soot evolution, it is involved directly in the evaluation of collisional diameter (coagulation and condensation) as well as the calculation of soot mass source terms (surface growth, oxidation, condensation). Then soot surface evolution should be considered via a joint volume-surface model, i.e., a bivariate description of soot particles accounting for both volume (mass) and surface evolution. Two different strategies have been proposed in this work and are detailed below.

6.2.1 Empirical morphological description

In classical Eulerian methods, the evaluation of soot particle surface evaluation means additional equations to solve, impacting significantly the computational cost. *Rodrigues et al.* [270] derived a relation between the soot particle volume v_p and surface s_p by fitting numerical results from soot models accounting for surface evolution [137, 158]:

$$(s_p/s_{C_2H_2}) = \begin{cases} (v_p/v_{C_2H_2})^{2/3} & \text{for } v_p < v_1, \\ (v_p/v_{C_2H_2})^{\theta(v_p)/3} & \text{for } v_p > v_1 \end{cases} \quad (6.22)$$

with

$$\theta(v_p) = 3.0 \frac{(\log(v_p/v_1)) + 2/3 (\log(v_1/v_{C_2H_2}))}{\log(v_p/v_{C_2H_2})} \quad (6.23)$$

where $v_1 = 10^{2.6} \text{ nm}^3$ is the volume above which a soot particle is no longer considered as spherical (Fig. 6.1), $s_{C_2H_2}$ and $v_{C_2H_2}$ refer respectively to the surface and the volume of a spherical C_2H_2 molecule. This empirical correlation is not universal, but it avoids to compute both the particle volume and surface and keeps an affordable computational cost.

6.2.2 Bi-variate soot description: Surface transport

In the Lagrangian formalism, a bivariate formulation does not imply additional computational cost and is straightforward. Therefore, a bi-variate description of soot particle surface is proposed following [157, 158]. At nucleation stage, the soot particle is considered spherical and the soot particle surface writes::

$$s_p = (36\pi)^{1/3} v_p^{2/3} \quad (6.24)$$

The soot surface then evolves either towards a spherical or an aggregate shape according to the physical processes involved. The corresponding source term for the soot particle

6. LAGRANGIAN SOOT TRACKING IN LAMINAR FLAMES.

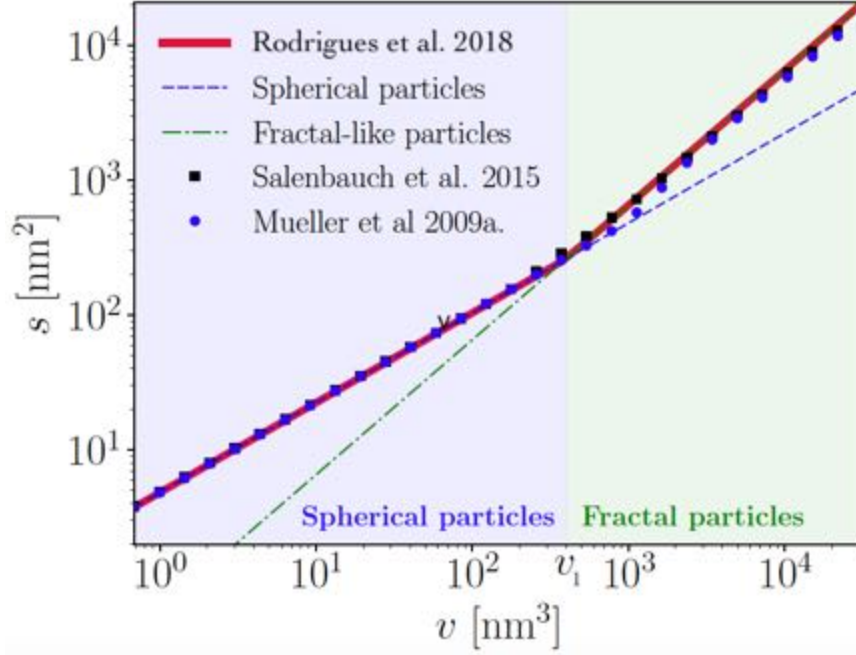


Figure 6.1: Presumed relationship between soot particle surface and volume. Data from the literature [137, 158] obtained with bi-variate moments resolution. (Extracted from [196])

surface [157, 158] expresses as:

$$\frac{ds_p}{dt} = \underbrace{\delta s_{V_{dim}}^{\text{frac}} \beta_{V_{dim}}^{\text{fm}}}_{\text{condensation}} N_{dim} + \underbrace{\delta s_{V_{C_2}}^{\text{frac}} \lambda k_{\text{sg}}}_{\text{surface growth}} s_p - \underbrace{\delta s_{V_{C_2}}^{\text{spher}} \lambda k_{\text{ox}}}_{\text{oxidation}} s_p \quad (6.25)$$

with:

1. δs_V^{frac} the particle surface variation in case of surface growth and condensation, following a fractal behavior [158]: $(\delta s_V^{\text{frac}} / s_p) = (2/3)(\delta v / v_p) n_p^\chi$, where n_p is the number of primary particles and $\chi = -0.2043$ [158].
2. $\delta s_V^{\text{spher}}$ the particle surface variation due to oxidation, keeping a spherical shape: $(\delta s_V^{\text{spher}} / s_p) = (2/3)(\delta v / v_p)$

Collisions are handled as pure aggregation. When a pair of particles (i, j) collide, their surface sum [158] and the surface of the resulting particle is given by:

$$s_{i+j} = s_i + s_j \quad (6.26)$$

In case of coalescence, the resulting soot surface is expressed as:

$$s_{i+j} = (36\pi)^{1/3} (v_i + v_j)^{2/3} \quad (6.27)$$

As discussed in Sec. 2.2, coalescence typically involves nascent soot particles while mature soot are more likely to agglomerate. Only agglomeration is considered in this

work to match the fractal-like shape of soot particles (Sec. 2.1). To go further, an appropriate model taking into account particles properties should be investigated [158] and is kept for future research.

6.3 Physical and numerical validation

The Lagrangian Soot Tracking method is based on the Lagrangian solver of AVBP which has been originally designed to handle two-phase flows and adapted to soot particles to take into account particle collisions for coagulation, as well as particle merging for the reduction number density. Soot physics and chemistry require a lot of particle properties to be tracked. To do so, the Lagrangian solver of AVBP has been upgraded to sort particles by cell number.

Coupled with a constant-number approach, it enables to evaluate properties for pair of particles in a very efficient way. Then, only particles in the current cell, i.e., the control volume, are treated.

The above methods have been thoroughly published and validated [195, 258, 259, 261, 267]. Here, their implementation in the AVBP solver is verified on canonical flames. First, a freely-propagating premixed flame is considered, and results are compared to a reference Monte-Carlo method using the same soot chemical source terms [157]. Then, the impact of the number of numerical particles on coagulation is investigated, as well as the impact of the constant-number approach on the PSD. This investigation is performed on zero-dimensional reactors and one-dimensional flames, where numerical results from a sectional approach are available [196].

6.3.1 Validation of physical models

The LST soot model is compared to the Discrete Sectional Method described in the work of *Rodrigues et al.* [270], using the same soot chemical model. The coupling with the gaseous phase is taken into account following the Lagrangian approach defined in Sec. 3.3. The accuracy of the Lagrangian Soot Tracking method is evaluated in a laminar freely-propagating premixed C_2H_4/AIR flame of equivalence ratio $\phi = 2.1$, initial temperature $T = 300K$ and at atmospheric pressure. The C2H4_A2.28_205_14_LG chemistry with A2 as soot precursor is used. To minimize numerical errors, a high number of numerical particles (2000/cell) and sections (100) are used respectively 2000 of numerical particles per control volume and 100 sections. Note that neither thermophoresis effect nor soot diffusivity are taken into account in both methods.

6. LAGRANGIAN SOOT TRACKING IN LAMINAR FLAMES.

The physico-chemical processes are evaluated individually with three different computations including:

- 1 **Nucleation only**
- 2 **Nucleation and surface growth**
- 3 **Nucleation and condensation**

Nucleation is always required to form soot. Then, surface growth and condensation are studied. The three computations lead to the same evolutions of soot number density and volume fraction. It is expected that both methods lead to the same results. This is effectively observed in Fig. 6.2, showing identical profiles.

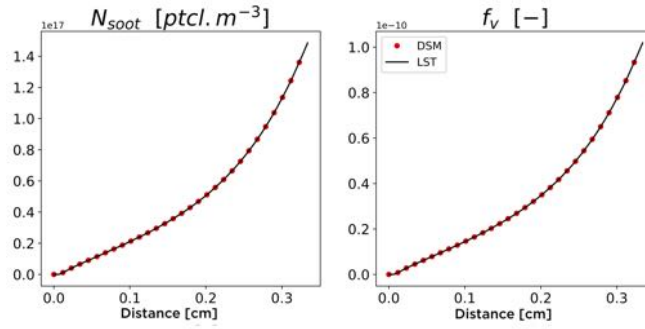
Coagulation is evaluated next. Since the choice of a stochastic algorithm has been retained in the LST, differences between both numerical methods are expected. Results are shown in Fig. 6.3. The soot volume fraction remains exactly the same in both cases, as coagulation conserves particle mass. However the soot number density N_{soot} is higher in LST suggesting that less collisions occur. This may significantly impact the PSD and further investigation should be considered to evaluate the performances of the collision algorithms of methods.

Finally, the comparison between numerical methods including all soot processes described in Sec. 6.1 is shown in Fig. 6.4. Although the soot evolution leads to identical results except for coagulation, the final comparison between both numerical methods slightly differ. The change of particle size distribution induced by coagulation leads to a slight underestimation of the soot volume fraction in LST compared to the sectional approach.

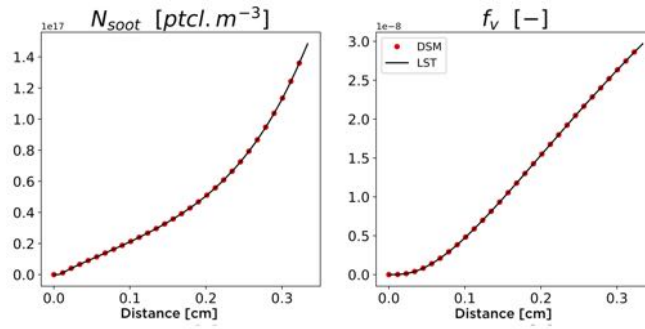
6.3.2 Validation of numerical algorithms

To keep an affordable numerical cost, the number of numerical particles / cell is minimized. The ability to correctly capture the particle size distribution with a small number of numerical particles is evaluated on the freely-propagating flame as well as in a 0D reactor.

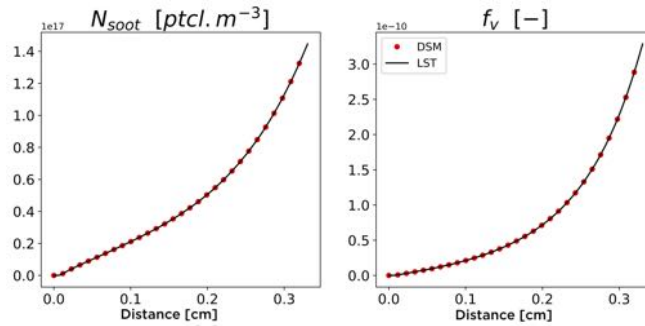
The influence of the number of numerical particles per control volume is shown in Fig. 6.5. As the number of numerical particles decreases the differences between LST and DSM slightly increase, and numerical noise appears. Despite these small discrepancies, results remain close to the well-discretized sectional method (over 100 sections) even for 25/50 particles per cell. Corresponding particle size distributions are plotted at



(a) Nucleation



(b) Nucleation and surface growth



(c) Nucleation and condensation

Figure 6.2: Comparison of soot number density and soot volume fraction between Lagrangian Soot Tracking (LST) and Discrete Sectional Method (DSM) on a freely propagating premixed flame.

6. LAGRANGIAN SOOT TRACKING IN LAMINAR FLAMES.

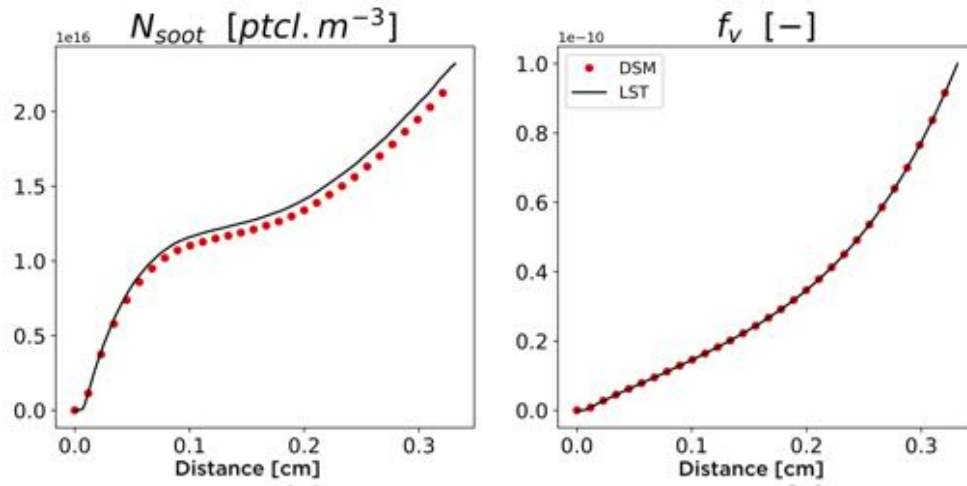


Figure 6.3: Comparison of soot number density and soot volume fraction between Lagrangian Soot Tracking (LST) and Discrete Sectional Method (DSM) on a freely propagating premixed flame considering only nucleation and coagulation .

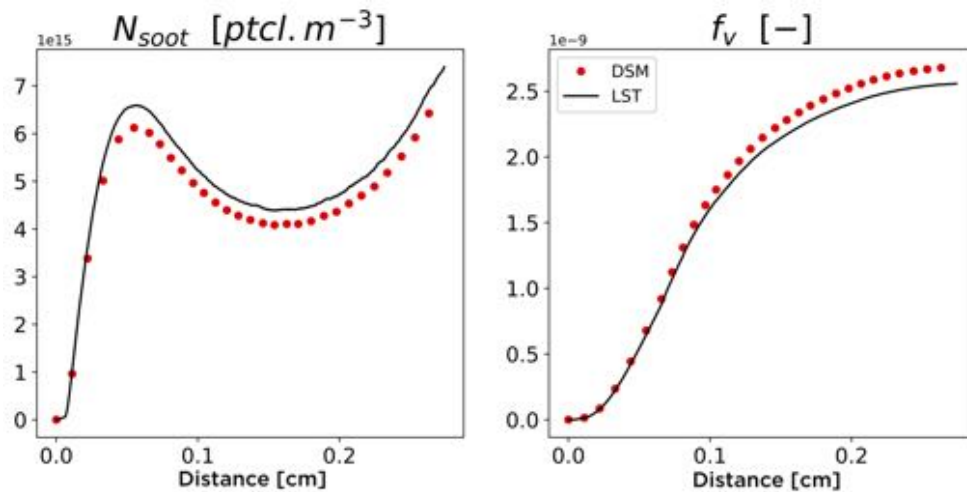


Figure 6.4: Comparison of soot number density and soot volume fraction between Lagrangian Soot Tracking (LST) and Discrete Sectional Method (DSM) on a freely propagating premixed flame considering all soot processes.

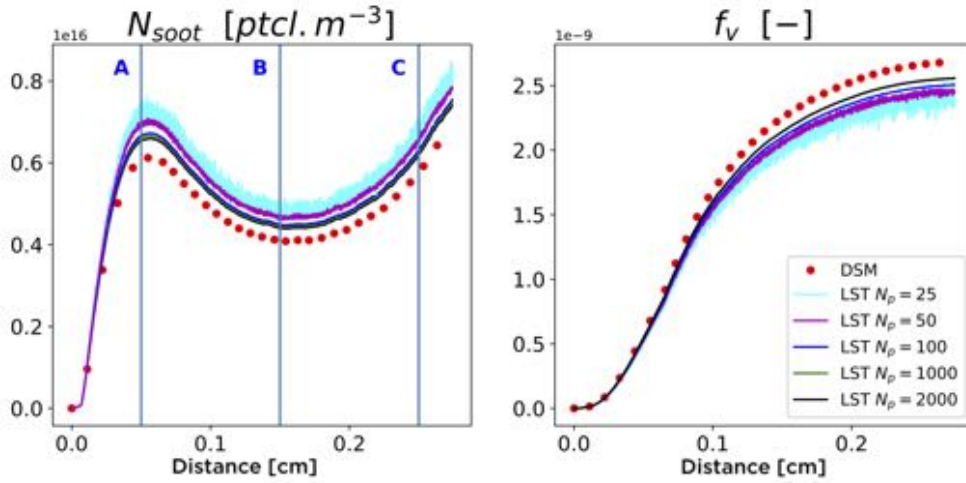


Figure 6.5: Influence of the number of numerical particles per cell (N_p) on soot in a freely propagating flame.

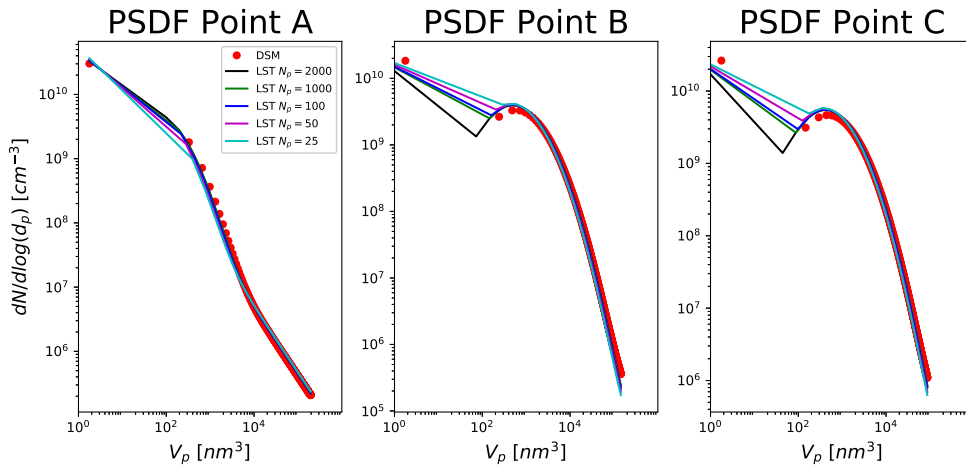


Figure 6.6: Particle size distribution at three locations (defined in Fig. 6.5) for different numbers of numerical particles per cell (N_p).

three locations (defined in Fig. 6.5) in Fig. 6.6. In all cases, a very good agreement with the sectional approach is found. The one-peak distribution in location A) is correctly captured for all computations. Further in the flame, in locations B) and C) two-peak distributions are observed and also correctly captured. As expected, the quality of the particle size distribution decreases with the number of numerical particles. The number of particles per cell seems to correspond to the number of sections and acts similarly on the quality of the particle size distribution [196].

To further evaluate the impact of the number of numerical particles on the particle size distribution, a 0D-reactor is considered with soot coagulation only. It is based on study cases proposed by *Oh and Sorensen* [329]. Considering a constant volume, a soot

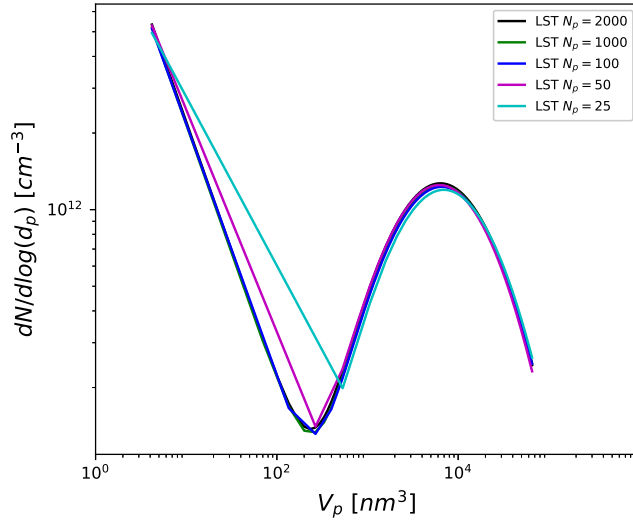


Figure 6.7: Particle size distribution in a 0D reactor for different number of numerical particles per cell (N_p), only coagulation is considered.

monodisperse population with a given size is deposited to obtain a soot volume fraction f_v around 10ppm in favorable thermodynamic conditions from a collisional point of view (atmospheric pressure and high temperature about 1700K). A small diameter (2nm) is considered corresponding to nascent soot particles, and 10 coagulation times τ_{coag} defined in Sec. 4.2.2 are computed. The resulting particle size distribution is shown in Fig. 6.7, confirming that collisions between weighted particles are correctly handled. The shape of this particle size distribution is similar over the whole range of computations, although missing discretization points are observed in the transition between the two peaks of the PSDF for small numbers of numerical particles.

6.4 Laminar flames: comparison with experiments

The soot model employed in this work has been thoroughly validated on both premixed and diffusion canonic configurations [196]. Here, its implementation in LST and its combination with gaseous chemistry are investigated and compared with experiment where either soot, PAH or PSDF measurements are available. The impact of soot precursors as well as the bi-variate description on soot formation are discussed.

The flames computed in Chapter 5 (without the soot model) and defined in Tab. 5.2 are again used to assess the soot model. Depending on the available measurements, soot volume fraction and/or PAH level are compared.

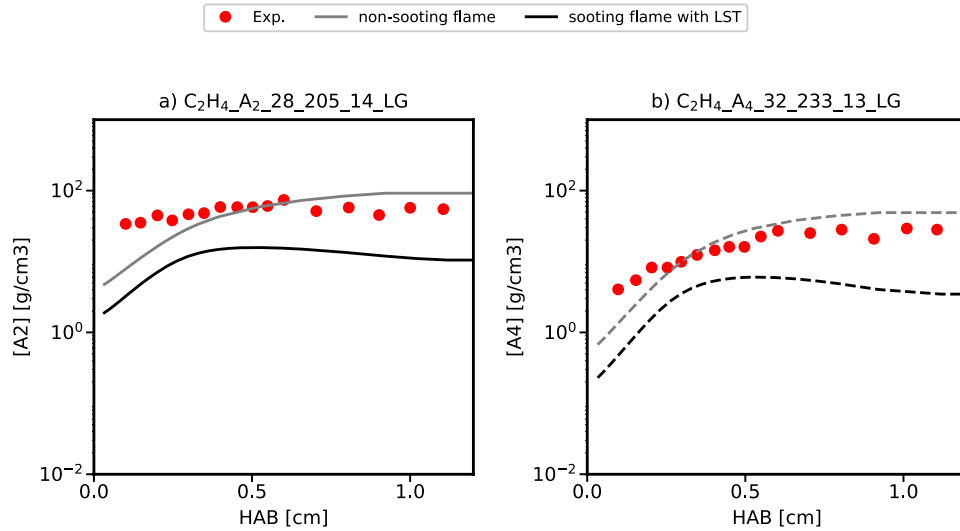


Figure 6.8: PAH prediction in Castaldi burner. Comparison between experiments [279] and numerical predictions with different soot precursors species.

Castaldi burner

In CASTALDI burner, no soot measurements are available and only *PAHs* are investigated, now taking into account *PAH* consumption by soot formation. The prediction of A2 and A4 with respectively C2H4_A2_28_205_14_LG and C2H4_A4_32_233_13_LG schemes (see Chapter 5) are shown in Fig. 6.8. Soot consumption were in a very good agreement with measurements, it impacts strongly *PAH* prediction (about one order of magnitude lower). However, the shape of *PAH* is better when considering soot formation. Considering the impact of soot onto *PAH* prediction, validation of chemical schemes should not neglect soot formation in their construction. However, experimental errors coming from experimental set-up for such *PAH* are large and more validation are required to conclude about the proposed reduced chemical schemes.

ISF5-Premixed Flames

In ISF5 flame, soot volume fraction f_v measurements are available. Soot prediction in ISF5 flames are compared in Fig. 6.9. Soot volume fraction is under-estimated at the end of the burner. Both reduced mechanism lead to similar soot prediction. Soot consumption is highlighted in Fig. 6.10, similarly to CASTALDI burner accounting for soot leads to a under-estimation of soot precursors profiles for both considered chemical schemes. These experiments have been done at atmospheric pressure, in rich flames few decades ago and the error on PAH measurements are pretty large. On the other part, recent soot nucleation model urge to account for soot nucleation reversibility [107, 144] and future work should pay attention to it.

6. LAGRANGIAN SOOT TRACKING IN LAMINAR FLAMES.

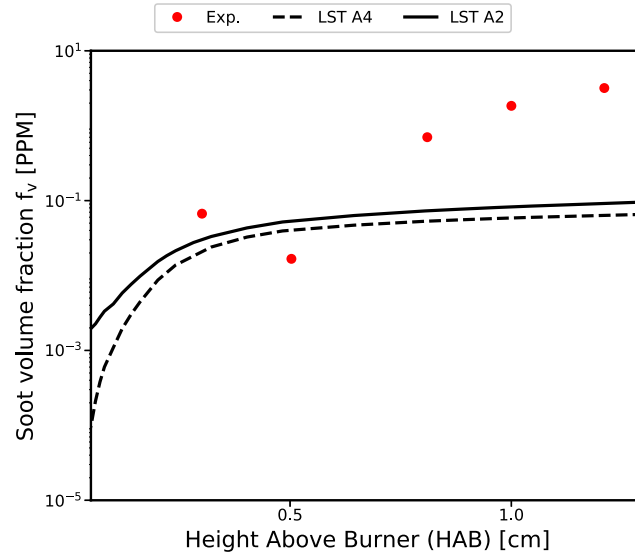


Figure 6.9: Soot prediction in ISF Premixed Flames 5. Comparison between experiments [280, 281] and Lagrangian Soot Tracking with different soot precursors species.

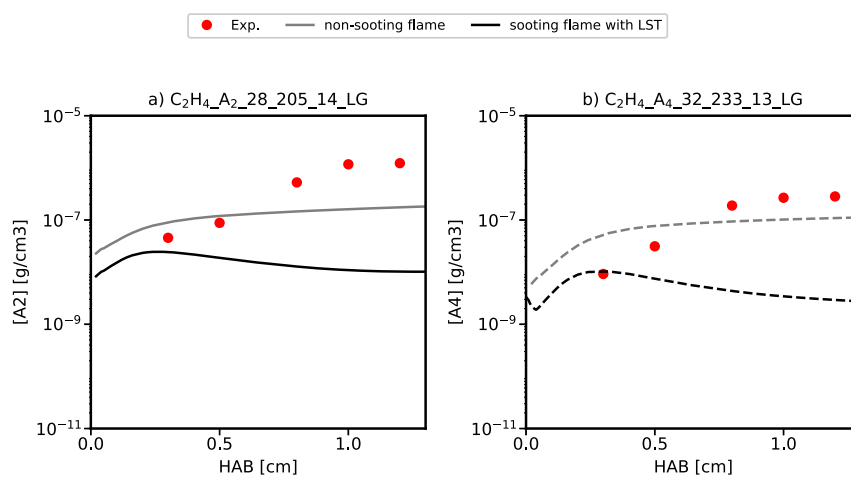


Figure 6.10: PAH prediction in ISF Premixed Flames 5. Comparison between experiments [280, 281] and numerical predictions with different soot precursors species.

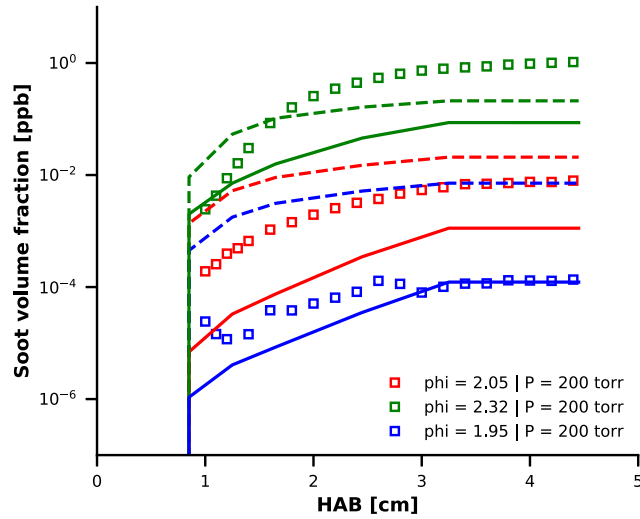
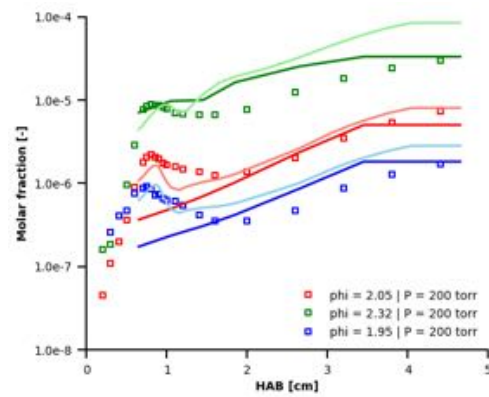


Figure 6.11: Soot prediction in nucleation flames. Comparison between experiments [285] and Lagrangian Soot Tracking with different soot precursors species.

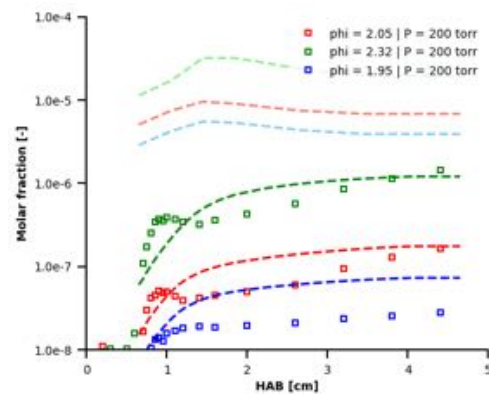
Nucleation Flames

Nucleation flames are suitable candidates to evaluate PAH. However level of soot are very low and very dependent of the PAH considered as the equivalence ratio decreases, and the procedure developed to measure soot and PAH are not easily applicable at high pressure [285]. In Fig. 6.11, soot volume fraction is computed for the three considered equivalence ratio. Only C2H4_A2_28_205_14_LG for small equivalence ratio $\phi = 1.95$ is able to retrieve experimental measurements where for the same equivalence ratio C2H4_A4_32_233_13_LG scheme based on A4 precursors over-estimates significantly f_v . Some discrepancies are observed on f_v for the transition from so-called nucleation flames where only nucleation contributes to total soot mass [285] and richer flame including surface growth. Both chemical schemes differ significantly for $\phi = 1.95$ and $\phi = 2.05$. Figure 6.12 presents the PAH description for each chemical schemes accounting for soot consumption or not. The shape of PAH profiles change considering soot consumption or not. Accounting for soot increase significantly the agreement between numerical and experimental PAH molar fraction. A better agreement for A2 with C2H4_A2_28_205_14_LG can be observed explaining why f_v prediction with C2H4_A2_28_205_14_LG are better. However, in general agreement between simulated and measured A2 and A4 are relatively good and it is thus expected that soot prediction are in a good agreement as well, which is not the case as depicted in Fig. 6.11. Then the accurate description of soot precursors is not sufficient confirming the need of more detailed soot nucleation model accounting for reversibility [107, 144] or larger PAHs [270].

6. LAGRANGIAN SOOT TRACKING IN LAMINAR FLAMES.



(a) A2 prediction.



(b) A4 prediction.

Figure 6.12: PAH predictions including soot consumption (dark) or not (light) in nucleation flames. Comparison between A2 and A4 measurements [285] and numerical approaches considering respectively C2H4_A2.28.205.14_LG (lines) and C2H4_A4.32.233.13_LG (dashed lines) chemical schemes.

6.4 Laminar flames: comparison with experiments

	C ₂ H ₄	O ₂	A _R
Molar fraction	0.163	0.237	0.600

Table 6.2: ISF6 Premixed laminar flame composition

6.4.1 Impact of soot precursors on soot evolution

To evaluate the impact of soot precursors to the particle size distribution function, the 1-D premixed laminar flame of *Abid et al.* [330] is retained since it presents the most complete measurements of the particles size distribution function within the ISF database¹, referenced as ISF6. It consists of a burner stabilized premixed ethylene/oxygen/argon flame with an equivalence ratio $\phi = 2.07$. The composition is defined in Tab. 6.2, it operates at 298 K and 1 atm with a inlet velocity of 8.0 cm/s. Note that several experimental techniques exist to measure particle size distribution of soot particles. In this flame, a stagnation plate is positioned at a defined height above the burner, it corresponds to a burner-stabilized stagnation (BSS) flames. Soot particles removal is integrated into this stagnation plate. When the soot particles are immediately diluted in a cold nitrogen flow and particle size distribution are obtained through a scanning mobility particle sizing, the soot volume fractions f_v and particles number density N_{part} are extracted from this PSDF.

For each height of the stagnation plate (H) a different flame is simulated with the correct boundary conditions (plate temperature). The temperature profiles obtained for each of the heights analyzed are presented in Fig. 6.13. For all these flames, a good agreement is obtained between experimental measurements and numerical temperatures validating the considered gaseous phase. Both reduced mechanism lead exactly to the same predicted temperature. The predicted temperature is slightly over-estimated in high height regions which may be due to the radiative transfers of large aggregates which is not accounted for. Results obtained in terms of global quantities (f_v and N_{part}) and PSDF are compared to experimental measurements from *Camacho et al.* [331] and numerical results from *Saggese et al.* [108] and *Rodrigues et al.* [196]. In the following a shift of 0.02 [cm] is considered to account for the aspiration of particles at the stagnation plate [108, 331].

Impact on global quantities

The comparison of global quantities (f_v , left, and N_{part} , right) are plotted in Fig. 6.14. Soot volume fraction are in good agreement especially with C2H4_A2-28_205_14_LG and close to the one obtained by *Saggese et al.* [108]. The associated N_{part} is however significantly over-estimated due to a high number of small particles as nascent particles con-

¹<https://www.adelaide.edu.au/cet/isfworkshop/>

6. LAGRANGIAN SOOT TRACKING IN LAMINAR FLAMES.

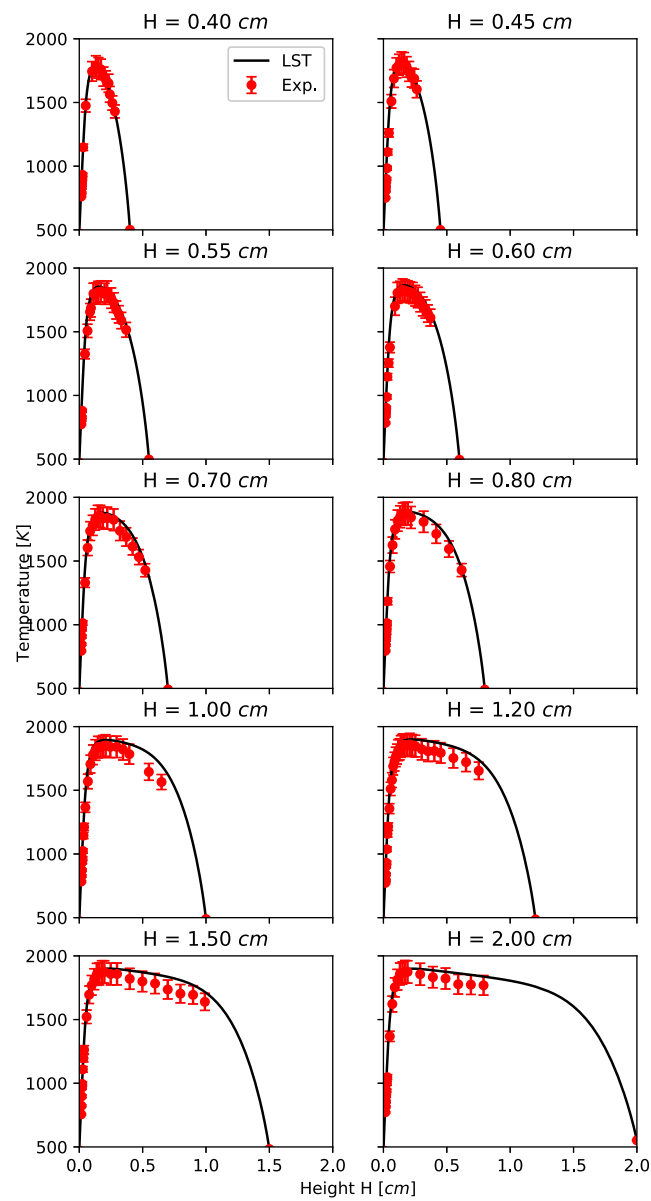


Figure 6.13: Temperature prediction in ISF Premixed Flames 6. Comparison between experiments [331] and Lagrangian Soot Tracking.

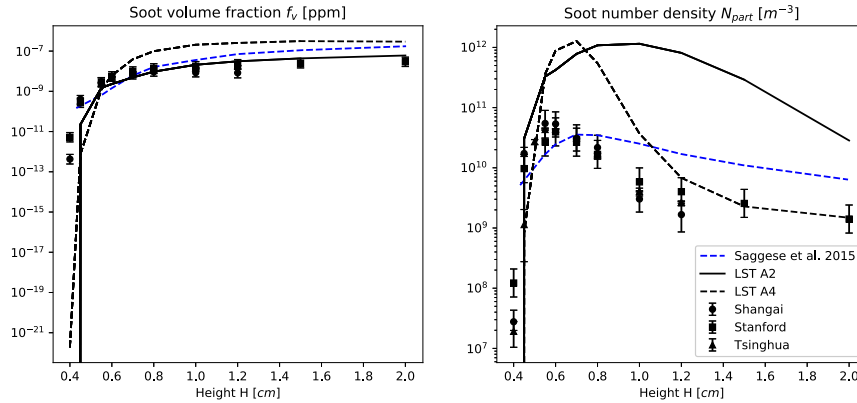


Figure 6.14: Soot prediction in ISF Premixed Flames 6. Comparison between experiments [331], numerical approaches from literature [108] and Lagrangian Soot Tracking with different soot precursors species.

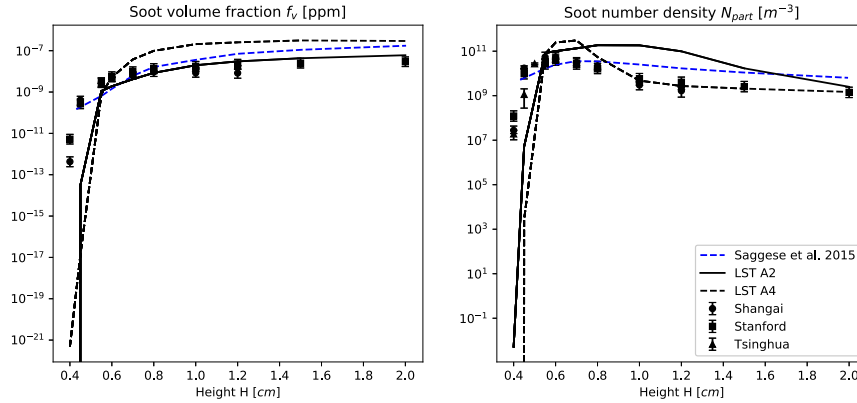


Figure 6.15: Soot prediction in ISF Premixed Flames 6. Comparison between experiments [331], numerical approaches from literature [108] and Lagrangian Soot Tracking with different soot precursors species neglecting particles with diameter smaller than 2 nm.

sidering A2 as precursor species. It can be observed that for C2H4_A4_32_233_13_LG , the correct shape is retrieved for both f_v and N_{part} but over-estimated. Experimentally, it is difficult to catch nanoparticles smaller than 2 – 3 nm. The removal of particles below 2 nm in the computation of N_{part} significantly increases the agreement between experimental and numerical N_{part} as observed in Fig. 6.15. However, the previous conclusion remains: a better f_v prediction is obtained with C2H4_A2_28_205_14_LG while N_{part} is well predicted by C2H4_A4_32_233_13_LG .

Impact on Particle Size Distribution

Figure 6.16 displays the numerical predictions for the particles size distribution at each height above the burner shifted by 0.2 cm similarly to Saggese et al. [108] and Rodrigues et al. [196]. The same experiments has been performed at three locations with three different BSS respectively in Shanghai, Stanford and Tsinghua [331]. The

6. LAGRANGIAN SOOT TRACKING IN LAMINAR FLAMES.

numerical prediction of *Saggese et al.* [108] and *Rodrigues et al.* [196] are also considered for comparison. The particles size distribution can be interpreted as shown in Fig. 6.17. It is then expected that the change of nucleation size according to the considered PAH (A2 or A4) shifts the particle size distribution towards large diameter. Figure 6.16 confirms this affirmation for height higher than 0.55 cm. The predicted particle size distribution is a good agreement with experimental measurements as well as the literature. However as the height increases, the differences between C2H4_A2_28_205_14_LG and C2H4_A4_32_233_13_LG increases. In addition to the shift of the PSD with C2H4_A4_32_233_13_LG, it seems that the nucleation rate is higher as well explaining the low level of PSD between the two-peaks. Despite a relatively good prediction on soot global properties, C2H4_A4_32_233_13_LG fails to correctly describe the PSD of ISF Premixed Flame 6 where PSD is bi-modal.

6.4.2 Bi-variate description of soot particles

The bi-variate description has been applied to previous computations showing good results similarly to literature [158]. This is especially true for the well-described ISF Premixed flame 6 validating the assumption of pure agglomeration retained in this work. To assess the impact of bi-variate description on soot prediction in ISF Premixed Flame 6, comparison with spherical assumption are considered for both reduced chemical schemes.

Impact on global quantities

Figure 6.18 presents the prediction of f_v and N_{part} for the considered reduced chemistry with and without the bi-variate description of soot particles. **Agg** states for Aggregates and **Sph** for Spherical. The predicted soot volume fraction between the two morphological description is very close while the predicted soot number density is overestimated considering spherical particles especially for C2H4_A4_32_233_13_LG. Same f_v but different N_{part} indicates different particles size distribution.

Impact on Particle Size Distribution

The particles size distribution assuming a spherical shape or not is shown in Fig. 6.19. Except for small height, the spherical shape assumption is not able to predict properly the PSD compared to the bi-variate description.

The use of a bi-variate description, the addition of a Lagrangian array, does not impact the computational cost, at least for the 1-D premixed flame investigated.

6.4 Laminar flames: comparison with experiments

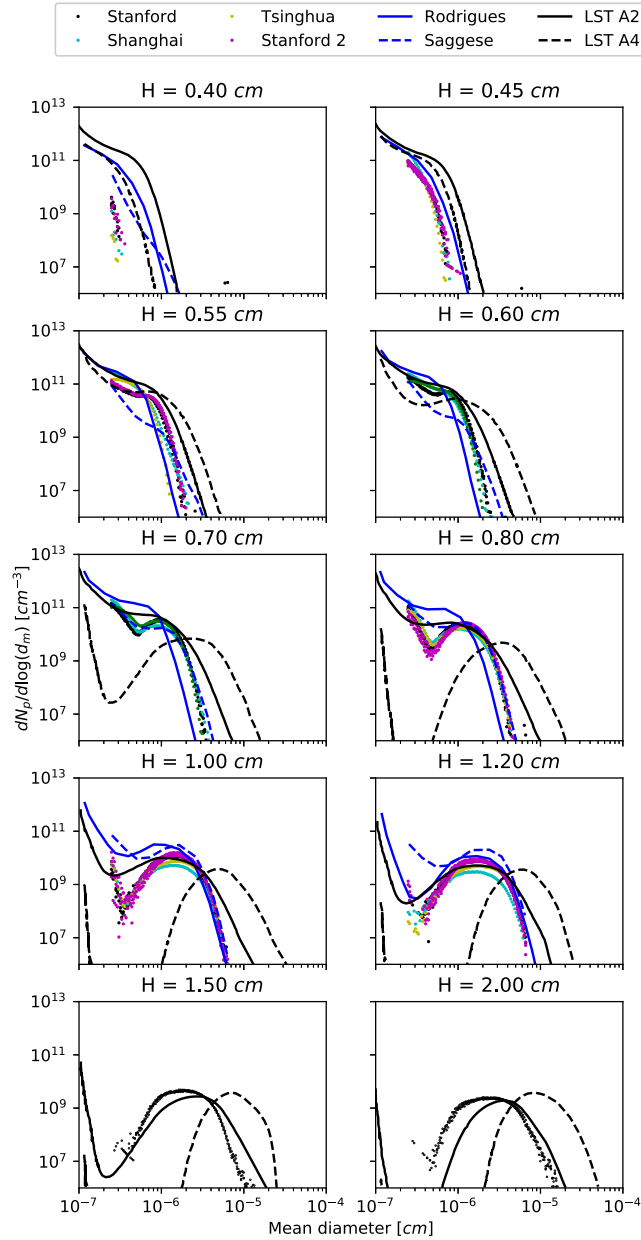


Figure 6.16: Particle size distribution function in ISF Premixed Flames 6. Comparison between experiments [331], numerical approaches from literature [108] and Lagrangian Soot Tracking with different soot precursor species.

6. LAGRANGIAN SOOT TRACKING IN LAMINAR FLAMES.

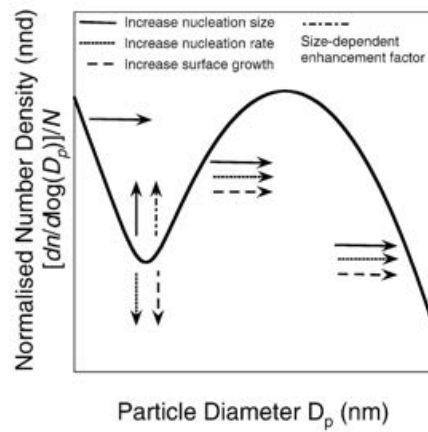


Figure 6.17: Influence of soot processes onto soot particles size distribution (Extracted from *Singh et al.* [332]).

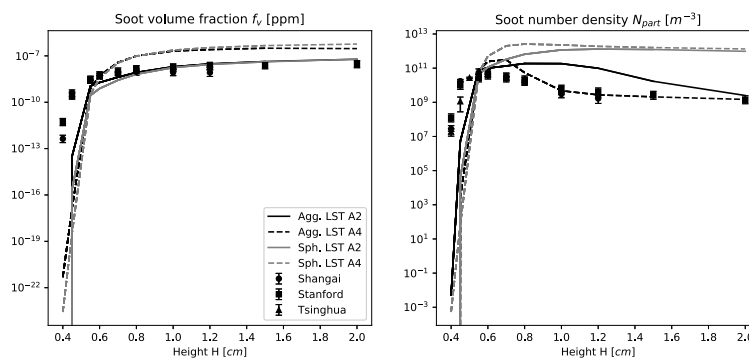


Figure 6.18: Effect of Bi-variate description on soot predictions. Comparison between numerical models and measurements.

6.4 Laminar flames: comparison with experiments

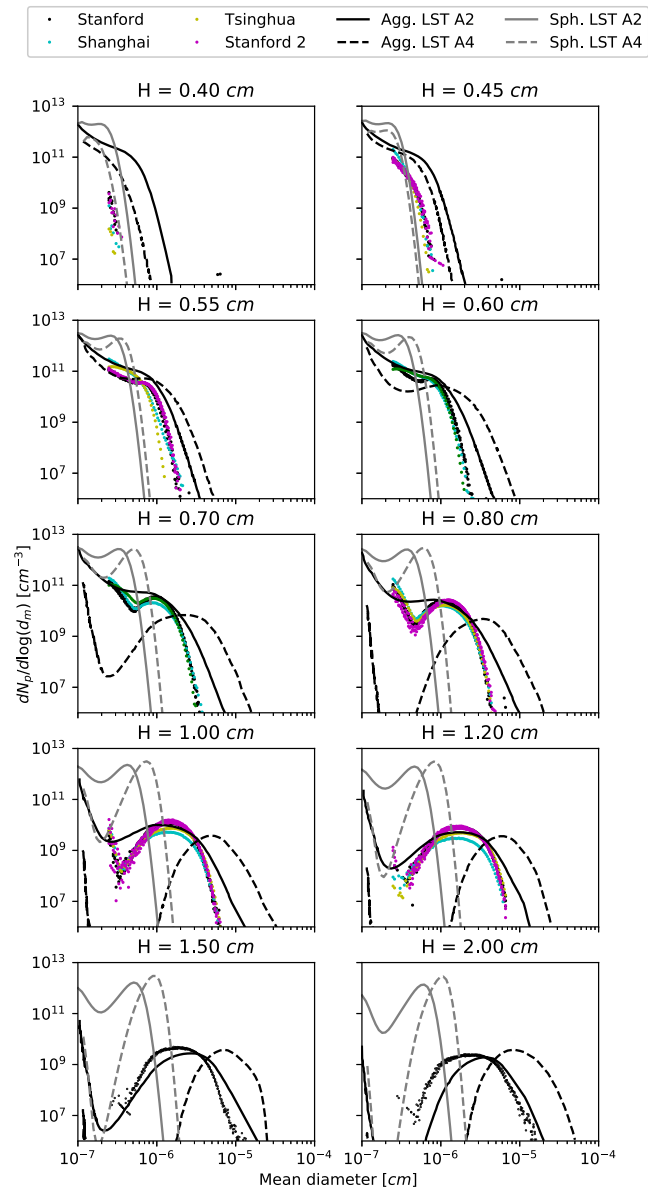


Figure 6.19: Effect of Bi-variate description on soot PSDF. Comparison between numerical models and measurements.

6.5 Conclusion

A reliable detailed soot model has been developed including a bi-variate description to account for soot morphology. The implementation of physical source terms has been validated through comparison with the sectional method. Similar results have been obtained using either sectional or lagrangian method. The impact of numerical method to significantly reduce the computational cost has been investigated. It has been observed that a relatively small number of particles per cell about 50 are sufficient to retrieve soot global quantity and to capture the particles size distribution. Additional numerical methods as the sorting of particles per control volume or the establishment of soot frequency enables a very efficient method in terms of computational cost.

The flame database used to validate the PAH chemistry has been calculated taking into account the soot consumption. The resulting PAH predictions, which were valid neglecting consumption from soot, have shown an underestimation in numerical predicted PAH and thus an underestimation of soot volume fraction as well, except for recent nucleation flames. Soot volume fraction has been also captured by the considered methodology. These low pressure methane flames are more reliable since the error of measured PAH and soot are lower than atmospheric flames. This study highlighted the strong dependency between PAH and soot, and PAH chemistry validation have to take into account soot consumption.

Two reduced chemical schemes C2H4_A2_28_205_14_LG and C2H4_A4_32_233_13_LG developed in Chapter 5 including respectively A2 and A4 as soot precursor species have been evaluated on a well-described premixed 1-D flame (ISF 6). Both gaseous description combined with the Lagrangian soot tracking have shown a satisfactory agreement compared to measured particles size distribution. And the bi-variate description have shown its ability to enhance the numerical predicted particles size distribution especially in bi-modal PSD where large aggregates appears.

Part III

LES of sooting flames

Chapter 7

Modeling of turbulent reacting flows

The goal of this chapter is to introduce the numerical methods and models used in this work to handle turbulent reacting flows. First, some theoretical aspects of turbulent combustion are presented. The fundamental concepts of LES, retained in this work, are briefly introduced along with the resulting filtered equations. Then, the interaction between turbulence and chemistry and associated numerical approaches are discussed. The retained approach to handle turbulence-chemistry interaction including recent developments from the literature is described as well as additional developments for soot particles. Finally, a methodology to account for thermal radiation through the coupling with Discrete Ordinate Method (DOM) solver is detailed.

Contents

7.1	Turbulent Flames	146
7.1.1	Turbulence basis	146
7.1.2	Turbulent premixed flames	147
7.1.3	Turbulent diffusion flames	149
7.1.4	Turbulent Partially-premixed flames	149
7.2	Large Eddy simulation	150
7.2.1	Filtered LES equations	151
7.2.2	Closure of filtered viscous terms	151
7.2.3	Closure of subgrid turbulent fluxes	152
7.3	Turbulence - Chemistry interactions	153
7.3.1	Thickened Flame model	154
7.3.2	Dynamic Thickened Flame model	155
7.3.3	Two-phase flow Thickened Flame model	157
7.3.4	Soot formation with the TF model	157
7.4	Thermal radiation modeling in turbulent sooting flames . .	158
7.4.1	Radiative Transfer Equation	159
7.4.2	Resolution of the RTE	160

7.1 Turbulent Flames

7.1.1 Turbulence basis

Practical combustion devices operate typically under turbulent conditions. Turbulent flows are characterized by high velocities, creating important velocity fluctuations that cannot be damped by the molecular viscosity. The flow is no more well structured in appearance, with disorganised large and small scale perturbations. In industrial devices, the turbulent nature of the flow is characterized by comparing the inertia forces which tend to disrupt the organisation of the flow with the viscous forces which to smooth velocity perturbations to recover a laminar flow, leading to the Reynolds number:

$$Re = \frac{U L}{\nu} \quad (7.1)$$

with U and L characteristic velocity and length of the flow and ν the kinematic viscosity of the fluid. The exact transition from laminar to turbulent regimes is only known in few academic configurations (such as pipe flows). In all cases, a high Re number characterizes a highly turbulent flow while when Re tends to 1, the flow is laminar. The mechanisms linking large scale perturbations of the flow with the smallest scales are described by the Kolmogorov theory. The energetic cascade, drawn in Fig. 7.1, represents the progressive decay of large structures (small wave number k) into smaller ones (large wave number k). The energy spectrum of Fig. 7.1 is made of three parts:

- The integral zone corresponding to the largest turbulent scales. These scales are also the most energetic ones. They are characterised by l_t the integral length scale and u' the characteristic large scale velocity fluctuation. A corresponding time scale $\tau_l = u'/l_t$ can be deduced. A turbulent Reynolds number is defined for these largest scales: $Re_t = u'l_t/\nu$.
- The inertial zone where large eddies break to form smaller eddies. Energy is just transferred to the new eddies but is little dissipated. The rate of energy transfer follows a $k^{-5/3}$ law in homogeneous isotropic turbulence [333].
- The dissipation zone corresponds to the smallest eddies of the flow, with a size close to the Kolmogorov length scale l_κ and a characteristic velocity u_κ . A corresponding time scale $\tau_\kappa = u_\kappa/l_\kappa$ can be deduced. These eddies are small enough to be rapidly dissipated by the molecular viscosity. The Reynolds number associated to these scales writes $Re_\kappa = u_\kappa l_\kappa/\nu = 1$.

In homogeneous isotropic turbulence, the integral and Kolmogorov length and velocity scales are linked via the dissipation rate ϵ of the kinetic energy. This dissipation rate

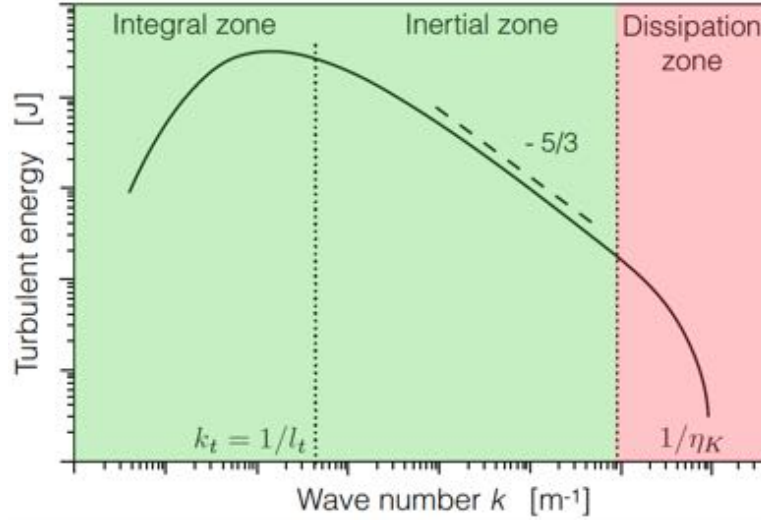


Figure 7.1: Turbulent energetic spectrum in a homogeneous isotropic turbulence, and characteristic dissipation zones.

can be estimated at the largest scale as:

$$\epsilon = 2\nu S_{ij}S_{ij} \quad (7.2)$$

with S_{ij} the deformation tensor:

$$S_{ij} = \frac{1}{2} \left(\frac{\partial u_j}{\partial x_i} + \frac{\partial u_i}{\partial x_j} \right) \quad (7.3)$$

Expressing ϵ at the smallest scales, and assuming constant ϵ , it is found that:

$$\frac{l_t}{l_\kappa} = Re_t^{3/4} \quad (7.4)$$

meaning that large turbulent Reynolds number flows create large energy cascades. Turbulent structures of various sizes may thus interact with the flame, changing its structure and properties.

7.1.2 Turbulent premixed flames

All turbulence length scales from l_t to l_κ may interact with the flame. Therefore, two dimensionless numbers are introduced:

- The Damköhler number which is the ratio between the time scale associated to the integral scale and the chemical time scale:

$$Da = \frac{\tau_t}{\tau_c} = \frac{l_t s_i^0}{\delta_i^0 u'} \quad (7.5)$$

7. MODELING OF TURBULENT REACTING FLOWS

- The Karlovitz number which is the ratio between the chemical time scale and the time scale corresponding to the Kolmogorov eddies:

$$Ka = \frac{\tau_c}{\tau_\kappa} = \frac{\delta_l^0}{l_\kappa} \frac{u^\kappa}{s_l^0} \quad (7.6)$$

By combining Da and Ka , it is possible to rewrite

$$Re_t = Da^2 Ka^2. \quad (7.7)$$

Many combustion diagrams have been proposed in the literature to summarize the various regimes of flame-turbulence interactions as functions of Ka and Da . Among all the diagram of Peters shown in Fig. 7.2, the flamelet regime or thin wrinkled flame regime was one of the first and corresponds to $Ka < 1$ and so necessarily $Da \gg 1$. In this regime, all turbulent scales are larger than the flame scales. The flame front is then wrinkled by the large eddies but the inner flame structure remains unchanged in that case, the turbulent flame front can be seen as an ensemble of flamelets, or laminar flames, distributed along a stretched and wrinkled front. The opposite case is found when $Da < 1$ and so necessarily $Ka \gg 1$, meaning that turbulent mixing occurs faster than chemical reactions. Turbulent structures can penetrate the reaction zone and the preheat zone, increasing turbulent diffusion. This situation is called the well stirred reactor regime or thickened flame regime. The intermediate regime is the thickened-wrinkled flame regime for which $Ka > 1$ and $Da > 1$. The flame thickness is larger than the Kolmogorov scale so small structures can penetrate the preheat zone and increase heat diffusion leading to a thicker flame. However, the flame thickness remains smaller than the integral length scale so that the flame keeps its laminar structure.

In most of practical hydrocarbon oxidation processes, the flamelet regime is the most relevant one. It has thus, been studied extensively, and is the basis of the modelling concept of flamelet tabulation. The main effect of turbulence is to increase the flame surface area by flame stretching and wrinkling. The direct consequence is an increase of the flame propagation speed. A turbulent flame speed s_T has been proposed by Abdel-Gayed [335] using the integral scale velocity fluctuation and the laminar flame speed:

$$\frac{s_T}{s_l^0} \propto 1 + \frac{u'}{s_l^0}. \quad (7.8)$$

For high velocity fluctuations, s_T reaches a plateau and can even drop if flame quenching occurs, when too high turbulent thermal diffusion takes the energy away from the flame front faster than it is produced by the chemistry.

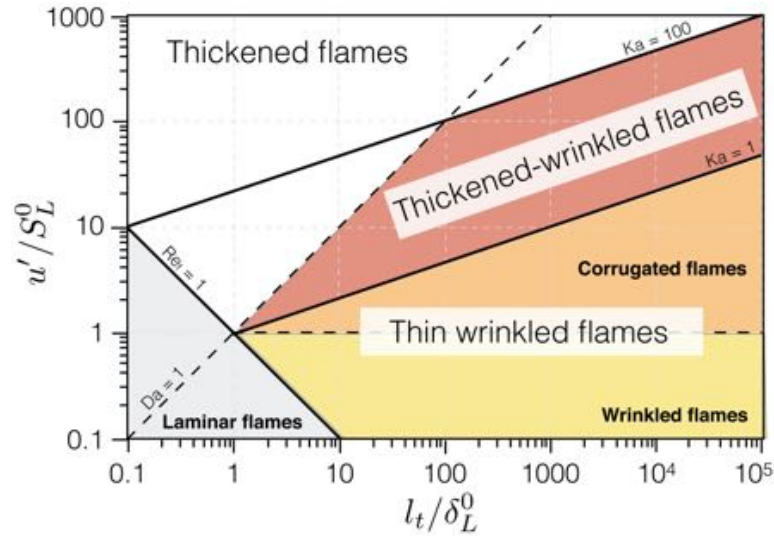


Figure 7.2: Combustion diagram for premixed turbulent combustion [334].

7.1.3 Turbulent diffusion flames

Even if diffusion flames do not have intrinsic time and length scales, similar combustion diagrams as for premixed flames have been derived. Based on a calibrated flame/vortex case where a flame thickness could be established, Cuenot & Poinot [336] proposed the combustion diagram shown in Fig. 7.3, where the flow time scale in Da is the inverse strain rate. Its extensions to turbulent diffusion flames is of course not straightforward but it offers a good description of controlling parameters. For a sufficient turbulent Reynolds number Re_t , three regimes are found which only depend on the Damköhler number of the diffusion flame. For high Da , the flame keeps a structure similar to its laminar structure. On the contrary, for low Damköhler number, quenching occurs because the chemical time scale is too high compared to the turbulent time scale. The intermediate case corresponds to a situation with strong unsteady effects.

7.1.4 Turbulent Partially-premixed flames

In real systems such as aeronautical gas turbines, combustion occurs in a partially-premixed regime. The ideal situation would be to use premixed fuel-air mixture to optimise the combustion efficiency. However, having a premixed fuel-air mixture before entering the combustion chamber is unsafe as it can ignite accidentally in the tank and destroy the engine. For this reason, mixing is only done when entering the combustion chamber. Systems such as swirlers inducing very high turbulence are used to mix fuel and air as fast as possible before reaching the flame. Still, because of incomplete mixing, a non-negligible part of the combustion may occur in a diffusion mode. As liquid fuels are used in such devices, evaporation of the polydisperse fuel spray leads

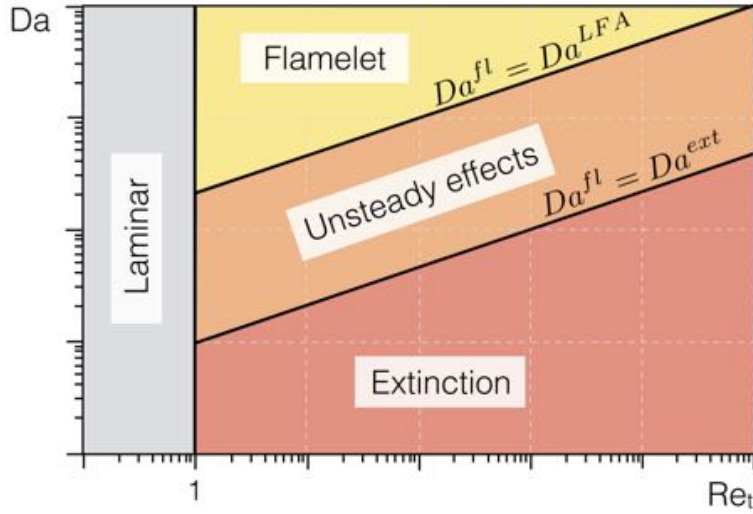


Figure 7.3: Combustion diagram for non-premixed turbulent combustion [336].

to non-uniformity of the mixture fraction. The gaseous mixture presents more or less heterogeneity depending on the quality of the evaporation process and its time scale as compared to the mixing time scale. If the evaporation time scale is too large, droplets can even cross the flame front creating particle spray flame structures, as shown in the following section.

To distinguish premixed from diffusion combustion, the Takeno index [337] TI can be used:

$$TI = \frac{\nabla Y_F \cdot \nabla Y_O}{|\nabla Y_F \cdot \nabla Y_O|}. \quad (7.9)$$

Considering that in a premixed one-dimensional flame, the gradients of the oxidizer and the fuel mass fractions have the same sign while they have opposite signs in a diffusion flame, the Takeno Index ranges from -1 for diffusion flames to $+1$ for premixed flames.

7.2 Large Eddy simulation

The numerical solution of the N-S equations over the whole range of turbulent length and time scales is called Direct Numerical Simulation (DNS). It requires a number of mesh points of the order of $10^3 Re_t^{9/4}$. Obviously, the DNS of realistic configurations characterized by high Re numbers, are currently out of reach. An approach that has received a great amount of attention in the combustion community for the past twenty years is the Large Eddy Simulation (LES).

In LES, a separation of scales is assumed, between the largest turbulent scales that are completely resolved on the grid, and the smallest scales that must be modeled. LES is thus a spatially filtered approach, for which subgrid-scale (sgs) closures must be

provided. Due to the universal nature of the smallest scales, deriving such models is expected to be facilitated. Furthermore, the prediction capability of LES is expected to be very high since most phenomena of interest in turbulent flows are associated with large scale and mid-scale motion, which are explicitly resolved.

7.2.1 Filtered LES equations

For a given variable Ω , the filtering operation denoted $\bar{\cdot}$ reads:

$$\bar{\Omega}(\mathbf{x}) = \int \Omega(\mathbf{y}) F_{\Delta}(\mathbf{x} - \mathbf{y}) \mathbf{d}\mathbf{y} \quad (7.10)$$

with F_{Δ} the filter kernel and Δ the filter width. As variable density flows are considered, a Favre-filtering operation (weighted by the density) denoted $\tilde{\cdot}$ is preferred. The resulting filtering operation on Ω reads:

$$\bar{\rho} \tilde{\Omega}(\mathbf{x}) = \int \rho \Omega(\mathbf{y}) F_{\Delta}(\mathbf{x} - \mathbf{y}) \mathbf{d}\mathbf{y} \quad (7.11)$$

Applied to the Navier-Stokes equations, the filtering procedure gives:

- Filtered Mass conservation

$$\frac{\partial \bar{\rho}}{\partial t} + \frac{\partial}{\partial x_j} (\bar{\rho} \tilde{u}_j) = 0. \quad (7.12)$$

- Filtered Species conservation

$$\frac{\partial \bar{\rho} \tilde{Y}_k}{\partial t} + \frac{\partial \bar{\rho} \tilde{Y}_k \tilde{u}_j}{\partial x_j} = - \frac{\partial}{\partial x_j} \left(\bar{J}_{j,k} + \bar{J}_{j,k}^t \right) + \bar{\omega}_k, \quad \text{for } k = 1, n_{spec}. \quad (7.13)$$

- Filtered Momentum conservation

$$\frac{\partial \bar{\rho} \tilde{u}_i}{\partial t} + \frac{\partial \bar{\rho} \tilde{u}_j \tilde{u}_i}{\partial x_j} = - \frac{\partial}{\partial x_j} \left(\bar{P} \delta_{ij} - \bar{\tau}_{ij} - \bar{\tau}_{ij}^t \right), \quad \text{for } i = 1, 2, 3. \quad (7.14)$$

- Filtered Energy conservation

$$\frac{\partial \bar{\rho} \tilde{E}}{\partial t} + \frac{\partial}{\partial x_j} \left(\bar{\rho} \tilde{E} \tilde{u}_j \right) = - \frac{\partial}{\partial x_j} \left(\overline{u_i (P \delta_{ij} - \tau_{ij})} + \bar{q}_j + \bar{q}_j^t \right) + \bar{\omega}_T. \quad (7.15)$$

7.2.2 Closure of filtered viscous terms

Expressions of the filtered viscous terms $\bar{J}_{j,k}$, $\bar{\tau}_{ij}$ and \bar{q}_j are given here.

- Diffusive species flux vector:

$$\bar{J}_{j,k} \simeq -\bar{\rho} \left(\bar{D}_k \frac{W_k}{\bar{W}} \frac{\partial \tilde{X}_k}{\partial x_j} - \tilde{Y}_k \tilde{V}_j^c \right) \quad (7.16)$$

with

$$\tilde{V}_j^c = \sum_{k=1}^{n_{spec}} \bar{D}_k \frac{W_k}{\bar{W}} \frac{\partial \tilde{X}_k}{\partial x_j} \quad \text{and} \quad \bar{D}_k \simeq \frac{\bar{\mu}}{\rho S c_k}. \quad (7.17)$$

7. MODELING OF TURBULENT REACTING FLOWS

- Laminar filtered stress tensor:

$$\bar{\tau}_{ij} \simeq 2\bar{\mu} \left(\tilde{S}_{ij} - \frac{1}{3} \delta_{ij} \tilde{S}_{ll} \right) \quad (7.18)$$

with

$$\tilde{S}_{ij} = \frac{1}{2} \left(\frac{\partial \tilde{u}_j}{\partial x_i} + \frac{\partial \tilde{u}_i}{\partial x_j} \right) \text{ and } \bar{\mu} \simeq \mu(\tilde{T}). \quad (7.19)$$

- Filtered heat flux vector

$$\bar{q}_j \simeq -\bar{\lambda} \frac{\partial \tilde{T}}{\partial x_j} + \sum_{k=1}^{n_{spec}} \bar{J}_{jk} \tilde{h}_{sk} \quad (7.20)$$

with

$$\bar{\lambda} = \frac{\bar{\mu} \bar{C}_p(\tilde{T})}{Pr}. \quad (7.21)$$

7.2.3 Closure of subgrid turbulent fluxes

Expressions of the unresolved turbulent Sub-Grid Scale (SGS) fluxes $\bar{J}_{j,k}^t$, $\bar{\tau}_{ij}^t$ and \bar{q}_j^t , are given here.

- The SGS Reynolds stress tensor is expressed as a diffusion contribution by introducing a turbulent viscosity μ_t . All unresolved small scales are then assumed to dissipate fluctuations. The form given to the SGS contribution is similar to the laminar one:

$$\bar{\tau}_{ij}^t = -\bar{\rho} (\widetilde{u_i u_j} - \tilde{u}_i \tilde{u}_j) = 2\mu_t \left(\tilde{S}_{ij} - \frac{1}{3} \delta_{ij} \tilde{S}_{ll} \right). \quad (7.22)$$

Many turbulent viscosity models to estimate μ_t are available in the literature and are not all cited here. The widely used **Smagorinsky model** [338] is efficient in homogeneous isotropic turbulence but was shown to be too dissipative for wall-bounded flows. This is corrected with the **WALE model** proposed by Ducros et al. [339], later improved by Nicoud et al. for rotating flows with the **SIGMA model** [340]. As this work focuses on flows in aeronautical combustors which are confined and where swirling flows are generated, the **SIGMA model** is used throughout this work except if stated otherwise. In this model, the turbulent viscosity is based on the singular values $\sigma_1 \geq \sigma_2 \geq \sigma_3$ of the velocity gradient tensor $\partial u_i / \partial x_j$:

$$\mu_t = \rho (C_\sigma \Delta)^2 \frac{\sigma_3 (\sigma_1 - \sigma_2) (\sigma_2 - \sigma_3)}{\sigma_1^2} \quad (7.23)$$

with $C_\sigma = 1.35$ and Δ the characteristic filter width based on the mesh cell size.

- The SGS species turbulent flux vector is also represented as a diffusive contribution with an associated turbulent species diffusivity D_k^t written similarly to the laminar species diffusivity:

$$\bar{J}_{j,k}^t = \bar{\rho} \left(\widetilde{u_j Y_k} - \tilde{u}_j \tilde{Y}_k \right) = -\bar{\rho} \left(D_k^t \frac{W_k}{\bar{W}} \frac{\partial \tilde{X}_k}{\partial x_j} - \tilde{Y}_k \tilde{V}_j^{c,t} \right) \quad (7.24)$$

with

$$D_k^t = \frac{\mu_t}{\rho S c_k^t} \text{ and } \tilde{V}_j^{c,t} = \sum_k D_k^t \frac{W_k}{\bar{W}} \frac{\partial \tilde{X}_k}{\partial x_j}. \quad (7.25)$$

A turbulent Schmidt number Sc_k^t is introduced to link the species turbulent diffusivities to the turbulent viscosity μ_t . In practice, $Sc_k^t = 0.60$ is used in this work. The turbulent correction velocity $\tilde{V}_j^{c,t}$ ensures mass conservation.

- Finally, the SGS energy flux vector is again represented as a diffusive contribution with an associated turbulent heat conduction coefficient λ^t linked to the turbulent viscosity μ_t with a turbulent Prandtl number $Pr^t = 0.60$ used throughout this work.

$$\bar{q}_j^t = -\bar{\rho} \left(\widetilde{u_j E} - \tilde{u}_j \tilde{E} \right) = -\lambda^t \frac{\partial \tilde{T}}{\partial x_j} + \sum_{k=1}^N \bar{J}_{j,k}^t \tilde{h}_{s,k} \quad (7.26)$$

with

$$\lambda^t = \frac{\mu_t \bar{C}_p}{Pr^t}. \quad (7.27)$$

7.3 Turbulence - Chemistry interactions

The flame front in typical applications is smaller than 1 mm, and requires to be sufficiently discretized. When considering ARCs, up to 10 – 20 points may be needed to resolve all species profiles across the flame. This level of discretization is usually below the LES filter size, and filtered source terms $\bar{\omega}_k$ and $\bar{\omega}_T$, named $\bar{\omega}$ in the rest of this section, need to be modeled. The model should then describe subgrid-scale interactions of the flame with the turbulence. A comprehensive review of models can be found in the book of Poinso & Veynante [197], and distinguishes premixed and non-premixed flames. In the context of LES, premixed combustion is often modeled with tabulated approaches, such as FGM (Flame Generated Manifold) [216] or **F-TACLES** [341]. An alternative is the **Thickened Flame** [342] approach, used in this work and detailed in Section 7.3.1.

Non-premixed combustion is also mostly computed with tabulated approaches, based on the mixture fraction z . Diffusion flames require an additional parameter, the strain rate, which controls its thickness. The Thickened Flame approach may be used [343] but it applies differently compared to premixed combustion.

7.3.1 Thickened Flame model

The **Thickened Flame** (TF) [342] model was originally derived for gaseous premixed combustion and was later extended to spray flames [238], as detailed in Sec. 7.3.3. The main idea of the TF model is to: (1) artificially thicken the flame front to resolve it on LES grids and (2) account for the sgs flame-turbulence interactions. Rewriting Eq. 3.7 and 3.8 as:

$$\delta_l \propto \sqrt{\frac{D_{th}}{\dot{\omega}}} \quad (7.28)$$

$$s_l^0 \propto \sqrt{D_{th}\dot{\omega}} \quad (7.29)$$

shows clearly that applying the transformation $D \rightarrow \mathcal{F}D$ and $\dot{\omega} \rightarrow \dot{\omega}/\mathcal{F}$ leads to a flame thickened by the value \mathcal{F} , but keeping the correct laminar flame speed. \mathcal{F} may be adjusted to obtain the desired number of grid points in the flame and allows to compute the flame on any LES grid.

However this transformation, by changing the flame scales, modifies its interaction with turbulence: it was shown in Sec. 7.1.2 that the turbulent wrinkling and stretching of the flame are directly controlled by the relative space and time scales of vortices and of the flame. As sketched in Fig. 7.4, a thickened flame is much less wrinkled than a thin flame as only the largest turbulent structures are able to perturb it. To recover this sub-grid scale effects, an efficiency function \mathcal{E} is applied via the transformation $D \rightarrow \mathcal{F}\mathcal{E}D$ and $\dot{\omega} \rightarrow \mathcal{E}\dot{\omega}/\mathcal{F}$. This way, the flame thickness is still $\mathcal{F}\delta_l$ but the flame speed of the thickened flame is now $\mathcal{E}S_l$.

The efficiency \mathcal{E} is evaluated as the ratio between the wrinkling of the non-thickened flame to the thickened one:

$$\mathcal{E} = \frac{\Xi(\delta_l)}{\Xi(\mathcal{F}\delta_l)}. \quad (7.30)$$

The wrinkling factor Ξ , which is a function of the flame thickness, is estimated assuming that there is no creation or destruction of flame surface at the subgrid scale level (equilibrium is reached) and is based on a characteristic turbulent velocity u'_Δ , at the filter scale Δ , given by Colin et al. [342]. In practice, the filter scale is taken as $\Delta = \mathcal{F}\delta_l$.

Numerous formulations have been proposed in the literature for Ξ and interested readers are referred to [344]. One of the most used form is the one of Colin et al. [342]:

$$\Xi(\delta_l) = 1 + \alpha (Re_t) \Gamma \left(\frac{\Delta}{\delta_l}, \frac{u'_\Delta}{S_l} \right) \frac{u'_\Delta}{S_l} \quad (7.31)$$

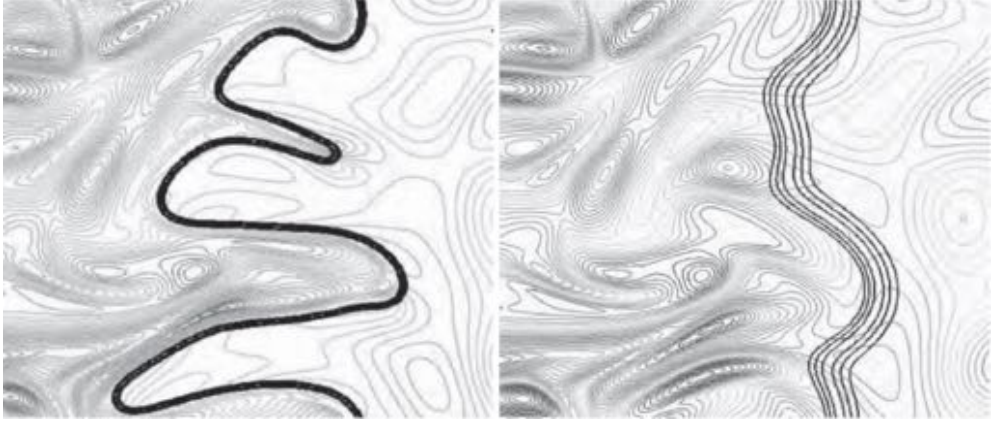


Figure 7.4: Flame-turbulence interaction for a thin and artificially thickened flame, studied by DNS [342].

with α a parameter depending on the turbulent Reynolds number and Γ a function that evaluates the effect of sgs strain rate from the sgs turbulence intensity and the filter size. A second formulation was proposed by Charlette et al. [345]:

$$\Xi(\delta_l) = \left(1 + \min \left[\frac{\Delta}{\delta_l}, \Gamma \left(\frac{\Delta}{\delta_l}, \frac{u'_{\Delta}}{S_l}, Re_{\Delta_e} \right) \frac{u'_{\Delta}}{S_l} \right] \right)^{\beta} \quad (7.32)$$

which introduces an exponent parameter β . In the static version of the Charlette model, $\beta = 0.5$. A Charlette Dynamic version [346, 347] was also proposed. Recognizing that in most application, u'_{Δ}/S_l is large, the wrinkling reduces to:

$$\Xi(\delta_l) = \left(\frac{\Delta}{\delta_l} \right)^{\beta} \quad (7.33)$$

showing that wrinkling depends almost solely on β . It is then a critical parameter, which may vary in space and time. The model is then improved by estimating β dynamically in space from the resolved progress variable field. It significantly improves the results in cases where turbulence is far from homogeneous and the additional computational cost is only 5 – 10 %.

7.3.2 Dynamic Thickened Flame model

If the transformation $D \rightarrow \mathcal{F}ED$ and $\dot{\omega} \rightarrow \mathcal{E}\dot{\omega}/\mathcal{F}$ is applied in the whole domain, mixing in non-premixed regions is undesirably accelerated. Indeed, the transformation is built to modify the flame and is meaningless if $\dot{\omega} = 0$. Therefore thickening must be applied only in the flame region. This is the **Dynamic Thickened Flame model** (DTFLES) [348], which needs a sensor \mathcal{S} to detect the flame front. The local thickening factor is then computed as:

$$\mathcal{F} = 1 + (\mathcal{F}_{\max} - 1) \mathcal{S} \quad (7.34)$$

7. MODELING OF TURBULENT REACTING FLOWS

with $\mathcal{F}_{max} = N_c \Delta_x / \delta_l$ the thickening factor required to obtain the desired number of grid points N_c in the flame front. N_c is generally close to 5 for GRCs, or 5 – 10 for ARCs due to stiff radical species profiles. The sensor definition depends on the type of chemistry description used. Sensors for GRCs and ARCs are different and detailed below.

7.3.2.1 Sensor for GRCs

For GRCs, the sensor \mathcal{S} is based on one of the global reaction steps. For example, choosing the fuel oxidation reaction, the following expression:

$$\Omega = Y_F^{n_F} Y_O^{n_O} \exp\left(-\Gamma \frac{E_a}{RT}\right) \quad (7.35)$$

is calculated and compared to a reference value Ω_0 pre-determined with a 1D flame calculation. The sensor is then written:

$$\mathcal{S} = \tanh\left(\beta' \frac{\Omega}{\Omega_0}\right) \quad (7.36)$$

with $\beta' \approx 50$. Equation [7.35](#) differs from the reaction rate by the factor Γ , introduced to extend the sensor outside the flame zone for numerical strictly reasons.

7.3.2.2 Relaxation Sensor for ARCs

The sensor based on a reaction rate is not adapted for ARCs as it is difficult to know which reaction is the most appropriate among all reactions in the ARC scheme. Indeed, some reactions occur in the pre-flame region while others are in the post-flame region, and selecting one reaction rate may lead to an unsatisfactory behaviour for other reactions. It seems then more appropriate to use the fuel source term $|\dot{\omega}_F|$, as proposed by Jaravel [\[349\]](#). Similarly to the sensor for GRCs, a comparison between local values and maximum value $|\dot{\omega}_F|_{1D}^{max}$ found in a 1D flame in representative conditions is used. The sensor writes:

$$\mathcal{S} = \max\left[\min\left(2 \frac{\mathcal{F}_{max} |\dot{\omega}_F|}{|\dot{\omega}_F|_{1D}^{max}} - 1, 1\right), 0\right] \quad (7.37)$$

However, although wide them reaction source terms, the fuel source term still does not extend over the entire flame region and a filtering procedure is applied to the sensor \mathcal{S} .

7.3.2.3 Generic Sensor

The above sensors are efficient, but they are based on reference 1D flame characteristics, which may become problematic for modified flames or spray flames. A generic and self-adapting method for flame front detection and thickening has been recently developed at CERFACS [\[350\]](#) and implemented in AVBP. The method can be decomposed in two steps:

- **Detection:** The detection is ensured by a geometrical shape analysis of the resolved field of heat release rate. It does not require any reference flame and only relies on the current solution.
- **Thickening:** Once the front is localized, the thickening factor is also determined from the flame shape. The resulting thickening is then automatically restricted to under-resolved flame regions. Thickening is then applied to the flame zone via numerical particles which travel through local flamelets. Thanks to this particle approach, the method can be applied to any type of mesh and in a parallel framework.

This generic approach does not need any user-input except from the desired number of cells in the flame, nor preliminary calibration. It is critical to correctly apply TFLES to complex cases with varying local conditions, complex chemistry or liquid fuel as in this work. For these cases, the *a priori* knowledge of the flame thickness is difficult or even not possible, and the standard thickening approach may lead to inadapted thickening, decreasing the accuracy of the simulation. Therefore, the generic sensor has been retained for all computations in this work. Note that, in this work, the thickened flame model is applied only for the premixed regime detected through the Takeno index (see Eq. 7.9). The thickened flame model for non-premixed flames is different [343], and out of the scope of this work.

7.3.3 Two-phase flow Thickened Flame model

As already mentioned, Thickened Flame model modifies the flame scales so that the interactions are modified. This is taken into account in the Two-Phase Thickened Flame model (TPTFLES) described in this section.

In order to preserve the scale ratio between the flame and the fuel droplets, all exchange terms between phases must be scaled in the flame zone: droplets evaporation rate and drag must be divided by \mathcal{F} . The scaling is done directly in the equations of both phases.

7.3.4 Soot formation with the TF model

For the same reason as for spray combustion, the TF model implies scaling of soot chemistry. All soot source terms are therefore divided by \mathcal{F} . To assess the validity of TP-TFLES for soot, tests are performed in a rich one-dimensional premixed flame. Three computations have been carried out:

- **Reference:** Resolved flame on a fine mesh without thickening.

7. MODELING OF TURBULENT REACTING FLOWS

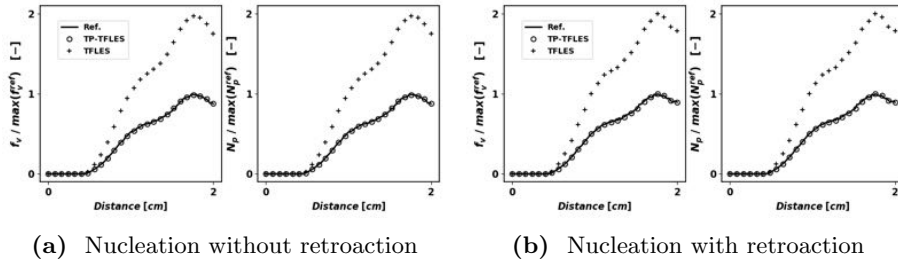


Figure 7.5: Comparison of predicted soot volume fraction (considering only nucleation) with and without soot model scaling in a rich premixed flame with constant thickening ($\mathcal{F} = 2$) and the resolved flame (without thickening).

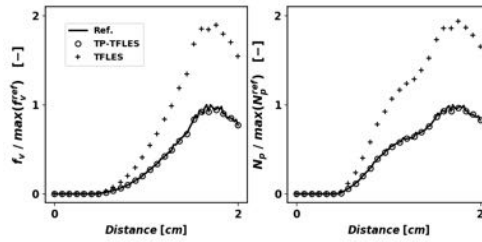


Figure 7.6: Comparison of predicted soot volume fraction (considering nucleation and surface growth) with and without soot model scaling in a rich premixed flame with constant thickening ($\mathcal{F} = 2$) and the resolved flame (without thickening).

- **TFLES:** Thickened flame model on a coarse mesh with a constant thickening factor $\mathcal{F} = 2$ **without** scaling of the soot model,
- **TP-TFLES:** Thickened flame model on a coarse mesh with a constant thickening factor $\mathcal{F} = 2$ **with** scaling of the soot model.

First, only soot nucleation is considered. Results are shown in Fig. [7.5](#), where it clearly appears that the soot model scaling allows to recover exactly the reference flame. Soot nucleation with and without retroaction has been investigated to ensure the good implementation of TP-TFLES.

The same methodology applied to nucleation and surface growth leads to the same conclusion as shown in Fig. [7.6](#)

In this work, TP-TFLES is considered for both soot particles and liquid droplets to correctly capture particles physics.

7.4 Thermal radiation modeling in turbulent sooting flames

Thermal radiation refers to the transport of energy via electromagnetic waves. Thermal radiation can be conceptualized as a stream of photons which carry energy. In highly emitting and absorbing media such as turbulent highly sooting flames, both emission

and absorption must be accounted for. The associated governing equation is the Radiative Transfer Equation (RTE) which describes the transport of photons and their interactions with the surrounding medium, via the radiative intensity. This quantity depends on position, direction and frequency, and therefore requires all directions of the solid angle and all frequencies.

Radiation does not follow the same rule as other of heat transfer modes, namely convection and conduction. First, radiation is a non-local phenomenon: energy content at a specific location results from instantaneous exchanges with the whole surrounding volume. Second, the directional and frequential dependency of radiative phenomena requires specific methods. Finally, thermal radiation propagates at the speed of light. Therefore, it reaches thermodynamic equilibrium much faster than the other energy transport processes. As a result, the temporal dependency of radiative quantities can be neglected and the equations are formulated in their steady form.

7.4.1 Radiative Transfer Equation

The Radiative Transfer Equation (RTE) for a medium of refractive index n and for wavelength ν , can be written as:

$$\begin{aligned} \frac{dI'_\nu}{ds} = & - \underbrace{\kappa_\nu I'_\nu}_{\text{Absorption}} - \underbrace{\sigma_\nu I'_\nu}_{\text{Scattering}} \\ & + \underbrace{\kappa_\nu n^2 I_\nu^\circ}_{\text{Emission by the medium}} + \underbrace{\frac{\sigma_\nu}{4\pi} \int_{4\pi} p_\nu(\mathbf{u}', \mathbf{u}, s) I'_\nu(\mathbf{u}', s) d\Omega'}_{\text{Received scattering}} \end{aligned} \quad (7.38)$$

where $I'_\nu(\mathbf{u}', s)$ is the local radiative intensity traveling in the direction \mathbf{y} and $p_\nu(\mathbf{u}', \mathbf{u}, s)$ is the phase function and corresponds to the probability that a ray in the direction \mathbf{u}' is scattered in the direction \mathbf{u} at the local position s . $d\Omega'$ corresponds to the infinitesimal solid angle of integration. I_ν° corresponds to the blackbody emissive intensity expressed with the Planck's law:

$$I_\nu^\circ(T) = \frac{2\pi hc_0^2 \nu^3}{n^2 \left[e^{\frac{h\nu}{k_b T}} - 1 \right]} \quad (7.39)$$

where h and k_b are respectively the Planck and Boltzmann constants, and c_0 the speed of light in vacuum.

Knowing the radiative intensity $I'_\nu(\mathbf{u}, s)$ for all wavelengths ν , directions \mathbf{u} and positions s , the radiative heat flux vector \mathbf{q}^R is deduced as:

$$\begin{aligned} \mathbf{q}^R &= \int_{\nu=0}^{\infty} \mathbf{q}_\nu^R d\nu \\ &= \int_{\nu=0}^{\infty} d\nu \int_{4\pi} I'_\nu(\mathbf{u}, s) \mathbf{u} d\Omega \end{aligned} \quad (7.40)$$

7. MODELING OF TURBULENT REACTING FLOWS

The volumic radiative power that must be added to the gaseous energy equation is then:

$$\begin{aligned} P^R &= -\nabla \cdot \mathbf{q}^R \\ &= -\int_{\nu=0}^{\infty} d\nu \int_{4\pi} \operatorname{div} [I'_\nu(\mathbf{u}, s)\mathbf{u}] d\Omega \end{aligned} \quad (7.41)$$

Then, using Eq. [7.38](#), the radiative power P_R can be expressed as:

$$P^R = -\int_{\nu=0}^{\infty} \left[\left(4\pi\kappa_\nu I_\nu^\circ - \int_{4\pi} \beta_\nu I'_\nu d\Omega + \frac{\sigma_\nu}{4\pi} \int_{4\pi} p_\nu(\mathbf{u}', \mathbf{u}, s) d\Omega \right) \right] d\nu \quad (7.42)$$

where $\beta_\nu = \kappa_\nu + \sigma_\nu$ is the total extinction.

If the medium is non-scattering ($\sigma_\nu = 0$), this equation is simplified to:

$$P^R = \underbrace{\int_{\nu=0}^{\infty} \left[\kappa_\nu \int_{4\pi} I'_\nu d\Omega \right] d\nu}_{\text{absorbed power}} - \underbrace{4\pi \int_{\nu=0}^{\infty} \kappa_\nu I_\nu^\circ d\nu}_{\text{emitted power}} \quad (7.43)$$

where contributions of absorbed power (P^a) and emitted power (P^e) can be identified.

7.4.2 Resolution of the RTE

Over the years, numerous approaches have been developed to solve the radiative heat transfer equation. The numerical methods for thermal radiation may be separated in two main categories: deterministic and statistical approaches.

Statistical approaches are derived from the stochastic Monte Carlo method (MC) tracking a large number of random trajectories of photons. This method is very accurate and can simulate complex physical phenomena without simplifying assumptions. Although its computational cost has been very restrictive for long to be applied to combustion applications, recent developments have shown promising results [\[351\]](#).

Deterministic methods rely on the discretization of the RTE in the phase space. The ray tracing method is very accurate but has a high computational cost and is therefore generally restricted to benchmark cases to provide reference solution. On the other side, P_N approaches, first introduced by Jeans [\[352\]](#) are widely used, but lack accuracy. Discrete Ordinates Method (DOM), initially proposed by Chandrasekhar [\[353\]](#) is known to provide a good trade-off between accuracy and computational cost. Recent advances on DOM can be found in the review of *Coelho* [\[354\]](#).

7.4.2.1 The PRISSMA solver

The radiative solver PRISSMA used for the present study relies on the DOM formalism. DOM consists in the discretization of RTE in space, frequency and solid angle. A numerical quadrature is used for the solid angle, while the frequential dependency is accounted for via a spectral model. The three levels of discretization are detailed in the following.

Angular discretization

The solid angle is discretized over a finite number of directions N_{dir} , specifically distributed through a numerical quadrature. For some quadratures, a weight is associated to each direction. The RTE is resolved in the entire domain for each direction, individually, all solutions being summed at the end. Various quadratures have been developed over the years [355, 356, 357]. Among them, the present calculations rely on the S_4 ($N_{dir} = 24$) quadratures. It belongs to the category of the S_N quadratures [355, 356, 357] for which the number of directions is given by $N_{dir} = N(N + 2)$. The accuracy and computational cost of a DOM computation are strongly influenced by the chosen quadrature. In particular, a too small number of discretized directions may lead to the so-called "Ray effect", corresponding to unseen zones between 2 directions.

Spatial discretization

The RTE is integrated using the finite volume approach. Different spatial differencing schemes may be used. In the solver PRISSMA, the exponential scheme [358], the step scheme [359] and the Diamond Mean Flux Scheme (DMFS) [360] are available. It was demonstrated that DMFS is well suited and efficient on unstructured grids [361] and leads to accurate results as long as the optical thickness of the mesh cells is low.

Spectral properties and models

In combustion, two sources of thermal radiation may be considered: non-luminous radiation induced by gaseous species and luminous radiation corresponding to the contribution of soot particles.

- **Non-luminous radiation:** Radiant species in flames are the combustion products H_2O , CO_2 and CO , all other molecules are mostly irrelevant due to low concentrations. Since the medium is considered non-scattering, only the absorption coefficient κ_ν is considered.

7. MODELING OF TURBULENT REACTING FLOWS

In a purely gaseous mixture, the absorption spectrum depends on the local mixture composition, temperature and pressure.

It is described with absorption values at discrete frequencies ("lines") for each molecule. With such description, the number of frequencies to be solved (i.e., number of RTE) is too large to keep a reasonable computational cost, then spectral models are introduced, aggregating frequencies in bands or even over the whole spectrum.

Line-by-line models reproduce each line of the spectrum providing the most accurate spectrum description. These spectra are experimentally measured and are accessible in databases. For infrared radiation over the temperature range encountered in a combustion chamber, the spectrum includes around one million lines.

Band models consist in a representation of the absorption frequency dependency in bands of given width, keeping a simplified frequency dependency. For this purpose, assumptions are made on the spectrum that may reduce its scope of application. Such spectral models are therefore developed for specific target applications.

They still represent a good compromise between accuracy and computational cost for application to industrial configurations with complex geometry. In PRISSMA, CK band model is available and acts as reference spectral model. However, in a multi-physics context, band models often stay too costly in computational time. In such case, global models for which the band width covers the entire spectrum are used. The absorption coefficient no longer depends on frequency. It was shown in [361, 362, 363] that global models provide good results for combustion applications at a reduced computational cost, in both academic configurations and real combustion chambers.

Therefore, a global model is retained for the absorption properties of H₂O, CO₂ and CO in the present study.

The robust Rank Correlated FS-NBKMck model [364, 365], namely RCFSK is an improved version of the FS-NBKMck (FSCK) model which does not require tuned input parameters to produce accurate results [365]. It has been implemented in PRISSMA and validated in 3 test cases proposed in *Poitou and André* [366]:

RTC1 Homogeneous cylinder, with black walls ($\epsilon = 1$) at 300K and a homogeneous gaseous temperature (two cases: 1200K and 1800K).

RTC2 Inhomogeneous cylinder [367], with black walls ($\epsilon = 1$) at 800K except for one surface at 300K, and non-homogeneous gaseous composition with spatial profiles of H₂O, CO₂ and temperature.

7.4 Thermal radiation modeling in turbulent sooting flames

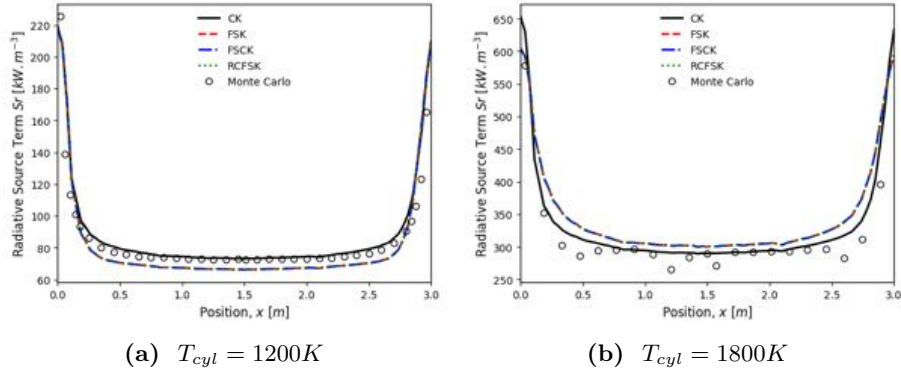


Figure 7.7: RTC1: Comparison between PRISSMA spectral models and the reference Monte-Carlo method

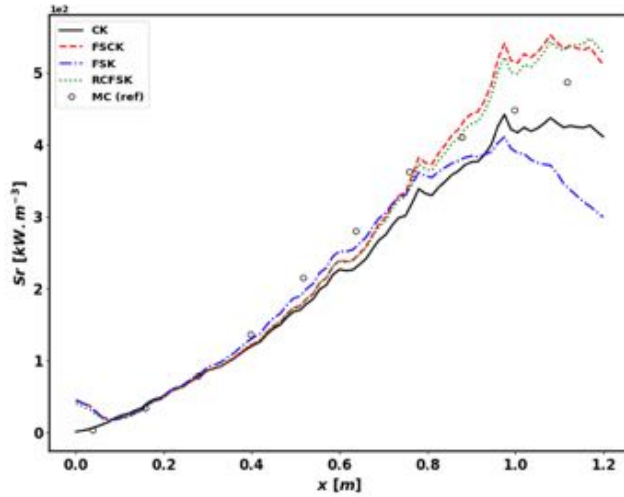


Figure 7.8: RTC2: Comparison between PRISSMA spectral models and the reference Monte-Carlo method

RTC3 **3D box** [368], representative of combustion with air at atmospheric pressure. The boundary conditions in X direction are cold black walls ($\epsilon = 1$) at $300K$ while the boundary conditions for Y and Z directions are purely reflecting ($\epsilon = 0$) to simulate infinite symmetry in those directions. Profiles are imposed along the X axis is imposed for the gaseous composition and temperature.

All test cases have been performed using three-dimensional unstructured tetrahedral meshes.

The radiative test cases have been computed with the various spectral models and results are shown in Fig. 7.7 to 7.9. For RTC1 and RTC2, the reference Monte-Carlo is shown to assess the accuracy of the implemented model in PRISSMA.

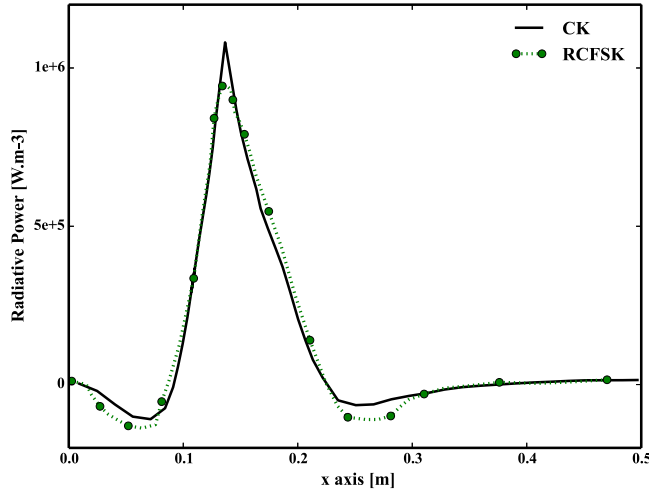


Figure 7.9: RTC3: Comparison between PRISSMA spectral models and the reference Monte-Carlo method

The results show that both RCFSK and FSK lead to similar predicted radiative source terms, as expected, and are close to CK and reference Monte-Carlo results. In Fig. 7.9, CK and RCFSK are compared on the third test case RTC3, where a very good agreement is also obtained. Note that RCFSK is much faster in terms of computational time (about ten times faster).

- Luminous radiation:** When a photon comes close to a soot particle, this photon can be absorbed or scattered. The scattering is due to diffraction and can be of two different types. When the mean distance l between soot particles is equal or smaller than the wavelength λ , the scattering by one particle can be affected by the presence of surrounding particles: this case is called dependent scattering. The second type of scattering is independent scattering, where $l \gg \lambda$ and the surrounding particles do not impact the individual scattering. However it has been demonstrated that for particles with diameter d_p smaller than $1\mu m$, (which is the case in the present work), scattering by soot particles can be neglected [369].

Radiative properties of soot particles follow the Rayleigh theory, derived from the Mie theory [370] in case of small particles ($\pi d_p/\lambda \ll 1$) [371]. The resulting soot absorption coefficient is a function of the soot volume fraction f_v and writes:

$$\kappa_\nu^{soot} = A_\nu \nu f_v \quad (7.44)$$

where A_ν is the absorption constant equal to $A_\nu = 550$

7.4.2.2 Gas spectral database

The gas spectral database NBKM [372, 373] has been implemented in PRISSMA and is used in this work. It replaces the SNB database [374] to cover a larger range of temperature [300-5000K] and pressure [1-8 bars]. Validations of NBKM implementation in PRISSMA are presented in App. B.

7. MODELING OF TURBULENT REACTING FLOWS

Chapter 8

LES in a confined pressurized burner

The objective of this Chapter is to investigate the capability of the methodologies developed in this work to accurately predict soot emissions in a realistic industrial configuration, the pressurized swirled combustor FIRST. This configuration is a benchmark for soot modeling and is a part of International Sooting Flame (ISF) workshop. In this work, the impact of the nucleating species as well as the impact of radiative heat transfer on the numerically predicted soot volume fraction are investigated.

After a description of the configuration and the experimental and numerical setups, the LES results are compared with experiments. The impact of local flow conditions on pollutant formation is further discussed and analyzed. The computational requirements for the proposed methodology as well as for the coupled computations are discussed as well.

Contents

8.1	The FIRST combustor	167
8.2	Numerical set-up	169
8.3	Results	172
8.3.1	Heat transfer analysis	173
8.3.2	Soot production	184
8.4	Computational cost	205
8.5	Conclusion	208

8.1 The FIRST combustor

The experimental configuration studied in this work is installed at DLR and was presented and investigated in numerous recent publications [23, 35, 375, 376, 377, 378, 379]. The burner was designed within the European project FIRST [375] to study soot formation in gas turbine combustors under elevated pressure, with or without secondary air dilution. It features a non-premixed swirled injection system consisting of three concentric nozzles and two radial swirlers as shown in Fig. 8.1. Air at room temperature is supplied to the flame through both the central (diameter 12.3mm) and annular (inner diameter 14.4mm, outer diameter 19.8mm) nozzles. The air flows are fed from

8. LES IN A CONFINED PRESSURIZED BURNER

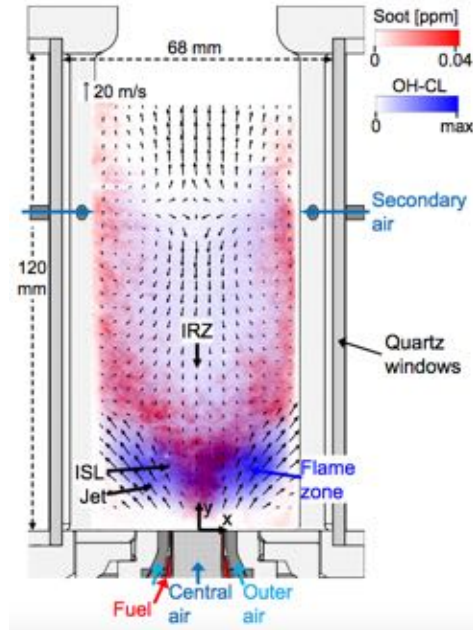


Figure 8.1: FIRST configuration with overlaid measured soot volume fraction (red) and OH chemiluminescence (blue) highlighting the flame (from [23].)

separate plenums and pass radial swirlers consisting of 8 channels for the central nozzle (width 4.2mm , height 5.4mm , swirl number 0.82) and 12 channels for the annular nozzle (width 3.2mm , height 4.5mm , swirl number 0.79). Gaseous fuel (C_2H_4) is injected at 300K between both air flows through 60 straight channels, forming a concentric ring. The fuel injection mimics the behavior of an atomizing lip, as observed in air-blast liquid atomizers [21]. All nozzle exit planes are located at the level of the combustion chamber dump plane. The combustion chamber measures 120mm in height, has a square section of $68 \times 68\text{mm}^2$, and features large optical accesses from all 4 sides. To enhance soot oxidation, additional air ducts (5mm diameter) inject secondary air into the combustor 80mm downstream the combustion chamber inlet.

The chosen operating point is reported in Table 8.1. The burner operates under overall lean conditions ($\phi_{glob} = 0.86$) but the primary combustion zone (PZ) is characterized by an overall rich equivalence ratio ($\phi = 1.2$). The experimental mean flame position and the presence of soot particles are highlighted respectively in blue and red in Fig. 8.1 as well as the recirculation zones, for the selected operating point. Soot particles are formed in Inner Shear Layers (ISL) and are convected along the walls with almost no soot particles in the inner recirculation zone (IRZ).

Available data

Comprehensive data obtained by several laser diagnostics are available for the selected operating point. The flow is characterized with velocity component statistics at sev-

\dot{m}_{air}	$\dot{m}_{air,oxy}$	\dot{m}_f	ϕ_{PZ}
$[kg \cdot s^{-1}]$	$[kg \cdot s^{-1}]$	$[kg \cdot s^{-1}]$	$[-]$
0.82×10^{-3}	4.04×10^{-3}	0.86×10^{-3}	1.2

Table 8.1: Experimental operating conditions at $P = 3$ bars [376].

eral positions downstream of the dump plane, obtained from Stereo-Particle Image Velocimetry (Stereo-PIV). Due to the high level of soot luminosity, two different detection schemes were employed. For flame analysis, temperature measurements at several locations in the combustor were obtained by Coherent Anti-Stokes Raman scattering (CARS), and Laser Induced Fluorescence (LIF) was used to provide a qualitative estimate of the OH radical distribution. Finally, Planar Laser-Induced Incandescence (LII) was used to measure the soot volume fraction. Recently within the European Project SOPRANO¹, additional important quantities have been measured [379]. Phosphor thermometry was used to measure the temperature of window surfaces, to be used as boundary conditions in the numerical simulation. Both inner and outer surface temperature measurements allow the derivation of the wall heat flux. Acetone seeding into C_2H_4 (acetone LIF) has been conducted to access fuel distribution and mixing with air. Acetone LIF enables the identification of prominent flow features like the Precessing Vortex Core (PVC) frequency. Note that the measurement of soot particle size is currently being performed within the SOPRANO project and will be available in the future.

8.2 Numerical set-up

The computational domain is displayed in Fig. 8.2 (a). It includes the channels of both air inlets, the combustion chamber, secondary air ducts and part of the outside atmosphere (not shown). The 60 straight channels for the fuel inlet are modeled by a continuous annular nozzle. The domain is discretized into a fully unstructured mesh using $\sim 40M$ tetrahedral elements, with a cell size of about $0.07mm$ in the very thin ($0.4mm$) fuel injection nozzle and in the primary mixing region. An image of the mesh with focus on the fuel injection zone can be seen in Fig. 8.2 (b). The axial direction is referred to as the z -axis, corresponding to the main flow direction, while the x -axis and y -axis denote the transverse directions.

All simulations are performed with the LES solver AVBP², previously introduced. The numerical set-up is similar to the one described by *Felden et al.* [35]. Inlet and outlet boundary conditions are treated according to the Navier-Stokes Characteristic

¹<http://www.soprano-h2020.eu/>

²<http://www.cerfacs.fr/avbp7x/>

8. LES IN A CONFINED PRESSURIZED BURNER

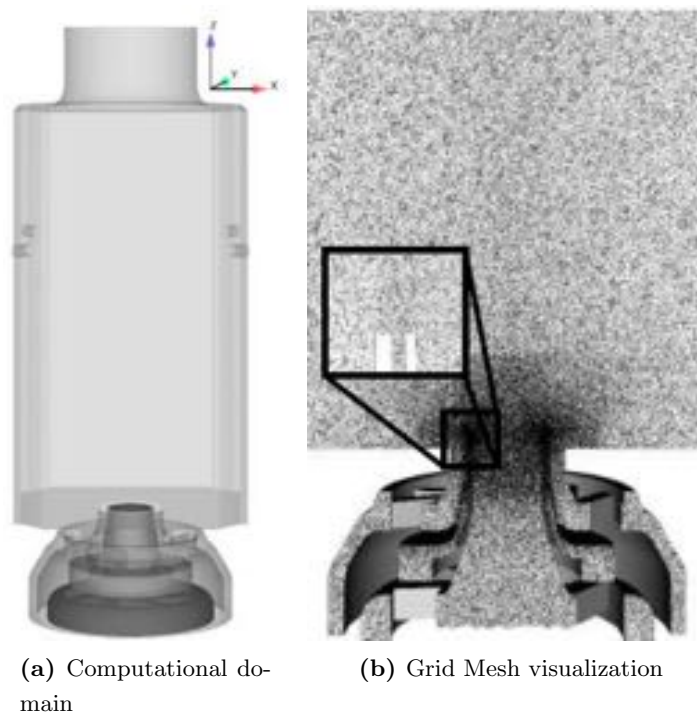


Figure 8.2: Computational domain and mesh of FIRST configuration.

Boundary Conditions formulation [380], and heat losses are applied at walls, using the measured temperature at inner and outer wall surfaces shown in Fig. 8.3. The bottom combustion chamber wall is set to 650 K as observed experimentally. Concerning the quartz windows, outer temperatures have been considered for boundary conditions and to compute the thermal conductivity, which varies strongly with the temperature. As conductivity was not provided by the quartz manufacturer, the polynomial fit recently proposed by *Rodrigues et al.* [381] was used:

$$\frac{k_q(T)}{k^0} = a_0 + a_1 \left(\frac{T}{T_0} \right) + a_2 \left(\frac{T}{T_0} \right)^2 + a_3 \left(\frac{T}{T_0} \right)^3 \quad (8.1)$$

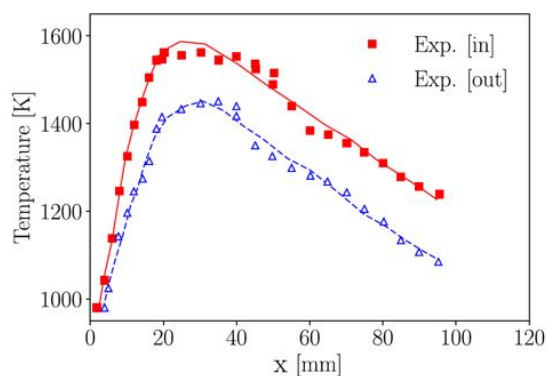


Figure 8.3: Experimental temperature at inner and outer walls (from [379].)

	Wall Heat Losses	Radiative + Wall Heat Losses
C2H4_A2_28_205_14_LG	RUN_HL_A2	RUN_CPL_A2
C2H4_A4_32_233_13_LG	RUN_HL_A4	RUN_CPL_A4

Table 8.2: List and names of performed computations, with the 2 reduced chemistries and with/without thermal radiation.

with $a_0 = 0.97980$, $a_1 = -0.10063$, $a_2 = 0.13677$, $a_3 = -0.011744$, $T_0 = 293K$ and $k^0 = k_q(T_0) = 1.38 \text{ W/m/K}$.

In sooting flames, the evaluation of radiative heat losses is important for two reasons:

- 1 soot particles and their evolution are strongly sensitive to local gaseous temperature;
- 2 soot particles may contribute significantly to the radiative budget and then modify the temperature distribution inside the combustor.

Recently, *Rodrigues et al* [196] have observed that for the considered operating point the soot particle volume fraction is not sufficient to significantly contribute to the radiative budget, which has been observed in the literature for soot volume fraction above $1ppm$. Still in this work, the impact of radiative heat transfer on soot via temperature distribution is investigated. To account for radiative heat transfer the AVBP solver is coupled with PRISSMA radiative solver described in Sec. 7.4, following the same rules as *Rodrigues et al*. [196]:

- Inlets and outlets are considered non-reflecting with a far-field temperature equal to 300K,
- The bottom chamber is considered opaque with an emissivity equal to 0.6,
- The quartz windows are taken at experimental wall temperatures with an emissivity equal to 0.65 representative of quartz at these temperatures.

The coupling procedure is detailed in Appendix C. The coupling frequency is set to $n_{cpl} = 100$, keeping the induced error on the predicted radiative power below 5%, according to *Rodrigues et al*. [351].

Both chemistry based on A2 and A4, respectively C2H4_A2_28_205_14_LG and C2H4_A4_32_233_13_LG have been considered to investigate the impact of soot precursors and nuclei size on the predicted soot volume fraction. All the computations performed are summarized in Tab. 8.2.

The numerical set up has been already validated in the work of *Felden et al*. [35] for both non-reactive and reactive cases and is summarized in Appendix D. Here the focus is put on soot and PAH prediction, and its sensitivity to heat transfer.

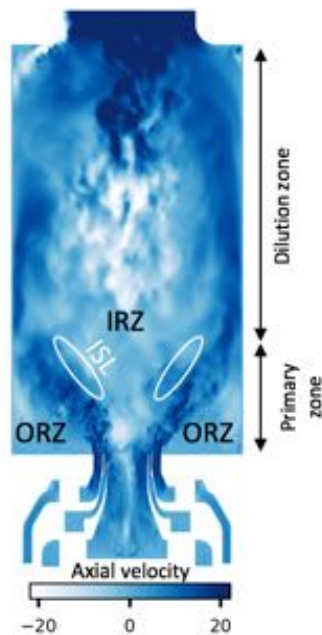


Figure 8.4: FIRST configuration: Instantaneous axial velocity field for case RUN_HL_A4 and flow features.

8.3 Results

The analysis is made in two parts:

- **Heat transfer analysis:** The validation of the proposed boundary conditions (heat losses) compared to measurements as well as the impact of radiative heat losses on the predicted flame and temperature distribution are presented. As the gaseous chemistry is not expected to impact the conclusions, only the A4 computations (RUN_HL_A4 and RUN_CPL_A4) are analysed.
- **Pollutant prediction:** The analysis of soot and PAH predictions are performed for all the cases. Comparison to experiment and analysis of the mechanisms driving the formation and oxidation of both soot and PAH are presented.

First, the instantaneous field of axial velocity for case RUN_HL_A4 is displayed in Fig. 8.4 to highlight flow structures of swirled stabilized burners where a large IRZ is located in the center of the combustion chamber, induced by the radial expansion of the swirled jets, and two outer recirculation zones (ORZ) are observed in the outer part of the swirled jets. The inner shear layer (ISL) corresponds to the boundary between the flame and the IRZ. The combustion chamber is divided in two zones: the primary combustion zone and dilution zone, clearly annotated.

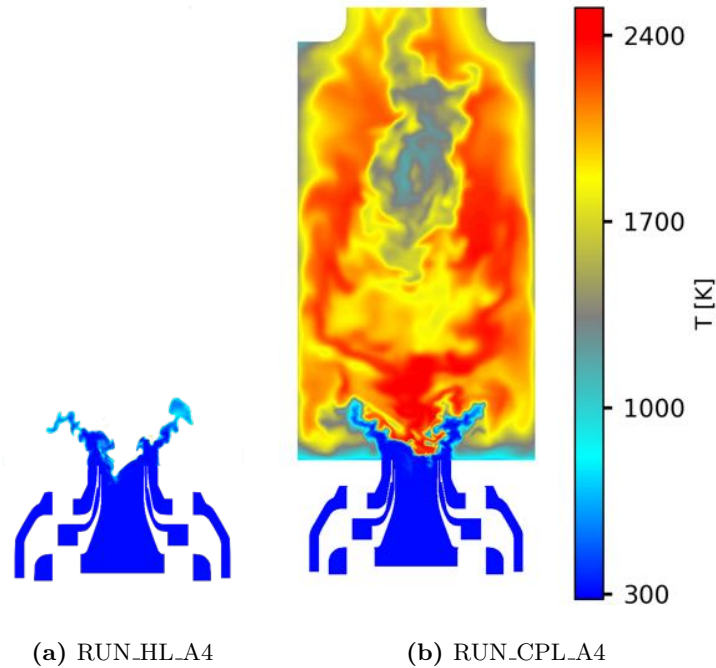


Figure 8.5: FIRST configuration: numerical instantaneous temperature profiles for cases RUN_HL_A4 (a) and RUN_CPL_A4 (b).

8.3.1 Heat transfer analysis

8.3.1.1 Temperature fields

Predicted instantaneous temperature fields for both cases are compared in Fig. 8.5. The main flow structures are characteristic of swirled stabilized burners where a large inner recirculation zone (IRZ) is located in the center of the combustion chamber, induced by the radial expansion of the swirled jets, and corner recirculation zones are observed in the outer part of the swirled jets. The secondary air injector at $h = 80\text{mm}$ promotes the mixing between the cold air injected and the hot burnt gases from combustion and leads to a lower temperature in the IRZ. The addition of radiative heat losses impacts mainly the primary zone, located in the first part of the combustor with increased heat losses, the flame stabilization point moves slightly upstream, as also observed that the flame stabilizes in the chamber when radiation is accounted for, as observed by *Rodrigues* [196]. The opening angle of the flame increases and the temperature at the bottom of the combustion chamber decreases.

These observations are confirmed with the mean temperature fields shown in Fig. 8.6, which clearly show that:

- the flame stabilizes higher in the combustion chamber,
- the temperature in the IRZ is lower,

8. LES IN A CONFINED PRESSURIZED BURNER

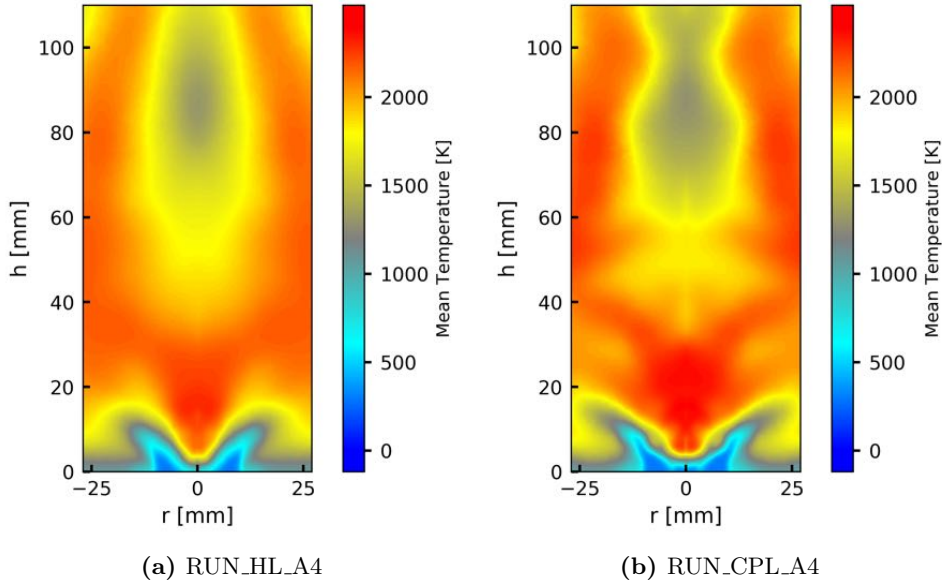


Figure 8.6: FIRST configuration: numerical mean temperature profiles for cases RUN_HL_A4 (a) and RUN_CPL_A4 (b).

- the opening angle of the flame is larger,
- the temperature is higher in the convective zone localized between the walls and the IRZ,
- the temperature of the ORZ is higher.

For a quantitative assessment of the numerical results, the predicted axial and radial temperature profiles are compared to measurements in Fig. 8.7. First a very good agreement is obtained for the axial profile with or without thermal radiation, with numerical results lying inside the experimental uncertainty (5%), except very close to the injector for the case without radiation. Overall, the case RUN_HL_A4 is slightly better. In the zone very close to the injector ($h = 3\text{mm}$) thermal radiation plays an important role and case RUN_CPL_A4 performs better, it enables to capture the good flame location. Although, radiation enables to retrieve the good location of the flame, the temperature of the flame is then over-estimated downstream the flame. However, it can be noted that all the predicted points are in the experimental width except for points close to the injector ($h = 1$ and 3mm) for the case RUN_HL_A4 .

The agreement is good on radial profiles but not as excellent as for axial profiles. Although the profile shape is well retrieved, both cases fail to predict the correct flame temperature at $h = 12\text{mm}$ and 18mm for a radial distance between 5 and 15mm, and results are worse for case RUN_CPL_A4 , which was not expected. This may be problematic since these zones correspond to nucleation zones where soot tends to grow

rapidly due to high levels of C_2H_2 and PAHs. Unfortunately these mechanisms are very sensitive to the gaseous temperature and then discrepancies must be kept in mind in the analysis of soot.

A better agreement is observed in the dilution zone, especially at $h = 45mm$ for which case RUN_CPL_A4 performs slightly better than case RUN_HL_A4 . However at other locations, it is interesting to observe that RUN_HL_A4 always presents a better agreement.

To go further, numerical and experimental probability density functions (PDF) of temperature are analysed. PDFs of temperature are plotted along the z-axis in Fig. 8.8. Consistently with the axial profiles of Fig. 8.7, a good agreement is observed for both numerical cases. At $h = 3mm$, it is notable that measurements never find burnt, hot gases contrary to numerical predicted temperature. The recurrent presence of fresh gas is captured only when considering radiative heat transfer.

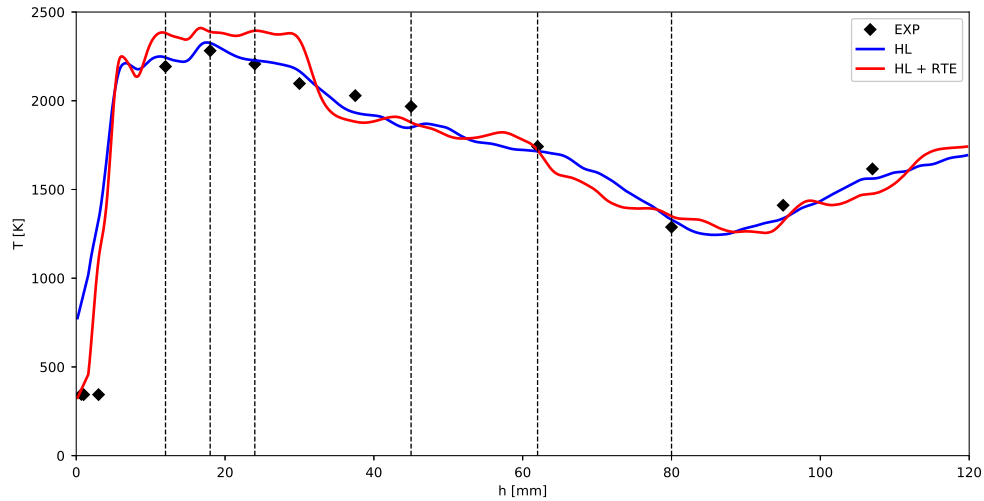
Figure 8.9 presents the PDF of temperature for different radial distances and heights. As observed from Fig. 8.7, discrepancies between simulation and experiment are visible. At the bottom of the combustion chamber, the numerical PDFs match the experimental one especially for case RUN_HL_A4 (Fig. 8.9(a)). However, both cases fail to predict the correct temperature at low height near the wall as suggested by Fig. 8.9(b) with a significant under-estimation about 400K. Figure 8.9(c) shows the PDF of temperature further downstream at $h = 18mm$ and $r = 8mm$, i.e., above the flame. At this location, RUN_CPL_A4 shows a better agreement with measurements compared to RUN_HL_A4 , which overestimates the temperature. Further in the radial direction, the measured PDF of temperature is very spread over the whole range of temperature (Fig. 8.9(d)). This shape is correctly captured by RUN_HL_A4 while the temperature is now overestimated in RUN_CPL_A4 . Finally the agreement with measured PDF of temperature improves with the downstream distance for both cases (Figs. 8.9(e),(f) and (g)). It can be noted that at $h = 44mm$, the PDF at $r = 8mm$ is better predicted in RUN_HL_A4 while at $r = 20mm$, RUN_CPL_A4 gives a better agreement. These varying performances of both models make it difficult to conclude about the best one.

Fully coupled simulations, including thermal conduction in walls, would be helpful to understand this thermal behavior.

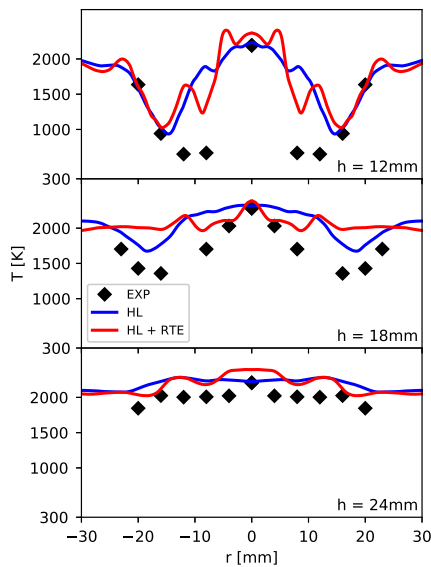
Focusing on radiative heat transfer, the mean radiative power P^R and the relative difference ΔT are shown in Fig. 8.10. ΔT is expressed in % and computed as:

$$\Delta T = \left| \frac{T_{CPL} - T_{HL}}{T_{CPL}} \right| \cdot 100 \quad (8.2)$$

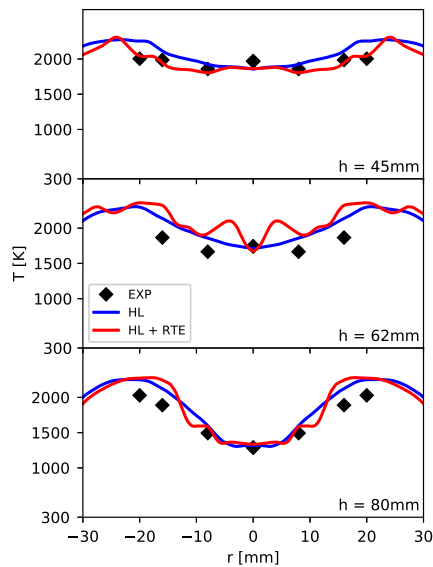
8. LES IN A CONFINED PRESSURIZED BURNER



(a) Axial Mean Temperature



(b) Radial Mean Temperature in the Primary Zone



(c) Radial Mean Temperature in the Dilution Zone

Figure 8.7: FIRST configuration: Axial (a) and radial (b and c) experimental and numerical temperature profiles. Simulations with (red lines) and without (blue lines) thermal radiation.

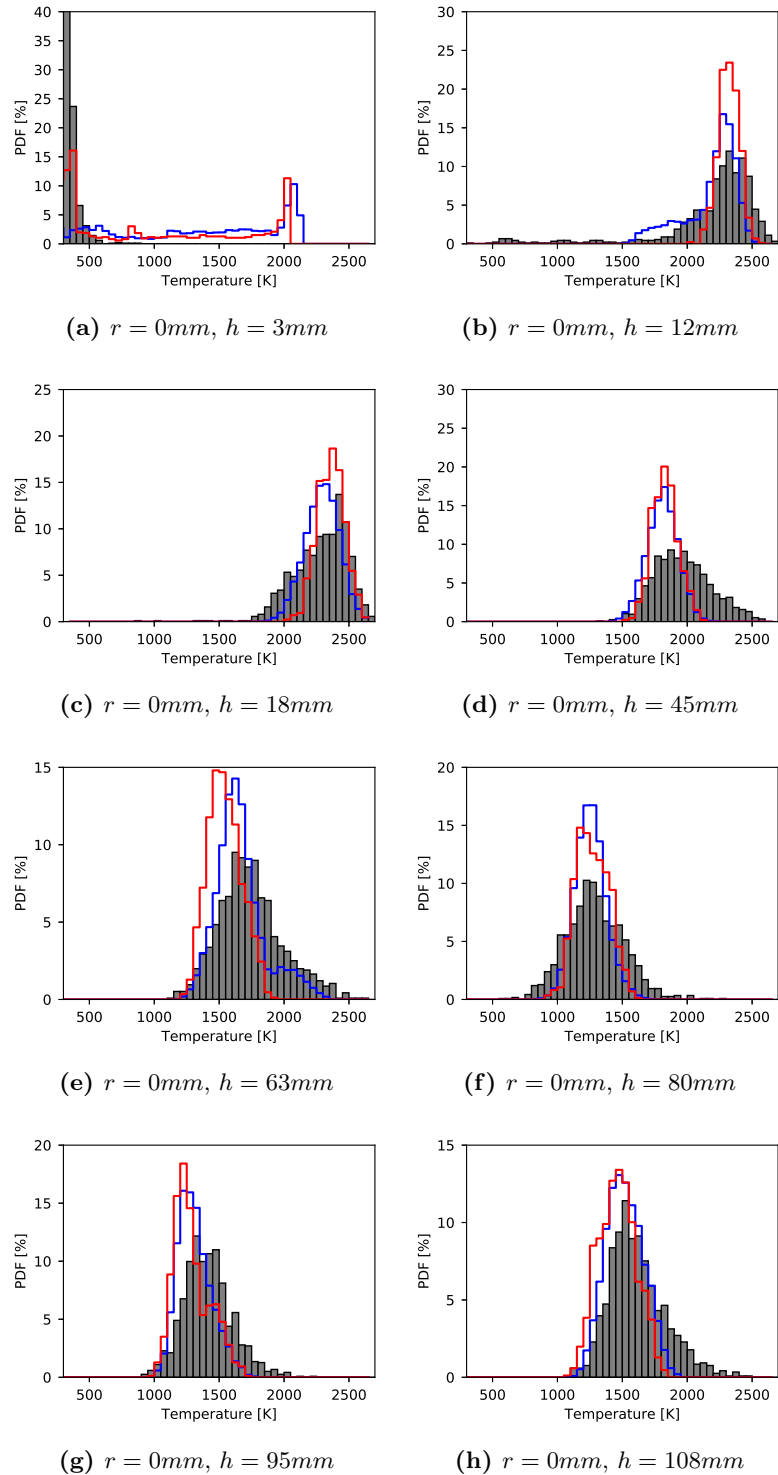


Figure 8.8: FIRST configuration: Probability Density Functions of temperature at various locations along the z-axis. Comparison between simulation with (red lines) and without (blue lines) thermal radiation, and CARS measurements (grey).

8. LES IN A CONFINED PRESSURIZED BURNER

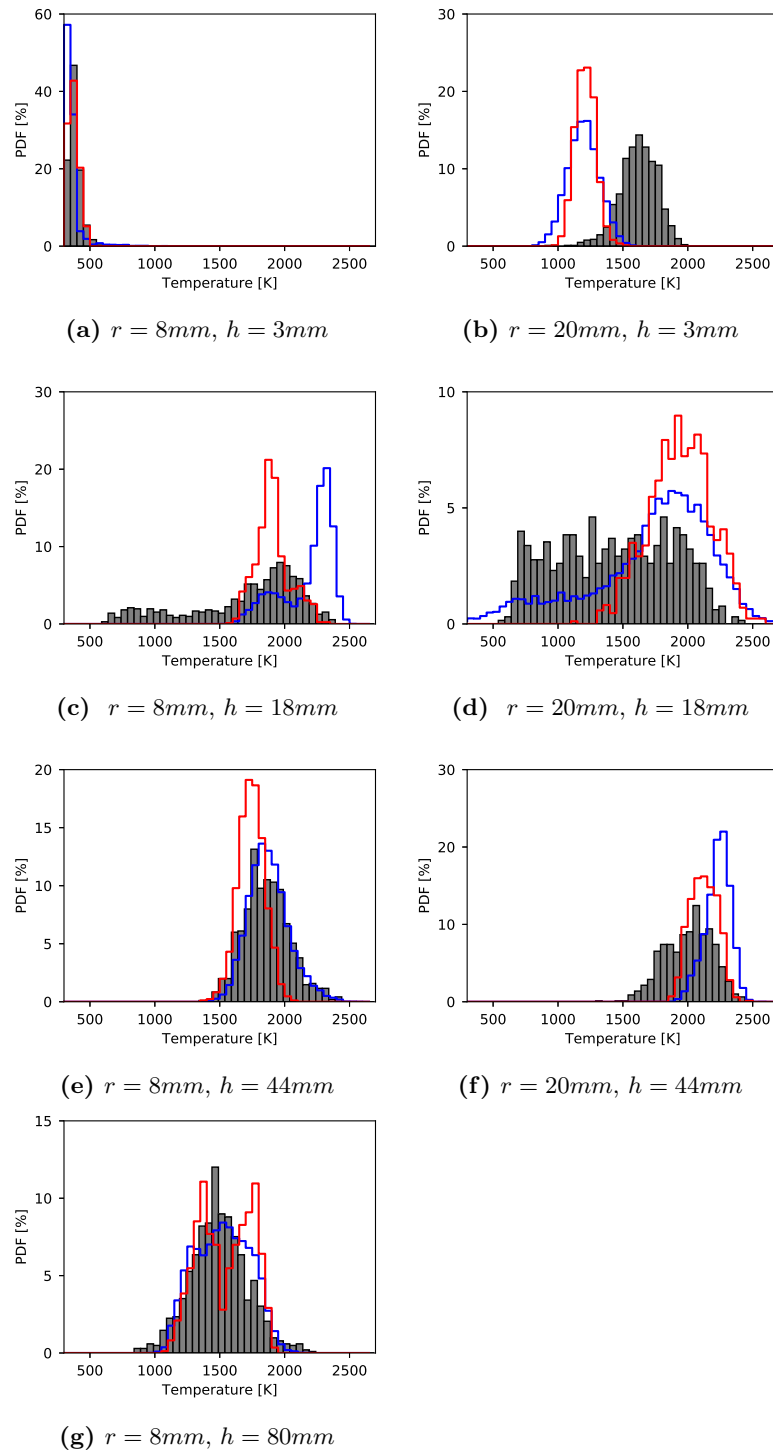


Figure 8.9: FIRST configuration: Probability Density Functions of temperature at various locations along the radial axis. Comparison between simulation with (red lines) and without (blue lines) thermal radiation, and CARS measurements (grey).

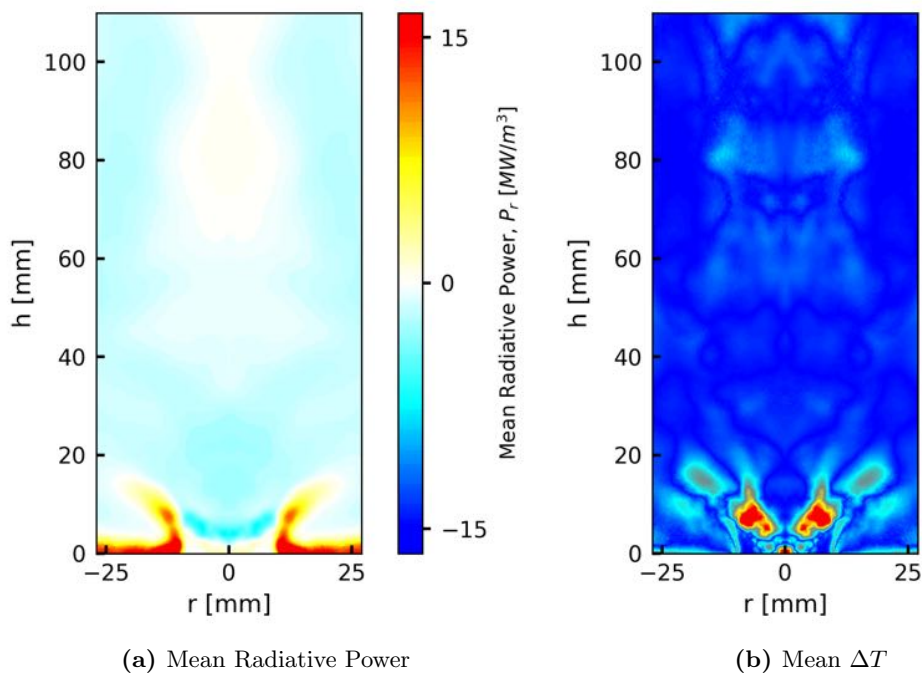


Figure 8.10: FIRST configuration: Mean Radiative Power (a) and ΔT (b) between cases with and without radiation (b).

The maximum radiative power is localized in the flame and in the bottom of the combustion chamber, where temperature differences are higher. Positive values of radiative power correspond to a decrease of gaseous temperature, and inversely. Then a gain of temperature is expected in the IRZ close to the flame due to the strong emission by hot gas in the flame. Radiative transfer concentrates in the primary zone while the dilution zone almost does not see any radiation. The radiative power obtained in this work, between 15 and -8 MW/m^3 is higher than in the works of *Rodrigues* [196], who found between 3 and -8 MW/m^3 , and *Dellinger* [382], who found between 5 and -5 MW/m^3 . The difference is localized in the flame zone while the radiative power is similar in the burnt gases downstream the flame. Figure 8.10(b) highlights the impact of radiation on the temperature field, with significant changes in the primary zone due to the different flame location between the two numerical cases. This re-distribution of temperature may impact significantly the formation of soot precursors which occurs in these regions and is much sensitive to the gaseous temperature.

8.3.1.2 Flame analysis

Figure 8.11 presents a comparison between OH-chemiluminescence and numerically predicted heat release rate for the two simulations RUN_HL_A4 and RUN_CPL_A4. Both cases capture the correct location of the maximum chemical activity, RUN_HL_A4

8. LES IN A CONFINED PRESSURIZED BURNER

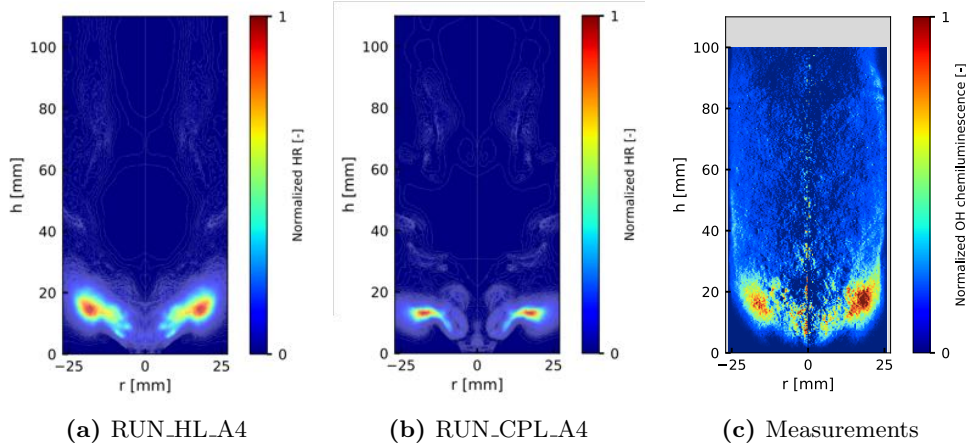


Figure 8.11: FIRST configuration: measured OH chemiluminescence versus numerical normalized Heat Release Rate for cases RUN_HL_A4 (a) and RUN_CPL_A4 (b).

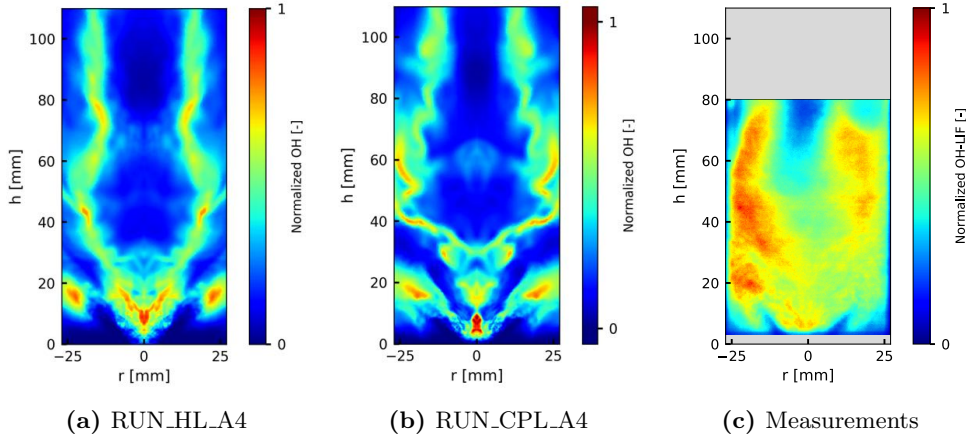


Figure 8.12: FIRST configuration: measured OH-LIF versus numerical normalized OH mass fraction field for cases RUN_HL_A4 (a) and RUN_CPL_A4 (b).

is in a very good agreement with measurements. The numerically predicted heat release is much thinner in RUN_CPL_A4 and has a different shape compared to experiment.

The comparison of OH radical shown in Fig. 8.12 leads to the same conclusion. The overall distribution is correct in both cases, but the agreement is better in RUN_HL_A4. Interestingly, a very good agreement is observed for RUN_CPL_A4 in the primary zone while the shape differs significantly downstream, with a larger central zone of free OH for $40\text{mm} < h < 80\text{mm}$.

Combustion regime The Takeno index, based on fuel as defined in Eq. 7.9 and conditioned on the fuel source term is shown in Fig. 8.13. In both cases a premixed flame front is obtained, as in previous numerical simulations [35, 196, 382]. This result highlights the role of the interactions between the inner shear layer and the precessing

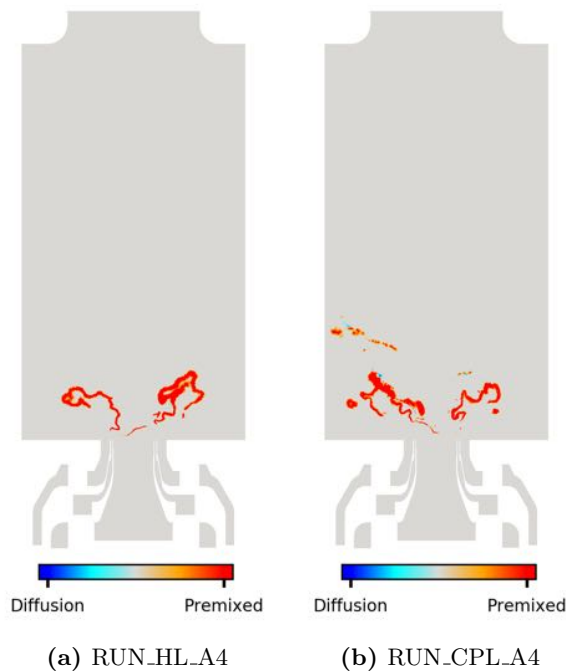


Figure 8.13: FIRST configuration: Takeno Index based on the fuel C_2H_4 .

vortex core (PVC) enabling a complete premixing of the fuel jet with incoming air [35].

However, heat release is not solely related to fuel combustion [35, 220, 383], and part of the flame fronts correspond to CO oxidation. Then a second Takeno index based on CO may be built, as shown in Fig. 8.14. It reveals diffusion flame structures, similar for both simulation cases, and corresponding to reaction fronts between unburnt products from the primary rich premixed flame with surrounding air.

The regime identification by the Takeno index, either based on C_2H_4 or CO, is confirmed by an inspection of the scatterplots of temperature as a function of the mixture fraction z and colored by the Takeno index. Both primary and dilution zones are investigated separately in Figs. 8.15 and 8.16 respectively. As expected from the previous analysis, both cases present very similar scatterplots. In the primary zone, several regimes co-exist:

- mixing between pure air and fuel,
- rich-premixed combustion, in accordance with the rich operating point in this zone ($\phi = 1.2$),
- non-premixed combustion between vitiated air and burnt products of the rich flame,
- lean-premixed combustion, also burning rich products with dilution air.

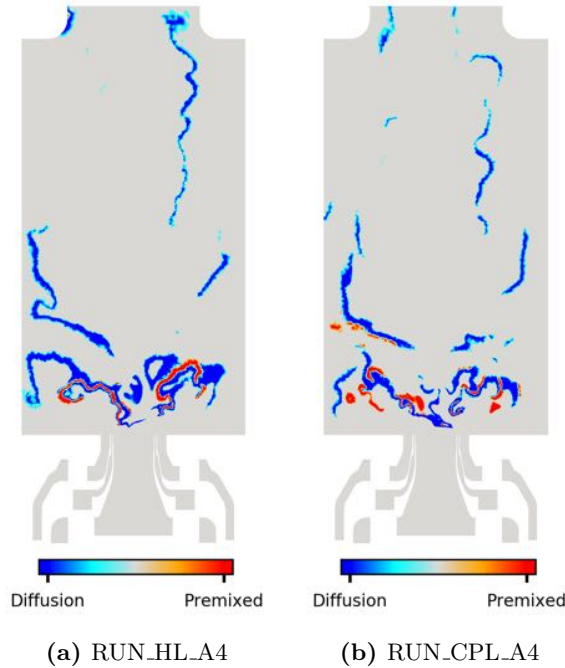


Figure 8.14: FIRST configuration: Takeno Index computed based on CO.

The last two regimes are due the oxidation of rich burnt gases produced by the rich-premixed flame, with air coming from the dilution zone through the IRZ as shown in Fig. 8.14. Despite strong similarities between both cases, RUN_CPL_A4 exhibits a small shift towards leaner mixtures, with slightly less rich-premixed combustion and more rich non-reacting mixing regions due to the higher flame stabilization location. In the dilution zone, scatterplots of Fig. 8.16 diffusion like regime and lean/stoichiometric premixed combustion co-exist. The same shift towards lean mixture and then a leaner combustion regime is observed for RUN_CPL_A4 .

8.3.1.3 Evaluation of the generic sensor for the TP-TFLES

The generic sensor introduced in Sec. 7.3.2.3 is considered for all simulations. As discussed in Sec. 7.3.2.3, the thickened flame model is applied only for the premixed regime, detected through the Takeno index. Instantaneous fields of Takeno index, heat release rate and thickening factor are displayed in Fig. 8.17. It can be observed that the heat release is correctly detected and thickened except in diffusion regions. The thickening factor F is small and enables to keep 6 points in the flame thickness. The flame has the same shape and structure than with the classical relaxation sensor.

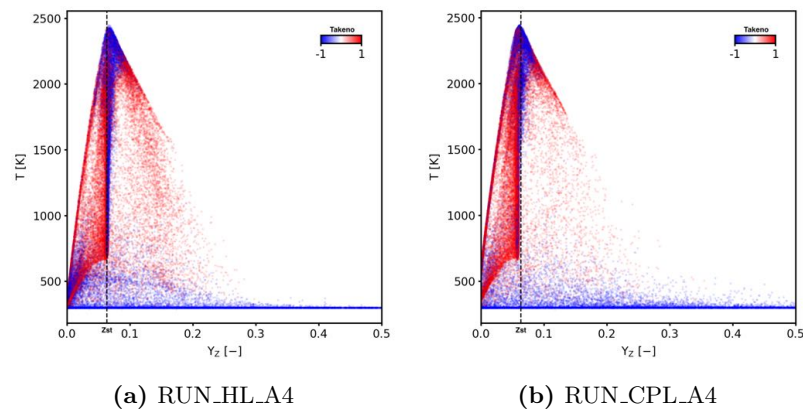


Figure 8.15: FIRST configuration: Scatterplots of temperature as a function of mixture fraction colored by the Takeno Index in the primary zone for cases RUN_HL_A4 (a) and RUN_CPL_A4 (b).

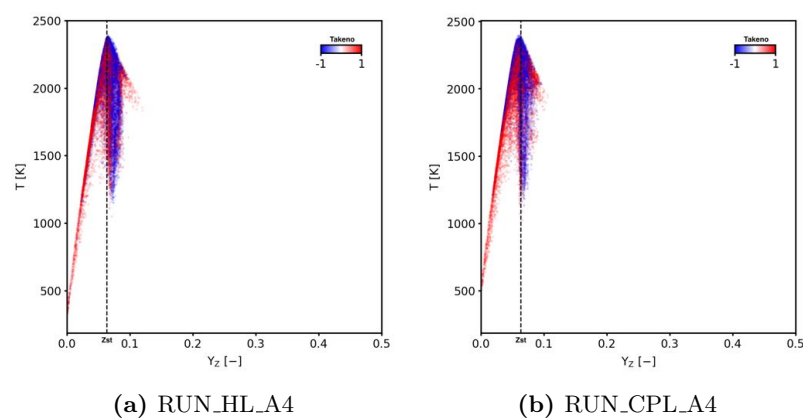


Figure 8.16: FIRST configuration: Scatterplots of temperature as a function of mixture fraction colored by the Takeno Index in the dilution zone for cases RUN_HL_A4 (a) and RUN_CPL_A4 (b).

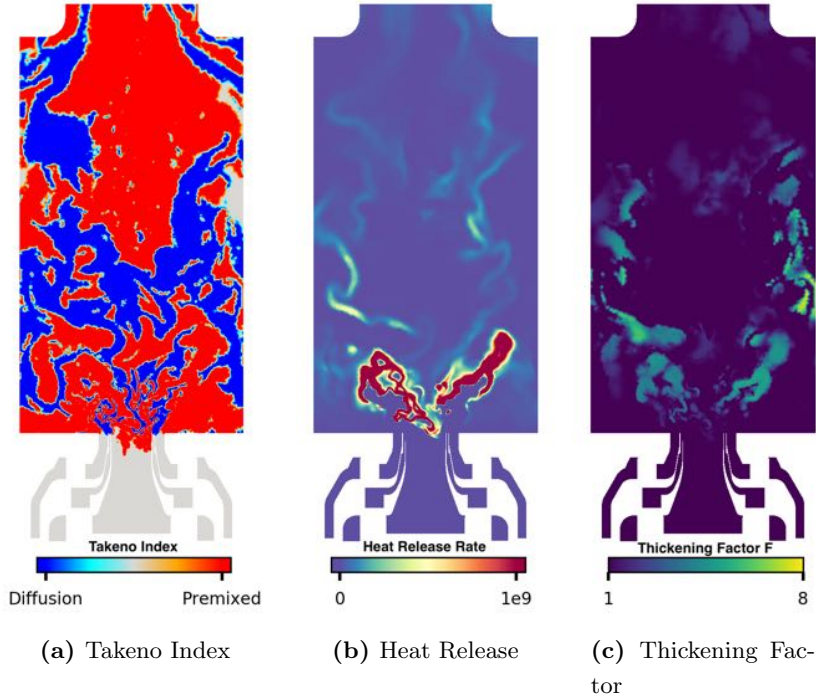


Figure 8.17: FIRST configuration: Takeno index (a), Heat Release rate (b) and thickening factor (c) for case RUN_HL_A4 .

8.3.2 Soot production

This subsection compares the fields of soot precursors and soot volume fraction for all computations defined in Tab. 8.2, and with measurements.

8.3.2.1 Soot precursors

As discussed in Chap. 2, C_2H_2 is a key species in the evolution of PAH and soot via the HACA mechanism. Figure 8.18 shows the obtained C_2H_2 in the 4 cases of Tab. 8.2. The shape of C_2H_2 is similar for cases RUN_HL_A2 and RUN_HL_A4 but a higher concentration is observed for RUN_HL_A4 . C_2H_2 is localized close downstream the flame along the inner shear layer (ISL) before reaching the walls. The presence of C_2H_2 can also be noticed below the ORZ, while recirculation zones are free of C_2H_2 . The level of C_2H_2 is approximatively two times higher with thermal radiation, and the field of C_2H_2 is separated in two zones. Neither C_2H_2 is observed below the ORZ nor along the walls when accounting for radiative heat losses.

Similar shapes, although finer, are observed for naphthalene (A2) in Fig. 8.19. Contrary to C_2H_2 , A2 is absent below the ORZ and along the walls. The level of A2 is higher for RUN_HL_A4 than RUN_HL_A2 , and about two times higher for RUN_CPL_A2 and RUN_CPL_A4 , as was already observed for C_2H_2 . In RUN_HL_A2 and RUN_CPL_A2 , A2 is the nucleating species, so that a lower concentration is indeed

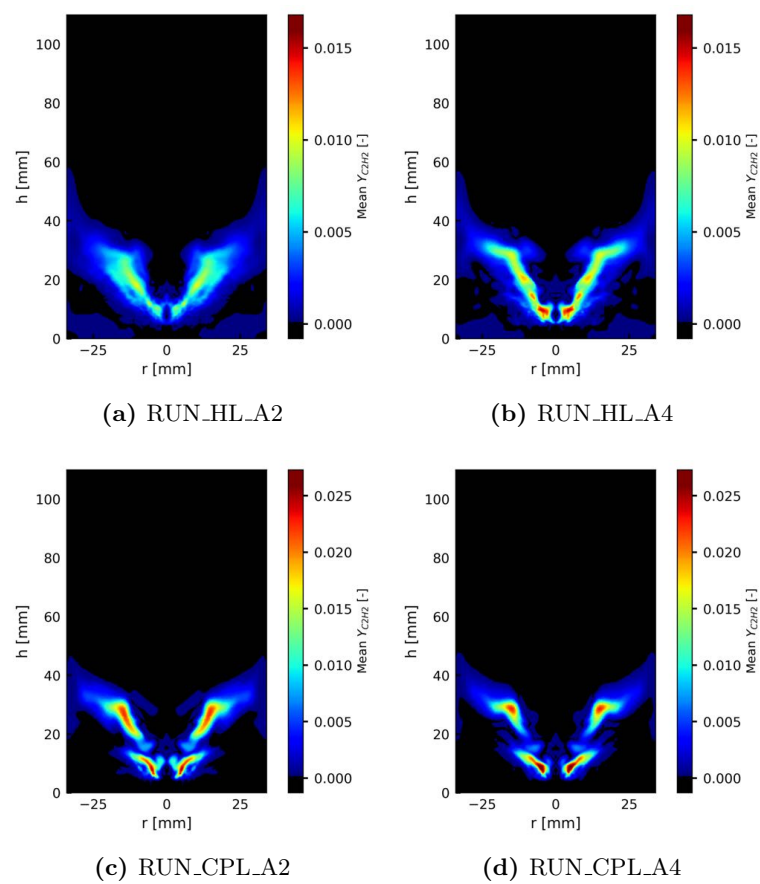


Figure 8.18: FIRST configuration: Numerically predicted C_2H_2 mass fraction for the 4 simulations.

8. LES IN A CONFINED PRESSURIZED BURNER

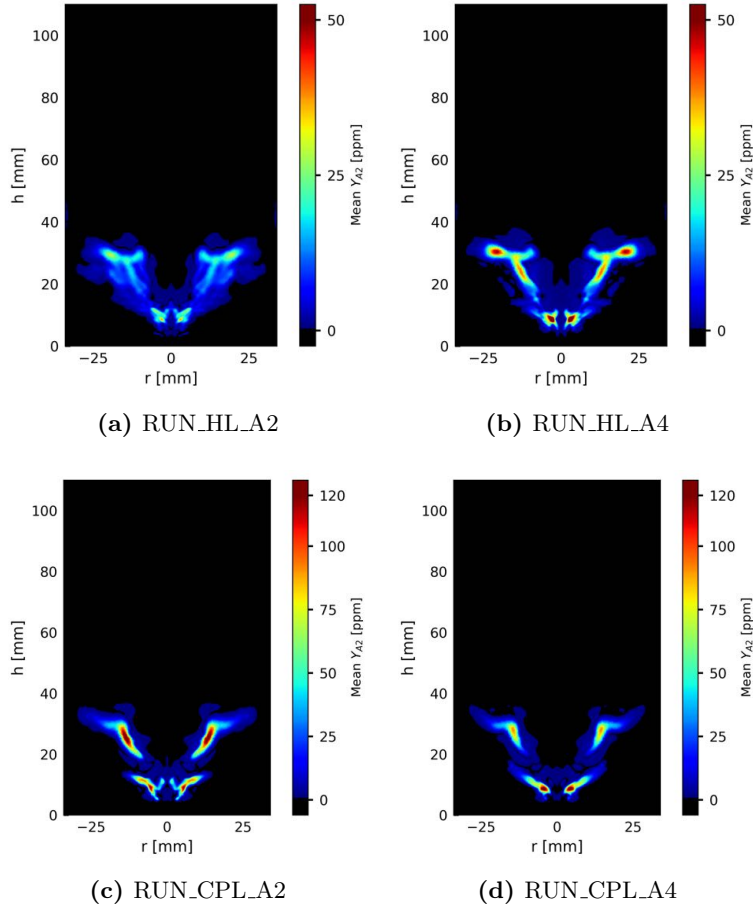


Figure 8.19: FIRST configuration: Numerically predicted A2 mass fraction for the 4 simulations.

expected compared to chemistry with $A4$. In all computations, small pockets of high $A2$ concentrations are observed which is also observed experimentally. Further analysis of PAH dynamics are required to understand these pockets, especially when accounting for radiative heat transfer.

Both RUN_HL_A4 and RUN_CPL_A4 give access to a larger PAH, pyrene ($A4$). The numerically predicted $A4$ is shown in Fig. 8.20. While $A2$ shape is highly correlated to C_2H_2 , here the correlation is less clear. As observed previously, $A4$ concentration is higher when accounting for radiative heat losses but the increase is restricted to small pockets. In case RUN_CPL_A4, something seems to prevent from any $A4$ close to the walls. In both computations a peak of $A4$ appears close to the injection system. Interestingly, looking at Figs 8.18, 8.19 and 8.20 shows that similar peak locations are found for all "soot precursors", especially when using the reduced chemistry C2H4.A4.32.233.13.LG.

Geigle et al. have measured PAH by Laser Induced Fluorescence (PAH-LIF) [377], which is reported in Fig. 8.21. The red isocontour corresponds to a soot volume fraction

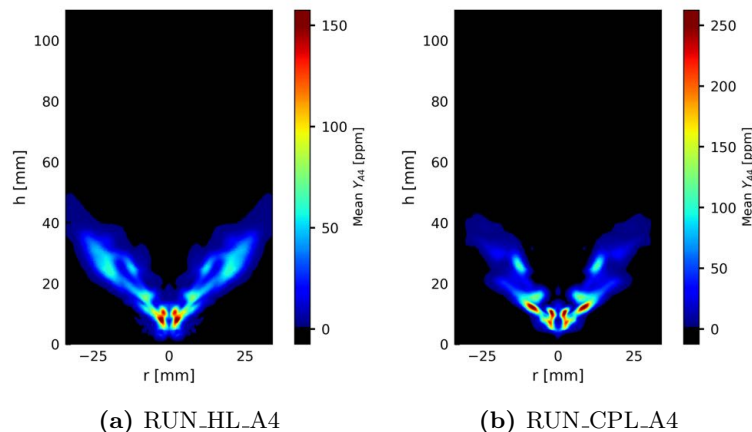


Figure 8.20: FIRST configuration: Numerically predicted A4 mass fraction for the cases RUN_HL_A4 and RUN_CPL_A4 .

f_v of 0.1 *ppb* measured by Laser Induced Incandescence(LII), highlighting the zones of presence of soot particles. As explained by *Geigle et al*, PAH-LIF is able to measure a wide range of aromatics from large PAH to small nascent soot particles ($d_p < 2 \text{ nm}$), especially the size range of A2-A4. PAH-LIF reveals the presence of PAH in the ISL and in the ORZ: soot particles are assumed to form in these regions and to be then convected, while growing through different processes (see Chap. 2) until being detected by LII.

The qualitative comparison between measured PAH and predicted soot precursors leads to the following observations:

- Measured PAH are localized in the ISL, similarly to soot precursors in all computations correctly appearing in the ISL between 5 and 40 mm .
- PAH are measured in the ORZ, while in this region none of the soot precursors from any computation has been observed in the ORZ, even small concentrations.
- PAH and soot are present close to the injector ($r = 0mm$, $h \sim 5mm$) in the experiment. As mentioned previously, a peak of soot precursors is observed close to the injector for all computations, especially when dealing with C2H4_A4_32_233_13_LG chemistry. It seems to correspond to a pocket of nucleation.
- The IRZ and walls beyond $h \sim 40mm$ are free of PAH in both experiment and simulations. Numerical average of PAH indicates no PAH in the IRZ nor further downstream the flame. This means that nucleation does not occur in these regions, so that the presence of soot particles there is due to convection from other zones where they are formed.

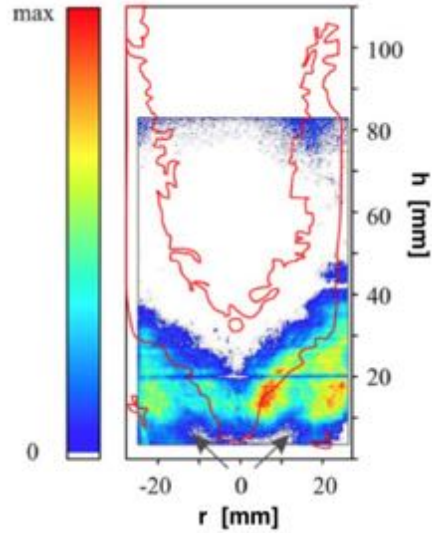


Figure 8.21: FIRST configuration: Average distribution of PAH measured by Laser Induced Fluorescence (LIF) and overlaid by red distribution isocontour ($f_v > 0.1$ ppb, red line), extracted from [377].

8.3.2.2 Soot particles

Figure [8.22] presents the measured soot volume fraction f_v by LII [376] compared to numerically predicted soot volume fraction for all computations. It has to be reminded that the diameter of nascent soot particles formed from A4 and A2 are smaller than $2nm$ and about $1.24nm$. With such small size, these nascent soot particles are not detected by the LII. A correct order of magnitude is found in all computations, especially for case RUN_HL_A4 .

The distribution of soot is highly correlated to the chosen nucleating species (A2 or A4). For RUN_HL_A2 and RUN_HL_A4 , soot particles are convected further downstream the flame as well as in the ORZ as observed experimentally but in very limited quantities. When accounting for radiative heat transfer, no soot particles are observed in the ORZ nor in the dilution zone and the soot distribution remains close to the nucleating species profile. However, the numerically predicted f_v is higher due to larger particles than in RUN_HL_A2 and RUN_HL_A4 .

A snapshot of soot particles with the flame highlighted by an isocontour of heat release rate colored by temperature is shown in Fig. [8.23] for case RUN_HL_A4 confirming the presence of soot particles in the dilution zone and the ORZ (red circle).

The quantitative comparison between numerically predicted f_v from RUN_HL_A4 , for which the best agreement is observed, with the measurements is shown in Fig. [8.24]. It confirms previous statements:

- A good order of magnitude ($f_{Vmax}^{num.} \sim 40ppm$) compared to experimental level of soot ($f_{Vmax}^{exp.} \sim 36ppm$) is found.

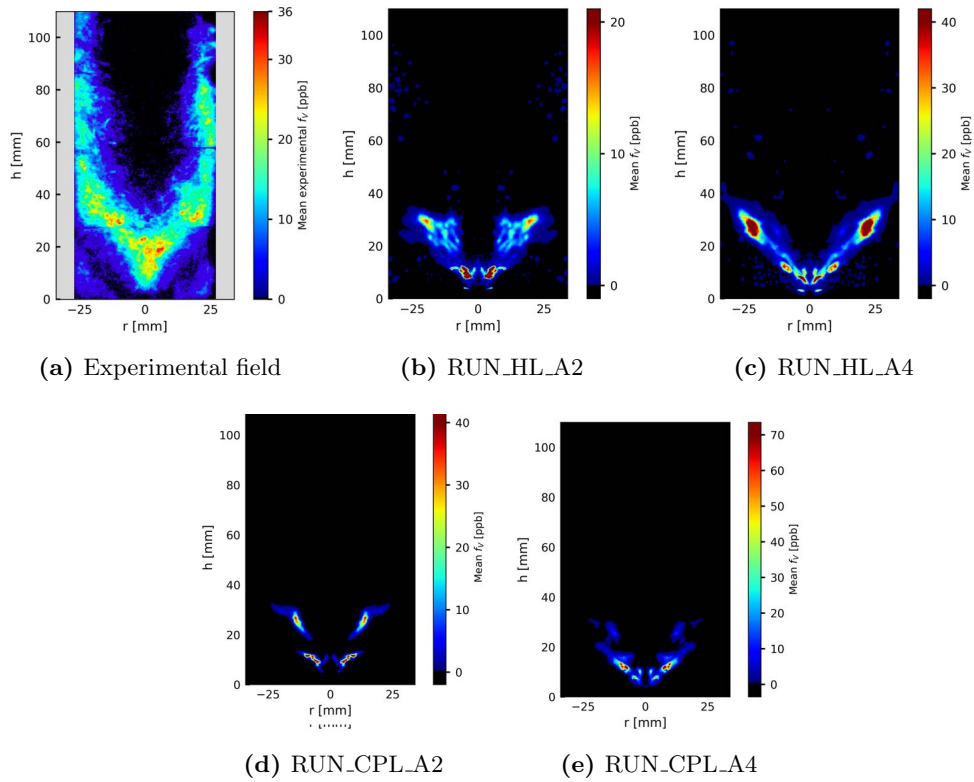


Figure 8.22: FIRST configuration: Numerically predicted soot volume fraction for all computations and comparison with measurements.

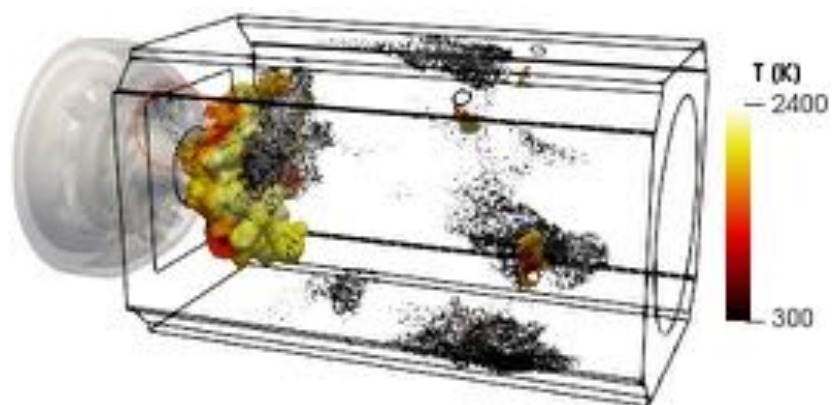


Figure 8.23: FIRST configuration: Instantaneous view of soot particles with an isovolume of heat release rate colored by the gaseous temperature for the case RUN_HLA4 . Red circle highlights soot presence in the ORZ.

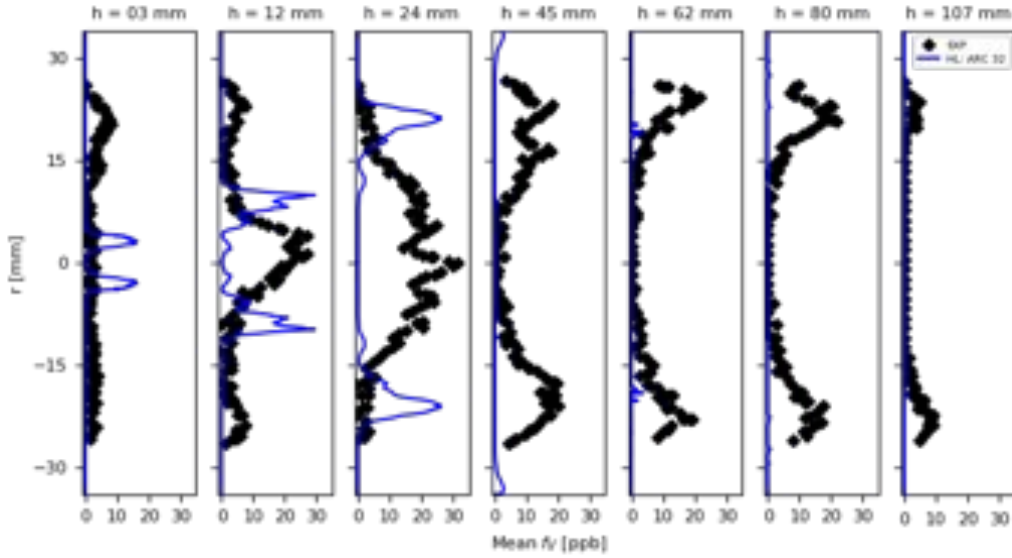


Figure 8.24: FIRST configuration: Radial mean f_v (blue line) compared with measurements (symbols) for the case RUN_HL_A4 : radial profiles at various heights.

- A significant shift towards the injector is observed for the numerically predicted f_v .
- RUN_HL_A4 fails to predict significant f_v in the ORZ ($r \sim 20mm$, $h = 03mm$), along the axial direction ($r = 0mm$) and in the dilution zone ($h > 45mm$).

The use of larger PAH tends to enhance soot production, in particular in this configuration and the considered operating point where nucleation and oxidation drive the soot volume fraction. As discussed in Chap. 2, reliable soot precursors should be even larger than A4. Recently, a sectional PAH model [143] was applied to this configuration, where large lumped PAHs allowed to obtain a very good agreement with measurements [23, 382]. Previous work also described that the spatial location of precursors is size dependent: large PAH tends to form further beyond the flame in the axial direction [196, 382].

8.3.2.3 Analysis of soot production mechanisms

Soot precursors

Figure 8.25 presents a sequence of both mixture fraction and C_2H_2 mass fraction with overlaid streamlines. The frequency of the PVC is found to be about $500Hz$, as observed in the literature for this operating point [378] and shown in Fig. 8.26. The PVC promotes mixing, and influences soot formation as well [384] via the formation of rich burnt gas pockets in a intermittent way. C_2H_2 is well correlated to the PVC although no significant soot is found in this region. It is also found that A2 is also correlated to

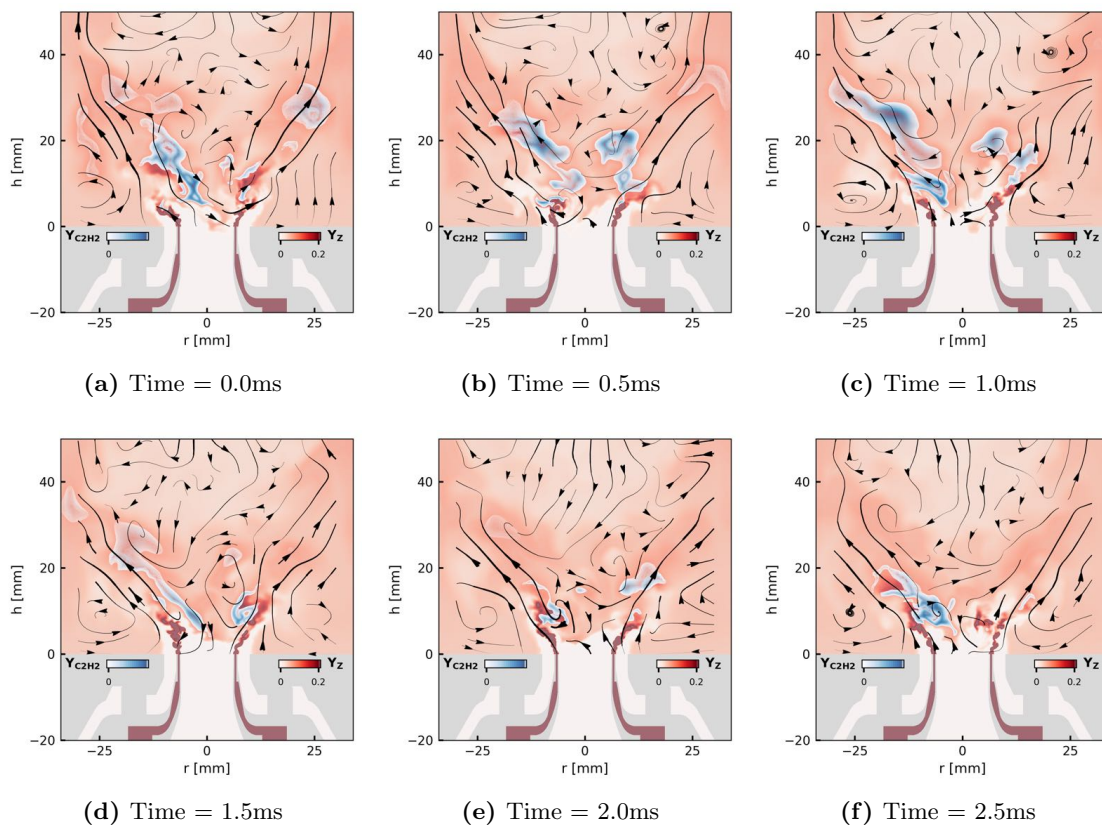


Figure 8.25: FIRST configuration: Sequence of mixture fraction Z with overlaid blue C_2H_2 mass fraction, flow field velocity is represented by arrowed streamlines with a width proportional to the local velocity intensity for the case RUN_HL_A4 .

the PVC, while A_4 is not (not present in this region).

Figure 8.25 also highlights the formation of C_2H_2 in rich burnt gases localized in the ISL. It can be observed that pockets of rich burnt gas are convected downstream the flame ($t = 0.0ms$), and that a significant part of these pockets are brought back upstream by the IRZ in already rich burnt gases promoting the formation of large and rich C_2H_2 pockets ($t = 0.5 - 1.0ms$). Note that the presence of C_2H_2 in the primary zone is observed all along the sequence.

In Fig. 8.27, the same sequence focuses on A_2 with the temperature field replacing the mixture fraction field. Despite similar average field shape, a strong intermittency is observed compared to C_2H_2 . As mentioned before, A_2 is highly correlated to C_2H_2 for the considered chemical scheme, which is clearly visible here.

As observed for Figs. 8.25 & 8.27, the presence of rich burnt gases is necessary but not sufficient to observe the formation of C_2H_2 or A_2 . Interestingly, the high temperature regions in the primary zone are free of soot precursors. These regions correspond to the diffusion flame front observed in Fig. 8.14 induced by CO oxidation.

8. LES IN A CONFINED PRESSURIZED BURNER

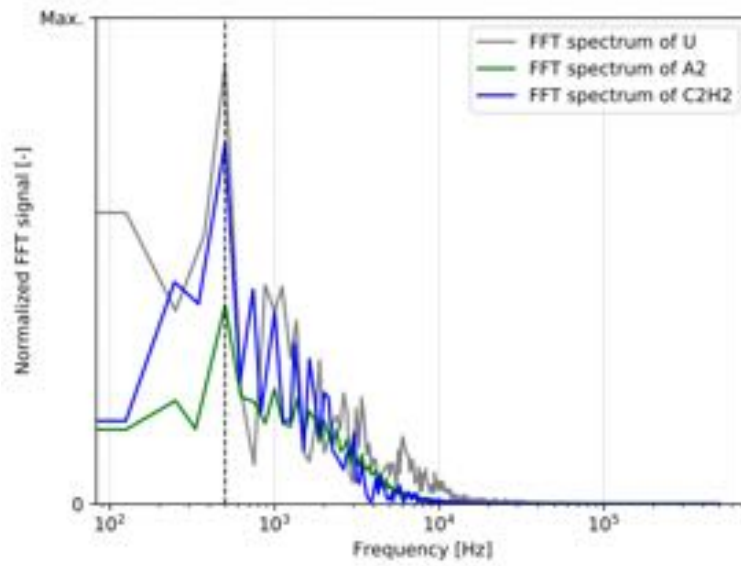


Figure 8.26: Case RUN_HL_A4 : Fast Fourier Transform at a probe location close to the injector ($r = 4\text{mm}$, $h = 3\text{mm}$).

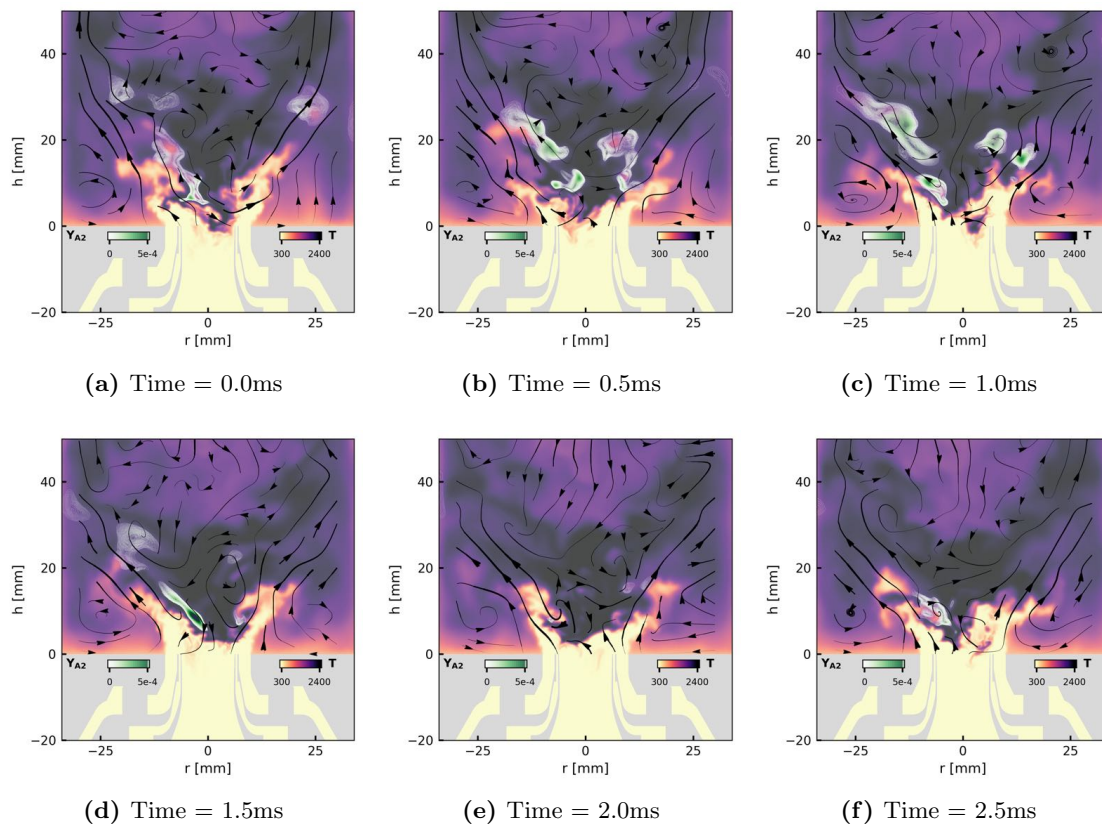


Figure 8.27: Case RUN_HL_A4 : Sequence of Temperature with overlaid green A2 mass fraction, flow field velocity is represented by arrowed streamlines with a width proportional to the local velocity intensity for the case RUN_HL_A4 .

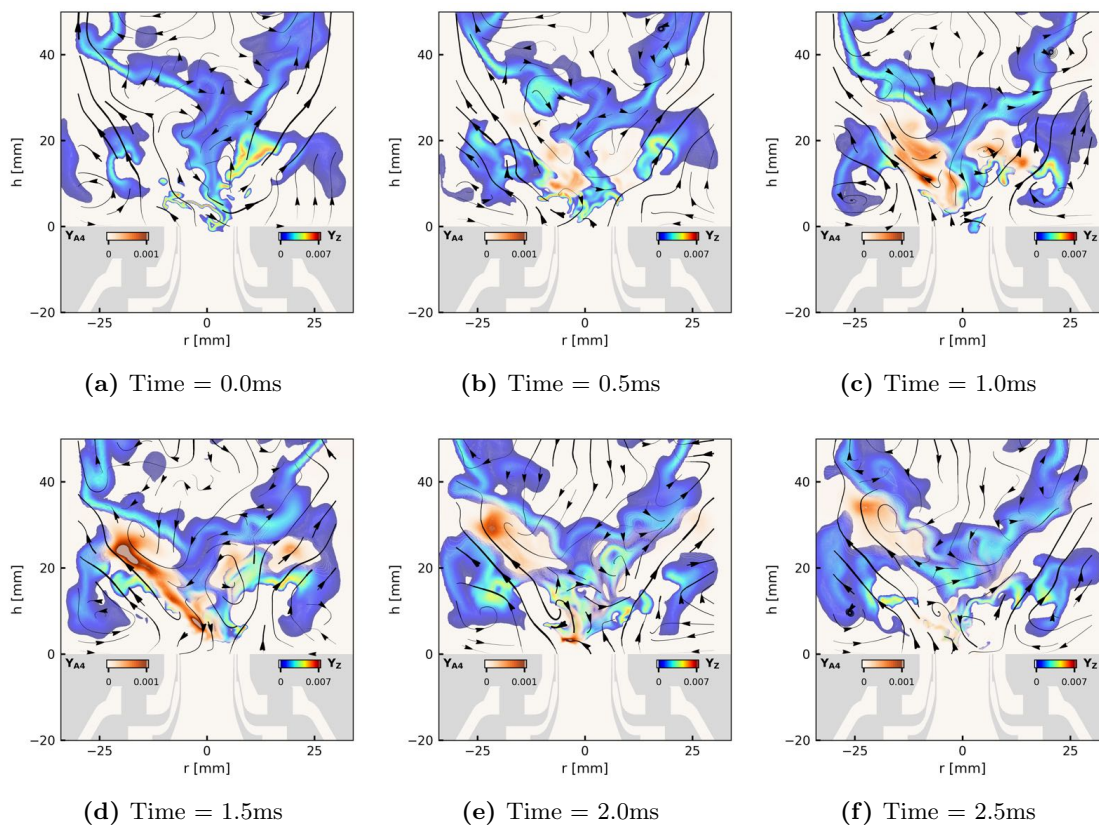


Figure 8.28: FIRST configuration: Sequence of OH mass fraction with overlaid orange A4 mass fraction, flow field velocity is represented by arrowed streamlines with a width proportional to the local velocity intensity for the case RUN_HL_A4 .

Finally, the sequence is shown for A4 and OH in Fig. [8.28](#). The CO diffusion flame front characterized by high temperature promotes the formation of OH, which is the main contributor of soot and precursors oxidation. With the retained PAH sub-mechanism, A4 originates from rich A2 pockets: high A2 concentration is observed at $t = 1ms$ in Fig. [8.27](#), after a period of time without A4 formation. Then A4 is formed, consuming A2, and convected downstream in OH-free, rich burnt gases region, where it continues to grow ($t = 1.5 - 2.0ms$). Finally both A2 and A4 are consumed by soot formation and OH-oxidation($t = 2.5ms$).

Soot particles

Soot formation from precursor species and soot oxidation by OH are competing constantly, leading to a low level of soot (about 40ppb) for the considered operating point. In this configuration, soot is formed in rich burnt gases pockets within the primary zone. Then these pockets are convected along the ISL and finally quickly oxidized by OH downstream the combustion chamber, under the effect of dilution which promotes the formation of OH. In the following, various aspects linked to this process are

8. LES IN A CONFINED PRESSURIZED BURNER

detailed:

- **Impact of strain rate:** Soot particles are localized in the ISL.
- **Soot intermittency:** Soot particles are found highly intermittent experimentally and numerically [23].
- **Impact of mixture fraction:** Rich burnt gases promote soot formation.
- **Impact of temperature:** High temperature seem unfavorable regions.
- **Impact of key species:** Soot source terms are linked to nucleating species (A4 for the analysis), C_2H_2 and oxidizing species OH.

These aspects are detailed for cases, RUN_HL_A4 and RUN_CPL_A4 , and discrepancies observed for RUN_CPL_A4 are analysed.

Impact of strain rate A response of PAH/soot formation to unsteady strain rate has been observed, especially in this configuration [384]. It has been shown that particles can be localized in the ISL where high strain resides. However it is attributed to soot convection while soot formation occurs in regions of both , a low velocity and low strain. This is explained by the chemical time scale for soot and soot precursors, significantly larger than combustion time scale (Fig. 5.7). Physical mechanism leading to PAH and soot are slow and require rich burnt gases and high residence time, while OH, which is formed in CO diffusion flame fronts is a stiff species favored by high strain rate.

The impact of unsteady strain rate is shown in Fig. 8.29 where conditional mean of precursors, soot and oxydizing species are plotted. It confirms that PAH are favored by low strain rates (slower flames), and the sensivity to strain rate increases with the size of the carbonaceous material. Contrary to PAH, higher level of OH is observed for high strain rate, i.e., faster and hotter flames (diffusion flames). These conclusions hold for both RUN_HL_A4 and RUN_CPL_A4 .

Soot intermittency Soot precursors species and soot volume fraction f_v intermittency are presented for both RUN_HL_A4 and RUN_CPL_A4 , respectively in Figs. 8.30 & 8.31. The intermittency is computed as the propability of finding a significant instantaneous value of the quantity. As observed for average fields, C_2H_2 and f_v are visible in the dilution zone and in the bottom of the combustion chamber, however with small levels which are negligible when looking at average fields. C_2H_2 is present outside the ORZ while soot particles are observed inside the ORZ due to convection of small particles in this region. A strong intermittency of A2 is observed as already suggested by Fig. 8.27. Soot particles formed in A4 regions are only sligthlty convected

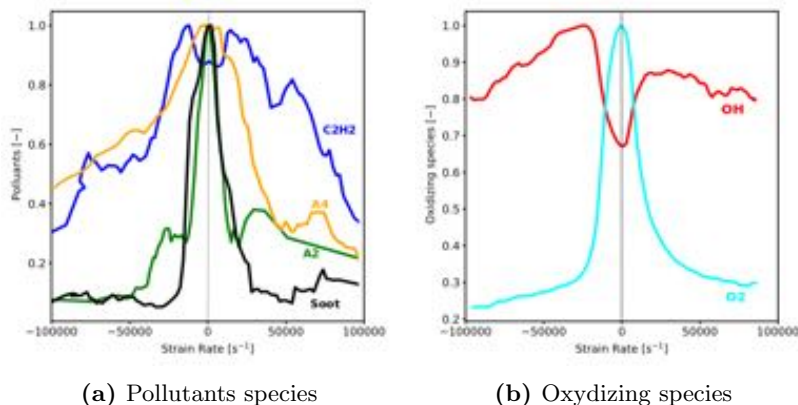


Figure 8.29: FIRST configuration: Conditional mean of precursors and soot (a) and oxidizing species (b) as function of the strain rate for the case RUN_HL_A4 .

downstream before disappearing due to complete oxidation, except for particles that are large enough to cross the OH region. These however remain too scarce to appear in the average fields. In Fig. 8.31, RUN_CPL_A4 exhibits a lower intermittency, and similar $A4$ and f_V fields: no soot particles are observed outside $A4$ regions.

Impact of mixture fraction Figure 8.32 presents a scatterplot of soot and precursors as a function of mixture fraction Y_z for both RUN_HL_A4 and RUN_CPL_A4 . All pollutants are formed in fuel rich zone, which is even more true for small soot precursors species. Only $A4$ is found in the lean side, convected from rich mixture before being fully oxidized. The lower OH oxidation of $A4$ may result from the reduction technique of the chemical scheme detailed in Chap. 5; only main reactive pathways in rich flame have been considered and OH oxidation may have been underestimated.

The shape of the scatterplots of Fig. 8.32 highlights the mechanism of soot formation. First C_2H_2 is formed in rich burnt gases inducing the formation of larger PAH through the HACA mechanism and finally leading to soot nucleation while being convected towards leaner mixture. Note that only gaseous species are considered in the computation of the mixture fraction, and that accounting for soot particles may shift the location of nucleating and key species distribution towards richer mixture. These processes are observed for both computations, however RUN_HL_A4 and RUN_CPL_A4 differ in some points:

- In RUN_HL_A4 , soot and $A4$ are found in rich mixture ($Y_z^{st} < Y_z < 0.1$) which corresponds to an equivalence ratio of $\phi = 1.5$ while $A2$ and C_2H_2 are localized in richer mixture. Interestingly, the peak of soot is located between the peaks of

8. LES IN A CONFINED PRESSURIZED BURNER

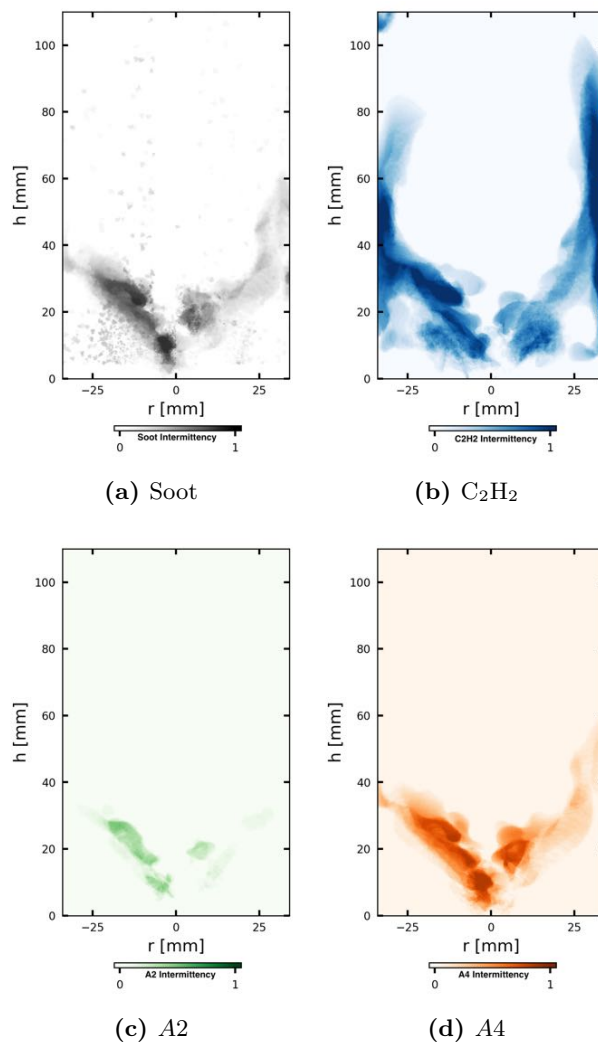


Figure 8.30: FIRST configuration: Soot and PAH intermittency over 20 *ms* for the case RUN_HL_A4 .

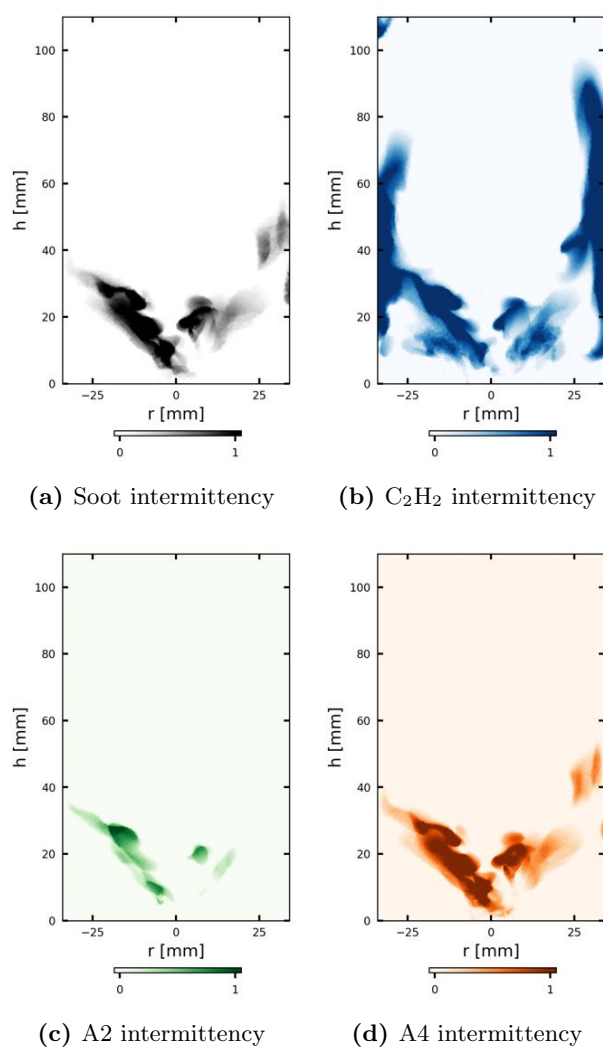


Figure 8.31: FIRST configuration: Soot and PAH intermittency over 20 *ms* for the case RUN_HLA4 .

8. LES IN A CONFINED PRESSURIZED BURNER

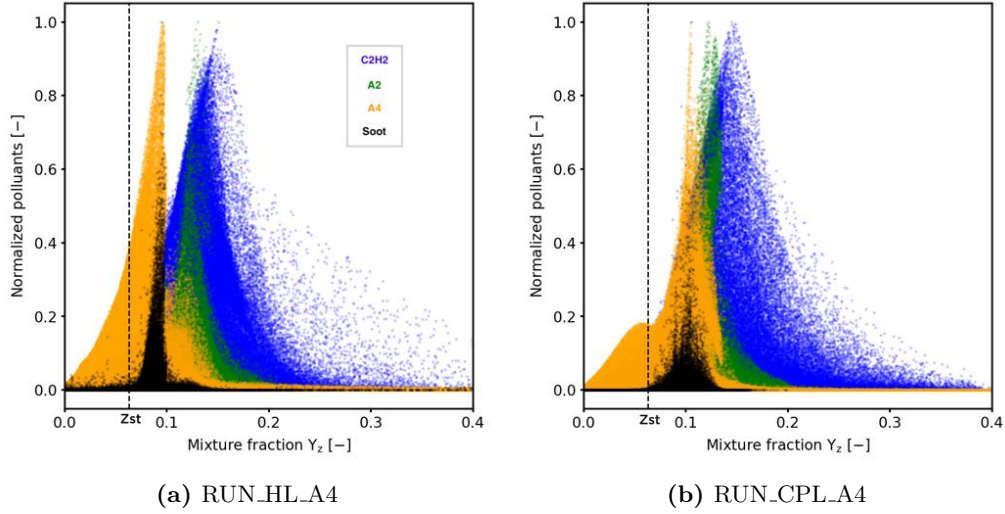


Figure 8.32: Scatterplots of soot volume fraction and precursors species as function of mixture fraction. Dashed line corresponds to the stoichiometric mixture fraction for the cases RUN_HL_A4 (a) and RUN_CPL_A4 (b).

A4 and A2, while one would expect A4 to peak further towards richer mixture, between soot and A2 peaks.

- In RUN_CPL_A4, pollutants are overall observed in richer mixture, especially A4. Surprisingly, A4 exhibits a bi-modal shape with a first peak in lean mixture and the second one in rich side. As shown previously, the levels of both A2 and A4 are about two times higher in RUN_CPL_A4 than RUN_HL_A4. The shift toward rich mixture corresponds to a location of pollutants closer to the flame than for RUN_HL_A4 (Figs. 8.30 & 8.31). The peak of soot is wider for RUN_CPL_A4 which was not expected since soot particles are observed in dilution zone and ORZ for RUN_HL_A4 and not for RUN_CPL_A4. The wider shape of soot distribution can be explained by the strong correlation between soot and A4 (observed previously) and then similar distribution in the mixture space. It is curious that the first mode of A4 distribution in lean mixture is not retrieved for soot, it may correspond to low level of A4 or A4 at low temperature region free of soot nucleation.

Impact of temperature In Fig. 8.33, scatterplots of pollutant species as functions of gaseous temperature are shown. The adiabatic temperature for the retained chemical mechanism C2H4_A4_32_233_13_LG is about $T_{adiab} = 2500K$. For both RUN_HL_A4 and RUN_CPL_A4, no soot particles are observed beyond $2400K$, although small amounts of A4 are observed at high temperature. The peak location of C₂H₂ and A2 as well as their shape are similar with or without radiative transfers. In case RUN_HL_A4

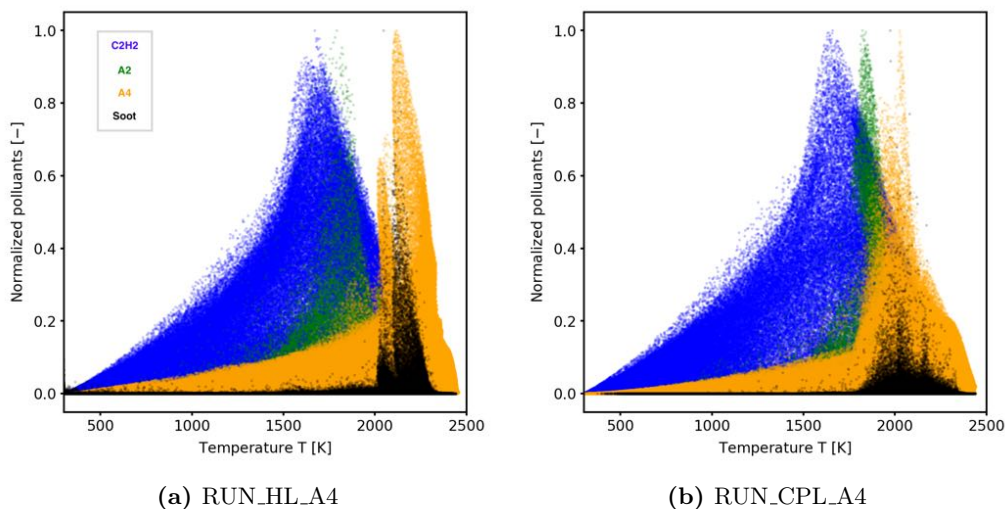


Figure 8.33: Scatterplots of soot volume fraction and precursors species as function of gaseous temperature for the cases RUN_HL_A4 (a) and RUN_CPL_A4 (b).

, soot and A4 are found at higher temperature than in RUN_CPL_A4 , i.e. at around 2200K. As observed for mixture fraction, scatterplots A4 and soot peaks are wider for RUN_CPL_A4 . To better understand these behaviors, source terms are investigated.

Positive source terms are shown in Fig. 8.34, where nucleation, condensation and surface growth source terms are colored by associated key species for both RUN_HL_A4 (top) and RUN_CPL_A4 (bottom). Nucleation and condensation operate roughly between 1750K and 2250K, and are proportional to A4 mass fraction: the peak of the source term corresponds to the peak observed in Fig. 8.33. Surface growth appears at lower temperature where C₂H₂ peaks and yet peaks at high temperature where C₂H₂ is low. Still, surface growth and condensation peak at high temperature, being proportional to soot surface, they are maximum where soot volume fraction is maximum. The main difference between RUN_HL_A4 and RUN_CPL_A4 is still the factor two observed previously when looking at C₂H₂, A4 or soot.

The negative soot source term, oxidation is investigated in Fig. 8.35. The oxidation rate has been conditioned by the presence of OH (left) and O₂ (right) for both RUN_HL_A4 and RUN_CPL_A4 . First, it highlights the leading contribution of OH oxidation in hot regions and O₂ oxidation in cold ones: oxidation by OH exhibits a peak at hot temperatures about two times higher than oxidation by O₂. The oxidation rate is of the same order as surface growth rate, cancelling a key soot source term. Finally, oxidation operates over a wide range of temperature, between 1200K and 2400K:

- Soot oxidation in low temperature zones ($1200K < T < 1750K$) can be explained by the high level of O₂ coming from the dilution jets,

8. LES IN A CONFINED PRESSURIZED BURNER

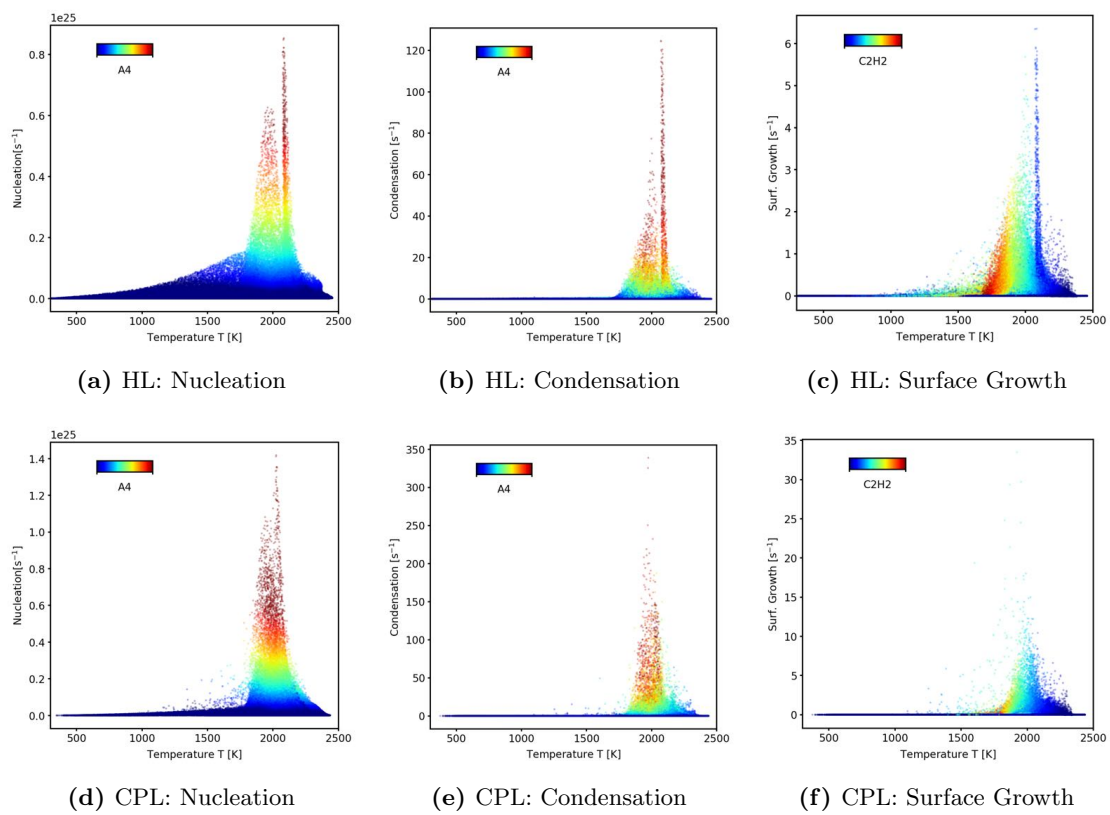


Figure 8.34: Scatterplots of soot source terms contributing to soot growth as functions of temperature, colored by respective key species for RUN_HL_A4 (top) and RUN_CPL_A4 (bottom).

- Oxidation by both O_2 and OH occurs in the main soot region ($1750K < T < 2250K$) where soot surface reaches high values,
- Oxidation at high temperature ($T > 2250K$) is driven by OH , which is formed in CO diffusion flames.

Focusing on high temperature regions, a peak around $T \sim 2300K$ is observed of oxidation by OH . No soot particles are observed beyond this temperature. As OH is not maximum at this temperature, this peak may be due to the temperature dependence of soot oxidation OH reaction and the high soot surface, knowing that high temperatures promote also soot coagulation increasing significantly soot surface. For RUN_CPL_A4, numerous peaks appear between $1900K$ and $2300K$, reacting values about two times higher than in RUN_HL_A4. As expected the oxidation rate is higher when accounting for radiative heat transfer, however this concerns only the peak levels, the background level being really similar between RUN_HL_A4 and RUN_CPL_A4. Other source terms present a factor two between the two cases, highlighting that precursors (C_2H_2 , A4) are more sensitive to heat transfer than oxidizing species.

Soot and key species Figure 8.36 reports scatterplots of f_v as a function of C_2H_2 , A4 and OH for RUN_HL_A4 (top) and RUN_CPL_A4 (bottom). Linear regressions are also plotted to highlight the dependencies. The PDF of both quantities (coordinates) are plotted as well at the top and at the right of the scatterplots. Note that following the previous observations, the plotted data is conditioned on high temperatures. As already observed in Figs. 8.34 and 8.35, soot source terms involve the whole range of C_2H_2 and A4 mass fraction. The linear regressions then show that the dependency flattens with thermal radiation. The same flattening is observed for the dependency of OH , with in addition a reduction of range of OH mass fraction. This suggests that species concentration is not the main factor for soot growth and oxidation, which must then be more related to soot surface.

8.3.2.4 Soot size

Figure 8.37 shows the joint PDF between soot volume fraction f_v and soot number density N_s both normalized for RUN_HL_A4 and RUN_CPL_A4. The PDFs appear very different in both cases, N_s staying small whatever f_v in RUN_CPL_A4. This is linked to the strong contribution of coagulation (decreasing N_s) in that case, and leads to a high soot size and surface. Note that the coagulation process is assumed to be pure aggregation, where soot surface doubles at each collision. The scatterplot of soot surface as a function of soot volume displayed in Fig. 8.38 confirms that for RUN_CPL_A4 the transition between spherical and aggregate particles appears right

8. LES IN A CONFINED PRESSURIZED BURNER

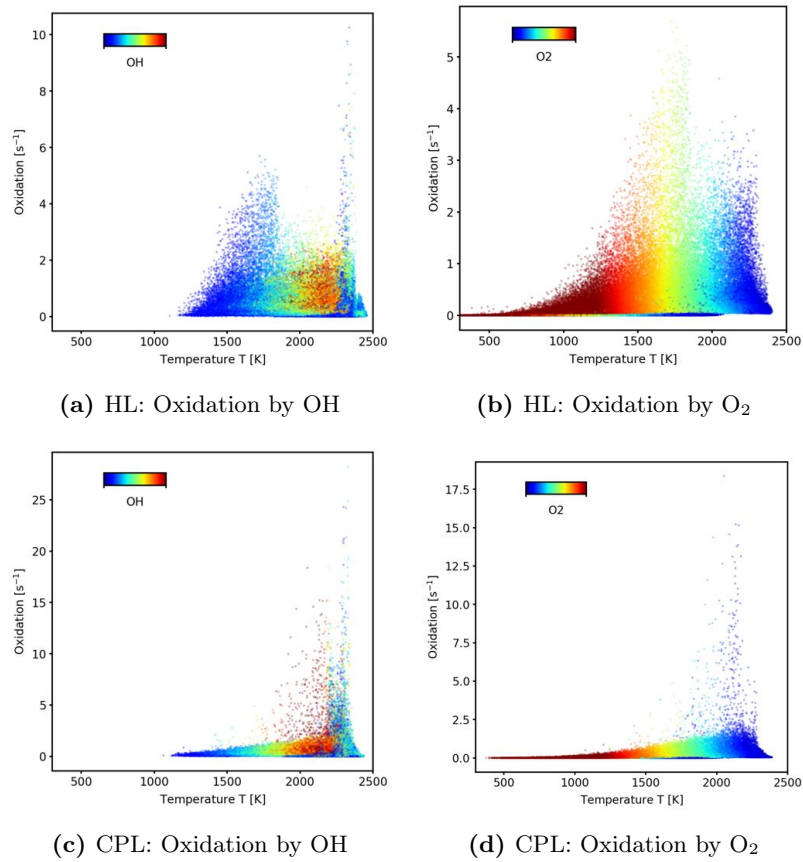


Figure 8.35: Scatterplots of soot oxidation source terms contributing to soot growth as functions of temperature colored by OH (left) and O₂ (right) for RUN_HL_A4 (top) and RUN_CPL_A4 (bottom).

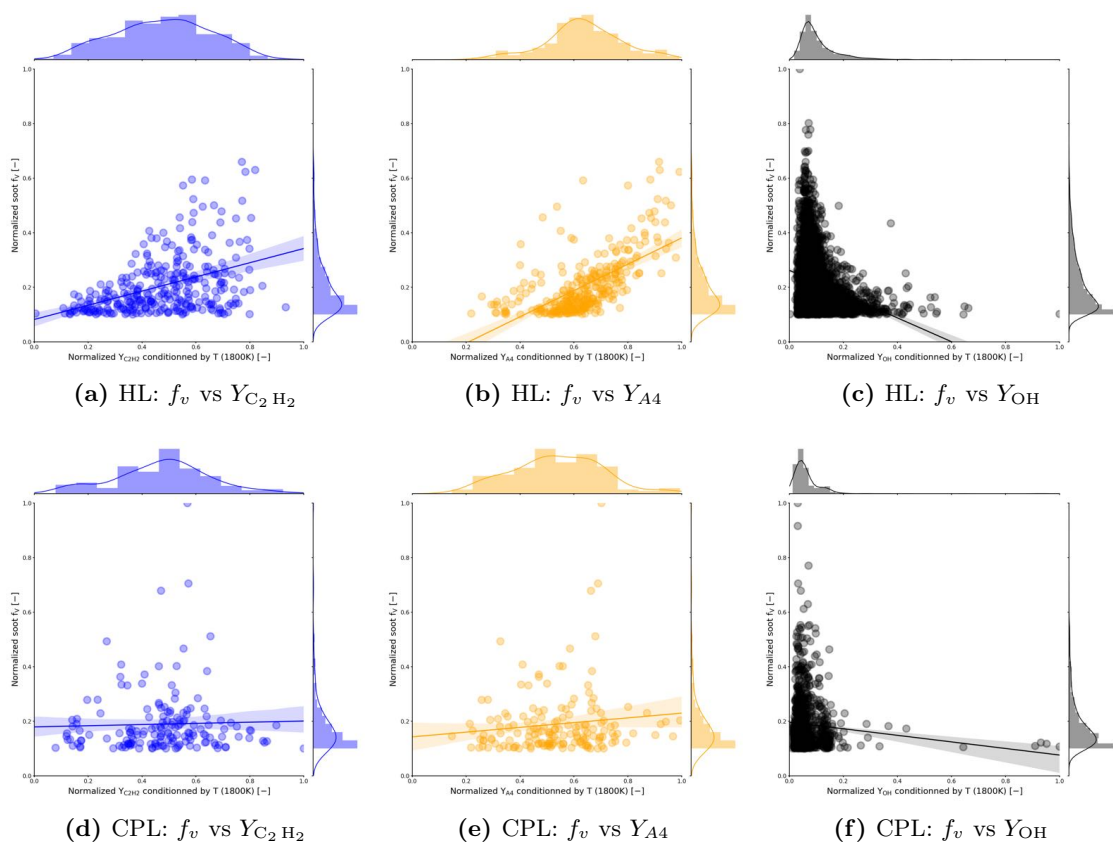


Figure 8.36: Scatterplots of soot volume fraction as a function of $Y_{C_2H_2}$ (left), Y_{A4} (center) and Y_{OH} (right) conditioned on high temperature for RUN_HL_A4 (top) and RUN_CPL_A4 (bottom). Linear regressions highlight the dependencies.

8. LES IN A CONFINED PRESSURIZED BURNER

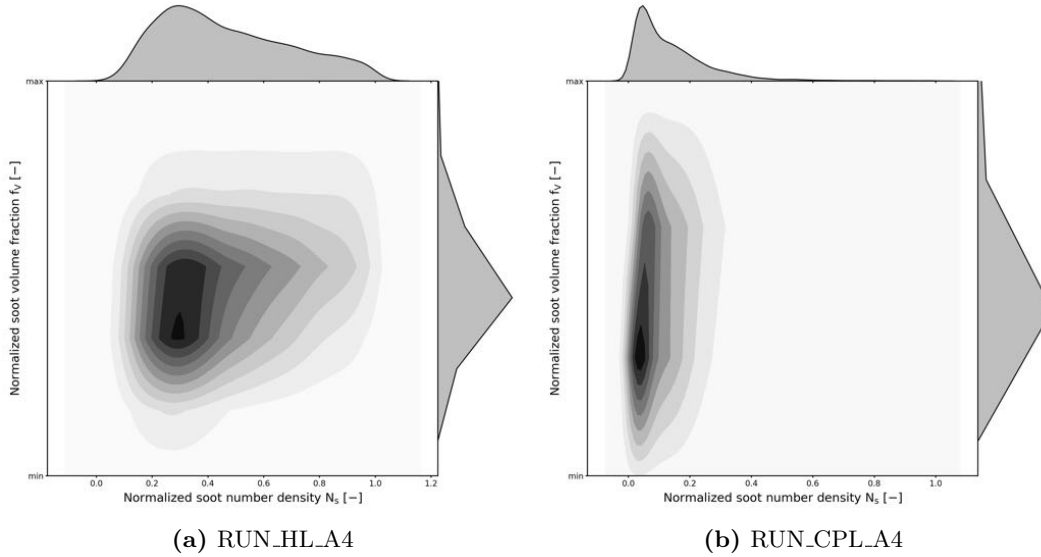


Figure 8.37: Joint PDF of soot volume fraction f_v as a function of soot number density N_s for the cases RUN_HL_A4 (a) and RUN_CPL_A4 (b).

after the nucleation. In case RUN_CPL_A4, high temperature and high soot number density due to high nucleation source term (about two times higher than RUN_HL_A4) promotes significantly soot coagulation. Then the assumption of pure aggregation leads to a significant overestimation of soot surface and then soot source terms. This assumption becomes critical for oxidation in this configuration.

An important feature of the proposed numerical approach is to give access to the statistical PSDF, presented at six locations for case RUN_HL_A4 in Fig. 8.39. Close to the injector along the z -axis at $r = 0\text{mm}$, $h = 3\text{mm}$ (Fig. 8.39(a)), the PSDF corresponds to a quasi-pure nucleation mode. The same distribution is observed at the same height, further in the radial direction at $r = 4\text{mm}$, $h = 3\text{mm}$ (Fig. 8.39(b)), but the intermittent presence of larger particles can be observed. Further downstream at $h = 12\text{mm}$ (Fig. 8.39(c to f)), the soot number density N_s increases. Along the z -axis, nucleation is still predominant while at larger $r = 4\text{mm}$ both nascent particles and larger particles are observed. Note that PSDF stays always unimodal for this case.

For comparison PSDF for RUN_CPL_A4 and RUN_HL_A4 are presented in Fig. 8.40. First, the number density N_s is found higher at all locations. The nucleation peak at $r = 0\text{mm}$, $h = 3\text{mm}$ (Fig. 8.40(a)) is more pronounced. Further downstream, the presence of larger particles is significantly more pronounced when accounting for radiative transfer, linked to stronger coagulation. The pure-aggregation mode promotes the impact of collisions on the soot size.

Here, the high nucleation rate and the over-estimated collision phase do not lead to a bimodal PSDF, soot growth here is mainly due to successive collisions impacting

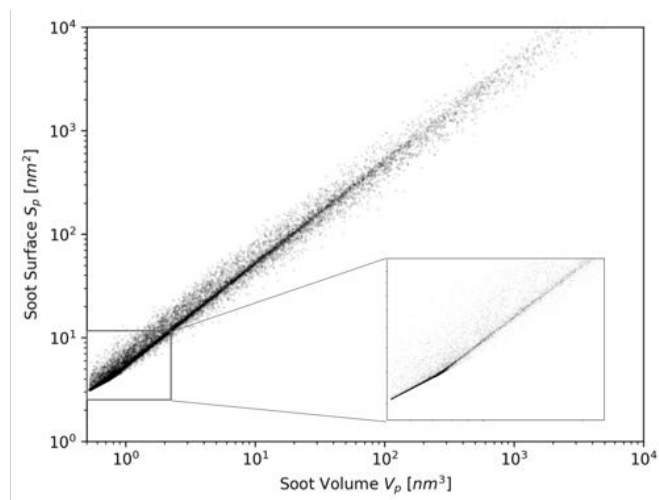


Figure 8.38: RUN_CPL_A4 : Scatterplot of soot surface as a function of soot volume V_p .

significantly the soot number density of large particles. In the work of *Rodrigues et al.* [37], the presence of bimodal PSDF is characterized by strong nucleation and particles coming from upstream who gained in mass mainly through condensation and surface growth processes. Their investigations show that the coagulation of already large particles results in the apparition of bimodal PSDF when large particles concentration is sufficiently large, and differs from the fast coagulation of incipient (small) soot particles observed in this work.

8.4 Computational cost

The comparison between LST and a Eulerian 2-equations semi-empirical model has been done in Chapter 4. Similar computational cost was found, demonstrating the efficiency of combined reduced chemistry and Lagrangian soot tracking.

The Lagrangian formalism is indeed well adapted to intermittent phenomena like soot formation, as the cost of Lagrangian computations is proportional to soot particles number and avoids computations in empty zones of the computational domain. Moreover, additional physical parameters like soot particle surface do not impact the computational cost.

Figure 8.41 presents the computational cost for the four computations as well as a reference case without soot particles. The computational cost corresponds to 1ms of physical time, and is an average over 10ms. The vertical line corresponds to the variation observed due to soot intermittency. It is found that the impact of soot particles computation remains reasonable in complex configurations, about 12%. This cost must be related to the two user-defined parameters defined in Chapter 4:

8. LES IN A CONFINED PRESSURIZED BURNER

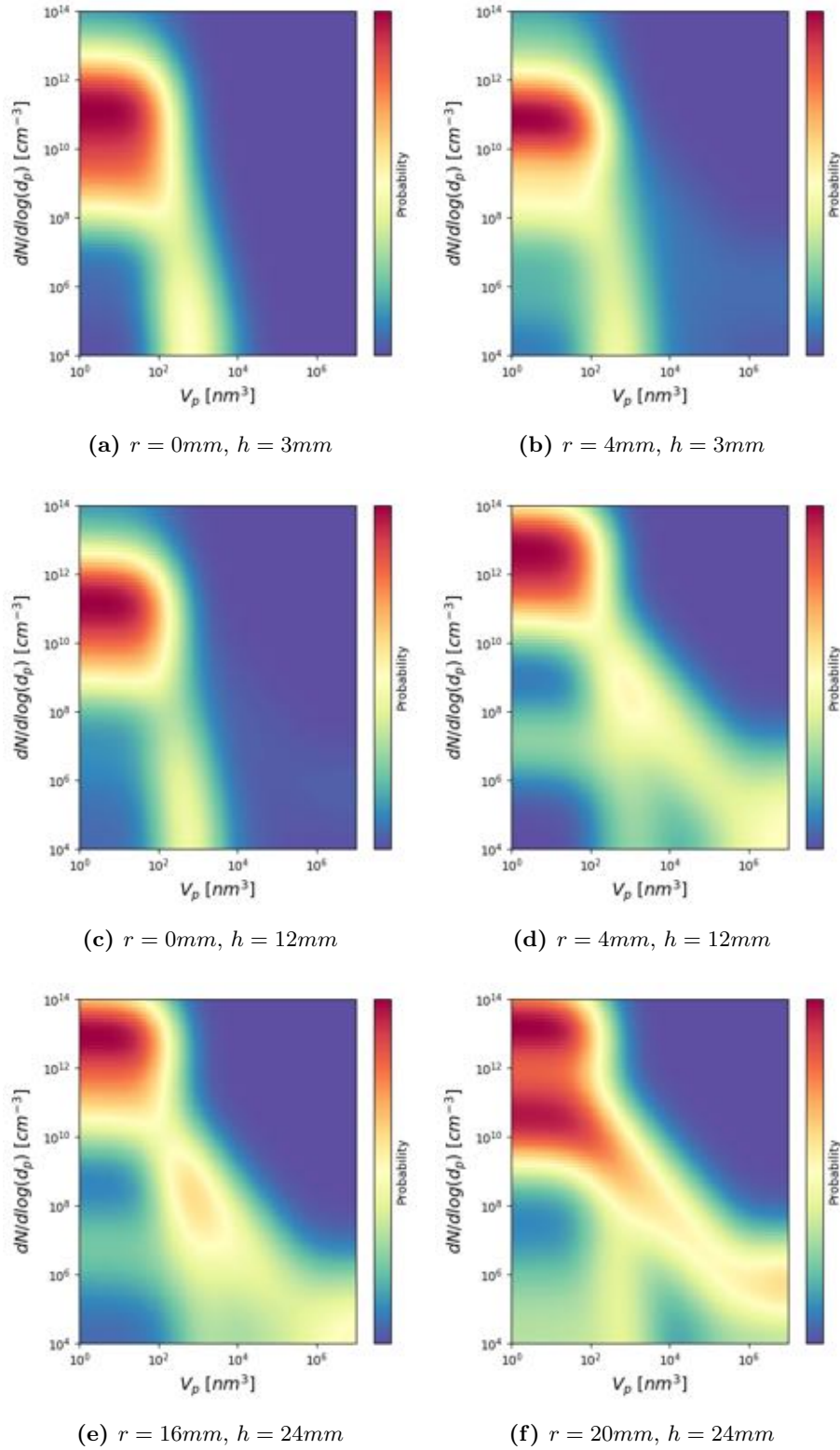


Figure 8.39: PSD at six different locations for the case RUN_HL-A4 .

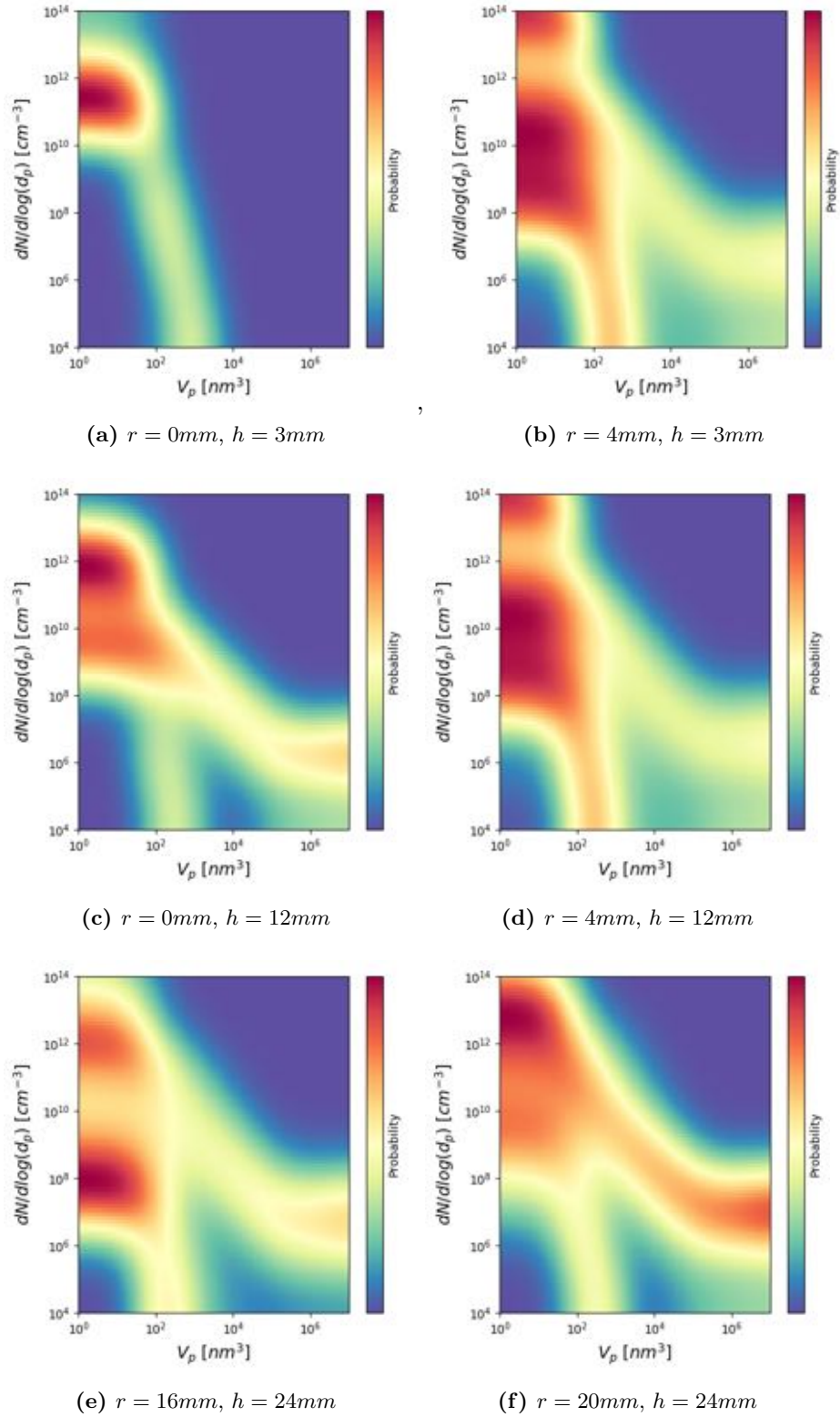


Figure 8.40: PSD at six different locations for the case RUN_CPL_A4 .

8. LES IN A CONFINED PRESSURIZED BURNER

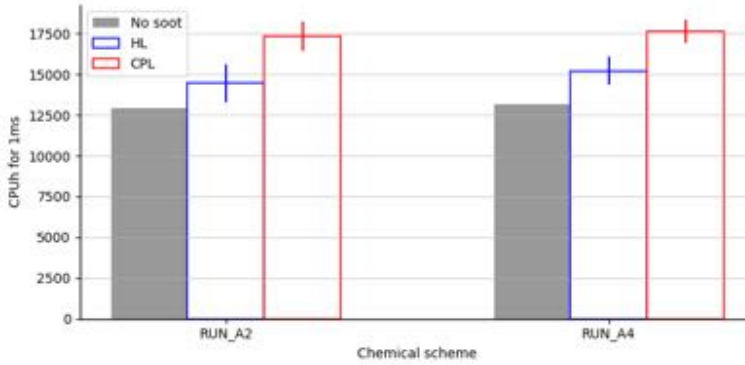


Figure 8.41: FIRST configuration: Computational time (CPU hours) for 1 *ms* of physical time for the different simulations.

f_s	1	1	5	5	10	10
N_{soot}^{max}	50	100	50	100	50	100
Lag. solver, %	46	87	12	20	8	15
Physics, %	4	3	4	3	4	2
Merging, %	4	3	3	2	5	4
Collisions, %	9	5	9	8	12	9
Transport, %	83	89	84	87	79	85

Table 8.3: Impact of user-defined numerical parameters on the lagrangian contribution to the computational time and contribution of each Lagrangian process within the Lagrangian algorithms.

- N_{soot}^{max} : maximum number of numerical particles per cell,
- f_s : soot computation frequency.

The impact of these parameters is given in Tab. [8.3](#). The contribution of the Lagrangian solver on the global computational time remains always low ($< 20\%$). The implementation of physical and numerical processes is efficient with a negligible contribution, while transport is the main contributor to the Lagrangian computational cost. Indeed, transport of soot particles means communications between computational partitions, with a cost proportional to the number of soot particles. This explains the increase of computational cost with N_{soot}^{max} . The soot frequency f_s appears as a key parameter to significantly reduce the computational cost. In the current computations, f_s was fixed to 5 and N_{soot}^{max} to 50, leading to the best cost/accuracy trade-off.

8.5 Conclusion

Several computations of the gaseous FIRST configuration were performed, with the intent to investigate the impact of the chemical scheme and radiative heat transfer on

the accuracy of soot prediction. Two reduced chemical schemes sharing the same C_2H_4 oxidation but different soot precursors description were investigated. For both chemical descriptions, the impact of radiative heat transfer was investigated.

A good agreement was obtained for main flame features, with a correct flame structure and shape. Radiative heat transfer slightly changes the flame position and shape.

In terms of soot prediction, the agreement between simulation and experiment is acceptable in view of the state-of-the-art. Better results are obtained with larger precursor. Despite a good order of magnitude, the distribution of soot particles is however different from experiment, with a spatial shift towards the bottom of the combustion chamber. The discrepancy is stronger with radiative heat transfer highlighting the high sensitivity of soot formation to temperature, in particular via the formation of OH, a key soot oxidizing species.

Further analysis showed that the distribution of soot particles is correlated to the distribution of OH distribution produced in diffusion flames. For the selected operating point, the competition between soot formation and oxidation leads to a small soot volume fraction. The use of larger PAHs to model soot formation is critical as shown by previous studies [196, 378, 382]. Moreover, the assumption of pure aggregation leads to an overestimation of soot surface promoting soot oxidation, especially when accounting for radiative heat transfer where nucleation rate was doubled. Coalescence should be considered at least for small soot particles.

For such small soot level ($f_v < 1ppm$), the impact of soot particles on the radiative power is insignificant (about 10%) [196].

Despite discrepancies which mostly result from uncertainties of soot physico-chemical processes, the capability of the retained methodology to predict soot formation at a reasonable computational cost is demonstrated. Further computations for case RUN_HL_A4 should be conducted accounting for both coalescence and aggregation, as well as larger PAH, to assess the ability of the proposed methodology to accurately predict soot emissions.

8. LES IN A CONFINED PRESSURIZED BURNER

Chapter 9

LES in a turbulent spray flame

In this Chapter, the soot model is validated considering liquid aviation jet fuel. The accuracy of the reduced chemistry for aviation jet fuel including PAH proposed in Chapter 5 is evaluated. Large Eddy Simulation of the sooting swirled turbulent spray JetA-1/air combustor measured at UTIAS is performed. It is considered in this work as a critical step before applying the model to real aeronautical industrial configurations. Due to liquid fuel injection, both soot particles and fuel droplets are handled by the Lagrangian solver. The objective is then to a better understanding soot formation in turbulent spray flames, the interaction between fuel droplets, turbulent flame, PAH and soot.

Section 9.1 introduces the target configuration. It is followed by the presentation of the numerical set-up in Sec. 9.2. Finally, results are analyzed in Sec. 9.3.

Contents

9.1	UTIAS Jet A-1 combustor	211
9.2	Numerical setup	212
9.3	Results	214
9.3.1	Non-reacting gaseous flow validation	214
9.3.2	Reacting two-phase flow	214
9.3.3	Spray flame - soot interaction	218
9.3.4	Particle dynamics and size distribution	222
9.4	Computational cost	224
9.5	Conclusions	226

9.1 UTIAS Jet A-1 combustor

To the best of our knowledge, only a handful of lab-scale experimental facilities are operated with real aviation jet fuel [213]. The configuration chosen in this work is the UTIAS Jet A-1 combustor [22], studied experimentally at University of Toronto Institute for Aerospace Studies. It is a swirl-stabilized spray flame and as such, is well representative of aeronautical burners. Soot measurements are available, which is quite unique an academic lab-scale combustor burning real aviation jet fuel [22]. The combustion chamber presented in Fig. 9.1, is a four quartz windows enclosure allowing optical access, of dimensions $94 \times 94 \times 188mm^3$ where the aspect ratio 2:1 is required

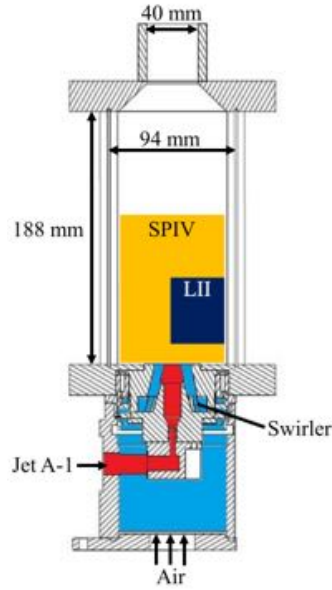


Figure 9.1: UTIAS configuration: Cross-sectional view of the burner assembly. Yellow box indicates the region mapped by the SPIV planar measurement, and dark blue box shows the region probed by the LII point measurement. (from [22]).

to handle the spray flames. A conical converging tunnel leads to a central exhaust pipe with a diameter of 40 mm. Air at ambient temperature passes through a radial swirler and enters the burner through an annular nozzle with an inner diameter of 5 mm and an outer diameter of 27.85 mm. The combustor is operated with Jet A-1 injected and atomized through a commercial pressure-swirl nozzle with a spray angle of 60°. The air and fuel nozzles are located at the inlet of the combustion chamber and the measured swirl number is about 0.55. The thermal power of the spray burner is 10kW. The operating point considered in this work corresponds to case A described in Wang *et al.* [22], with an air mass flow rate of 5.8 g/s and a fuel mass flow rate of 0.22g/s. The combustor operates at atmospheric pressure and ambient temperature, and global equivalence ratio is $\phi_{global} = 0.55$. The measurement techniques are detailed in [22], they include Particle Image Velocimetry and AC-LII [22] for soot volume fraction and primary soot particle size. The quasi-axisymmetric feature of the combustor allows to restrict soot measurement to one half of the combustor.

9.2 Numerical setup

The computational domain comprises the entire combustion chamber together with the swirler. It is discretized with 30 million tetrahedra of size varying from 0.25 mm in the swirler to about 0.4 mm in the spray and flame region, as shown in Fig. 9.2. Simulations are performed using AVBP with a numerical set-up similar to the one described in Chapter 8 for the FIRST configuration. For Jet-A1, the JetAPAH_29_233_15_LG

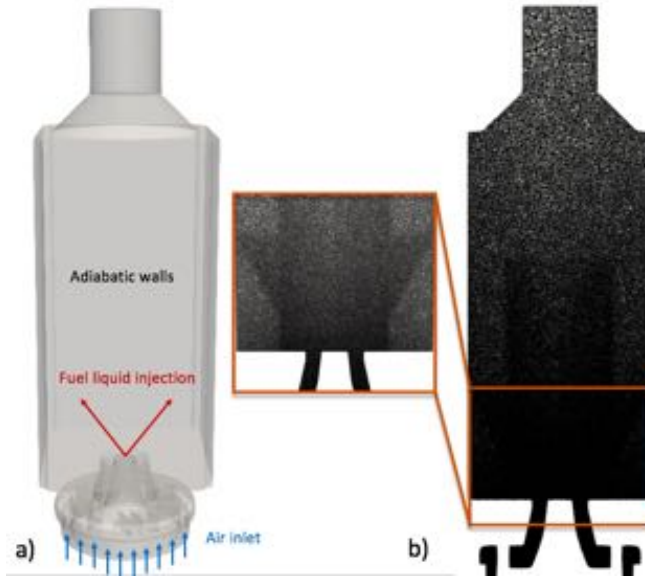


Figure 9.2: a) UTIAS computational domain. b) Numerical grid and local refinement near injectors.

reduced chemistry is used. As the fuel is liquid, a polydisperse spray injection boundary condition at the pressure-swirl nozzle is applied with the FIMUR injection model introduced in Sec. 3.3.5. The spray is injected at a temperature of $300K$, with an angle of 60° and a Rosin-Rammler diameter distribution parametrized with a SMD of $33\mu m$ and a q coefficient of 2.2, with these parameters, the spray is assumed to be fully atomized and secondary break-up is omitted. The SMD was determined with the correlation of *Lefebvre et al.* [385]: following *Lefebvre et al.* correlation [385] without secondary break-up model.

$$d_{SMD} = 2.25 \left(\frac{\sigma \mu_f \dot{m}_f}{\rho_o \Delta_P^2} \right)^{0.25} \quad (9.1)$$

where σ is the surface tension, μ_f the fuel viscosity, ρ_o the air density and Δ_P the pressure drop.

As the spray does not strongly impact the chamber walls, no complex model for droplet-wall interaction is used. As in Chapter 8, the maximum number of numerical soot particles per cell is set to $N_{soot}^{max} = 50$ and the soot frequency is set to $f_s = 5$. The MGNS merging approach is retained (see Chapter 4) and the assumption of pure aggregation for soot collisions is kept. A2 is the only available soot precursor described in JetAPAH_29_233_15_LG .

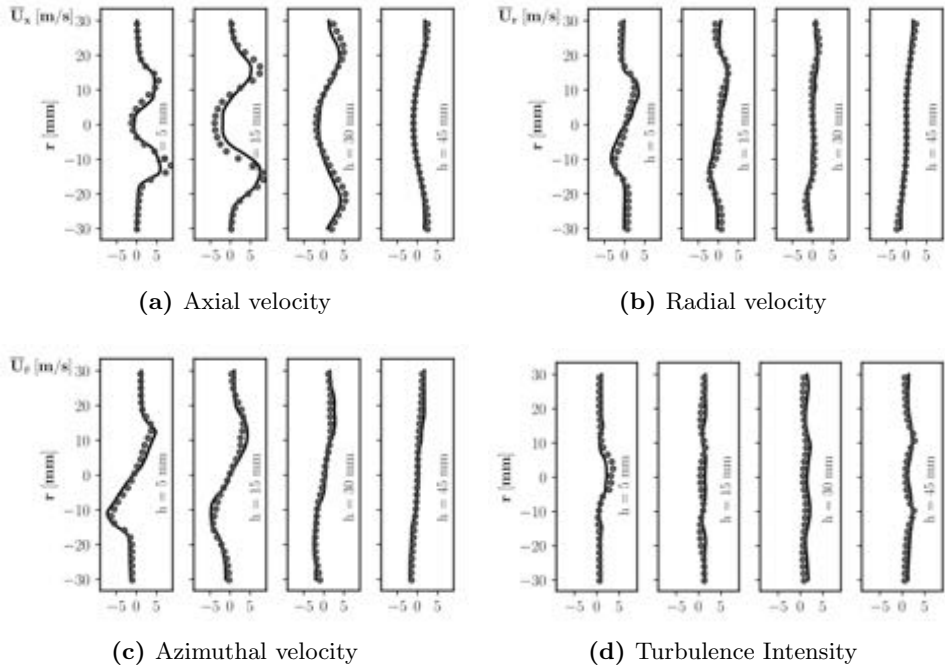


Figure 9.3: UTIAS configuration: Profiles of time-averaged velocity components and turbulent intensity at axial position $5mm$, $15mm$, $30mm$ and $45mm$ in non-reacting conditions. Symbols: experiment, black line: LES.

9.3 Results

9.3.1 Non-reacting gaseous flow validation

First, the non-reacting gas velocity fields are compared to experiment. Profiles extracted at four axial positions downstream the injector, marked in Fig. 9.5, are presented in Figure 9.3. A very good agreement is found, with a correct description of the IRZ, both in width and velocity magnitude. The swirl number of 0.55, i.e., below the critical swirl number of 0.6, leads to a long and narrowed IRZ along the axial axis, as shown in Fig. 9.4, and to two small ORZ. The small swirl number and the large spray angle prevent from the presence of fuel droplets in the IRZ [22].

9.3.2 Reacting two-phase flow

9.3.2.1 Flow field validation

The instantaneous flow topology is presented in Fig. 9.5. The long and narrowed IRZ and small ORZ observed in Sec. 9.3.1 persist in reacting conditions. Figure 9.5 details also the measurements boxes and locations used for SPIV (gray) and LII (black). The white isocontours of liquid volume fraction highlight the instantaneous presence of fuel droplets: the IRZ is almost free of fuel droplets, and only few droplets hit the walls. These two-phase flow features are clearly visible in Fig. 9.6 showing mean quantities.

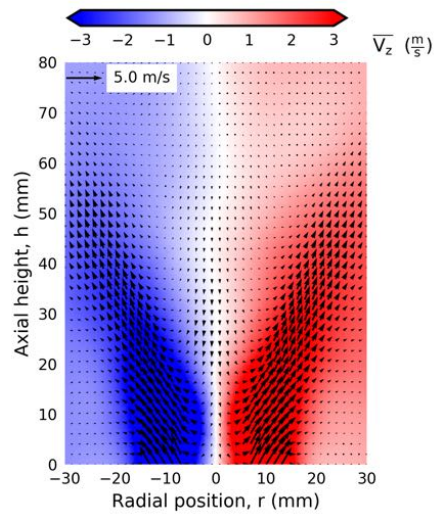


Figure 9.4: UTIAS configuration: Average axial velocity from LES in a mid-plane cut.

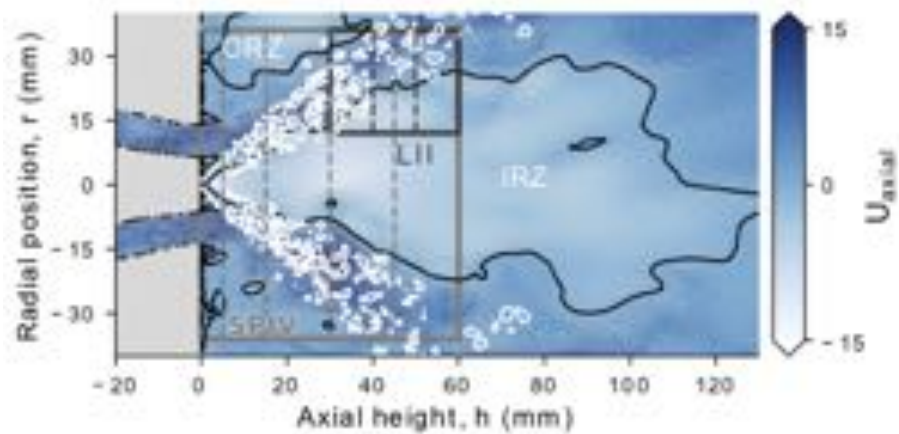


Figure 9.5: UTIAS configuration: Instantaneous axial velocity from LES in a mid-plane cut. Black line: isoline of zero-axial velocity to mark recirculate zones. The spray is superimposed in white via the liquid volume fraction.

9. LES IN A TURBULENT SPRAY FLAME

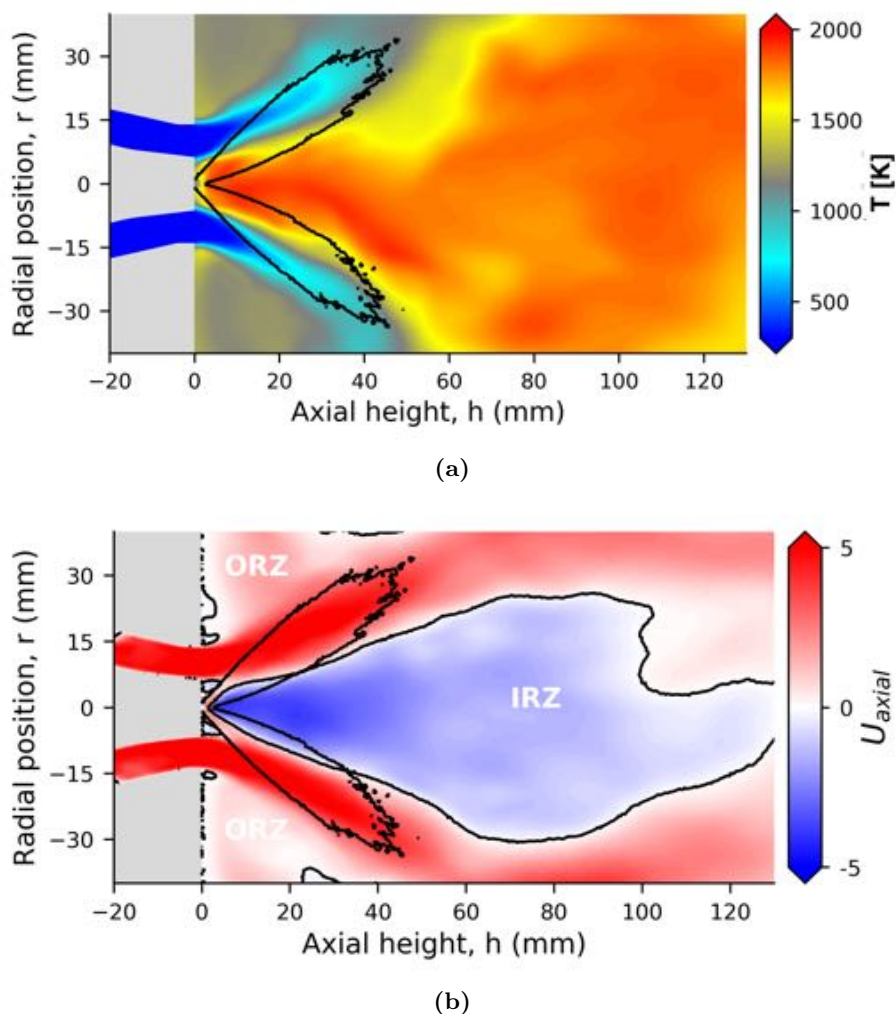


Figure 9.6: Time-averaged fields of temperature (top) and axial velocity (bottom). Black isocontours of liquid volume fraction correspond to the spray location and zero axial velocity (bottom).

The time-averaged field of temperature with a black isocontour of liquid volume fraction is shown in Fig. 9.6a. Hot burnt gas are brought back through the IRZ close to the injector, promoting fuel droplet evaporation and mixing. The flame exhibits a V-shape with a significant length. It is interesting to note that the spray, first encountering hot burnt gas, then extends to the low temperature air flow.

The flame is highlighted by an iso-contour of heat release rate in the top of Fig. 9.7. The flame exhibits a V-shape and is discussed further in Sec. 9.3.2.2.

Profiles of time-averaged velocities at four axial positions are compared to experiment in Fig. 9.8. Averages were computed over 30ms, i.e., 6 flow through times. A very good agreement between LES and measurements for mean axial, radial, azimuthal velocity and turbulence intensity is found. At the first two locations, some discrepancies can be observed due to interference of the spray with SPIV, as explained by Wang et

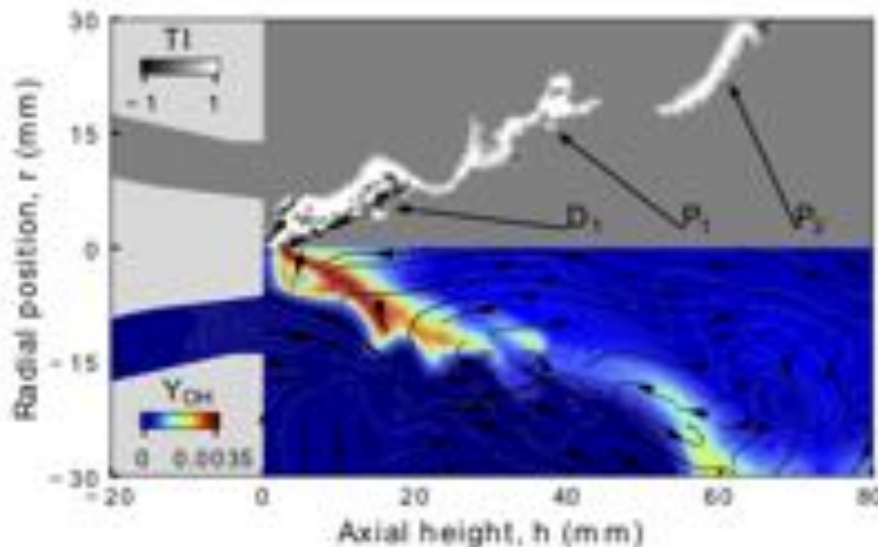


Figure 9.7: UTIAS configuration: Instantaneous Takeno Index conditioned by heat release rate (top) and OH mass fraction with superimposed streamlines (bottom).

al. [22]. The high levels of turbulence intensity near injector regions can be attributed to the presence of a small PVC, observed in both non-reacting (Fig. 9.3) and reacting conditions (Fig. 9.8).

9.3.2.2 Flame structure

The combustion regime is identified using the Takeno Index (TI). Following the work of Felden *et al.* [213] when using reduced chemistry, fuel-based TI is not adapted and a lumped species is used, defined as:

$$Y_{cs} = Y_{\text{JetA-1}} + \sum_{\text{pyro.prod}} Y_{\text{pyro.prod}} + Y_{\text{C}_2\text{H}_2} \quad (9.2)$$

The resulting Takeno index is given by:

$$TI = (\nabla Y_{CS} \cdot \nabla Y_{O_2}) / (\|\nabla Y_{CS}\| \cdot \|\nabla Y_{O_2}\|) \quad (9.3)$$

This Takeno Index is displayed on the top part of Fig. 9.7. Both diffusion and premixed flame fronts appear. The flame front D_1 , located close to injection exhibits a thin diffusion flame front with high concentration of OH, lying in the shear layer between the spray and the IRZ, as displayed in the bottom part of Fig. 9.7. This diffusion flame may be understood with the temperature of Fig. 9.6a: at injection, droplets meet burnt hot gas, which enhance their evaporation but lead to too rich mixture for premixed burning. The fuel vapor then burn with the cold air jet in a non-premixed mode. Otherwise the flame front is mainly of premixed nature. In the flame zone P_1 , air is diluted with burnt gases and the equivalence ratio has sufficiently decreased to allow premixed burning.

9. LES IN A TURBULENT SPRAY FLAME

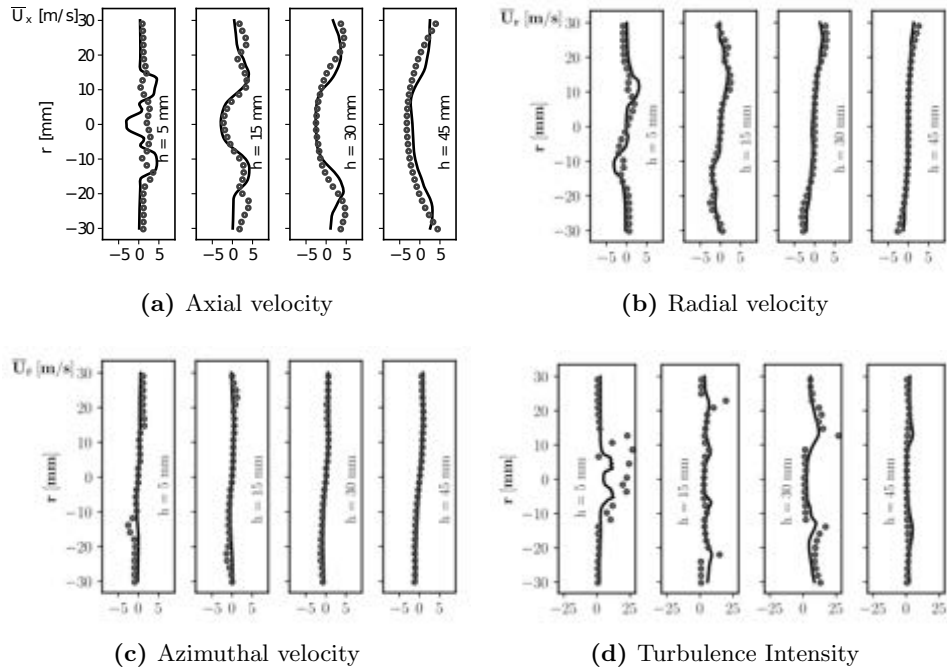


Figure 9.8: UTIAS configuration: Profiles of time-averaged mean velocity and turbulent intensity at axial position 5 mm , 15 mm , 30 mm and 45 mm in reacting conditions. Symbols: experiment, black line: LES.

Finally, a second mainly premixed flame front P_2 is observed, detached from P_1 flame front due to a local quenching event. In this zone, few droplets vaporize and a lean premixed flame appears. Local diffusion flames due to the heterogeneous mixing explain the high concentration of OH in this third flame front.

9.3.2.3 Soot prediction

Soot particles are measured in the LII box highlighted in dark grey in Fig. 9.5, corresponding to the zone where soot mainly appears [22]. A small amount is found (about 5 ppb), exclusively located at the tip of the spray. Both soot volume fraction and primary soot diameter are compared to measurements at four locations in Fig. 9.9. A very reasonable agreement is found for both quantities. Soot is slightly underpredicted far downstream the flame. The IRZ prevents the formation of soot in this region as observed experimentally [22] due to high strain. Note that only soot particles larger than 2 nm have been retained for comparison with LII measurements, in accordance with the LII detection size limit.

9.3.3 Spray flame - soot interaction

Figure 9.10 shows the spray, represented by grey circles, with in the bottom part an instantaneous field of the lumped species defined in Sec. 9.3.2.2 and in the top part,

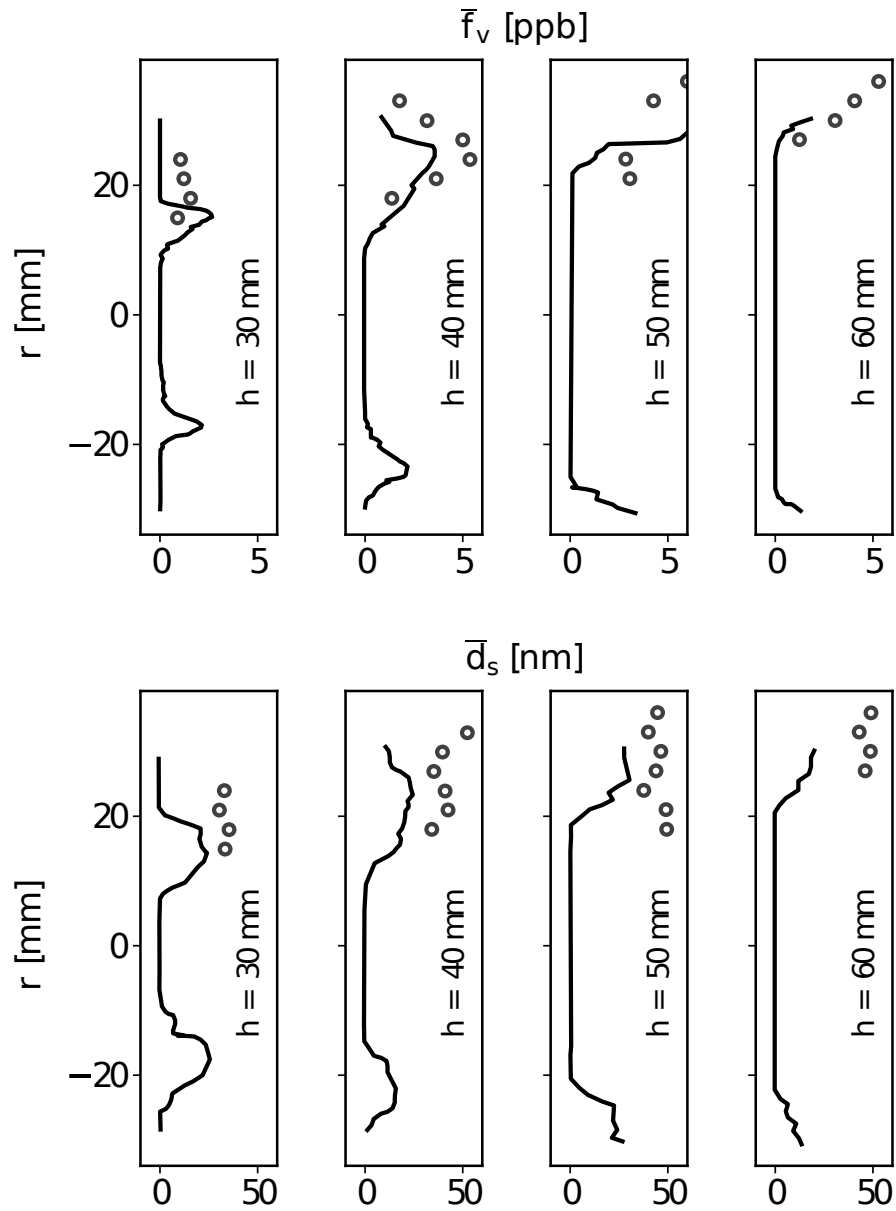


Figure 9.9: UTIAS configuration: Radial profiles of mean soot volume fraction (top) and mean soot primary diameter (bottom) at four axial positions: LES (line) vs LII measurements (symbols).

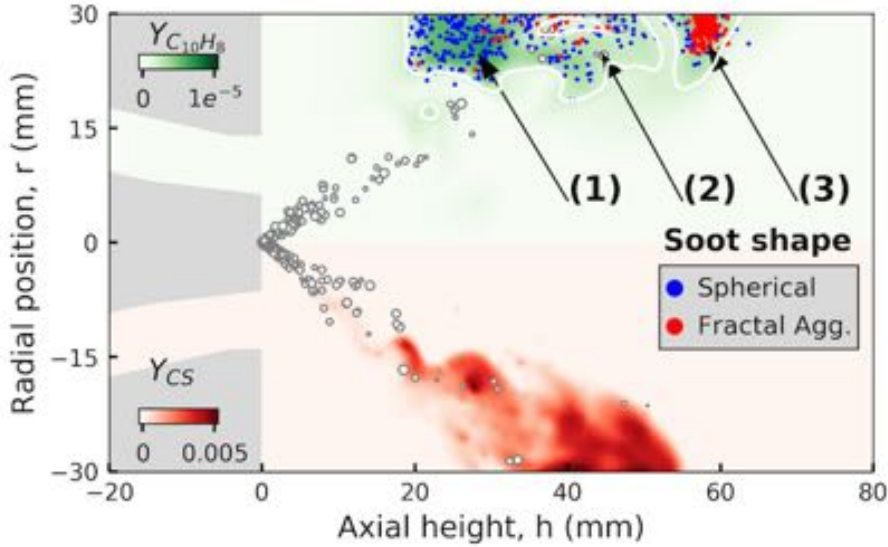


Figure 9.10: UTIAS configuration: Instantaneous field of naphthalene mass fraction (top) with overlaid iso-contours of soot nucleation and soot particles. Instantaneous Y_{CS} field (bottom) with some droplets represented by circles.

the field of naphthalene ($C_{10}H_8$ or $A2$) with soot particles. A rich mixture is found, composed of vaporized fuel and C_2H_2 . In the top part the white iso-contour corresponds to the nucleation zone where the source term defined in Eq. 6.3 is large enough for soot inception. Soot particles are represented by dots (only one particle out of one thousand is shown for clarity). Fractal aggregates (red dot) are distinguished from spherical particles (blue) according to their surface. Soot is located where concentration of $C_{10}H_8$ and temperature are high. Three zones are distinguished. First a nucleation region (1) correspond to the formation of fresh nucleated particles. Particles are then convected downstream in rich Y_{CS} zone, where fractal aggregates form. The zone (2) is favorable for soot growth in near-walls region where the higher residence time and the presence of $C_{10}H_8$ increases respectively condensation rate. Finally, in zone (3) the soot particles cross the high OH concentration region, leading to their full oxidation. Both soot and droplets intermittency, indicating the probability of having (1) or not having (0) particles, over 30 ms are plotted in Fig. 9.11. Note that the soot intermittency is low compared to the one observed in the FIRST configuration of Chap. 8 (Fig. 8.30). This confirms that soot particles are mostly form at the tip of the spray, in the near-wall regions. The location of soot particles qualitatively coincides with experimental visualisation shown in Fig. 9.12, where red boxes correspond to the presence of soot indicated by their high emission in the visible spectrum.

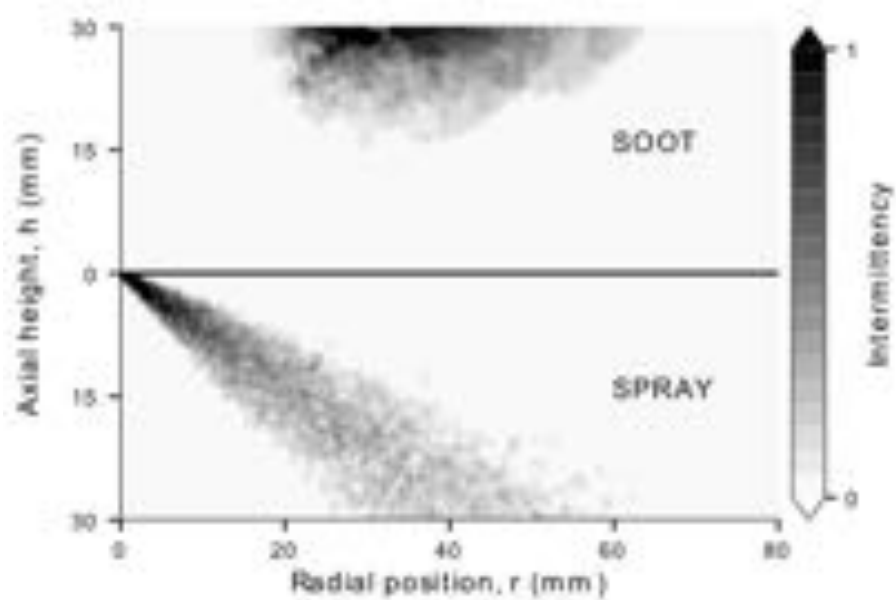


Figure 9.11: UTIAS configuration: Spray and Soot particles intermittency over 30 ms.



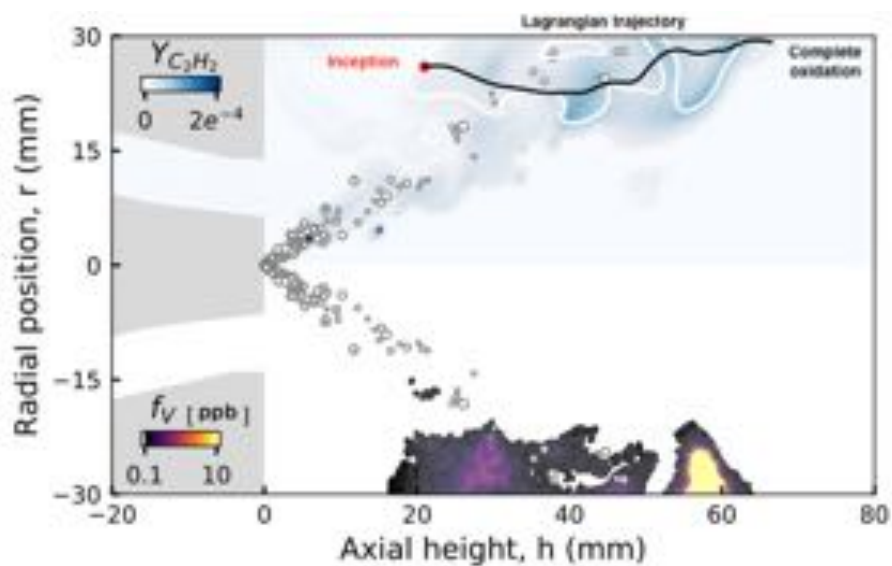
Figure 9.12: UTIAS configuration: Visualization of soot for the selected operating conditions. (Courtesy of Wang *et al.*)

9.3.4 Particle dynamics and size distribution

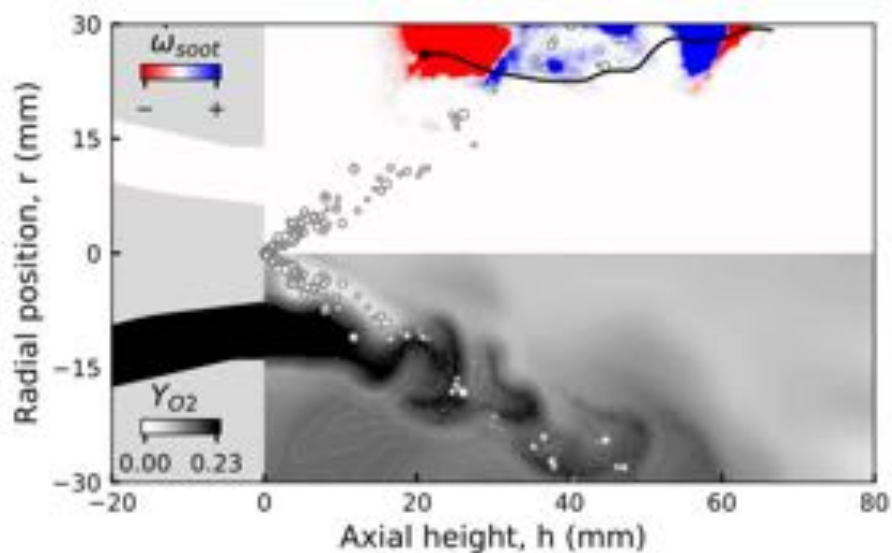
The Lagrangian trajectory displayed in Fig. 9.13 corresponds to the trajectory of a single soot particle. The Lagrangian trajectory is studied over a set of Lagrangian solution following the particle identity number until its complete oxidation corresponding to roughly 10 *ms* chosen long enough to analyse soot evolution. The shown instantaneous field is taken at the time of inception of the studied particle. Figure 9.13a shows a field of C₂H₂ (top) with overlaid white isocontour corresponding to soot nucleation and soot volume fraction ($f_v > 0.1ppb$) (bottom). Additionally, the soot mass source term \dot{m}_p (top) and O₂ mass fraction (bottom) are displayed in Fig. 9.13b. The source term \dot{m}_p does not account for nucleation and only contains surface growth, condensation and oxidation. The presence of O₂ prevents from soot particles in the bottom of the combustion chamber ($h < 20mm$), by inducing a strong oxidation source term in the bottom part of soot nucleation zone ($20mm < h < 30mm$). Then soot growth is driven by the presence of rich pockets of C₂H₂ downstream the nucleation point ($30mm < h < 50mm$). Because of the absence of significant levels of C₁₀H₈ condensation does not occur (see Fig. 9.10), the levels of C₁₀H₈ contribute mainly to nucleation. The soot growth source term appears at $h \sim 50mm$ very much distributed and scarce, as a result of the large fuel droplets. A downstream pocket of C₁₀H₈ leads to a strong condensation rate. Finally soot particles encounter a region of high OH (see Fig. 9.7) resulting in their complete oxidation.

To confirm these observations, the evolutions of soot source terms, flow features and PSDF are plotted along the Lagrangian trajectory in Fig. 9.14. The Lagrangian evolution of the PSDF exhibits overall a one-peak shape as expected from the low level of soot volume fraction ($\sim 10ppb$). However a small second peak can be distinguished at three locations, marked (1), (2) and (3) at half trajectory ($3ms < t < 8ms$) before complete oxidation. These peaks are reported in Fig. 9.14. As shown in Fig. 9.13b, the first peak is linked to surface growth and collision, while the two others are linked to condensation and coagulation. The analysis of liquid volume fraction indicates also that these peaks are preceded by the presence of fuel droplets and tend to form in premixed flames while oxidation by OH is located in diffusion flames.

To go further, the statistical PSDF is investigated at four locations and displayed in Fig. 9.15. These locations correspond to the maximum soot volume fraction observed experimentally (see Fig. 9.9). In the first location ($r = 15mm, h = 30mm$), a narrow unimodal shape can be distinguished, corresponding to the nucleation mode. Larger particles are present but stay insignificant in terms of number density. Further downstream ($r = 20mm, h = 40mm$), a similar shape is observed with more large particles.



(a)



(b)

Figure 9.13: UTIAS configuration: a) C_2H_2 (top) and f_v (bottom), b) soot source term (top) and O_2 (bottom). In both images, the spray is represented by circles and one example of soot trajectory is shown.

9. LES IN A TURBULENT SPRAY FLAME

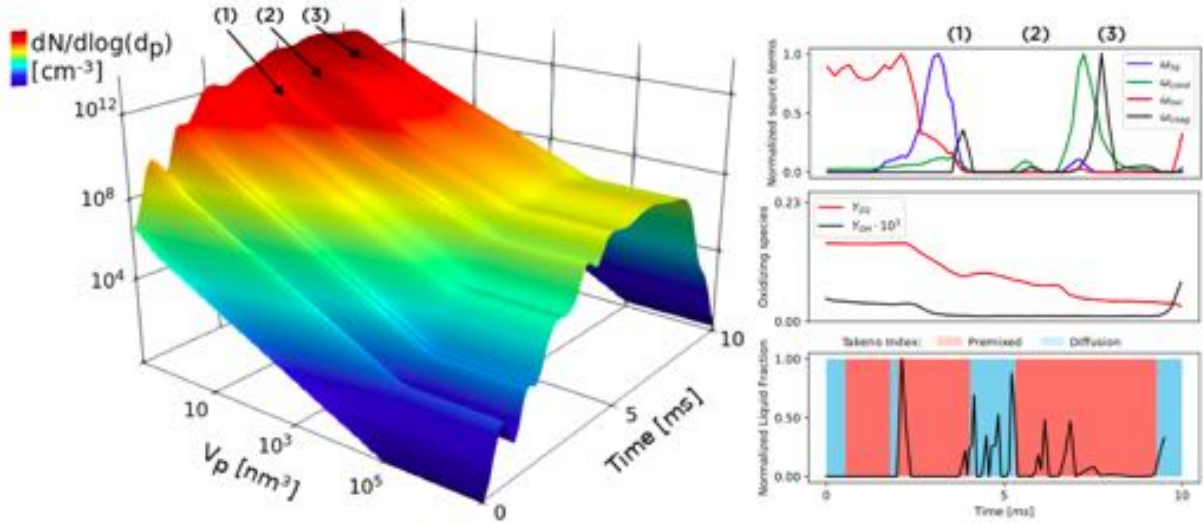


Figure 9.14: UTIAS configuration: a) PSDF evolution along the Lagrangian trajectory. b) Soot source terms (top), oxidizing species mass fractions (middle) and liquid volume fraction (bottom) along the particle trajectory.

	Without soot particles	With soot particles
CPUh for one convective time	76200	88944
% of time spent for the Lagrangian solver	8	12.5

Table 9.1: UTIAS configuration: Comparison of computational times with and without the computation of soot particles.

The numerically-predicted peak of soot volume fraction ($r = 25\text{mm}$, $h = 50\text{mm}$) exhibits much more soot particles (nascent and large particles) but intermittently at this location. No bimodal PSDF is observed. Finally ($r = 30\text{mm}$, $h = 60\text{mm}$), the number density of soot particles decreases for both nascent and large soot particles suggesting an efficient soot oxidation.

9.4 Computational cost

The computational cost of the UTIAS configuration with and without soot particles is reported in Tab. 9.1. In this configuration, approximately $100M$ of numerical soot particles are computed, while no more than $30k$ fuel droplets are present. Fortunately, the computational cost of the soot model is not proportional to the number of numerical soot particles thanks to the numerical strategy detailed in Chap. 4. Finally the amount of time spent in the Lagrangian solver remains affordable, representing only 12.5% of the total computational cost.

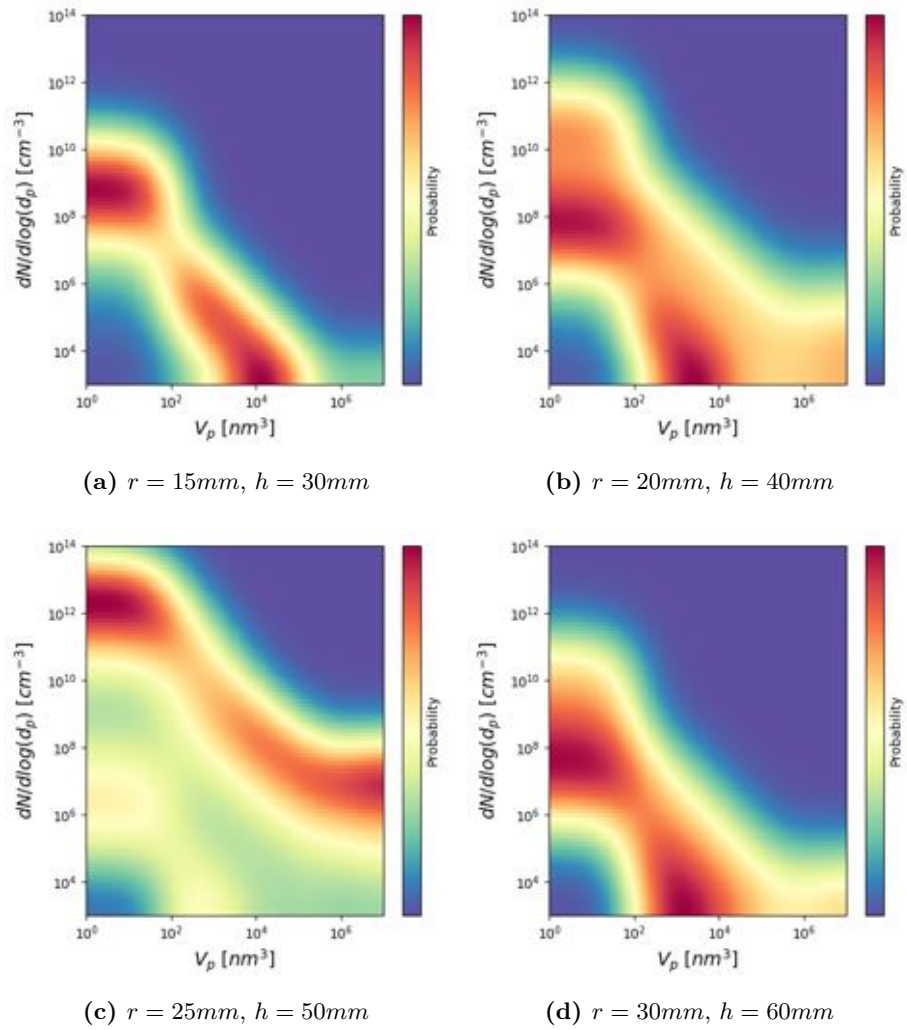


Figure 9.15: UTIAS configuration: Statistical PSDF at four locations.

9.5 Conclusions

A reduced mechanism for Jet A-1 using HyChem model including PAH chemistry has been validated for soot prediction in turbulent spray flames. The reduced mechanism is coupled with the Lagrangian Soot Tracking method to handle soot evolution using a bivariate description (volume-surface). The turbulent spray flame UTIAS Jet A-1 burner has been calculated and compared with measurements when available. Results confirm that the proposed approach is able to capture both the volume and shape of soot particles in a complex configuration burning complex fuel. The Lagrangian trajectory of soot particle has been analysed giving more insight about the localization and the dynamics of soot particles. Finally the PSDF has been investigated along the Lagrangian trajectory as well as the statistical PSDF at different locations. Although all PSDF exhibit a one-peak shape typical of such low soot volume fraction levels (*ppb*), two-peak shapes have been observed along the Lagrangian trajectory.

Chapter 10

Conclusions and perspectives

This thesis aims at developing a methodology for soot prediction applicable to complex industrial geometries including detailed soot chemistry. It is based on the use of both Analytically Reduced Chemistry (ARC), including accurate PAH description and a Lagrangian based soot model. Concerning flame chemistry including PAH, ARC have been derived for ethylene, and kerosene flames up to PAH and validated by comparison with detailed chemistry. The Lagrangian formalism is conceptually simple and is particularly suited for the simulation of soot particles as additional variables can be easily transported for the particles without additional cost. In this thesis, Lagrangian Soot Tracking (LST) has been developed with the implementation of both reliable numerical methods and physical processes to model soot chemistry. A thorough validation of the methodology has been performed on one-dimensional laminar cases and compared with measurements and a mature existing sectional approach, showing that a satisfactory prediction of soot particles and PSDF is obtained with LST approach. To validate the methodology coupling ARC to LST, experimentally well-characterized laminar flames from the International Sooting Flame (ISF) workshop have been computed. A very good agreement for PAH and soot has been obtained.

The methodology is then applied to two academic turbulent swirled configurations involving different technical aspects. In the confined pressurized ethylene-air burner (FIRST) configuration measured at DLR, the reference case for ISF, two ARCs have been derived varying the PAH sub-mechanism in order to highlight the impact of the selected nucleating species on the soot results. The impact of radiative heat transfer has also been investigated, resulting in four LES. Both the flame structure and the soot formation are well reproduced for all computations. Results have shown the impact of the nucleating species in the final soot levels and soot intermittency, confirming the key role of large PAH, especially in a configuration where nucleation is in constant competition with oxidation. Results without radiative heat transfer have been found in better agreement with measurements, except in the root of the flame. The surface-volume particle description where soot coagulation is modeled as pure aggregation, has been found to overestimate soot particles surface and thus soot oxidation rate.

The second application is a turbulent confined swirled spray Jet A-1/air burner (UTIAS

10. CONCLUSIONS AND PERSPECTIVES

Jet A-1 burner) measured at UTIAS. The aviation jet fuel oxidation chemistry is modeled by the recent HyChem methodology proposed by the group of Pr. Wang at Stanford. Combining HyChem reactions for jet A1 pyrolysis and ARC for ethylene oxidation, very good agreement for both the reacting flow field and the soot formation is obtained when comparing to available measurements. The results have illustrated the significant impact of liquid fuel pyrolysis in the soot formation, highlighting the contribution of aromatics included in the aviation jet fuel. Despite the overall lean conditions, the accumulation of rich fuel mixture close to the walls due to the flame confinement has been found to be responsible of soot formation, contrary to the FIRST configuration where hydrodynamic instabilities drive the soot formation.

Overall, satisfactory prediction of soot particles at an affordable computational cost has been achieved on both academic configurations considered, representative of aeronautical combustors featuring high-pressure, dilution jets, swirled flows and aviation jet fuel. It demonstrates the prediction capability of the proposed methodology. In this work, the development of a newly Lagrangian based soot model has required a long validation phase. The actual soot chemistry is based on soot sectional model for validation purpose, done in laminar flames only, confirming LST accuracy, but does not take full advantages of the Lagrangian formalism. Thus, the Lagrangian based soot model can be improved by including additional phenomena occurring in soot formation:

- Soot thermophoresis can be accounted for and may be significant in near-wall regions, when dealing with confined turbulent flames.
- A criteria to distinguish pure-aggregation from coalescence as well as the transition phase [103, 382] should be employed in future work to accurately capture soot surface evolution and then soot morphology.
- The evolution of active sites through H description [103], to account for soot surface reactivity in surface growth and oxidation rates, could be introduced without additional computational cost.
- The implementation of more realistic boundary conditions for soot particles which may impact the soot distribution in confined turbulent flames, can be intended following two-phase flow developments.
- The merging of particles can be enhanced following recent works [195] avoiding the transport of redundant numerical particles.

The Lagrangian based soot model has been introduced as an alternative to classical approaches to accurately model soot PSDF in complex configuration without any assumption at an affordable computational cost. The approach meets its initial objectives,

Lagrangian based soot model is found affordable for all computations considered in this work with a small overcost confirming its application towards industrial configurations, already under way in real aeronautical engines at Safran Aircraft Engines and Safran Helicopters Engines through the SOPRANO H2020 project.

10. CONCLUSIONS AND PERSPECTIVES

Bibliography

- [1] Airbus, “Global market forecast 2018-2034,” 2019. [10](#)
- [2] C. Guerreiro, A. G. Ortiz, F. de Leeuw, M. Viana, and J. Horálek, *Air quality in Europe-2016 report*. Publications Office of the European Union, 2016. [11](#), [14](#)
- [3] M. Masiol and R. M. Harrison, “Aircraft engine exhaust emissions and other airport-related contributions to ambient air pollution: A review,” *Atmospheric Environment*, vol. 95, pp. 409–455, 2014. [11](#)
- [4] D. S. Lee, D. W. Fahey, P. M. Forster, P. J. Newton, R. C. Wit, L. L. Lim, B. Owen, and R. Sausen, “Aviation and global climate change in the 21st century,” *Atmospheric Environment*, vol. 43, no. 22-23, pp. 3520–3537, 2009. [11](#)
- [5] H. Shen, Y. Huang, R. Wang, D. Zhu, W. Li, G. Shen, B. Wang, Y. Zhang, Y. Chen, Y. Lu, *et al.*, “Global atmospheric emissions of polycyclic aromatic hydrocarbons from 1960 to 2008 and future predictions,” *Environmental Science & Technology*, vol. 47, no. 12, pp. 6415–6424, 2013. [11](#)
- [6] H. Wang, “Formation of nascent soot and other condensed-phase materials in flames,” *Proc. Combust. Inst.*, vol. 33, no. 1, pp. 41–67, 2011. [11](#), [17](#), [21](#), [29](#), [33](#), [35](#), [36](#), [104](#), [105](#)
- [7] W. H. Organization *et al.*, “Hazard prevention and control in the work environment:: airborne dust,” 1999. [12](#)
- [8] ICAO, “Annex 16 to the convention on international civil aviation: Environmental protection, volume ii: Aircraft engine emissions, international civil aviation organization (icao), fourth edition, july 2017,” 2017. [12](#), [16](#)
- [9] M. Shiraiwa, K. Selzle, and U. Pöschl, “Hazardous components and health effects of atmospheric aerosol particles: reactive oxygen species, soot, polycyclic aromatic compounds and allergenic proteins,” *Free Radical Research*, vol. 46, no. 8, pp. 927–939, 2012. [12](#), [13](#)
- [10] A. Saxon and D. Diaz-Sanchez, “Air pollution and allergy: you are what you breathe,” *Nature Immunology*, vol. 6, no. 3, p. 223, 2005. [12](#)
- [11] T. F. Stocker, D. Qin, G.-K. Plattner, M. Tignor, S. K. Allen, J. Boschung, A. Nauels, Y. Xia, V. Bex, P. M. Midgley, *et al.*, “Climate change 2013: The physical science basis,” 2013. [13](#)

BIBLIOGRAPHY

- [12] T. C. Bond and R. W. Bergstrom, “Light absorption by carbonaceous particles: An investigative review,” *Aerosol Science and Technology*, vol. 40, no. 1, pp. 27–67, 2006. [13](#)
- [13] T. C. Bond, S. J. Doherty, D. W. Fahey, P. M. Forster, T. Berntsen, B. J. DeAngelo, M. G. Flanner, S. Ghan, B. Kärcher, D. Koch, *et al.*, “Bounding the role of black carbon in the climate system: A scientific assessment,” *Journal of Geophysical Research: Atmospheres*, vol. 118, no. 11, pp. 5380–5552, 2013. [13](#)
- [14] J. H. Seinfeld, C. Bretherton, K. S. Carslaw, H. Coe, P. J. DeMott, E. J. Dunlea, G. Feingold, S. Ghan, A. B. Guenther, R. Kahn, *et al.*, “Improving our fundamental understanding of the role of aerosol- cloud interactions in the climate system,” *Proceedings of the National Academy of Sciences*, vol. 113, no. 21, pp. 5781–5790, 2016. [13](#)
- [15] B. Kärcher, “Formation and radiative forcing of contrail cirrus,” *Nature communications*, vol. 9, no. 1, pp. 1–17, 2018. [13](#), [14](#)
- [16] U. Schumann, “On conditions for contrail formation from aircraft exhausts,” *Meteorologische Zeitschrift*, pp. 4–23, 1996. [14](#)
- [17] D. S. Lee, G. Pitari, V. Grewe, K. Gierens, J. Penner, A. Petzold, M. Prather, U. Schumann, A. Bais, T. Berntsen, *et al.*, “Transport impacts on atmosphere and climate: Aviation,” *Atmospheric environment*, vol. 44, no. 37, pp. 4678–4734, 2010. [14](#)
- [18] D. Delhaye, F.-X. Ouf, D. Ferry, I. K. Ortega, O. Penanhoat, S. Peillon, F. Salm, X. Vancassel, C. Focsa, C. Irimiea, *et al.*, “The mermose project: Characterization of particulate matter emissions of a commercial aircraft engine,” *Journal of Aerosol Science*, vol. 105, pp. 48–63, 2017. [14](#), [22](#), [27](#)
- [19] M. Saffaripour, K. A. Thomson, G. J. Smallwood, and P. Lobo, “A review on the morphological properties of non-volatile particulate matter emissions from aircraft turbine engines,” *Journal of Aerosol Science*, p. 105467, 2019. [14](#)
- [20] F. Collin-Bastiani, *Modeling and Large Eddy Simulation of Two-Phase Ignition in Gas Turbines*. PhD thesis, Institut National Polytechnique de Toulouse-INPT, 2019. [15](#)
- [21] A. H. Lefebvre, D. R. Ballal, and D. W. Bahr, *Gas turbine combustion: alternative fuels and emissions*. 2010. [15](#), [168](#)

- [22] L.-Y. Wang, C. K. Bauer, and Ö. L. Gülder, “Soot and flow field in turbulent swirl-stabilized spray flames of jet a-1 in a model combustor,” *Proc. Combust. Inst.*, vol. 37, no. 4, pp. 5437–5444, 2019. [15](#), [115](#), [211](#), [212](#), [214](#), [217](#), [218](#)
- [23] M. Stöhr, K. Geigle, R. Hedef, I. Boxx, C. Carter, M. Grader, and P. Gerlinger, “Time-resolved study of transient soot formation in an aero-engine model combustor at elevated pressure,” *Proc. Combust. Inst.*, vol. 37, no. 4, pp. 5421–5428, 2019. [16](#), [167](#), [168](#), [190](#), [194](#)
- [24] F. Collin-Bastiani, J. Marrero-Santiago, E. Riber, G. Cabot, B. Renou, and B. Cuenot, “A joint experimental and numerical study of ignition in a spray burner,” *Proc. Combust. Inst.*, vol. 37, no. 4, pp. 5047–5055, 2019. [16](#), [17](#), [65](#)
- [25] L. Gicquel, G. Staffelbach, and T. Poinso, “Large Eddy Simulations of gaseous flames in gas turbine combustion chambers,” *Progress in Energy and Combustion Science*, vol. 38, no. 6, pp. 782–817, 2012. [17](#)
- [26] P. Wolf, G. Staffelbach, L. Y. Gicquel, J.-D. Müller, and T. Poinso, “Acoustic and large eddy simulation studies of azimuthal modes in annular combustion chambers,” *Combustion and Flame*, vol. 159, no. 11, pp. 3398–3413, 2012. [17](#)
- [27] B. Rochette, F. Collin-Bastiani, L. Gicquel, O. Vermorel, D. Veynante, and T. Poinso, “Influence of chemical schemes, numerical method and dynamic turbulent combustion modeling on LES of premixed turbulent flames,” *Combust. Flame*, vol. 191, pp. 417–430, 2018. [17](#)
- [28] M. Ihme and H. Pitsch, “Modeling of radiation and nitric oxide formation in turbulent nonpremixed flames using a flamelet/progress variable formulation,” *Physics of Fluids*, vol. 20, no. 5, p. 055110, 2008. [17](#), [62](#), [63](#)
- [29] C. Locci, O. Colin, D. Poitou, and F. Mauss, “A tabulated, flamelet based no model for large eddy simulations of non premixed turbulent jets with enthalpy loss,” *Flow, Turbulence and Combustion*, vol. 94, no. 4, pp. 691–729, 2015. [17](#)
- [30] T. Jaravel, E. Riber, B. Cuenot, and G. Bulat, “Large Eddy Simulation of an industrial gas turbine combustor using reduced chemistry with accurate pollutant prediction,” *Proc. Combust. Inst.*, vol. 36, no. 3, pp. 3817–3825, 2017. [17](#), [62](#), [65](#)
- [31] T. Jaravel, E. Riber, B. Cuenot, and P. Pepiot, “Prediction of flame structure and pollutant formation of sandia flame d using large eddy simulation with direct integration of chemical kinetics,” *Combustion and Flame*, vol. 188, pp. 180–198, 2018. [17](#), [62](#), [100](#)

BIBLIOGRAPHY

- [32] J. Lamouroux, S. Richard, Q. Male, G. Staffelbach, A. Dauplain, and A. Misdariis, “On the combination of large eddy simulation and phenomenological soot modeling to calculate the smoke index from aero-engines over a large range of operating conditions,” *J. Eng. Gas Turbines and Power*, vol. 140, no. 10, p. 101501, 2018. [17](#), [18](#)
- [33] G. Lecocq, D. Poitou, I. Hernández, F. Duchaine, E. Riber, and B. Cuenot, “A methodology for soot prediction including thermal radiation in complex industrial burners,” *Flow, Turbulence and Combustion*, vol. 92, no. 4, pp. 947–970, 2014. [18](#), [84](#)
- [34] B. Franzelli, E. Riber, B. Cuenot, and M. Ihme, “Numerical modeling of soot production in aero-engine combustors using large eddy simulations,” in *ASME Turbo Expo*, vol. 56697, p. V04BT04A049, 2015. [18](#)
- [35] A. Felden, E. Riber, and B. Cuenot, “Impact of direct integration of analytically reduced chemistry in les of a sooting swirled non-premixed combustor,” *Combustion and Flame*, vol. 191, pp. 270–286, 2018. [18](#), [62](#), [65](#), [83](#), [84](#), [86](#), [100](#), [167](#), [169](#), [171](#), [180](#), [181](#)
- [36] M. E. Mueller and H. Pitsch, “Les model for sooting turbulent nonpremixed flames,” *Combustion and Flame*, vol. 159, no. 6, pp. 2166–2180, 2012. [19](#), [65](#), [104](#)
- [37] P. Rodrigues, B. Franzelli, R. Vicquelin, O. Gicquel, and N. Darabiha, “Coupling an les approach and a soot sectional model for the study of sooting turbulent non-premixed flames,” *Combustion and Flame*, vol. 190, pp. 477–499, 2018. [19](#), [40](#), [43](#), [65](#), [85](#), [205](#)
- [38] M. Lucchesi, A. Abdelgadir, A. Attili, and F. Bisetti, “Simulation and analysis of the soot particle size distribution in a turbulent nonpremixed flame,” *Combustion and Flame*, vol. 178, pp. 35–45, 2017. [19](#), [41](#), [76](#)
- [39] P. Pepiot-Desjardins and H. Pitsch, “An efficient error-propagation-based reduction method for large chemical kinetic mechanisms,” *Combust. Flame*, vol. 154, no. 1-2, pp. 67–81, 2008. [19](#), [60](#), [92](#), [98](#), [99](#)
- [40] A. Felden, P. Pepiot, L. Esclapez, E. Riber, and B. Cuenot, “Including analytically reduced chemistry (ARC) in CFD applications,” *Acta Astronautica*, vol. 158, pp. 444–459, 2019. [19](#)
- [41] R. L. Vander Wal, A. Yezerets, N. W. Currier, D. H. Kim, and C. M. Wang, “Hrtem study of diesel soot collected from diesel particulate filters,” *Carbon*, vol. 45, no. 1, pp. 70–77, 2007. [21](#), [22](#)

- [42] C. M. Megaridis and R. A. Dobbins, “Morphological description of flame-generated materials,” *Combustion science and technology*, vol. 71, no. 1-3, pp. 95–109, 1990. [21](#)
- [43] R. Puri, T. Richardson, R. Santoro, and R. Dobbins, “Aerosol dynamic processes of soot aggregates in a laminar ethene diffusion flame,” *Combustion and Flame*, vol. 92, no. 3, pp. 320–333, 1993. [21](#)
- [44] M. Kholghy, M. Saffaripour, C. Yip, and M. J. Thomson, “The evolution of soot morphology in a laminar coflow diffusion flame of a surrogate for jet a-1,” *Combustion and Flame*, vol. 160, no. 10, pp. 2119–2130, 2013. [21](#)
- [45] S. Chatterjee and Ö. L. Gülder, “Soot concentration and primary particle size in swirl-stabilized non-premixed turbulent flames of ethylene and air,” *Experimental Thermal and Fluid Science*, vol. 95, pp. 73–80, 2018. [21](#)
- [46] R. L. Vander Wal, V. M. Bryg, and C.-H. Huang, “Aircraft engine particulate matter: macro-micro-and nanostructure by hrtem and chemistry by xps,” *Combustion and Flame*, vol. 161, no. 2, pp. 602–611, 2014. [21](#), [22](#), [23](#)
- [47] G. Vitiello, G. De Falco, F. Picca, M. Commodo, G. D’Errico, P. Minutolo, and A. D’Anna, “Role of radicals in carbon clustering and soot inception: A combined epr and raman spectroscopic study,” *Combustion and Flame*, vol. 205, pp. 286–294, 2019. [22](#), [24](#)
- [48] Ü. Ö. Köylü and G. M. Faeth, “Structure of overfire soot in buoyant turbulent diffusion flames at long residence times,” *Combustion and Flame*, vol. 89, no. 2, pp. 140–156, 1992. [22](#)
- [49] T. Charalampopoulos and H. Chang, “Agglomerate parameters and fractal dimension of soot using light scattering—effects on surface growth,” *Combustion and Flame*, vol. 87, no. 1, pp. 89–99, 1991. [24](#)
- [50] C. Sorensen, J. Cai, and N. Lu, “Light-scattering measurements of monomer size, monomers per aggregate, and fractal dimension for soot aggregates in flames,” *Applied Optics*, vol. 31, no. 30, pp. 6547–6557, 1992. [24](#)
- [51] Ü. Ö. Köylü, G. Faeth, T. L. Farias, and M. d. G. Carvalho, “Fractal and projected structure properties of soot aggregates,” *Combustion and Flame*, vol. 100, no. 4, pp. 621–633, 1995. [24](#)
- [52] M. M. Maricq and N. Xu, “The effective density and fractal dimension of soot particles from premixed flames and motor vehicle exhaust,” *Journal of Aerosol Science*, vol. 35, no. 10, pp. 1251–1274, 2004. [24](#)

BIBLIOGRAPHY

- [53] A. E. Karataş and Ö. L. Gülder, “Soot formation in high pressure laminar diffusion flames,” *Progress in Energy and Combustion Science*, vol. 38, no. 6, pp. 818–845, 2012. [24](#)
- [54] A. M. Vargas and Ö. L. Gülder, “Pressure dependence of primary soot particle size determined using thermophoretic sampling in laminar methane-air diffusion flames,” *Proc. Combust. Inst.*, vol. 36, no. 1, pp. 975–984, 2017. [24](#)
- [55] A. M. Vargas, *Design and Development of a Thermophoretic Soot Sampling System for High-Pressure Laminar Diffusion Flames*. PhD thesis, 2016. [25](#)
- [56] H. Böhm, D. Hesse, H. Jander, B. Lüers, J. Pietscher, H. Wagner, and M. Weiss, “The influence of pressure and temperature on soot formation in premixed flames,” in *Symposium (International) on Combustion*, vol. 22, pp. 403–411, Elsevier, 1989. [25](#)
- [57] B. Zhao, Z. Yang, Z. Li, M. V. Johnston, and H. Wang, “Particle size distribution function of incipient soot in laminar premixed ethylene flames: effect of flame temperature,” *Proc. Combust. Inst.*, vol. 30, no. 1, pp. 1441–1448, 2005. [25](#), [30](#), [31](#), [77](#)
- [58] Z. Hong, D. Davidson, S. Vasu, and R. Hanson, “The effect of oxygenates on soot formation in rich heptane mixtures: a shock tube study,” *Fuel*, vol. 88, no. 10, pp. 1901–1906, 2009. [25](#)
- [59] B. Apicella, A. Tregrossi, A. Ciajolo, J. Abrahamson, R. L. Vander Wal, and C. Russo, “The effect of temperature on soot properties in premixed ethylene flames,” *Combustion science and technology*, pp. 1–13, 2019. [26](#)
- [60] M. Alfè, B. Apicella, R. Barbella, J.-N. Rouzaud, A. Tregrossi, and A. Ciajolo, “Structure–property relationship in nanostructures of young and mature soot in premixed flames,” *Proc. Combust. Inst.*, vol. 32, no. 1, pp. 697–704, 2009. [26](#), [27](#)
- [61] C. Russo, F. Stanzione, A. Ciajolo, and A. Tregrossi, “Study on the contribution of different molecular weight species to the absorption uv–visible spectra of flame-formed carbon species,” *Proc. Combust. Inst.*, vol. 34, no. 2, pp. 3661–3668, 2013. [26](#)
- [62] I. C. Jaramillo, C. K. Gaddam, R. L. Vander Wal, C.-H. Huang, J. D. Levinthal, and J. S. Lighty, “Soot oxidation kinetics under pressurized conditions,” *Combustion and Flame*, vol. 161, no. 11, pp. 2951–2965, 2014. [26](#)

- [63] M. L. Botero, D. Chen, S. González-Calera, D. Jefferson, and M. Kraft, “HRTEM evaluation of soot particles produced by the non-premixed combustion of liquid fuels,” *Carbon*, vol. 96, pp. 459–473, 2016. [27](#)
- [64] C. Saggese, A. V. Singh, X. Xue, C. Chu, M. R. Kholghy, T. Zhang, J. Camacho, J. Giaccai, J. H. Miller, M. J. Thomson, *et al.*, “The distillation curve and sooting propensity of a typical jet fuel,” *Fuel*, vol. 235, pp. 350–362, 2019. [27](#), [114](#)
- [65] I. C. Jaramillo, A. Sturrock, H. Ghiassi, D. J. Woller, C. E. Deering-Rice, J. S. Lighty, R. Paine, C. Reilly, and K. E. Kelly, “Effects of fuel components and combustion particle physicochemical properties on toxicological responses of lung cells,” *Journal of Environmental Science and Health, Part A*, vol. 53, no. 4, pp. 295–309, 2018. [27](#)
- [66] P. W., *Chemical and Physical Pathways of PAH and Soot Formation in Laminar Flames*. PhD thesis, ULB, 2019. [28](#), [33](#), [44](#), [93](#), [105](#)
- [67] M. Frenklach, D. W. Clary, W. C. Gardiner Jr, and S. E. Stein, “Detailed kinetic modeling of soot formation in shock-tube pyrolysis of acetylene,” in *Symposium (International) on Combustion*, vol. 20, pp. 887–901, Elsevier, 1985. [28](#), [29](#), [119](#)
- [68] J. A. Miller and C. F. Melius, “Kinetic and thermodynamic issues in the formation of aromatic compounds in flames of aliphatic fuels,” *Combustion and Flame*, vol. 91, no. 1, pp. 21–39, 1992. [29](#)
- [69] M. Frenklach and H. Wang, “Detailed mechanism and modeling of soot particle formation,” in *Soot formation in combustion*, pp. 165–192, Springer, Berlin, Heidelberg, 1994. [29](#), [31](#), [32](#)
- [70] A. M. Mebel, A. Landera, and R. I. Kaiser, “Formation mechanisms of naphthalene and indene: from the interstellar medium to combustion flames,” *The Journal of Physical Chemistry A*, vol. 121, no. 5, pp. 901–926, 2017. [29](#)
- [71] R. G. Butler and I. Glassman, “Cyclopentadiene combustion in a plug flow reactor near 1150 K,” *Proc. Combust. Inst.*, vol. 32, no. 1, pp. 395–402, 2009. [29](#)
- [72] M. R. Djokic, K. M. Van Geem, C. Cavallotti, A. Frassoldati, E. Ranzi, and G. B. Marin, “An experimental and kinetic modeling study of cyclopentadiene pyrolysis: First growth of polycyclic aromatic hydrocarbons,” *Combustion and Flame*, vol. 161, no. 11, pp. 2739–2751, 2014. [29](#)
- [73] D. H. Kim, J. A. Mulholland, D. Wang, and A. Violi, “Pyrolytic hydrocarbon growth from cyclopentadiene,” *The Journal of Physical Chemistry A*, vol. 114, no. 47, pp. 12411–12416, 2010. [29](#)

BIBLIOGRAPHY

- [74] C. Cavallotti, D. Polino, A. Frassoldati, and E. Ranzi, “Analysis of some reaction pathways active during cyclopentadiene pyrolysis,” *The Journal of Physical Chemistry A*, vol. 116, no. 13, pp. 3313–3324, 2012. [29](#)
- [75] A. E. Long, S. S. Merchant, A. G. Vandeputte, H.-H. Carstensen, A. J. Vervust, G. B. Marin, K. M. Van Geem, and W. H. Green, “Pressure dependent kinetic analysis of pathways to naphthalene from cyclopentadienyl recombination,” *Combustion and Flame*, vol. 187, pp. 247–256, 2018. [29](#)
- [76] H. Kroto, “Space, stars, c60, and soot,” *Science*, vol. 242, no. 4882, pp. 1139–1145, 1988. [30](#)
- [77] M. Frenklach and H. Wang, “Detailed modeling of soot particle nucleation and growth,” *Symp. (Int.) Combust.*, vol. 23, no. 1, pp. 1559–1566, 1991. [30](#), [32](#), [39](#)
- [78] C. A. Schuetz and M. Frenklach, “Nucleation of soot: molecular dynamics simulations of pyrene dimerization,” *Proc. Combust. Inst.*, vol. 29, no. 2, pp. 2307–2314, 2002. [30](#), [33](#), [36](#), [104](#)
- [79] A. D’Anna, “Combustion-formed nanoparticles,” *Proc. Combust. Inst.*, vol. 32, no. 1, pp. 593–613, 2009. [30](#)
- [80] K. Johansson, M. Head-Gordon, P. Schrader, K. Wilson, and H. Michelsen, “Resonance-stabilized hydrocarbon-radical chain reactions may explain soot inception and growth,” *Science*, vol. 361, no. 6406, pp. 997–1000, 2018. [30](#)
- [81] M. Thomson and T. Mitra, “A radical approach to soot formation,” *Science*, vol. 361, no. 6406, pp. 978–979, 2018. [31](#)
- [82] B. Haynes and H. G. Wagner, “The surface growth phenomenon in soot formation,” *Zeitschrift für Physikalische Chemie*, vol. 133, no. 2, pp. 201–213, 1982. [31](#)
- [83] S. J. Harris and A. M. Weiner, “Surface growth of soot particles in premixed ethylene/air flames,” *Combustion science and technology*, vol. 31, no. 3-4, pp. 155–167, 1983. [31](#)
- [84] M. Frenklach, “Reaction mechanism of soot formation in flames,” *Physical chemistry chemical Physics*, vol. 4, no. 11, pp. 2028–2037, 2002. [32](#), [42](#)
- [85] G. Blanquart and H. Pitsch, “A joint volume-surface-hydrogen multi-variate model for soot formation,” *Combustion generated fine carbonaceous particles*, pp. 437–463, 2009. [32](#), [100](#), [104](#), [118](#)

- [86] R. Whitesides and M. Frenklach, “Effect of reaction kinetics on graphene-edge morphology and composition,” *Zeitschrift für Physikalische Chemie*, vol. 229, no. 4, pp. 597–614, 2015. [32](#)
- [87] M. Frenklach, R. I. Singh, and A. M. Mebel, “On the low-temperature limit of haca,” *Proc. Combust. Inst.*, vol. 37, no. 1, pp. 969–976, 2019. [32](#)
- [88] H. Wang, D. Du, C. Sung, and C. K. Law, “Experiments and numerical simulation on soot formation in opposed-jet ethylene diffusion flames,” in *Symposium (International) on Combustion*, vol. 26, pp. 2359–2368, Elsevier, 1996. [32](#)
- [89] F. Mauß, T. Schäfer, and H. Bockhorn, “Inception and growth of soot particles in dependence on the surrounding gas phase,” *Combustion and Flame*, vol. 99, no. 3-4, pp. 697–705, 1994. [32](#), [119](#), [120](#)
- [90] F. MAUSS*, K. Netzell, and H. Lehtiniemi, “Aspects of modeling soot formation in turbulent diffusion flames,” *Combustion science and technology*, vol. 178, no. 10-11, pp. 1871–1885, 2006. [32](#), [119](#), [120](#)
- [91] M. Frenklach and J. Warnatz, “Detailed modeling of pah profiles in a sooting low-pressure acetylene flame,” *Combustion science and technology*, vol. 51, no. 4-6, pp. 265–283, 1987. [32](#)
- [92] H. Pitsch, “Detailed kinetic reaction mechanism for ignition and oxidation of α -methylnaphthalene,” in *Symposium (International) on Combustion*, vol. 26, pp. 721–728, Elsevier, 1996. [32](#)
- [93] J. Hwang and S. Chung, “Growth of soot particles in counterflow diffusion flames of ethylene,” *Combustion and Flame*, vol. 125, no. 1-2, pp. 752–762, 2001. [32](#)
- [94] Y. Wang, A. Raj, and S. H. Chung, “A pah growth mechanism and synergistic effect on pah formation in counterflow diffusion flames,” *Combustion and Flame*, vol. 160, no. 9, pp. 1667–1676, 2013. [32](#), [92](#), [93](#), [97](#), [98](#), [107](#), [114](#)
- [95] H.-B. Zhang, D. Hou, C. K. Law, and X. You, “Role of carbon-addition and hydrogen-migration reactions in soot surface growth,” *The Journal of Physical Chemistry A*, vol. 120, no. 5, pp. 683–689, 2016. [32](#)
- [96] S. J. Harris and A. M. Weiner, “Determination of the rate constant for soot surface growth,” *Combustion science and technology*, vol. 32, no. 5-6, pp. 267–275, 1983. [32](#)

BIBLIOGRAPHY

- [97] A. Kazakov, H. Wang, and M. Frenklach, “Detailed modeling of soot formation in laminar premixed ethylene flames at a pressure of 10 bar,” *Combustion and Flame*, vol. 100, no. 1-2, pp. 111–120, 1995. [32](#)
- [98] S. B. Dworkin, Q. Zhang, M. J. Thomson, N. A. Slavinskaya, and U. Riedel, “Application of an enhanced pah growth model to soot formation in a laminar coflow ethylene/air diffusion flame,” *Combustion and Flame*, vol. 158, no. 9, pp. 1682–1695, 2011. [32](#), [39](#), [43](#)
- [99] R. Lindstedt and B. Waldheim, “Modeling of soot particle size distributions in premixed stagnation flow flames,” *Proc. Combust. Inst.*, vol. 34, no. 1, pp. 1861–1868, 2013. [32](#), [39](#), [43](#), [104](#)
- [100] A. Veshkini, S. B. Dworkin, and M. J. Thomson, “A soot particle surface reactivity model applied to a wide range of laminar ethylene/air flames,” *Combustion and Flame*, vol. 161, no. 12, pp. 3191–3200, 2014. [32](#)
- [101] J. Appel, H. Bockhorn, and M. Frenklach, “Kinetic modeling of soot formation with detailed chemistry and physics: laminar premixed flames of c2 hydrocarbons,” *Combustion and Flame*, vol. 121, no. 1-2, pp. 122–136, 2000. [32](#) [34](#)
- [102] M. B. Colket and R. J. Hall, “Successes and uncertainties in modeling soot formation in laminar, premixed flames,” in *Soot formation in combustion*, pp. 442–470, Springer, 1994. [32](#)
- [103] G. Blanquart and H. Pitsch, “Analyzing the effects of temperature on soot formation with a joint volume-surface-hydrogen model,” *Combustion and Flame*, vol. 156, no. 8, pp. 1614–1626, 2009. [32](#), [42](#), [118](#), [228](#)
- [104] M. Saffaripour, A. Veshkini, M. Kholghy, and M. J. Thomson, “Experimental investigation and detailed modeling of soot aggregate formation and size distribution in laminar coflow diffusion flames of jet a-1, a synthetic kerosene, and n-decane,” *Combustion and Flame*, vol. 161, no. 3, pp. 848–863, 2014. [33](#)
- [105] M. Sirignano, J. Kent, and A. D’Anna, “Modeling formation and oxidation of soot in nonpremixed flames,” *Energy & Fuels*, vol. 27, no. 4, pp. 2303–2315, 2013. [33](#), [35](#), [44](#)
- [106] H. Sabbah, L. Biennier, S. J. Klippenstein, I. R. Sims, and B. R. Rowe, “Exploring the role of pahs in the formation of soot: pyrene dimerization,” *The Journal of Physical Chemistry Letters*, vol. 1, no. 19, pp. 2962–2967, 2010. [33](#), [104](#)

- [107] N. Eaves, S. Dworkin, and M. Thomson, “The importance of reversibility in modeling soot nucleation and condensation processes,” *Proc. Combust. Inst.*, vol. 35, no. 2, pp. 1787–1794, 2015. [33](#), [39](#), [131](#), [133](#)
- [108] C. Saggese, S. Ferrario, J. Camacho, A. Cuoci, A. Frassoldati, E. Ranzi, H. Wang, and T. Faravelli, “Kinetic modeling of particle size distribution of soot in a premixed burner-stabilized stagnation ethylene flame,” *Combustion and Flame*, vol. 162, no. 9, pp. 3356–3369, 2015. [33](#), [44](#), [64](#), [105](#), [106](#), [135](#), [137](#), [138](#), [139](#)
- [109] A. Barone, A. d’Alessio, and A. d’Anna, “Morphological characterization of the early process of soot formation by atomic force microscopy,” *Combustion and Flame*, vol. 132, no. 1-2, pp. 181–187, 2003. [33](#)
- [110] B. Zhao, K. Uchikawa, and H. Wang, “A comparative study of nanoparticles in premixed flames by scanning mobility particle sizer, small angle neutron scattering, and transmission electron microscopy,” *Proc. Combust. Inst.*, vol. 31, no. 1, pp. 851–860, 2007. [33](#)
- [111] A. D. Abid, N. Heinz, E. D. Tolmachoff, D. J. Phares, C. S. Campbell, and H. Wang, “On evolution of particle size distribution functions of incipient soot in premixed ethylene–oxygen–argon flames,” *Combustion and Flame*, vol. 154, no. 4, pp. 775–788, 2008. [33](#)
- [112] A. D’Alessio, A. Barone, R. Cau, A. D’Anna, and P. Minutolo, “Surface deposition and coagulation efficiency of combustion generated nanoparticles in the size range from 1 to 10 nm,” *Proc. Combust. Inst.*, vol. 30, no. 2, pp. 2595–2603, 2005. [34](#)
- [113] L. Sgro, A. De Filippo, G. Lanzuolo, and A. D’Alessio, “Characterization of nanoparticles of organic carbon (noc) produced in rich premixed flames by differential mobility analysis,” *Proc. Combust. Inst.*, vol. 31, no. 1, pp. 631–638, 2007. [34](#)
- [114] L. Sgro, A. Barone, M. Commodo, A. D’Alessio, A. De Filippo, G. Lanzuolo, and P. Minutolo, “Measurement of nanoparticles of organic carbon in non-sooting flame conditions,” *Proc. Combust. Inst.*, vol. 32, no. 1, pp. 689–696, 2009. [34](#)
- [115] M. Sirignano and A. D’Anna, “Coagulation of combustion generated nanoparticles in low and intermediate temperature regimes: An experimental study,” *Proc. Combust. Inst.*, vol. 34, no. 1, pp. 1877–1884, 2013. [34](#)

BIBLIOGRAPHY

- [116] B. R. Stanmore, J.-F. Brillhac, and P. Gilot, “The oxidation of soot: a review of experiments, mechanisms and models,” *Carbon*, vol. 39, no. 15, pp. 2247–2268, 2001. [34](#)
- [117] A. Cavaliere, R. Barbella, A. Ciajolo, A. D’Anna, and R. Ragucci, “Fuel and soot oxidation in diesel-like conditions,” in *Symposium (International) on Combustion*, vol. 25, pp. 167–174, Elsevier, 1994. [34](#)
- [118] C. P. Fenimore and G. W. Jones, “Oxidation of soot by hydroxyl radicals,” *The Journal of Physical Chemistry*, vol. 71, no. 3, pp. 593–597, 1967. [34](#)
- [119] K. Neoh, J. Howard, and A. Sarofim, “Effect of oxidation on the physical structure of soot,” in *Symposium (International) on Combustion*, vol. 20, pp. 951–957, Elsevier, 1985. [34](#), [35](#)
- [120] P. Roth, O. Brandt, and S. Von Gersum, “High temperature oxidation of suspended soot particles verified by CO and CO₂ measurements,” in *Proc. Combust. Inst.*, vol. 23, pp. 1485–1491, Elsevier, 1991. [34](#)
- [121] J. Nagle and R. Strickland-Constable, “Oxidation of carbon between 1000–2000°C,” in *Proceedings of the Fifth Conference on Carbon*, pp. 154 – 164, Pergamon, 1962. [34](#)
- [122] M. Frenklach, Z. Liu, R. I. Singh, G. R. Galimova, V. N. Azyazov, and A. M. Mebel, “Detailed, sterically-resolved modeling of soot oxidation: Role of O atoms, interplay with particle nanostructure, and emergence of inner particle burning,” *Combustion and Flame*, vol. 188, pp. 284–306, 2018. [34](#), [35](#)
- [123] A. D. Sediako, C. Soong, J. Y. Howe, M. R. Kholghy, and M. J. Thomson, “Real-time observation of soot aggregate oxidation in an environmental transmission electron microscope,” *Proc. Combust. Inst.*, vol. 36, no. 1, pp. 841–851, 2017. [34](#), [35](#)
- [124] C. A. Echavarria, I. C. Jaramillo, A. F. Sarofim, and J. S. Lighty, “Studies of soot oxidation and fragmentation in a two-stage burner under fuel-lean and fuel-rich conditions,” *Proc. Combust. Inst.*, vol. 33, no. 1, pp. 659–666, 2011. [35](#)
- [125] C. A. Echavarria, I. C. Jaramillo, A. F. Sarofim, and J. S. Lighty, “Burnout of soot particles in a two-stage burner with a jp-8 surrogate fuel,” *Combustion and Flame*, vol. 159, no. 7, pp. 2441–2448, 2012. [35](#)
- [126] H. M. Hulburt and S. Katz, “Some problems in particle technology: A statistical mechanical formulation,” *Chemical Engineering Science*, vol. 19, no. 8, pp. 555–574, 1964. [36](#)

- [127] A. D. Randolph, “A population balance for countable entities,” *The Canadian Journal of Chemical Engineering*, vol. 42, no. 6, pp. 280–281, 1964. [36](#)
- [128] M. V. Smoluchowski, “Three discourses on diffusion, brownian movements, and the coagulation of colloid particles,” *Phys. Z. Sowjet.*, vol. 17, pp. 557–571, 1916. [36](#), [38](#)
- [129] J. Solsvik and H. A. Jakobsen, “The foundation of the population balance equation: a review,” *Journal of Dispersion Science and Technology*, vol. 36, no. 4, pp. 510–520, 2015. [36](#)
- [130] A. Kazakov and M. Frenklach, “Dynamic modeling of soot particle coagulation and aggregation: Implementation with the method of moments and application to high-pressure laminar premixed flames,” *Combustion and Flame*, vol. 114, no. 3-4, pp. 484–501, 1998. [37](#)
- [131] S. J. Harris and I. M. Kennedy, “The coagulation of soot particles with van der waals forces,” *Combustion science and technology*, vol. 59, no. 4-6, pp. 443–454, 1988. [37](#)
- [132] H. Müller, “Zur allgemeinen theorie ser raschen koagulation,” *Kolloidchemische Beihefte*, vol. 27, no. 6-12, pp. 223–250, 1928. [38](#)
- [133] L. Waldmann and K. Schmitt, “Thermophoresis and diffusiophoresis of aerosols,” in *Aerosol Science*, vol. 148, Academic Press New York, 1966. [39](#)
- [134] B. Derjaguin, A. Storozhilova, and Y. I. Rabinovich, “Experimental verification of the theory of thermophoresis of aerosol particles,” *Journal of Colloid and Interface Science*, vol. 21, no. 1, pp. 35–58, 1966. [39](#)
- [135] P. S. Epstein, “On the resistance experienced by spheres in their motion through gases,” *Physical Review*, vol. 23, no. 6, p. 710, 1924. [39](#)
- [136] J. Cai and C. Sorensen, “Diffusion of fractal aggregates in the free molecular regime,” *Physical Review E*, vol. 50, no. 5, p. 3397, 1994. [39](#)
- [137] S. Salenbauch, A. Cuoci, A. Frassoldati, C. Saggese, T. Faravelli, and C. Hasse, “Modeling soot formation in premixed flames using an extended conditional quadrature method of moments,” *Combustion and Flame*, vol. 162, no. 6, pp. 2529–2543, 2015. [39](#), [42](#), [104](#), [123](#), [124](#)
- [138] K. C. Kalvakala, V. R. Katta, and S. K. Aggarwal, “Effects of oxygen-enrichment and fuel unsaturation on soot and nox emissions in ethylene, propane, and propene flames,” *Combustion and Flame*, vol. 187, pp. 217–229, 2018. [39](#)

BIBLIOGRAPHY

- [139] N. Slavinskaya and P. Frank, “A modelling study of aromatic soot precursors formation in laminar methane and ethene flames,” *Combustion and Flame*, vol. 156, no. 9, pp. 1705–1722, 2009. [39](#), [108](#), [109](#)
- [140] Y. Wang, A. Raj, and S. H. Chung, “Soot modeling of counterflow diffusion flames of ethylene-based binary mixture fuels,” *Combustion and Flame*, vol. 162, no. 3, pp. 586–596, 2015. [39](#)
- [141] L. Xu, F. Yan, M. Zhou, Y. Wang, and S. H. Chung, “Experimental and soot modeling studies of ethylene counterflow diffusion flames: Non-monotonic influence of the oxidizer composition on soot formation,” *Combustion and Flame*, vol. 197, pp. 304–318, 2018. [39](#)
- [142] A. Veshkini, N. A. Eaves, S. B. Dworkin, and M. J. Thomson, “Application of pah-condensation reversibility in modeling soot growth in laminar premixed and nonpremixed flames,” *Combustion and Flame*, vol. 167, pp. 335–352, 2016. [39](#), [104](#)
- [143] C. Eberle, P. Gerlinger, and M. Aigner, “A sectional PAH model with reversible PAH chemistry for CFD soot simulations,” *Combustion and Flame*, vol. 179, pp. 63–73, 2017. [39](#), [43](#), [65](#), [100](#), [104](#), [105](#), [109](#), [190](#)
- [144] D. Aubagnac-Karkar, A. El Bakali, and P. Desgroux, “Soot particles inception and pah condensation modelling applied in a soot model utilizing a sectional method,” *Combustion and Flame*, vol. 189, pp. 190–206, 2018. [39](#), [43](#), [97](#), [131](#), [133](#)
- [145] K. Johansson, J. Lai, S. Skeen, D. Popolan-Vaida, K. Wilson, N. Hansen, A. Violi, and H. Michelsen, “Soot precursor formation and limitations of the stabilomer grid,” *Proc. Combust. Inst.*, vol. 35, no. 2, pp. 1819–1826, 2015. [39](#)
- [146] K. O. Johansson, T. Dillstrom, P. Elvati, M. F. Campbell, P. E. Schrader, D. M. Popolan-Vaida, N. K. Richards-Henderson, K. R. Wilson, A. Violi, and H. A. Michelsen, “Radical–radical reactions, pyrene nucleation, and incipient soot formation in combustion,” *Proc. Combust. Inst.*, vol. 36, no. 1, pp. 799–806, 2017. [39](#)
- [147] J. Y. Lai, P. Elvati, and A. Violi, “Stochastic atomistic simulation of polycyclic aromatic hydrocarbon growth in combustion,” *Physical Chemistry Chemical Physics*, vol. 16, no. 17, pp. 7969–7979, 2014. [39](#)
- [148] A. Violi, “Modeling of soot particle inception in aromatic and aliphatic premixed flames,” *Combustion and Flame*, vol. 139, no. 4, pp. 279–287, 2004. [39](#)

- [149] S. H. Chung and A. Violi, “Insights on the nanoparticle formation process in counterflow diffusion flames,” *Carbon*, vol. 45, no. 12, pp. 2400–2410, 2007. [39](#)
- [150] P. Elvati, V. Dillstrom, and A. Violi, “Oxygen driven soot formation,” *Proc. Combust. Inst.*, vol. 36, no. 1, pp. 825–832, 2017. [39](#)
- [151] I. M. Kennedy, “Models of soot formation and oxidation,” *Progress in Energy and Combustion Science*, vol. 23, no. 2, pp. 95–132, 1997. [40](#)
- [152] P. Tesner, E. Tsygankova, L. Guilazetdinov, V. Zuyev, and G. Loshakova, “The formation of soot from aromatic hydrocarbons in diffusion flames of hydrocarbon-hydrogen mixtures,” *Combustion and Flame*, vol. 17, no. 3, pp. 279–285, 1971. [40](#)
- [153] I. M. Kennedy, W. Kollmann, and J.-Y. Chen, “A model for soot formation in a laminar diffusion flame,” *Combustion and Flame*, vol. 81, no. 1, pp. 73–85, 1990. [40](#)
- [154] R. Said, A. Garo, and R. Borghi, “Soot formation modeling for turbulent flames,” *Combustion and Flame*, vol. 108, no. 1-2, pp. 71–86, 1997. [40](#)
- [155] K. M. Leung, R. P. Lindstedt, and W. Jones, “A simplified reaction mechanism for soot formation in nonpremixed flames,” *Combustion and Flame*, vol. 87, no. 3-4, pp. 289–305, 1991. [40](#), [83](#), [84](#), [85](#)
- [156] S. Brookes and J. Moss, “Predictions of soot and thermal radiation properties in confined turbulent jet diffusion flames,” *Combustion and Flame*, vol. 116, no. 4, pp. 486–503, 1999. [40](#), [45](#)
- [157] B. Franzelli, A. Vié, and N. Darabiha, “A three-equation model for the prediction of soot emissions in les of gas turbines,” *Proc. Combust. Inst.*, vol. 37, no. 4, pp. 5411–5419, 2019. [40](#), [123](#), [124](#), [125](#)
- [158] M. E. Mueller, G. Blanquart, and H. Pitsch, “A joint volume-surface model of soot aggregation with the method of moments,” *Proc. Combust. Inst.*, vol. 32 I, no. 1, pp. 785–792, 2009. [40](#), [123](#), [124](#), [125](#), [138](#)
- [159] P. Mitchell and M. Frenklach, “Monte carlo simulation of soot aggregation with simultaneous surface growth-why primary particles appear spherical,” in *Symposium (International) on Combustion*, vol. 27, pp. 1507–1514, Elsevier, 1998. [41](#)

BIBLIOGRAPHY

- [160] M. Balthasar and M. Kraft, “A stochastic approach to calculate the particle size distribution function of soot particles in laminar premixed flames,” *Combustion and Flame*, vol. 133, no. 3, pp. 289–298, 2003. [41](#), [76](#), [89](#)
- [161] M. Celnik, R. Patterson, M. Kraft, and W. Wagner, “Coupling a stochastic soot population balance to gas-phase chemistry using operator splitting,” *Combustion and Flame*, vol. 148, no. 3, pp. 158–176, 2007. [41](#)
- [162] M. Frenklach and S. J. Harris, “Aerosol dynamics modeling using the method of moments,” *Journal of Colloid and Interface Science*, vol. 118, no. 1, pp. 252–261, 1987. [42](#)
- [163] M. Frenklach, “Method of moments with interpolative closure,” *Chemical Engineering Science*, vol. 57, no. 12, pp. 2229–2239, 2002. [42](#)
- [164] D. L. Marchisio and R. O. Fox, “Solution of population balance equations using the direct quadrature method of moments,” *Journal of Aerosol Science*, vol. 36, no. 1, pp. 43–73, 2005. [42](#)
- [165] M. E. Mueller, G. Blanquart, and H. Pitsch, “Hybrid method of moments for modeling soot formation and growth,” *Combustion and Flame*, vol. 156, no. 6, pp. 1143–1155, 2009. [42](#)
- [166] C. Yuan, F. Laurent, and R. Fox, “An extended quadrature method of moments for population balance equations,” *Journal of Aerosol Science*, vol. 51, pp. 1–23, 2012. [42](#)
- [167] E. Madadi-Kandjani and A. Passalacqua, “An extended quadrature-based moment method with log-normal kernel density functions,” *Chemical Engineering Science*, vol. 131, pp. 323–339, 2015. [42](#)
- [168] T. T. Nguyen, F. Laurent, R. O. Fox, and M. Massot, “Solution of population balance equations in applications with fine particles: mathematical modeling and numerical schemes,” *Journal of Computational Physics*, vol. 325, pp. 129–156, 2016. [42](#)
- [169] P. Selvaraj, P. G. Arias, B. J. Lee, H. G. Im, Y. Wang, Y. Gao, S. Park, S. M. Sarathy, T. Lu, and S. H. Chung, “A computational study of ethylene–air sooting flames: Effects of large polycyclic aromatic hydrocarbons,” *Combustion and Flame*, vol. 163, pp. 427–436, 2016. [42](#)

- [170] S. Salenbauch, C. Hasse, M. Vanni, and D. L. Marchisio, “A numerically robust method of moments with number density function reconstruction and its application to soot formation, growth and oxidation,” *Journal of Aerosol Science*, vol. 128, pp. 34–49, 2019. [42](#)
- [171] Y. Wang and S. H. Chung, “Soot formation in laminar counterflow flames,” *Progress in Energy and Combustion Science*, vol. 74, pp. 152–238, 2019. [42](#)
- [172] M. E. Mueller and H. Pitsch, “Large eddy simulation of soot evolution in an aircraft combustor,” *Phys. Fluids*, vol. 25, no. 11, 2013. [42](#)
- [173] M. Smooke, C. McEnally, L. Pfefferle, R. Hall, and M. Colket, “Computational and experimental study of soot formation in a coflow, laminar diffusion flame,” *Combustion and Flame*, vol. 117, no. 1-2, pp. 117–139, 1999. [43](#)
- [174] D. Aubagnac-Karkar, J.-B. Michel, O. Colin, P. E. Vervisch-Kljakic, and N. Darabiha, “Sectional soot model coupled to tabulated chemistry for diesel rans simulations,” *Combustion and Flame*, vol. 162, no. 8, pp. 3081–3099, 2015. [43](#)
- [175] Q. Zhang, M. Thomson, H. Guo, F. Liu, and G. Smallwood, “A numerical study of soot aggregate formation in a laminar coflow diffusion flame,” *Combustion and Flame*, vol. 156, no. 3, pp. 697–705, 2009. [43](#)
- [176] F. Yan, L. Xu, Y. Wang, S. Park, S. M. Sarathy, and S. H. Chung, “On the opposing effects of methanol and ethanol addition on pah and soot formation in ethylene counterflow diffusion flames,” *Combustion and Flame*, vol. 202, pp. 228–242, 2019. [43](#)
- [177] T. Blacha, M. Di Domenico, P. Gerlinger, and M. Aigner, “Soot predictions in premixed and non-premixed laminar flames using a sectional approach for pahs and soot,” *Combustion and Flame*, vol. 159, no. 1, pp. 181–193, 2012. [43](#), [104](#)
- [178] F. Gelbard and J. H. Seinfeld, “Simulation of multicomponent aerosol dynamics,” *Journal of Colloid and Interface Science*, vol. 78, no. 2, pp. 485–501, 1980. [43](#)
- [179] K. Netzell, H. Lehtiniemi, and F. Mauss, “Calculating the soot particle size distribution function in turbulent diffusion flames using a sectional method,” *Proc. Combust. Inst.*, vol. 31, no. 1, pp. 667–674, 2007. [43](#), [121](#)
- [180] C. J. Pope and J. B. Howard, “Simultaneous particle and molecule modeling (spamm): An approach for combining sectional aerosol equations and elementary gas-phase reactions,” *Aerosol Science and Technology*, vol. 27, no. 1, pp. 73–94, 1997. [44](#), [105](#)

BIBLIOGRAPHY

- [181] H. Richter, S. Granata, W. H. Green, and J. B. Howard, “Detailed modeling of pah and soot formation in a laminar premixed benzene/oxygen/argon low-pressure flame,” *Proc. Combust. Inst.*, vol. 30, no. 1, pp. 1397–1405, 2005. [44](#), [104](#), [105](#)
- [182] A. D’Anna and J. Kent, “A model of particulate and species formation applied to laminar, nonpremixed flames for three aliphatic-hydrocarbon fuels,” *Combustion and Flame*, vol. 152, no. 4, pp. 573–587, 2008. [44](#), [100](#), [106](#)
- [183] M. Sirignano, J. Kent, and A. D’Anna, “Detailed modeling of size distribution functions and hydrogen content in combustion-formed particles,” *Combustion and Flame*, vol. 157, no. 6, pp. 1211–1219, 2010. [44](#)
- [184] A. L. Bodor, B. Franzelli, T. Faravelli, and A. Cuoci, “A post processing technique to predict primary particle size of sooting flames based on a chemical discrete sectional model: Application to diluted coflow flames,” *Combustion and Flame*, vol. 208, pp. 122–138, 2019. [44](#)
- [185] W. M. F. W. Mahmood, A. LaRocca, P. J. Shayler, F. Bonatesta, and I. Pegg, “Predicted paths of soot particles in the cylinders of a direct injection diesel engine,” 2012. [45](#), [119](#)
- [186] M. A. Zuber, W. M. F. W. Mahmood, Z. Harun, Z. Z. Abidin, A. La Rocca, P. Shayler, and F. Bonatesta, “Modeling of in-cylinder soot particle size evolution and distribution in a direct injection diesel engine,” 2015. [45](#), [119](#)
- [187] V. R. Katta, L. G. Blevins, and W. M. Roquemore, “Dynamics of an inverse diffusion flame and its role in polycyclic-aromatic-hydrocarbon and soot formation,” *Combustion and Flame*, vol. 142, no. 1-2, pp. 33–51, 2005. [45](#), [119](#)
- [188] A. Fuentes, S. Rouvreau, P. Joulain, J.-P. Vantelon, G. Legros, J. L. Torero, and A. Fernandez-Pello, “Sooting behavior dynamics of a non-buoyant laminar diffusion flame,” *Combustion science and technology*, vol. 179, no. 1-2, pp. 3–19, 2007. [45](#)
- [189] P. Zhang, R. M. Roberts, and A. Bénard, “Computational guidelines and an empirical model for particle deposition in curved pipes using an eulerian-lagrangian approach,” *Journal of Aerosol Science*, vol. 53, pp. 1–20, 2012. [45](#)
- [190] V. Katta, R. Forlines, W. Roquemore, W. Anderson, J. Zelina, J. Gord, S. Stouffer, and S. Roy, “Experimental and computational study on partially premixed flames in a centerbody burner,” *Combustion and Flame*, vol. 158, no. 3, pp. 511–524, 2011. [45](#)

- [191] W. Roquemore, V. Katta, S. Stouffer, V. Belovich, R. Pawlik, M. Arstingstall, G. Justinger, J. Gord, A. Lynch, J. Zelina, *et al.*, “Soot studies of laminar diffusion flames with recirculation zones,” *Proc. Combust. Inst.*, vol. 32, no. 1, pp. 729–736, 2009. [45](#)
- [192] M. Zuber, W. Mahmood, Z. Harun, and Z. Z. Abidin, “Soot particle size distribution near the cylinder wall in a direct injection diesel engine,” *Journal of Engineering Science and Technology*, vol. 13, no. 6, pp. 1540–1549, 2018. [45](#)
- [193] J. C. Ong, K. M. Pang, J. H. Walther, J.-H. Ho, and H. K. Ng, “Evaluation of a lagrangian soot tracking method for the prediction of primary soot particle size under engine-like conditions,” *Journal of Aerosol Science*, vol. 115, pp. 70–95, 2018. [45](#), [76](#), [119](#)
- [194] L. Gallen, A. Felden, E. Riber, and B. Cuenot, “Lagrangian tracking of soot particles in les of gas turbines,” *Proc. Combust. Inst.*, vol. 37, no. 4, pp. 5429–5436, 2019. [45](#), [84](#), [87](#)
- [195] N. Dellinger, N. Bertier, F. Dupoirieux, and G. Legros, “Hybrid eulerian-lagrangian method for soot modelling applied to ethylene-air premixed flames,” *Energy*, vol. 194, p. 116858, 2020. [45](#), [82](#), [100](#), [104](#), [125](#), [228](#)
- [196] P. Rodrigues, *Modélisation multiphysique de flammes turbulentes suitées avec la prise en compte des transferts radiatifs et des transferts de chaleur pariétaux*. PhD thesis, 2018. [46](#), [117](#), [120](#), [121](#), [124](#), [125](#), [129](#), [130](#), [135](#), [137](#), [138](#), [171](#), [173](#), [179](#), [180](#), [190](#), [209](#)
- [197] T. Poinso and D. Veynante, *Theoretical and Numerical Combustion*. Third Edition (www.cerfacs.fr/elearning), 2011. [53](#), [54](#), [55](#), [56](#), [153](#)
- [198] S. M. Candel and T. Poinso, “Flame stretch and the balance equation for the flame surface area,” *Combustion science and technology*, vol. 70, pp. 1–15, 1990. [54](#)
- [199] R. W. Bilger, S. H. Starner, and R. J. Kee, “On reduced mechanisms for methane-air combustion in nonpremixed flames,” *Combustion and Flame*, vol. 80, pp. 135–149, 1990. [56](#)
- [200] J. Hirschfelder, C. Curtis, and B. Bird, *Molecular Theory of Gases and Liquids*. John Wiley & Sons, 1954 ed., 1954. [58](#)
- [201] H. Wang, X. You, A. V. Joshi, S. G. Davis, A. Laskin, F. Egolfopoulos, and C. Law, “Usc mech version ii. high-temperature combustion reaction model of h2/co/c1-c4 compounds,” 2007. [59](#), [114](#)

BIBLIOGRAPHY

- [202] P. Dagaut and M. Cathonnet, “The ignition, oxidation, and combustion of kerosene: A review of experimental and kinetic modeling,” *Progress in Energy and Combustion Science*, vol. 32, no. 1, pp. 48–92, 2006. [59](#), [112](#), [113](#)
- [203] E. Ranzi, A. Frassoldati, R. Grana, A. Cuoci, T. Faravelli, A. Kelley, and C. K. Law, “Hierarchical and comparative kinetic modeling of laminar flame speeds of hydrocarbon and oxygenated fuels,” *Progress in Energy and Combustion Science*, vol. 38, no. 4, pp. 468–501, 2012. [59](#)
- [204] E. Ranzi, C. Cavallotti, A. Cuoci, A. Frassoldati, M. Pelucchi, and T. Faravelli, “New reaction classes in the kinetic modeling of low temperature oxidation of n-alkanes,” *Combustion and Flame*, vol. 162, no. 5, pp. 1679–1691, 2015. [59](#)
- [205] T. Lu, C. K. Law, C. S. Yoo, and J. H. Chen, “Dynamic stiffness removal for direct numerical simulations,” *Combustion and Flame*, vol. 156, no. 8, pp. 1542–1551, 2009. [60](#)
- [206] T. Lu and C. K. Law, “A directed relation graph method for mechanism reduction,” *Proc. Combust. Inst.*, vol. 30, no. 1, pp. 1333–1341, 2005. [60](#)
- [207] T. Turanyi, A. Tomlin, and M. Pilling, “On the error of the quasi-steady-state approximation,” *The Journal of Physical Chemistry*, vol. 97, no. 1, pp. 163–172, 1993. [61](#)
- [208] T. Løvås, D. Nilsson, and F. Mauss, “Automatic reduction procedure for chemical mechanisms applied to premixed methane/air flames,” *Proc. Combust. Inst.*, vol. 28, no. 2, pp. 1809–1815, 2000. [61](#)
- [209] T. Lu and C. K. Law, “A criterion based on computational singular perturbation for the identification of quasi steady state species: A reduced mechanism for methane oxidation with no chemistry,” *Combustion and Flame*, vol. 154, no. 4, pp. 761–774, 2008. [61](#)
- [210] T. Løvås, P. Amnéus, F. Mauss, and E. Mastorakos, “Comparison of automatic reduction procedures for ignition chemistry,” *Proc. Combust. Inst.*, vol. 29, no. 1, pp. 1387–1393, 2002. [61](#), [100](#)
- [211] N. Jaouen, L. Vervisch, P. Domingo, and G. Ribert, “Automatic reduction and optimisation of chemistry for turbulent combustion modelling: Impact of the canonical problem,” *Combustion and Flame*, vol. 175, pp. 60–79, 2017. [62](#), [65](#)
- [212] B. Franzelli, A. Vié, M. Boileau, B. Fiorina, and N. Darabiha, “Large eddy simulation of swirled spray flame using detailed and tabulated chemical descriptions,” *Flow, Turbulence and Combustion*, vol. 98, no. 2, pp. 633–661, 2017. [62](#), [65](#)

- [213] A. Felden, L. Esclapez, E. Riber, B. Cuenot, and H. Wang, “Including real fuel chemistry in LES of turbulent spray combustion,” *Combust. Flame*, vol. 193, pp. 397–416, 2018. [62](#), [65](#), [83](#), [85](#), [114](#), [211](#), [217](#)
- [214] N. Peters, “Laminar diffusion flamelet models in non-premixed turbulent combustion,” *Progress in Energy and Combustion Science*, vol. 10, no. 3, pp. 319–339, 1984. [62](#)
- [215] O. Gicquel, N. Darabiha, and D. Thévenin, “Laminar premixed hydrogen/air counterflow flame simulations using flame prolongation of ildm with differential diffusion,” *Proc. Combust. Inst.*, vol. 28, no. 2, pp. 1901–1908, 2000. [62](#)
- [216] J. Van Oijen, F. Lammers, and L. De Goey, “Modeling of complex premixed burner systems by using flamelet-generated manifolds,” *Combustion and Flame*, vol. 127, no. 3, pp. 2124–2134, 2001. [62](#), [153](#)
- [217] C. D. Pierce and P. Moin, “Progress-variable approach for large-eddy simulation of non-premixed turbulent combustion,” *Journal of fluid Mechanics*, vol. 504, pp. 73–97, 2004. [62](#)
- [218] H. Pitsch, “Large-eddy simulation of turbulent combustion,” *Annu. Rev. Fluid Mech.*, vol. 38, pp. 453–482, 2006. [62](#), [63](#)
- [219] B. Fiorina, R. Mercier, G. Kuenne, A. Ketelheun, A. Avdić, J. Janicka, D. Geyer, A. Dreizler, E. Alenius, C. Duwig, P. Trisjono, K. Kleinheinz, S. Kang, H. Pitsch, F. Proch, F. Cavallo Marincola, and A. Kempf, “Challenging modeling strategies for les of non-adiabatic turbulent stratified combustion,” *Combustion and Flame*, vol. 162, no. 11, pp. 4264–4282, 2015. [62](#), [63](#)
- [220] B. Fiorina, O. Gicquel, L. Vervisch, S. Carpentier, and N. Darabiha, “Approximating the chemical structure of partially premixed and diffusion counterflow flames using fpi flamelet tabulation,” *Combustion and Flame*, vol. 140, no. 3, pp. 147–160, 2005. [63](#), [181](#)
- [221] B. Franzelli, B. Fiorina, and N. Darabiha, “A tabulated chemistry method for spray combustion,” *Proc. Combust. Inst.*, vol. 34, no. 1, pp. 1659–1666, 2013. [63](#)
- [222] W. Jones and R. Lindstedt, “Global reaction schemes for hydrocarbon combustion,” *Combustion and Flame*, vol. 73, no. 3, pp. 233–249, 1988. [63](#)
- [223] B. Franzelli, E. Riber, M. Sanjosé, and T. Poinso, “A two-step chemical scheme for kerosene–air premixed flames,” *Combustion and Flame*, vol. 157, no. 7, pp. 1364–1373, 2010. [63](#), [113](#)

BIBLIOGRAPHY

- [224] W. Polifke, W. Geng, and K. Döbbeling, “Optimization of rate coefficients for simplified reaction mechanisms with genetic algorithms,” *Combustion and Flame*, vol. 113, no. 1-2, pp. 119–134, 1998. [63](#)
- [225] A. Abou-Taouk, B. Farcy, P. Domingo, L. Vervisch, S. Sadasivuni, and L.-E. Eriksson, “Optimized reduced chemistry and molecular transport for large eddy simulation of partially premixed combustion in a gas turbine,” *Combustion science and technology*, vol. 188, no. 1, pp. 21–39, 2016. [63](#)
- [226] L. Elliott, D. Ingham, A. Kyne, N. Mera, M. Pourkashanian, and C. Wilson, “Genetic algorithms for optimisation of chemical kinetics reaction mechanisms,” *Progress in Energy and Combustion Science*, vol. 30, no. 3, pp. 297–328, 2004. [63](#)
- [227] M. Cailler, N. Darabiha, D. Veynante, and B. Fiorina, “Building-up virtual optimized mechanism for flame modeling,” *Proc. Combust. Inst.*, vol. 36, no. 1, pp. 1251–1258, 2017. [64](#), [65](#)
- [228] G. Maio, M. Cailler, R. Mercier, and B. Fiorina, “Virtual chemistry for temperature and co prediction in les of non-adiabatic turbulent flames,” *Proc. Combust. Inst.*, vol. 37, no. 2, pp. 2591–2599, 2019. [64](#)
- [229] M. Cailler, N. Darabiha, and B. Fiorina, “Development of a virtual optimized chemistry method. application to hydrocarbon/air combustion,” *Combustion and Flame*, vol. 211, pp. 281–302, 2020. [64](#)
- [230] H. M. Colmán, A. Cuoci, N. Darabiha, and B. Fiorina, “A reduced virtual chemistry model for soot prediction in hydrocarbon-air flames,” in *ICDERS*, vol. 27, 2019. [64](#), [65](#)
- [231] F. Bisetti, G. Blanquart, M. E. Mueller, and H. Pitsch, “On the formation and early evolution of soot in turbulent nonpremixed flames,” *Combust. Flame*, vol. 159, no. 1, pp. 317–335, 2012. [65](#), [76](#), [92](#), [93](#), [94](#), [97](#), [98](#), [99](#), [100](#), [116](#)
- [232] C. Laurent, L. Esclapez, D. Maestro, G. Staffelbach, B. Cuenot, L. Selle, T. Schmitt, F. Duchaine, and T. Poinsot, “Flame–wall interaction effects on the flame root stabilization mechanisms of a doubly-transcritical O_2/CH_4 cryogenic flame,” *Proc. Combust. Inst.*, vol. 37, no. 4, pp. 5147–5154, 2019. [65](#)
- [233] G. Marta, *Development and validation of the Euler-Lagrange formulation on a parallel and unstructured solver for large-eddy simulation*. PhD thesis, Institut National Polytechnique de Toulouse-INPT, 2009. [66](#), [75](#)

- [234] F. Jaegle, *LES of two-phase flow in aero-engines*. PhD thesis, Université de Toulouse - Ecole doctorale MEGeP, CERFACS - CFD Team, Toulouse, December 2009. [66](#), [75](#)
- [235] J.-M. Senoner, *Simulations aux grandes échelles de l'écoulement diphasique dans un brûleur aéronautique par une approche Euler-Lagrange*. PhD thesis, Institut National Polytechnique de Toulouse-INPT, 2010. [66](#), [75](#)
- [236] P. Sierra Sánchez, *Modeling the dispersion and evaporation of sprays in aeronautical combustion chambers*. PhD thesis, Institut National Polytechnique de Toulouse-INPT, 2012. [66](#), [70](#), [75](#)
- [237] G. Chaussonnet, *Modeling of liquid film and breakup phenomena in Large-Eddy Simulations of aeroengines fueled by airblast atomizers*. PhD thesis, Institut National Polytechnique de Toulouse-INPT, 2014. [66](#), [75](#)
- [238] D. Paulhiac, *Modélisation de la combustion d'un spray dans un brûleur aéronautique*. PhD thesis, Institut National Polytechnique de Toulouse-INPT, 2015. [66](#), [75](#), [83](#), [154](#)
- [239] N. Iafrate, *Simulation aux grandes échelles diphasique dans les moteurs downsizes à allumage commandé*. PhD thesis, 2016. [66](#)
- [240] J. D. Schwarzkopf, M. Sommerfeld, C. T. Crowe, and Y. Tsuji, *Multiphase flows with droplets and particles*. CRC press, 2011. [67](#), [69](#)
- [241] C. W. Oseen, *Hydrodynamik*. Leipzig, 1927. [68](#)
- [242] L. Schiller and A. Naumann, "A drag coefficient correlation," *VDI Zeitung*, vol. 77, pp. 318–320, 1935. [68](#)
- [243] D. B. Spalding, "The combustion of liquid fuels," in *4th Symp. (Int.) on Combustion*, pp. 847–864, The Combustion Institute, Pittsburgh, 1953. [68](#)
- [244] R. S. Miller, K. Harstad, and J. Bellan, "Evaluation of equilibrium and non-equilibrium evaporation models for many-droplet gas-liquid flow simulations," *Int. J. Multiphase Flow*, vol. 24, no. 6, pp. 1025–1055, 1998. [70](#)
- [245] C. Wilke, "A viscosity equation for gas mixtures," *The Journal of Chemical Physics*, vol. 18, no. 4, pp. 517–519, 1950. [70](#)
- [246] W. E. Ranz and W. R. Marshall, "Evaporation from drops," *Chem. Eng. Prog.*, vol. 48, no. 4, p. 173, 1952. [71](#)

BIBLIOGRAPHY

- [247] B. Abramzon and W. A. Sirignano, “Droplet vaporisation model for spray combustion calculations,” *Int. J. Heat and Mass Transfer*, vol. 9, pp. 1605–1618, 1989. [72](#)
- [248] M. Sanjosé, J. Senoner, F. Jaegle, B. Cuenot, S. Moreau, and T. Poinso, “Fuel injection model for euler–euler and euler–lagrange large-eddy simulations of an evaporating spray inside an aeronautical combustor,” *Int. J. Multiphase Flow*, vol. 37, no. 5, pp. 514–529, 2011. [73](#)
- [249] A. Attili and F. Bisetti, “Application of a robust and efficient lagrangian particle scheme to soot transport in turbulent flames,” *Computers & Fluids*, vol. 84, pp. 164–175, 2013. [76](#)
- [250] H. Pitsch, E. Riesmeier, and N. Peters, “Unsteady flamelet modeling of soot formation in turbulent diffusion flames,” *Combustion science and technology*, vol. 158, no. 1, pp. 389–406, 2000. [76](#)
- [251] D. O. Lignell, J. C. Hewson, and J. H. Chen, “A-priori analysis of conditional moment closure modeling of a temporal ethylene jet flame with soot formation using direct numerical simulation,” *Proc. Combust. Inst.*, vol. 32, no. 1, pp. 1491 – 1498, 2009. [76](#)
- [252] K. Liffman, “A direct simulation monte-carlo method for cluster coagulation,” *Journal of Computational Physics*, vol. 100, no. 1, pp. 116–127, 1992. [77](#)
- [253] M. Smith and T. Matsoukas, “Constant-number monte carlo simulation of population balances,” *Chemical Engineering Science*, vol. 53, no. 9, pp. 1777–1786, 1998. [77](#)
- [254] Y. Lin, K. Lee, and T. Matsoukas, “Solution of the population balance equation using constant-number monte carlo,” *Chemical Engineering Science*, vol. 57, no. 12, pp. 2241–2252, 2002. [77](#), [78](#)
- [255] X. Hao, H. Zhao, Z. Xu, and C. Zheng, “Population balance-monte carlo simulation for gas-to-particle synthesis of nanoparticles,” *Aerosol Science and Technology*, vol. 47, no. 10, pp. 1125–1133, 2013. [78](#), [80](#), [81](#)
- [256] W. J. Menz, J. Akroyd, and M. Kraft, “Stochastic solution of population balance equations for reactor networks,” *Journal of Computational Physics*, vol. 256, pp. 615–629, 2014. [78](#)
- [257] R. Garg, C. Narayanan, and S. Subramaniam, “A numerically convergent lagrangian–eulerian simulation method for dispersed two-phase flows,” *International Journal of Multiphase Flow*, vol. 35, no. 4, pp. 376–388, 2009. [78](#)

- [258] H. Tofighian, E. Amani, and M. Saffar-Avval, “Parcel-number-density control algorithms for the efficient simulation of particle-laden two-phase flows,” *J. Comput. Phys.*, vol. 387, pp. 569–588, 2019. [78](#), [125](#)
- [259] G. Kotalczyk and F. E. Kruis, “A monte carlo method for the simulation of coagulation and nucleation based on weighted particles and the concepts of stochastic resolution and merging,” *J. Comput. Phys.*, vol. 340, pp. 276–296, 2017. [79](#), [80](#), [125](#)
- [260] M. Vranic, T. Grismayer, J. L. Martins, R. A. Fonseca, and L. O. Silva, “Particle merging algorithm for pic codes,” *Computer Physics Communications*, vol. 191, pp. 65–73, 2015. [79](#)
- [261] W. Villafana, F. Pechereau, O. Vermorel, and B. Cuenot, “3d particle-in-cell simulation of a thruster anode layer,” in *APS Meeting Abstracts*, 2018. [79](#), [125](#)
- [262] J. Wei and F. E. Kruis, “A gpu-based parallelized monte-carlo method for particle coagulation using an acceptance–rejection strategy,” *Chemical Engineering Science*, vol. 104, pp. 451–459, 2013. [80](#), [81](#)
- [263] A. Khadilkar, P. L. Rozelle, and S. V. Pisupati, “Models of agglomerate growth in fluidized bed reactors: Critical review, status and applications,” *Powder Technology*, vol. 264, pp. 216–228, 2014. [80](#), [81](#)
- [264] G. Bird, “Monte carlo simulation of gas flows,” *Annual Review of Fluid Mechanics*, vol. 10, no. 1, pp. 11–31, 1978. [80](#)
- [265] P. J. O’Rourke, “Collective drop effects on vaporizing liquid sprays,” 1981. [80](#)
- [266] Y. Tsuji, T. Tanaka, and T. Ishida, “Lagrangian numerical simulation of plug flow of cohesionless particles in a horizontal pipe,” *Powder Technology*, vol. 71, no. 3, pp. 239–250, 1992. [80](#)
- [267] F. E. Kruis, A. Maisels, and H. Fissan, “Direct simulation monte carlo method for particle coagulation and aggregation,” *AIChE Journal*, vol. 46, no. 9, pp. 1735–1742, 2000. [80](#), [81](#), [125](#)
- [268] P. Fede, O. Simonin, and P. Villedieu, “Monte-carlo simulation of colliding particles or coalescing droplets transported by a turbulent flow in the framework of a joint fluid–particle pdf approach,” *International Journal of Multiphase Flow*, vol. 74, pp. 165–183, 2015. [82](#)

BIBLIOGRAPHY

- [269] M. Tsurikov, K. P. Geigle, V. Krüger, Y. Schneider-Kühnle, W. Stricker, R. Lück-erath, R. Hadeff, and M. Aigner, “Laser-based investigation of soot formation in laminar premixed flames at atmospheric and elevated pressures,” *Combustion science and technology*, vol. 177, no. 10, pp. 1835–1862, 2005. [86](#)
- [270] P. Rodrigues, B. Franzelli, R. Vicquelin, O. Gicquel, and N. Darabiha, “Unsteady dynamics of pah and soot particles in laminar counterflow diffusion flames,” *Proc. Combust. Inst.*, vol. 36, no. 1, pp. 927–934, 2017. [92](#), [104](#), [118](#), [119](#), [123](#), [125](#), [133](#)
- [271] G. Blanquart, P. Pepiot-Desjardins, and H. Pitsch, “Chemical mechanism for high temperature combustion of engine relevant fuels with emphasis on soot pre-cursors,” *Combustion and Flame*, vol. 156, no. 3, pp. 588–607, 2009. [92](#), [93](#), [99](#), [108](#)
- [272] N. Slavinskaya, A. Mirzayeva, R. Whitside, J. Starke, M. Abbasi, M. Auyelkhanzy, and V. Chernov, “A modelling study of acetylene oxidation and pyrolysis,” *Combustion and Flame*, vol. 210, pp. 25–42, 2019. [92](#), [93](#)
- [273] N. A. Slavinskaya, U. Riedel, S. B. Dworkin, and M. J. Thomson, “Detailed numerical modeling of pah formation and growth in non-premixed ethylene and ethane flames,” *Combustion and Flame*, vol. 159, no. 3, pp. 979–995, 2012. [92](#)
- [274] V. Chernov, M. J. Thomson, S. B. Dworkin, N. A. Slavinskaya, and U. Riedel, “Soot formation with c1 and c2 fuels using an improved chemical mechanism for pah growth,” *Combustion and Flame*, vol. 161, no. 2, pp. 592–601, 2014. [92](#), [109](#)
- [275] W. Pejpichestakul, A. Frassoldati, A. Parente, and T. Faravelli, “Kinetic model-ing of soot formation in premixed burner-stabilized stagnation ethylene flames at heavily sooting condition,” *Fuel*, vol. 234, pp. 199–206, 2018. [92](#), [93](#)
- [276] M. Hassan, K. Aung, O. Kwon, and G. Faeth, “Properties of laminar premixed hydrocarbon/air flames at various pressures,” *Journal of Propulsion and Power*, vol. 14, no. 4, pp. 479–488, 1998. [93](#), [99](#)
- [277] F. Egolfopoulos, D. Zhu, and C. K. Law, “Experimental and numerical determi-nation of laminar flame speeds: Mixtures of c2-hydrocarbons with oxygen and nitrogen,” in *Proc. Combust. Inst.*, vol. 23, pp. 471–478, Elsevier, 1991. [93](#), [99](#)
- [278] G. Jomaas, X. Zheng, D. Zhu, and C. K. Law, “Experimental determination of counterflow ignition temperatures and laminar flame speeds of c2–c3 hydrocar-bons at atmospheric and elevated pressures,” *Proc. Combust. Inst.*, vol. 30, no. 1, pp. 193–200, 2005. [93](#), [99](#)

- [279] M. J. Castaldi, N. M. Marinov, C. F. Melius, J. Huang, S. M. Senkan, W. J. Pit, and C. K. Westbrook, “Experimental and modeling investigation of aromatic and polycyclic aromatic hydrocarbon formation in a premixed ethylene flame,” in *Proc. Combust. Inst.*, vol. 26, pp. 693–702, Elsevier, 1996. [94](#), [95](#), [109](#), [131](#)
- [280] A. Ciajolo, A. D’Anna, R. Barbella, A. Tregrossi, and A. Violi, “The effect of temperature on soot inception in premixed ethylene flames,” in *Proc. Combust. Inst.*, vol. 26, pp. 2327–2333, Elsevier, 1996. [94](#), [96](#), [110](#), [132](#)
- [281] A. Ciajolo, A. Tregrossi, R. Barbella, R. Ragucci, B. Apicella, and M. De Joannon, “The relation between ultraviolet-excited fluorescence spectroscopy and aromatic species formed in rich laminar ethylene flames,” *Combustion and Flame*, vol. 125, no. 4, pp. 1225–1229, 2001. [94](#), [96](#), [110](#), [132](#)
- [282] T. Mouton, X. Mercier, M. Wartel, N. Lamoureux, and P. Desgroux, “Laser-induced incandescence technique to identify soot nucleation and very small particles in low-pressure methane flames,” *Applied Physics B*, vol. 112, no. 3, pp. 369–379, 2013. [94](#)
- [283] H. Bladh, N.-E. Olofsson, T. Mouton, J. Simonsson, X. Mercier, A. Faccinetto, P.-E. Bengtsson, and P. Desgroux, “Probing the smallest soot particles in low-sooting premixed flames using laser-induced incandescence,” *Proc. Combust. Inst.*, vol. 35, no. 2, pp. 1843–1850, 2015. [94](#)
- [284] T. Mouton, X. Mercier, and P. Desgroux, “Isomer discrimination of pahs formed in sooting flames by jet-cooled laser-induced fluorescence: application to the measurement of pyrene and fluoranthene,” *Applied Physics B*, vol. 122, no. 5, p. 123, 2016. [94](#)
- [285] P. Desgroux, A. Faccinetto, X. Mercier, T. Mouton, D. A. Karkar, and A. El Bakali, “Comparative study of the soot formation process in a “nucleation” and a “sooting” low pressure premixed methane flame,” *Combustion and Flame*, vol. 184, pp. 153–166, 2017. [94](#), [97](#), [98](#), [111](#), [133](#), [134](#)
- [286] A. Van Maaren, D. Thung, and L. R. H. DE GOEY, “Measurement of flame temperature and adiabatic burning velocity of methane/air mixtures,” *Combustion science and technology*, vol. 96, no. 4-6, pp. 327–344, 1994. [97](#)
- [287] A. El Bakali, X. Mercier, M. Wartel, F. Acevedo, I. Burns, L. Gasnot, J.-F. Pauwels, and P. Desgroux, “Modeling of pahs in low pressure sooting premixed methane flame,” *Energy*, vol. 43, no. 1, pp. 73–84, 2012. [97](#)

BIBLIOGRAPHY

- [288] A. Violi, A. D'Anna, and A. D'Alessio, "Modeling of particulate formation in combustion and pyrolysis," *Chemical Engineering Science*, vol. 54, no. 15-16, pp. 3433–3442, 1999. [100](#)
- [289] D. Wong, R. Whitesides, C. Schuetz, M. Frenklach, H. Bockhorn, A. D'Anna, A. Sarofim, and H. Wang, "Combustion generated fine carbonaceous particles," *Bockhorn, H*, pp. 275–285, 2007. [100](#)
- [290] J. Bhatt and R. Lindstedt, "Analysis of the impact of agglomeration and surface chemistry models on soot formation and oxidation," *Proc. Combust. Inst.*, vol. 32, no. 1, pp. 713–720, 2009. [100](#), [104](#)
- [291] Y. Xuan and G. Blanquart, "Effects of aromatic chemistry-turbulence interactions on soot formation in a turbulent non-premixed flame," *Proc. Combust. Inst.*, vol. 35, no. 2, pp. 1911–1919, 2015. [100](#)
- [292] C. Sung, Y. Huang, and J. Eng, "Effects of reformer gas addition on the laminar flame speeds and flammability limits of n-butane and iso-butane flames," *Combustion and Flame*, vol. 126, no. 3, pp. 1699–1713, 2001. [100](#)
- [293] T. Lu and C. K. Law, "Strategies for mechanism reduction for large hydrocarbons: n-heptane," *Combustion and Flame*, vol. 154, no. 1-2, pp. 153–163, 2008. [100](#)
- [294] H. G. Im and J. H. Chen, "Structure and propagation of triple flames in partially premixed hydrogen–air mixtures," *Combustion and Flame*, vol. 119, no. 4, pp. 436–454, 1999. [100](#)
- [295] T. Jaravel, *Prediction of pollutants in gas turbines using large eddy simulation*. PhD thesis, Institut National Polytechnique de Toulouse-INPT, 2017. [101](#), [113](#)
- [296] A. Felden, *Development of Analytically Reduced Chemistries (ARC) and applications in Large Eddy Simulations (LES) of turbulent combustion*. PhD thesis, Institut National Polytechnique de Toulouse-INPT, 2017. [101](#)
- [297] J. Appel, H. Bockhorn, and M. Wulkow, "A detailed numerical study of the evolution of soot particle size distributions in laminar premixed flames," *Chemosphere*, vol. 42, no. 5-7, pp. 635–645, 2001. [104](#)
- [298] J. Singh, M. Balthasar, M. Kraft, and W. Wagner, "Stochastic modeling of soot particle size and age distributions in laminar premixed flames," *Proc. Combust. Inst.*, vol. 30, no. 1, pp. 1457–1465, 2005. [104](#)

- [299] T. S. Totton, A. J. Misquitta, and M. Kraft, “A quantitative study of the clustering of polycyclic aromatic hydrocarbons at high temperatures,” *Physical Chemistry Chemical Physics*, vol. 14, no. 12, pp. 4081–4094, 2012. [104](#)
- [300] T. Zhang, L. Zhao, M. R. Kholghy, S. Thion, and M. J. Thomson, “Detailed investigation of soot formation from jet fuel in a diffusion flame with comprehensive and hybrid chemical mechanisms,” *Proc. Combust. Inst.*, vol. 37, no. 2, pp. 2037–2045, 2019. [104](#), [114](#), [115](#)
- [301] M. Di Domenico, P. Gerlinger, and M. Aigner, “Development and validation of a new soot formation model for gas turbine combustor simulations,” vol. 157, no. 2, pp. 246 – 258, 2010. [104](#)
- [302] P. Vlasov and J. Warnatz, “Detailed kinetic modeling of soot formation in hydrocarbon pyrolysis behind shock waves,” *Proc. Combust. Inst.*, vol. 29, no. 2, pp. 2335 – 2341, 2002. [105](#)
- [303] K. M. Pang, H. K. Ng, and S. Gan, “Development of an integrated reduced fuel oxidation and soot precursor formation mechanism for CFD simulations of diesel combustion,” *Fuel*, vol. 90, no. 9, pp. 2902–2914, 2011. [106](#)
- [304] B. Pang, M.-Z. Xie, M. Jia, and Y.-D. Liu, “Development of a phenomenological soot model coupled with a skeletal PAH mechanism for practical engine simulation,” *Energy & Fuels*, vol. 27, no. 3, pp. 1699–1711, 2013. [107](#), [108](#), [109](#)
- [305] A. E. Bakali, J.-L. Delfau, and C. Vovelle, “Experimental study of 1 atmosphere, rich, premixed n-heptane and iso-octane flames,” *Combustion science and technology*, vol. 140, no. 1-6, pp. 69–91, 1998. [107](#)
- [306] F. Inal and S. M. Senkan, “Effects of equivalence ratio on species and soot concentrations in premixed n-heptane flames,” *Combustion and Flame*, vol. 131, no. 1-2, pp. 16–28, 2002. [107](#)
- [307] A. D’Anna, M. Alfe, B. Apicella, A. Tregrossi, and A. Ciajolo, “Effect of fuel/air ratio and aromaticity on sooting behavior of premixed heptane flames,” *Energy & Fuels*, vol. 21, no. 5, pp. 2655–2662, 2007. [107](#)
- [308] A. Raj, I. D. C. Prada, A. A. Amer, and S. H. Chung, “A reaction mechanism for gasoline surrogate fuels for large polycyclic aromatic hydrocarbons,” *Combustion and Flame*, vol. 159, no. 2, pp. 500–515, 2012. [107](#), [108](#)
- [309] C. Marchal, J.-L. Delfau, C. Vovelle, G. Moréac, C. Mounai, F. Mauss, *et al.*, “Modelling of aromatics and soot formation from large fuel molecules,” *Proc. Combust. Inst.*, vol. 32, no. 1, pp. 753–759, 2009. [108](#)

BIBLIOGRAPHY

- [310] Z. Qin, V. V. Lissianski, H. Yang, W. C. Gardiner, S. G. Davis, and H. Wang, “Combustion chemistry of propane: a case study of detailed reaction mechanism optimization,” *Proc. Combust. Inst.*, vol. 28, no. 2, pp. 1663–1669, 2000. [108](#)
- [311] Y. Ra and R. D. Reitz, “A combustion model for IC engine combustion simulations with multi-component fuels,” *Combustion and Flame*, vol. 158, no. 1, pp. 69–90, 2011. [108](#)
- [312] T. Edwards and L. Maurice, “Surrogate mixtures to represent complex aviation and rockets fuels,” *J. Propuls. Power*, vol. 17, no. 2, pp. 461–466, 2001. [112](#)
- [313] C. Wood, V. McDonell, R. Smith, and G. Samuelsen, “Development and application of a surrogate distillate fuel,” *J. Propuls. Power*, vol. 5, no. 4, pp. 399–405, 1989. [113](#)
- [314] A. Violi, S. Yan, E. Eddings, A. Sarofim, S. Granata, T. Faravelli, and E. Ranzi, “Experimental formulation and kinetic model for jp-8 surrogate mixtures,” *Combust. Sci. Technol.*, vol. 174, no. 11-12, pp. 399–417, 2002. [113](#)
- [315] S. Dooley, S. H. Won, S. Jahangirian, Y. Ju, F. L. Dryer, H. Wang, and M. A. Oehlschlaeger, “The combustion kinetics of a synthetic paraffinic jet aviation fuel and a fundamentally formulated, experimentally validated surrogate fuel,” *Combust. Flame*, vol. 159, no. 10, pp. 3014–3020, 2012. [113](#)
- [316] K. Narayanaswamy, H. Pitsch, and P. Pepiot, “A component library framework for deriving kinetic mechanisms for multi-component fuel surrogates: Application for jet fuel surrogates,” *Combust. Flame*, vol. 165, pp. 288–309, 2016. [113](#)
- [317] M. Keita, A. Nicolle, and A. El Bakali, “A wide range kinetic modeling study of pah formation from liquid transportation fuels combustion,” *Combustion and Flame*, vol. 174, pp. 50–67, 2016. [113](#)
- [318] J. Luche, M. Reuillon, J.-C. Boettner, and M. Cathonnet, “Reduction of large detailed kinetic mechanisms: application to kerosene/air combustion,” *Combustion science and technology*, vol. 176, no. 11, pp. 1935–1963, 2004. [113](#)
- [319] B. Sirjean, E. Dames, D. Sheen, and H. Wang, “Simplified chemical kinetic models for high-temperature oxidation of c1 to c12 n-alkanes,” in *6th US National Combustion Meeting*, 2009. [113](#)
- [320] A. Vié, B. Franzelli, Y. Gao, T. Lu, H. Wang, and M. Ihme, “Analysis of segregation and bifurcation in turbulent spray flames: A 3d counterflow configuration,” *Proc. Combust. Inst.*, vol. 35, no. 2, pp. 1675–1683, 2015. [113](#)

- [321] H. Wang, R. Xu, K. Wang, C. T. Bowman, R. K. Hanson, D. F. Davidson, K. Brezinsky, and F. N. Egolfopoulos, “A physics-based approach to modeling real-fuel combustion chemistry-i. evidence from experiments, and thermodynamic, chemical kinetic and statistical considerations,” *Combust. Flame*, vol. 193, pp. 502–519, 2018. [113](#)
- [322] R. Xu, K. Wang, S. Banerjee, J. Shao, T. Parise, Y. Zhu, S. Wang, A. Movaghar, D. J. Lee, R. Zhao, *et al.*, “A physics-based approach to modeling real-fuel combustion chemistry–ii. reaction kinetic models of jet and rocket fuels,” *Combustion and Flame*, vol. 193, pp. 520–537, 2018. [113](#)
- [323] Y. Tao, R. Xu, K. Wang, J. Shao, S. E. Johnson, A. Movaghar, X. Han, J.-W. Park, T. Lu, K. Brezinsky, *et al.*, “A physics-based approach to modeling real-fuel combustion chemistry–iii. reaction kinetic model of JP10,” *Combustion and Flame*, vol. 198, pp. 466–476, 2018. [113](#)
- [324] C. Saggese, K. Wan, R. Xu, Y. Tao, C. T. Bowman, J.-W. Park, T. Lu, and H. Wang, “A physics-based approach to modeling real-fuel combustion chemistry–v. nox formation from a typical jet a,” *Combustion and Flame*, vol. 212, pp. 270–278, 2020. [114](#)
- [325] F. Piscaglia, A. Onorati, C. Rutland, and D. E. Foster, “Multi-dimensional modeling of the soot deposition mechanism in diesel particulate filters,” *SAE International Journal of Fuels and Lubricants*, vol. 1, no. 1, pp. 210–230, 2009. [119](#)
- [326] K. Neoh, J. Howard, and A. Sarofim, “Soot oxidation in flames,” in *Particulate Carbon*, pp. 261–282, Springer, 1981. [120](#)
- [327] A. El-Leathy, F. Xu, and G. Faeth, “Soot surface growth and oxidation in laminar unsaturated-hydrocarbon/air diffusion flames,” in *40th AIAA Aerospace Sciences Meeting & Exhibit*, p. 1116, 2002. [120](#)
- [328] F. Xu, A. El-Leathy, C. Kim, and G. Faeth, “Soot surface oxidation in hydrocarbon/air diffusion flames at atmospheric pressure,” *Combustion and Flame*, vol. 132, no. 1-2, pp. 43–57, 2003. [120](#)
- [329] C. Oh and C. Sorensen, “Light scattering study of fractal cluster aggregation near the free molecular regime,” *Journal of Aerosol Science*, vol. 28, no. 6, pp. 937–957, 1997. [129](#)

BIBLIOGRAPHY

- [330] A. D. Abid, J. Camacho, D. A. Sheen, and H. Wang, “Quantitative measurement of soot particle size distribution in premixed flames—the burner-stabilized stagnation flame approach,” *Combustion and Flame*, vol. 156, no. 10, pp. 1862–1870, 2009. [135](#)
- [331] J. Camacho, Y. Tao, and H. Wang, “Kinetics of nascent soot oxidation by molecular oxygen in a flow reactor,” *Proc. Combust. Inst.*, vol. 35, no. 2, pp. 1887–1894, 2015. [135](#), [136](#), [137](#), [139](#)
- [332] J. Singh, R. I. Patterson, M. Kraft, and H. Wang, “Numerical simulation and sensitivity analysis of detailed soot particle size distribution in laminar premixed ethylene flames,” *Combustion and Flame*, vol. 145, no. 1-2, pp. 117–127, 2006. [140](#)
- [333] A. N. Kolmogorov, “The local structure of turbulence in incompressible viscous fluid for very large reynolds numbers,” *C. R. Acad. Sci. , USSR*, vol. 30, p. 301, 1941. [146](#)
- [334] N. Peters, *Turbulent Combustion*. Cambridge University Press, 2001. [149](#)
- [335] R. G. Abdel-Gayed, D. Bradley, M. N. Hamid, and M. Lawes, “Lewis number effects on turbulent burning velocity,” *Proc. Combust. Inst.*, vol. 20, pp. 505–512, 1984. [148](#)
- [336] B. Cuenot and T. Poinso, “Effects of curvature and unsteadiness in diffusion flames. implications for turbulent diffusion flames,” *Proc. Combust. Inst.*, vol. 25, pp. 1383–1390, 1994. [149](#), [150](#)
- [337] T. Takeno, M. Murayama, and Y. Tanida, “Fractal analysis of turbulent premixed flame surface,” *Experiments in Fluids*, vol. 10, pp. 61–70, 1990. [150](#)
- [338] J. Smagorinsky, “General circulation experiments with the primitive equations: 1. the basic experiment.,” *Mon. Weather Rev. ,* vol. 91, pp. 99–164, 1963. [152](#)
- [339] F. Ducros, F. Nicoud, and T. Poinso, “Wall-adapating local eddy-viscosity models for simulations in complex geometries,” in *ICFD*, pp. 293–300, Baines M. J., 1998. [152](#)
- [340] F. Nicoud, H. Baya Toda, O. Cabrit, S. Bose, and J. Lee, “Using singular values to build a subgrid-scale model for large eddy simulations,” *Physics of Fluids*, vol. 23, no. 8, p. 085106, 2011. [152](#)

- [341] B. Fiorina, R. Vicquelin, P. Auzillon, N. Darabiha, O. Gicquel, and D. Veynante, “A filtered tabulated chemistry model for les of premixed combustion,” *Combustion and Flame*, vol. 157, no. 3, pp. 465–475, 2010. [153](#)
- [342] O. Colin, F. Ducros, D. Veynante, and T. Poinso, “A thickened flame model for large eddy simulations of turbulent premixed combustion,” Tech. Rep. HEP/123-qed, CERFACS, 1999. [153](#), [154](#), [155](#)
- [343] F. Shum-Kivan, J. M. Santiago, A. Verdier, E. Riber, B. Renou, G. Cabot, and B. Cuenot, “Experimental and numerical analysis of a turbulent spray flame structure,” *Proc. Combust. Inst.*, vol. 36, no. 2, pp. 2567–2575, 2017. [153](#), [157](#)
- [344] P. S. Volpiani, *Modèle de plissement dynamique pour la simulation aux grandes échelles de la combustion turbulente prémélangée*. PhD thesis, Université Paris-Saclay, 2017. [154](#)
- [345] F. Charlette, D. Veynante, and C. Meneveau, “A power-law wrinkling model for LES of premixed turbulent combustion: Part I - non-dynamic formulation and initial tests,” *Combustion and Flame*, vol. 131, pp. 159–180, 2002. [155](#)
- [346] F. Charlette, C. Meneveau, and D. Veynante, “A power-law flame wrinkling model for les of premixed turbulent combustion part ii: dynamic formulation,” *Combustion and Flame*, vol. 131, no. 1-2, pp. 181–197, 2002. [155](#)
- [347] G. Wang, M. Boileau, D. Veynante, and K. Truffin, “Large eddy simulation of a growing turbulent premixed flame kernel using a dynamic flame surface density model,” *Combustion and Flame*, vol. 159, no. 8, pp. 2742–2754, 2012. [155](#)
- [348] J.-P. L gier, T. Poinso, and D. Veynante, “Dynamically thickened flame LES model for premixed and non-premixed turbulent combustion,” in *Proceedings of the Summer Program*, pp. 157–168, Center for Turbulence Research, NASA Ames/Stanford Univ., 2000. [155](#)
- [349] T. Jaravel, *Prediction of pollutants in gas turbines using large eddy simulation*. PhD thesis, 2016. [156](#)
- [350] B. Rochette, E. Riber, B. Cuenot, and O. Vermorel, “A generic and self-adapting method for flame detection and thickening in the thickened flame model,” *Combustion and Flame*, vol. 212, pp. 448–458, 2020. [156](#), [285](#)
- [351] P. Rodrigues, O. Gicquel, B. Franzelli, N. Darabiha, and R. Vicquelin, “Analysis of radiative transfer in a turbulent sooting jet flame using a monte carlo method coupled to large eddy simulation,” *Journal of Quantitative Spectroscopy and Radiative Transfer*, vol. 235, pp. 187–203, 2019. [160](#), [171](#)

BIBLIOGRAPHY

- [352] J. Jeans, “The equations of radiative transfer of energy,” *Monthly Notices of the Royal Astronomical Society*, vol. 78, pp. 28–36, 1917. [160](#)
- [353] S. Chandrasekhar, *Radiative transfer*. Courier Corporation, 2013. [160](#)
- [354] P. J. Coelho, “Advances in the discrete ordinates and finite volume methods for the solution of radiative heat transfer problems in participating media,” *Journal of Quantitative Spectroscopy and Radiative Transfer*, vol. 145, pp. 121–146, 2014. [160](#)
- [355] B. G. Carlson, “More precise definition of the discrete ordinates method,” 1971. [161](#)
- [356] W. Fiveland, “Discrete ordinate methods for radiative heat transfer in isotropically and anisotropically scattering media,” *Journal of Heat Transfer*, vol. 109, no. 3, 1987. [161](#)
- [357] J. Truelove, “Discrete-ordinate solutions of the radiation transport equation,” *Journal of Heat Transfer*, vol. 109, no. 4, 1987. [161](#)
- [358] M. Sakami and A. Charette, “A new differencing scheme for the discrete-ordinates method in complex geometries,” *Revue générale de thermique*, vol. 37, no. 6, pp. 440–449, 1998. [161](#)
- [359] J. Liu, H. Shang, and Y. Chen, “Development of an unstructured radiation model applicable for two-dimensional planar, axisymmetric, and three-dimensional geometries,” *Journal of Quantitative Spectroscopy and Radiative Transfer*, vol. 66, no. 1, pp. 17–33, 2000. [161](#)
- [360] J. Strohle, U. Schnell, and K. R. Hein, “A mean flux discrete ordinates interpolation scheme for general co-ordinates,” in *Int. Comm. Heat and Mass Transfer*, Begel House Inc., 2001. [161](#)
- [361] D. Poitou, J. Amaya, C. Bushan Singh, D. Joseph, M. El Hafi, and B. Cuenot, “Validity limits for the global model fs-snbck for combustion applications,” *Proceedings of Eurotherm83–Computational Thermal Radiation in Participating Media III*, 2009. [161](#), [162](#)
- [362] J. Amaya, O. Cabrit, D. Poitou, B. Cuenot, and M. El Hafi, “Unsteady coupling of navier–stokes and radiative heat transfer solvers applied to an anisothermal multicomponent turbulent channel flow,” *Journal of Quantitative Spectroscopy and Radiative Transfer*, vol. 111, no. 2, pp. 295–301, 2010. [162](#)

- [363] D. Poitou, M. El Hafi, and B. Cuenot, “Analysis of radiation modeling for turbulent combustion: development of a methodology to couple turbulent combustion and radiative heat transfer in les,” *Journal of Heat Transfer*, vol. 133, no. 6, 2011. [162](#)
- [364] V. P. Solovjov, F. Andre, D. Lemonnier, and B. W. Webb, “The rank correlated slw model of gas radiation in non-uniform media,” *Journal of Quantitative Spectroscopy and Radiative Transfer*, vol. 197, pp. 26–44, 2017. [162](#)
- [365] V. P. Solovjov, B. W. Webb, and F. Andre, “The rank correlated fsk model for prediction of gas radiation in non-uniform media, and its relationship to the rank correlated slw model,” *Journal of Quantitative Spectroscopy and Radiative Transfer*, vol. 214, pp. 120–132, 2018. [162](#)
- [366] D. Poitou and F. Andre, “Comparison of databases for radiative heat transfer calculations in combustion applications with the NBKMcK model,” *Int. J. Thermal Sciences*, vol. 64, pp. 11–21, 2013. [162](#)
- [367] P. J. Coelho, P. Perez, and M. El Hafi, “Benchmark numerical solutions for radiative heat transfer in two-dimensional axisymmetric enclosures with nongray sooting media,” *Numerical Heat Transfer: Part B: Fundamentals*, vol. 43, no. 5, pp. 425–444, 2003. [162](#)
- [368] F. Liu, Ö. Gülder, G. Smallwood, and Y. Ju, “Non-grey gas radiative transfer analyses using the statistical narrow-band model,” *Int. J. Heat and Mass Transfer*, vol. 41, no. 14, pp. 2227–2236, 1998. [163](#)
- [369] G. Okyay, *Impact of the morphology of soot aggregates on their radiative properties and the subsequent radiative heat transfer through sooty gaseous mixtures*. PhD thesis, 2016. [164](#)
- [370] H. C. Hulst and H. C. van de Hulst, *Light scattering by small particles*. Courier Corporation, 1981. [164](#)
- [371] C. F. Bohren and D. R. Huffman, *Absorption and scattering of light by small particles*. John Wiley & Sons, 2008. [164](#)
- [372] F. André and R. Vaillon, “Generalization of the k-moment method using the maximum entropy principle. application to the nbkm and full spectrum slmb gas radiation models,” *Journal of Quantitative Spectroscopy and Radiative Transfer*, vol. 113, no. 12, pp. 1508–1520, 2012. [165](#), [281](#)

BIBLIOGRAPHY

- [373] F. André, H. Longfeng, and V. P. Solovjov V, “An exact formulation of k-distribution methods in non-uniform gaseous media and its approximate treatment within the multi-spectral framework,” in *Journal of Physics: Conference Series*, vol. 676, p. 012001, IOP Publishing, 2016. [165](#), [281](#)
- [374] A. Soufiani and J. Taine, “High temperature gas radiative property parameters of statistical narrow-band model for H₂O, CO₂ and CO, and correlated-k model for H₂O and CO₂,” *Int. J. Heat and Mass Transfer*, vol. 40, no. 4, pp. 987–991, 1997. [165](#)
- [375] K. P. Geigle, R. Hadeif, and W. Meier, “Soot formation and flame characterization of an aero-engine model combustor burning ethylene at elevated pressure,” in *ASME Turbo Expo*, 2013. [167](#)
- [376] K. P. Geigle, M. Köhler, W. O’Loughlin, and W. Meier, “Investigation of soot formation in pressurized swirl flames by laser measurements of temperature, flame structures and soot concentrations,” *Proc. Combust. Inst.*, vol. 35, no. 3, pp. 3373–3380, 2015. [167](#), [169](#), [188](#)
- [377] K. P. Geigle, W. O’Loughlin, R. Hadeif, and W. Meier, “Visualization of soot inception in turbulent pressurized flames by simultaneous measurement of laser-induced fluorescence of polycyclic aromatic hydrocarbons and laser-induced incandescence, and correlation to oh distributions,” *Applied Physics B*, vol. 119, no. 4, pp. 717–730, 2015. [167](#), [186](#), [188](#)
- [378] C. Eberle, P. Gerlinger, K. P. Geigle, and M. Aigner, “Numerical investigation of transient soot evolution processes in an aero-engine model combustor,” *Combustion science and technology*, vol. 187, no. 12, pp. 1841–1866, 2015. [167](#), [190](#), [209](#)
- [379] P. Nau, Z. Yin, K. P. Geigle, and W. Meier, “Wall temperature measurements at elevated pressures and high temperatures in sooting flames in a gas turbine model combustor,” *Applied Physics B*, vol. 123, no. 12, p. 279, 2017. [167](#), [169](#), [170](#)
- [380] T. Poinso and S. Lele, “Boundary conditions for direct simulations of compressible viscous flows,” *J. Comput. Phys.*, vol. 101, no. 1, pp. 104–129, 1992. [170](#)
- [381] P. Rodrigues, O. Gicquel, N. Darabiha, K. P. Geigle, and R. Vicquelin, “Assessment of external heat transfer modeling of a laboratory-scale combustor: Effects of pressure-housing environment and semi-transparent viewing windows,” *Journal of Engineering for Gas Turbines and Power*, vol. 141, no. 3, 2019. [170](#)

- [382] N. Dellinger, *Modélisation de la formation et de l'évolution des particules de suie en approche hybride Euler-Lagrange pour la simulation de foyers aéronautiques*. PhD thesis, 2019. [179](#), [180](#), [190](#), [209](#), [228](#)
- [383] E. Knudsen and H. Pitsch, “A general flamelet transformation useful for distinguishing between premixed and non-premixed modes of combustion,” *Combustion and Flame*, vol. 156, no. 3, pp. 678–696, 2009. [181](#)
- [384] K. P. Geigle, R. Hadeif, M. Stöhr, and W. Meier, “Flow field characterization of pressurized sooting swirl flames and relation to soot distributions,” *Proc. Combust. Inst.*, vol. 36, no. 3, pp. 3917–3924, 2017. [190](#), [194](#), [285](#)
- [385] A. Lefebvre and X. Wang, “Mean drop sizes from pressure-swirl nozzles,” *J. Propuls. Power*, vol. 3, no. 1, pp. 11–18, 1987. [213](#)
- [386] F. Duchaine, S. Jauré, D. Poitou, E. Quémerais, G. Staffelbach, T. Morel, and L. Gicquel, “Analysis of high performance conjugate heat transfer with the open-palm coupler,” *Computational Science & Discovery*, vol. 8, no. 1, p. 015003, 2015. [283](#)
- [387] A. Refloch, B. Courbet, A. Murrone, P. Villedieu, C. Laurent, P. Gilbank, J. Troyes, L. Tessé, G. Chaineray, J. Dargaud, *et al.*, “Cedre software,” 2011. [283](#)
- [388] O. Colin and M. Rudgyard, “Development of high-order taylor–galerkin schemes for les,” *J. Comput. Phys.*, vol. 162, no. 2, pp. 338–371, 2000. [285](#)
- [389] F. Nicoud and F. Ducros, “Subgrid-scale stress modelling based on the square of the velocity gradient,” *Flow, Turb. and Combustion*, vol. 62, no. 3, pp. 183–200, 1999. [285](#)
- [390] O. Colin, F. Ducros, D. Veynante, and T. Poinso, “A thickened flame model for large eddy simulations of turbulent premixed combustion,” *Phys. Fluids*, vol. 12, no. 7, pp. 1843–1863, 2000. [285](#)

BIBLIOGRAPHY

Appendices

Appendix A

Article on Lagrangian soot tracking methodology

L. Gallen et al., Lagrangian tracking of soot particles in LES of gas turbines, Proceedings of the Combustion Institute (2019),
<https://doi.org/10.1016/j.proci.2018.06.013>



Lagrangian tracking of soot particles in LES of gas turbines

Lucien Gallen*, Anne Felden, Eleonore Riber, Bénédicte Cuenot

CERFACS, 42 avenue Gaspard Coriolis, Toulouse 31047, France

Received 1 December 2017; accepted 2 June 2018

Available online xxx

Abstract

Expected stringent legislation on particulate matter (PM) emission by gas turbine combustors is currently motivating considerable efforts to better understand, model and predict soot formation. This complex phenomenon is very difficult to study in detail with experiment, and numerical simulation is an essential complementary tool. Considering that the chemistry of soot particles strongly depends on their size, the numerical prediction of soot formation requires the description of their size distribution. To do so, either Eulerian methods (sectional or moments), or stochastic Lagrangian approaches are reported in the literature. In the present work a far more simple semi-deterministic Lagrangian approach is proposed. Combined to the semi-empirical model of Leung et al. (1991) for soot chemistry, the Lagrangian approach is first validated on a one-dimensional premixed ethylene-air flame. The model is then applied to a gaseous non-premixed ethylene-air burner measured at DLR and computed with Large Eddy Simulation (LES). The gaseous chemistry is described with an Analytically Reduced Chemistry (ARC) to guarantee a good prediction of combustion and gaseous soot precursors. Results are validated against experiment and compared, in terms of accuracy and CPU cost, to an Eulerian semi-empirical model. To the authors knowledge, it is the first time that such Lagrangian particle tracking approach is used for soot. Results obtained in terms of accuracy and computing time are very encouraging.

© 2018 The Combustion Institute. Published by Elsevier Inc. All rights reserved.

Keywords: Soot particles; Lagrangian tracking; Large Eddy Simulation; Gas turbine

1. Introduction

Particulate Matter (PM) emitted from practical combustion devices contribute to air pollution, which has a strong negative impact on the population health [1] and air quality. This includes soot, which results from a complex gaseous and

heterogeneous chemical process. When emitted at high altitude, soot increases significantly the local concentration of aerosols in the atmosphere inducing a possible artificial radiative forcing via the formation of contrails. On the ground, emitted soot particles can be inhaled and, depending on their size, penetrate more or less deeply in the human body where it can trigger specific diseases. In this context, the design of the next generation of combustor devices with limited soot emission has become a major challenge for engine man-

* Corresponding author.

E-mail address: gallen@cerfacs.fr (L. Gallen).

<https://doi.org/10.1016/j.proci.2018.06.013>

1540-7489 © 2018 The Combustion Institute. Published by Elsevier Inc. All rights reserved.

ufacturers. To do so numerical simulation is an essential tool which, if sufficiently accurate, allows a better understanding and control of soot formation.

Soot particle size is not only critical for their toxicity, but also for their formation / destruction processes, as these involve heterogeneous chemistry at the particle surface. The prediction of soot particle formation therefore requires to describe their size distribution. A population of soot particles is then represented by its local and instantaneous Number Density Function (NDF), defined as the number of particles of a given size. The NDF is often bimodal due to the constant inception of very small soot particles and the final large aggregates resulting from successive collisions and surface reactions [2]. The NDF is the solution of the Population Balance Equation (PBE), which is solved using statistical approaches. Three classes of resolution methods of the PBE are commonly used: the Method of Moments (MOM), the Sectional Method (SM), and the Monte Carlo (MC) stochastic Lagrangian approach. The MOM aims at calculating a set of statistical moments of the NDF [3–6], while SM [7–9] and MC directly solve the PBE to obtain the NDF. Although they have allowed to obtain very good results [10,11], these methods are complex, demand specific numerics and are computationally expensive.

An alternative is proposed in the present work, based on a simple semi-deterministic Lagrangian approach. The method is deterministic in the sense that physical particles are tracked, contrary to MC dealing with stochastic particles. It however still includes stochastic processes such as collisions. To limit the computational time, only a subset of particles is computed, representative of all particles possibly present in a control volume. With this strategy, Lagrangian particle tracking becomes affordable in real complex geometries such as aircraft or internal engines. The choice of such a Lagrangian formalism for nano-particles is still on the fringes of the official methods. The reason is to be found in the prohibitive computational cost of the Lagrangian tracking of all physical particles in a 3D complex configuration. As a consequence, most Lagrangian calculations are restricted to the resolution of realizability issues in MOM [12]. An attempt of deterministic Lagrangian calculation of soot has been made very recently by Ong et al. [13] where however the interactions between particles were neglected. This considerably simplified the implementation but also significantly reduced the accuracy as particle interactions are essential. Today, both the progress made in parallel computing and the semi-deterministic Lagrangian concept allow to overcome this computational cost issue, as will be demonstrated in the present paper. This requires however an optimum parallel efficiency of the Lagrangian solver, as well as a careful control of statistical convergence.

In the following, the derivation of the semi-deterministic Lagrangian method is explained in details. Combined to a semi-empirical model for soot evolution [14], it is then validated in a one-dimensional sooting premixed flame. Finally, an experimental gaseous ethylene-air non-premixed burner [15] already investigated with LES and a one-section SM approach [16,17] is used to assess the computational cost and accuracy provided by the new Lagrangian method.

2. Soot modeling

2.1. Lagrangian formalism

The present methodology is based on the Discrete Particle Simulation (DPS), similar to what is used for spray computations. Contrary to dilute sprays, soot particle populations are dense, so that collisions have a high probability and must be accounted for. Indeed, they play an essential role in the soot particles size distribution. The proposed approach, so-called EL POLY, relies on the following assumptions:

- *Dynamics*: soot particles are tracers. This means that neither drag nor thermophoresis effects are taken into account. Considering that soot are mostly nanometric and evolve in highly turbulent flows (low Stokes number), this assumption seems reasonable.
- *Temperature*: Soot particle temperature is homogeneous and equal to the surrounding gas temperature. This assumption is also justified by the nanometric size of the particles.
- *Shape*: The particles are spherical. This is clearly a very strong assumption that is not true in most cases, but is done here as a first step for the demonstration of the new Lagrangian approach. It will be shown that this approach is a good framework to relax this assumption in future works.

In the DPS approach, particles are handled as point sources, having properties like temperature, size, velocity, surface area, collision diameter, etc. just as in stochastic methods [10]. In particular the spherical assumption can be easily relaxed through the particle surface or a joint surface-volume model [18]. In addition, as only a subset of physical particles are computed in the semi-deterministic concept, each particle also has a weight w_k (also denoted *rparcel*) representing the number of physical particles having the same properties at the same location and time. Being not constant nor uniform, this *rparcel* is not a user-defined parameter, but varies for each particle and results from the control of statistical convergence. The objective is to describe with sufficient accuracy the NDF in each control volume (mesh cell), given a maximum allowed number of computed particles per control

volume N_{soot}^{max} . To do so, at each time step, particles grouping is revisited via conservative merging operations based on criteria of properties proximity (size, location). This merging process will be described in Section 2.3.

2.2. The Leung model

The chosen soot model is the semi-empirical, two-equations Leung model [14], employed in many previous studies [16,17,19]. The model describes soot as a monodisperse particle size distribution population, and was written in both Eulerian and Lagrangian formulations. Although this model is too simple to be quantitatively accurate, this choice was made to ease the comparison between Eulerian and Lagrangian approaches, which is the main objective of this paper.

In the Leung model, the soot particle mass evolves as:

$$\frac{dm_p}{dt} = \frac{\dot{\omega}_s}{N} - \frac{m_p}{N} \dot{\omega}_n N_A \left[\frac{\text{kg}}{\text{s}} \right] \quad (1)$$

where N is the soot particle number density per volume, N_A is the Avogadro number and m_p is the particle mass. $\dot{\omega}_n$ and $\dot{\omega}_s$ refer to soot number density and mass fraction source terms, and are detailed later in this Section. Note that condensation is not taken into account. The monodisperse approach has been validated [17] in non-premixed laminar ethylene-air flames studied experimentally by Hwang and Chung [20] and often used for soot modeling validation. The gas-phase chemistry was described by an Analytically Reduced Chemistry including 29 species, among which 11 were set in Quasi Steady State [17]. The reaction rate constants of the Leung model have been calibrated in order to improve soot prediction. This is a standard procedure for such simple model, that has anyway a limited accuracy. It is however not the objective here to demonstrate the validity of the Leung model, but rather to guarantee a correct behavior before focusing on the soot numerical formalism. The source terms of the Leung model are now detailed.

2.2.1. Nucleation

Nucleation processes characterize the inception of the nascent soot particles (nuclei). The corresponding source term reads:

$$\dot{\omega}_{n,nu} = \frac{R_{nu}}{N} \left(M_s - m_{p,nu} N_A \frac{2}{C_{min}} \right) \quad (2)$$

where $\dot{\omega}_{n,nu}$ is the nucleation part of the source term $\dot{\omega}_n$, M_s is the soot molecular weight, C_{min} is a constant, and R_{nu} is the nucleation reaction rate defined by Leung et al. [14]:

$$R_{nu} = k_{nu}(T) [\text{C}_2\text{H}_2] \quad (3)$$

where k refers to the reaction rate (from [17]), T is the gas temperature, and $[-]$ stands for molar concentration. As the Lagrangian formalism is

based on discrete particles, a new particle is created only after the nucleation source term is found sufficiently large. The new particle then has an initial weight equal to the number of generated nuclei, and is injected at a random position in the control volume with a given initial diameter. This initial diameter can be retrieved analytically from Eq. (2), considering that nuclei are formed at the end of the nucleation process, i.e., $\dot{\omega}_{n,nu} = 0$. This gives an initial value of 0.98 nm, which will be used in all simulations presented in this paper.

In the current model, nucleation contributes only to the inception of soot particles and does not modify their properties. Therefore it does not contribute to the source term $\dot{\omega}_s$.

2.2.2. Surface reactions

Surface reactions act on the soot mass fraction source term $\dot{\omega}_s$ in Eq. (1) with two contributions:

$$\dot{\omega}_s = \dot{\omega}_{s,sg} - \dot{\omega}_{s,ox} \left[\frac{\text{kg}}{\text{m}^3 \text{ s}} \right] \quad (4)$$

where subscripts sg and ox refer to surface growth and oxidation, and respectively read:

$$\dot{\omega}_{s,sg} = k_{sg}(T) [\text{C}_2\text{H}_2] S^{1/2} M_s \quad (5)$$

$$\dot{\omega}_{s,ox} = (k_{ox,\text{O}_2}(T) [\text{O}_2] + k_{ox,\text{OH}}(T) X_{\text{OH}}) S M_s \quad (6)$$

where X_{OH} refers to the molar fraction of OH species. Surface reactions are directly linked to the soot surface area per unit volume $S = \pi/4 d_p^2 N$, if spherical particles of diameter d_p are assumed.

2.2.3. Coagulation

For a monodisperse size distribution of soot particles, the coagulation source term reduces to the same global source term for all particles. Polydisperse coagulation is more complex and has been widely investigated for particles and aerosols [21–23]. Usually stochastic approaches are used. In the present approach, the deterministic Lagrangian tracking of a subset of physical particles does not allow to realize all possible coagulation events and a probability of coagulation is introduced. Coagulation events are then computed according to this probability. Following Kruis et al. [24], we start from binary collisions. Considering a particle pair (i, j) with $i \neq j$, $\beta_{i,j}$ (called coagulation kernel) describes the collision rate between both particles. For symmetry reasons $\beta_{i,j} = \beta_{j,i}$ and the total coagulation rate between all particles represented by the pair (i, j) is $\beta_{i,j}^* = \max(\omega_i, \omega_j) \beta_{i,j} / v$, with v the control volume. The coagulation kernel is calculated in the free molecular regime as in the original Leung model:

$$\beta_{i,j} = C_a \sqrt{\frac{\pi \kappa T}{2 \rho_s}} \left(\frac{1}{v_i} + \frac{1}{v_j} \right)^{\frac{1}{2}} (d_{p,i} + d_{p,j})^2 \left[\frac{\text{m}^3}{\text{s}} \right] \quad (7)$$

where C_a is the agglomeration rate constant equal to 9.0 higher than the commonly used value around 2.0 [9], κ is the Boltzmann constant, and ρ_s is the soot density equal to 2000 [kg · m⁻³]. The free molecular regime assumption considers that the two particles of volume v_i and v_j have a size much smaller than the mean free path in the gas. The probability of coagulation for each pair of particles (i, j) is then $P_{i,j} = \beta_{i,j}^* / \sum_{k,l} \beta_{k,l}^*$.

This probability is used in the Lagrangian tracking approach as follows:

1. At the cell level, $\beta_{i,j}^*$ is computed for each pair of particles (i, j), and the maximum coagulation rate in the cell β_{max}^* is determined.
2. The acceptance-rejection method [25] is applied: selecting a pair of soot particles (i, j), coagulation occurs if $r \leq \beta_{i,j}^* / \beta_{max}^*$, where $r \in [0, 1]$ is a random number. Otherwise, the selected pair does not coagulate, and the operation is repeated until one coagulating pair is found [26].
3. The selected coagulation event is realized according to the constant-number method [26].
4. The coagulation time step is computed as the inverse of the sum of all coagulation rates: $\tau_{coa} = 1 / \sum_{i,j} \beta_{i,j}^*$ [24,27], and an event-driven coagulation process is applied: as soon as one coagulation event takes place, a waiting time τ_{coa} is set before the next coagulation event.

The above coagulation model assumes that the particles in the control volume are sufficiently numerous, and describe a sufficient number of discrete states of particles to fully describe coagulation statistics.

2.3. Control of statistical convergence

Lagrangian approaches require a minimum number of particles to reach statistical convergence. On the other hand, the inception of nascent soot particles implies the constant creation of new particles in the control volume, increasing their number in an uncontrolled way. In MC simulations, resizing [28] or constant-number approaches [29] are applied to nucleation [30]. In the present Lagrangian formulation, the constant-number approach is retained. This implies defining a maximum number of particles, sufficient to reach statistical convergence, and merging of weighted particles to keep their number below the maximum, as was already used in [2]. Particles can be removed randomly [21,30,31] but in order to enhance statistical convergence, it is more efficient to merge particles with close enough properties (size here) [26]. To do so, particles and their weights are controlled as follows:

Table 1

Contribution of the Lagrangian solver to the computational time for different values of f_s and maximum relative error on soot prediction for the ISF Target Flame 4.

Soot frequency, f_s	1	5	10	20
Lagrangian solver, %	25	9	6	4
Maximum error, %	0	3.3	18	37

- *Maximum number of particles:* A constant threshold value N_{soot}^{max} is applied to control the number of computed particles which are merged if $N > N_{soot}^{max}$.
- *Particle creation:* The nascent particles are created with a weight dictated by both the control volume and the numerical timestep to guarantee a number of particles below N_{soot}^{max} .
- *Merging:* Particle merging is controlled by a criterion based on their position and diameter.

3. Validation in laminar flames

The Lagrangian polydisperse methodology (EL POLY) was implemented in the code AVBP jointly developed by CERFACS and IFPEN. To benefit from the difference between the compressible flow timestep controlled by acoustics, and the particle motion convective timestep which is much larger, Lagrangian iterations are performed only after a number f_s (soot frequency) of flow iterations. This leads to a significant gain of computational cost without losing accuracy, as illustrated in Table 1 showing the contribution of the Lagrangian solver to the total computational time for different values of f_s . The value of the soot frequency f_s depends on the case and the numerical setup, and can be estimated as $f_s = \alpha \tau_{min} / \tau_f$, where τ_f is a flow time scale and τ_{min} corresponds to the minimum characteristic time of soot processes among nucleation, surface reactions and coagulation. The coefficient α allows to filter out some unsteadiness of the flow and depends on the application. In the present case $\alpha = 2$. Note that the soot frequency has to be chosen carefully to guarantee a maximum gain in computational cost and a minimum error. To assess the quality of the proposed method applied to gas turbines, the pressurised 1D premixed ethylene/air sooting flame from the International Sooting Flame workshop (ISF Target Flame 4 : Laminar Premixed Pressurised 2 [32]) is first computed. The equivalence ratio is high: $\phi = 2.3$ ($C/O = 0.766$), and the pressure is 3 bars. For this flame f_s is estimated at 5, for which the error is still found negligible (See Table 1). Higher values lead to significantly higher errors.

For this case N_{soot}^{max} is set to 20 per control volume. Soot has been computed with both the monodisperse (in both Eulerian (EE) and Lagrangian (EL MONO) formulations) and polydis-

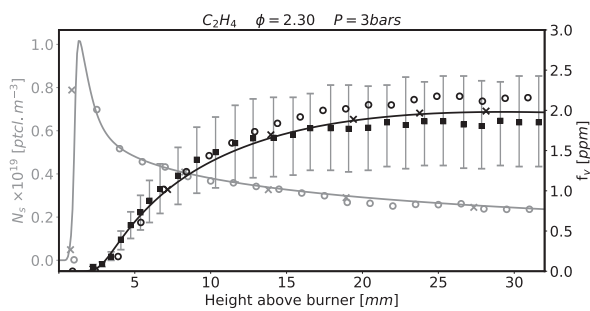


Fig. 1. Soot number density (left axis, grey line) and soot volume fraction (right axis, black line) in the ISF Target Flame 4 (Laminar Premixed Pressurised 2). Comparison between experiment [32] (squares), EE (lines), EL MONO (crosses) and EL POLY (circles).

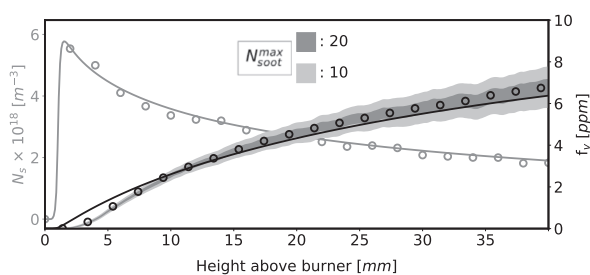


Fig. 2. Soot number density (left axis) and soot volume fraction (right axis) for coagulation in the ISF Target Flame 4 (Laminar Premixed Pressurised 2). Comparison between EE (lines) and EL POLY (symbols) with the stochastic noise (shaded area).

perse (EL POLY) approach. For EL MONO, the soot particle mass is governed by Eq. (1), the nuclei diameter is set to the mean diameter and the coagulation is based on Eq. (7) where particles have the same diameter. Results are compared in Fig. 1.

As expected EE and EL MONO are strictly identical and reproduce well the experiment as in [17]. The EL POLY approach gives also the same soot number density, but a slightly higher soot volume fraction downstream the flame.

To go further, the same 1D sooting flame is computed without surface reactions, in order to focus on coagulation. As the EL POLY approach for coagulation is stochastic, several computations have been performed. Results are compared to the EE approach in Fig. 2. EL POLY introduces a slight stochastic noise on soot volume fraction directly linked to N_{soot}^{max} . The stochastic noise induced by $N_{soot}^{max} = 20$ seems reasonable compared to $N_{soot}^{max} = 10$. However, near the exit the statistical average of soot volume fraction is slightly higher while the average soot number density is slightly lower. This is due to polydispersity which promotes the coagulation of the largest particles. The number of particles is negatively impacted whereas the soot diameter increases.

Table 2

Experimental operating conditions at $P = 3$ bars [15].

\dot{m}_{air} [kg · s ⁻¹]	$\dot{m}_{air,oxi}$ [kg · s ⁻¹]	\dot{m}_f [kg · s ⁻¹]	ϕ_{PZ} [–]
0.82×10^{-3}	4.04×10^{-3}	0.86×10^{-3}	1.2

4. Application to a realistic combustion chamber

4.1. Configuration and numerical set-up

The configuration studied in this work is an experimental set-up installed at DLR [33] referred to as ISF-3 Target Flame 1. It is one of the target pressurized flame within the International Sooting Flame (ISF) workshop. It is designed to study soot formation in gas turbine combustors under elevated pressure, burning ethylene with or without secondary air dilution. The combustor is presented in Fig. 3, also illustrating the flow topology by displaying the instantaneous axial velocity field. The chosen operating point is summarized in Table 2. The burner operates under overall lean conditions ($\phi_{glob} = 0.86$) but the primary combustion zone (PZ) is characterized by an overall rich equivalence ratio ($\phi = 1.2$).

The numerical strategy used for the LES of this configuration is fully described and validated in [17]. The domain is discretized into a fully unstructured mesh using 40M tetrahedral elements, and the flow and flame equations are solved with a third order in space and time numerical scheme [34]. The same ARC described in Section 3 is employed, associated with the DTFLES turbulent combustion model [35] and the WALE [36] turbulence model. Two simulations including soot, one with EE approach and the other with EL POLY approach were performed for comparison. An instantaneous field of temperature in a mid-cut plane is displayed in Fig. 4(a). As suggested by the white superimposed acetylene isocontour, soot is massively generated in the PZ, downstream the (rich) main flame. The dilution holes are responsible for the temperature decrease along the main axis, visible in Fig. 4(b) where the comparison with experiment shows a very good agreement.

4.2. Soot prediction

Figure 5 presents a qualitative comparison of time-averaged soot mass fraction fields obtained with both formalisms and the experimental results. In both simulations a good order of magnitude and distribution of soot volume fraction is retrieved. The Eulerian and Lagrangian descriptions lead to very similar results, confirming the validity of our Lagrangian particle tracking approach. The different formalisms however lead to slight differences for oxidation. This is due to the removal of particles with a diameter lower than the nuclei ($=0.98$ nm)

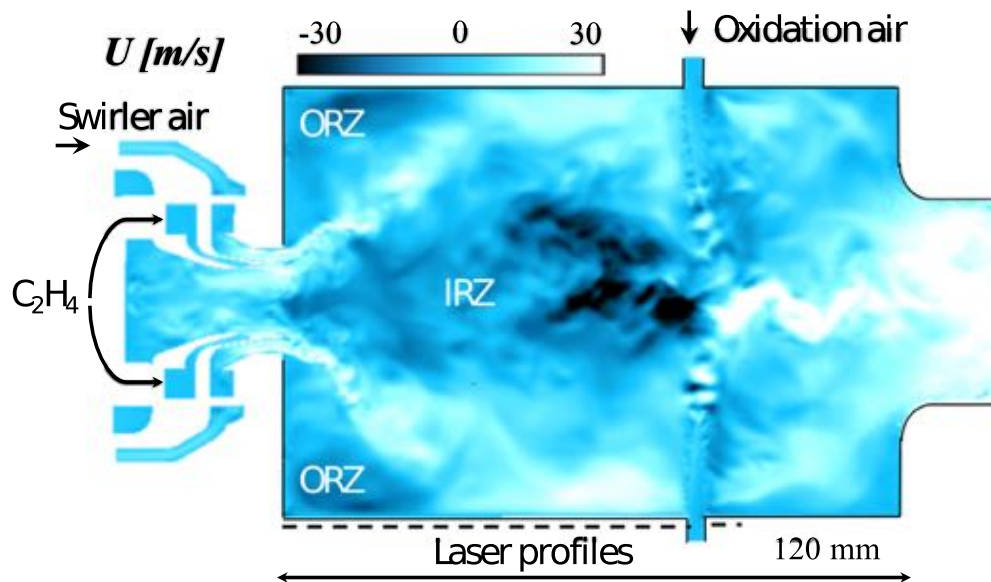


Fig. 3. ISF-3 Target Flame 1: Instantaneous axial velocity from LES in a mid-plane cut.

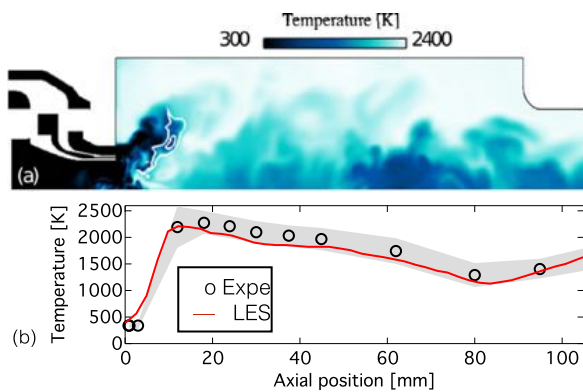


Fig. 4. ISF-3 Target Flame 1: (a) Instantaneous temperature field with superimposed with acetylene level. (b) Mean axial temperature profile with experimental distribution width (shaded area).

in the Lagrangian approach, in order to avoid computing small residual diameter particles, whereas all particles are kept in the EE approach. A white isocontour of diameter at the nuclei value in Fig. 5b confirms that results for EE and EL POLY are very similar for soot particles larger than nuclei. The main difference between both approaches is the NDF, which is reduced to a Dirac function in the Eulerian approach. Figure 6 shows the instantaneous presence of soot particles (for easier visualization only 1 over 100 particles are displayed). Particles are displayed in four bins of size from nuclei size to 20 nm diameter. Streamlines thickened by the velocity magnitude illustrate the interaction with particle dynamics. The flame position, O_2 and C_2H_2 mass fractions explain why soot remains in the primary zone (Fig. 5). As already seen, soot is formed mainly in post-flame zones rich in C_2H_2 , the soot precursor used in the Leung model. Soot particles are then quickly oxidized al-

though the level of O_2 has significantly decreased in this burnt gas region. Oxidized particles are removed as soon as their size falls below the nuclei size. Only few particles are able to subsist slightly longer downstream until they meet the dilution air jets where they are in turn oxidized. The NDFs obtained with the Lagrangian approach at four probes P1–P4 represented by large circles on the snapshot are also available in Fig. 6. Although no validation can be made due to the lack of measurement, results demonstrate that the EL POLY approach is capable to describe the NDF with sufficient statistical convergence. The first probe (P1) located in the rich C_2H_2 regions exhibits a single-peak NDF shape due to the strong nucleation in this zone. The bimodality of the soot NDF is retrieved at the fourth probe (furthest from the flame) as expected. The comparison of the mean diameter obtained is also plot in Fig. 6 for each probes.

As mentioned in the Introduction, access to the NDF is critical to improve soot modeling. The current results demonstrate that the Lagrangian particle tracking approach is a promising technique to increase the accuracy of soot prediction. This conclusion is re-enforced by the computing times reported in Table 3 for each formalism. Overall the computational time of the Lagrangian approach is of the same order of magnitude than the monodisperse Eulerian approach. This means that the Lagrangian approach gives the NDF at the same computational cost as a monodisperse approach, and allows to envisage sophisticated soot chemistry models in real complex geometries. Note that detailed soot chemistry models may involve additional properties like surface or H/C ratio. If adding such properties is easier with particles than in Eulerian methods [10], it may require more numerical particles to reach sufficient accuracy and

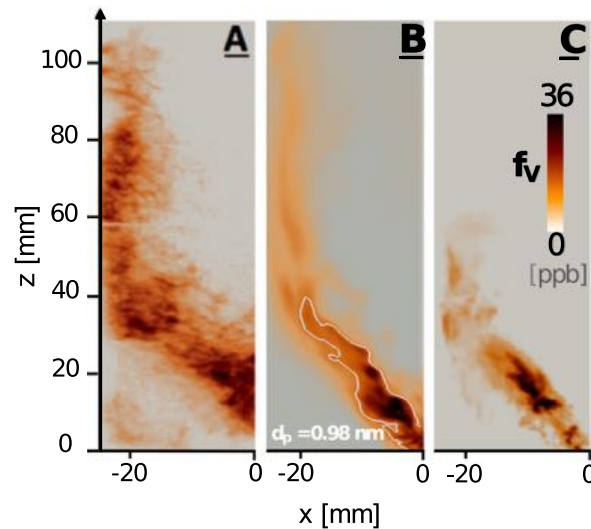


Fig. 5. ISF-3 Target Flame 1: Comparison of (A) time-averaged LII soot measurements with time-averaged soot volume fraction from LES using (B) the monodisperse Eulerian (EE) and (C) the polydisperse Lagrangian (EL POLY) approaches. Soot diameter isocontour $d_p = 0.98$ nm is shown in white.

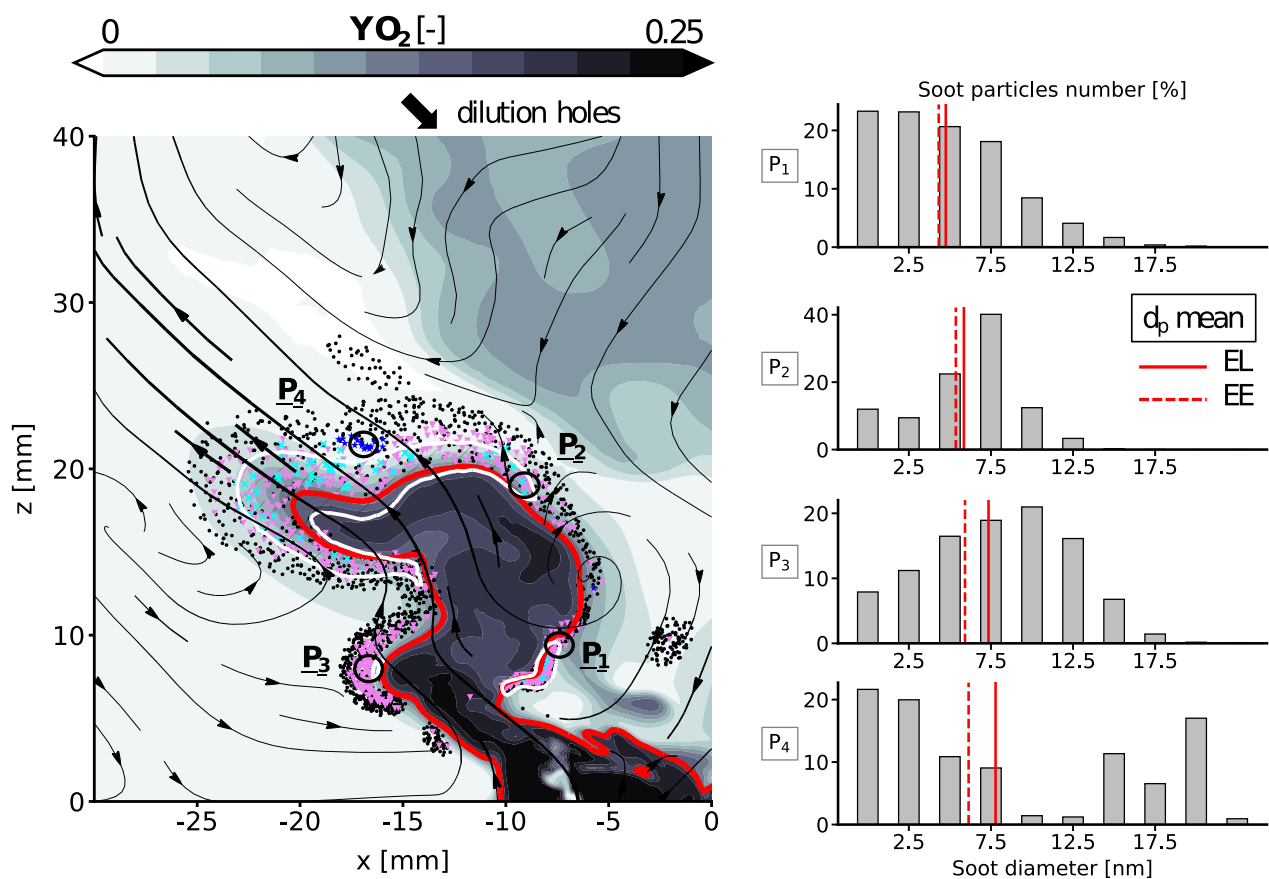


Fig. 6. ISF-3 Target Flame 1: Instantaneous soot presence (symbols) in the primary zone with superimposed streamlines, O_2 mass fraction (grey scale), one isocontour of acetylene (white), the isocontour of Temperature at $T = 1200$ K (red). Four bins of particles are represented: nuclei to 2.5 nm (\bullet), 2.5–7.5 nm (\blacktriangledown), 7.5–12.5 nm (\times) and 12.5–20 nm (\star). Finally, 4 probes are defined and their respective NDF are shown. (For interpretation of the references to color in this figure legend, the reader is referred to the web version of this article.)

Table 3

Summary of computational requirements for the computation of 1 ms physical time.

	EE		EL POLY		
f_s	–	1	5	1	5
N_{soot}^{max}	–	10	10	20	20
CPUh	12,500	20,250	13,600	26,650	14,675

then increase the computational cost. However, Table 3 shows that increasing the number of particles will impact the computational cost to a reasonable extent. Another additional complexity will be to include PAH chemistry. This can be achieved either with the use of look-up table [19] or by directly calculating lumped PAHS, as in the 3 sections model of [37]. Both methods induce a low additional cost. All these issues associated to detailed soot chemistry models will be investigated in a future work.

5. Conclusions

A semi-deterministic Lagrangian particle tracking methodology has been introduced and validated for soot prediction in combustion chambers. Validation on a one-dimensional sooting flame and a gaseous non-premixed burner has been performed by comparison with the original Eulerian Leung model and experiment when available. Results confirm that the approach is suitable for soot modeling and provides accurate results in reasonable computing time. Although further validations are required to assess the accuracy of the predicted NDF, the proposed formalism is ready to include more sophisticated soot models based on more particle properties.

Acknowledgments

This work was performed using HPC resources from GENCI (Grant no. A0032B10157): CINES, IDRIS and TGCC. Funding from the European Union within the project SOPRANO (Soot Processes and Radiation in Aeronautical innovative combustion) Horizon 2020 Grant agreement no. 690724 is gratefully acknowledged.

References

- [1] M. Shiraiwa, K. Selzle, U. Pöschl, *Free Radic. Res.* 46 (8) (2012) 927–939.
- [2] B. Zhao, Z. Yang, Z. Li, M.V. Johnston, H. Wang, *Proc. Comb. Inst.* 30 (1) (2005) 1441–1448.
- [3] M. Frenklach, *Chem. Eng. Sci.* 57 (12) (2002) 2229–2239.
- [4] D.L. Marchisio, R.O. Fox, *J. Aerosol Sci.* 36 (1) (2005) 43–73.
- [5] M.E. Mueller, G. Blanquart, H. Pitsch, *Combust. Flame* 156 (6) (2009) 1143–1155.
- [6] M.E. Mueller, H. Pitsch, *Phys. Fluids* 25 (11) (2013).
- [7] P. Rodrigues, B. Franzelli, R. Vicquelin, O. Gicquel, N. Darabiha, *Proc. Combust. Inst.* 36 (1) (2017) 927–934.
- [8] C. Eberle, P. Gerlinger, K. Geigle, M. Aigner, Soot Predictions in an Aero-Engine Model Combustor at Elevated Pressure Using URANS and Finite-Rate Chemistry, 50th AIAA/ASME/SAE/ASEE Joint Propulsion Conference, 2014, pp. 1–14.
- [9] P. Rodrigues, B. Franzelli, R. Vicquelin, O. Gicquel, N. Darabiha, *Combust. Flame* 190 (2018) 477–499.
- [10] M. Balthasar, M. Kraft, *Combust. Flame* 133 (3) (2003) 289–298.
- [11] M. Lucchesi, A. Abdelgadir, A. Attili, F. Bisetti, *Combust. Flame* 178 (2017) 35–45.
- [12] A. Attili, F. Bisetti, *Comput. Fluids* 84 (2013) 164–175.
- [13] J.C. Ong, K.M. Pang, J.H. Walther, J.-H. Ho, H.K. Ng, *J. Aerosol Sci.* 115 (2018) 70–95.
- [14] K.M. Leung, R.P. Lindstedt, W.P. Jones, *Combust. Flame* 87 (1991) 289–305.
- [15] K.P. Geigle, R. Hedef, M. Stoehr, W. Meier, *Proc. Comb. Inst.* 000 (2015) 1–8.
- [16] B. Franzelli, E. Riber, B. Cuenot, M. Ihme, *Proc. GT2015, ASME Turbo* (2016) 1–11.
- [17] A. Felden, E. Riber, B. Cuenot, *Combust. Flame* 191 (2018) 270–286.
- [18] M.E. Mueller, G. Blanquart, H. Pitsch, *Proc. Combust. Inst.* 32 I (1) (2009) 785–792.
- [19] G. Lecocq, D. Poitou, I. Hernández, F. Duchaine, E. Riber, B. Cuenot, *Flow Turb. Combust.* 92 (4) (2014) 947–970.
- [20] J.Y. Hwang, S.H. Chung, *Combust. Flame* 125 (1) (2001) 752–762.
- [21] X. Hao, H. Zhao, Z. Xu, C. Zheng, *Aerosol Sci. Tech.* 47 (10) (2013) 1125–1133.
- [22] J. Wei, F.E. Kruis, *Chemical Eng. Sci.* 104 (2013) 451–459.
- [23] A. Khadilkar, P.L. Rozelle, S.V. Pisupati, *Powder Technol.* 264 (2014) 216–228.
- [24] F.E. Kruis, A. Maisels, H. Fissan, *AIChE J.* 46 (9) (2000) 1735–1742.
- [25] A.L. Garcia, C. Van Den Broeck, M. Aertsens, R. Serneels, *Phys. A Stat. Mech. Appl.* 143 (3) (1987) 535–546.
- [26] G. Kotalczyk, F.E. Kruis, *J. Comput. Phys.* 340 (2017) 276–296.
- [27] Z. Xu, H. Zhao, C. Zheng, *J. Comput. Phys.* 281 (2015) 844–863.
- [28] K. Liffman, *J. Comput. Phys.* 100 (1) (1992) 116–127.
- [29] M. Smith, T. Matsoukas, *Chem. Eng. Sci.* 53 (9) (1998) 1777–1786.
- [30] Y. Lin, K. Lee, T. Matsoukas, *Chem. Eng. Sci.* 57 (12) (2002) 2241–2252.
- [31] W.J. Menz, J. Akroyd, M. Kraft, *J. Comput. Phys.* 256 (2014) 615–629.
- [32] M. Tsurikov, K.P. Geigle, V. Krüger, et al., *Combust. Sc. Tech.* 177 (10) (2005) 1835–1862.
- [33] K.P. Geigle, R. Hedef, W. Meier, *J. Eng. Gas Turb. Power* 136 (2) (2014) 021505.
- [34] O. Colin, M. Rudgyard, *J. Comput. Phys.* 162 (2) (2000) 338–371.
- [35] O. Colin, F. Ducros, D. Veynante, T. Poinso, *Phys. Fluids* 12 (7) (2000) 1843–1863.
- [36] F. Nicoud, F. Ducros, *Flow, Turb. Combust.* 62 (3) (1999) 183–200.
- [37] C. Eberle, P. Gerlinger, M. Aigner, *Combust. Flame* 179 (2017) 63–73.

Appendix B

Gas spectral database

The gas spectral database NBKM [372, 373] has been implemented in PRISSMA and validated on three test cases defined in Sec. 7.4.2.1

The numerical predicted radiative power (P^R) using PRISSMA with the previous SNB and the new NBKM database, as well as the reference computation from the literature using Monte-Carlo using line-by-line spectral database. Results for test case RTC1 are shown in Fig. B.1 as expected the predicted radiative power using SNB or NBKM spectral database leads to similar results, very close to the reference Monte-Carlo for both temperature considered, representative of combustion media.

The case RTC2, with a inhomogeneous composition and temperature is plotted in Fig. B.2. The predicted Radiative Power are superimposed following the reference computations.

Finally, the third test case RTC3 is computed leading in this case to exactly same predicted radiative power for both spectral databases shown in Fig. B.3.

These three test cases validated the implementation of the NBKM database in PRISSMA radiative solver.

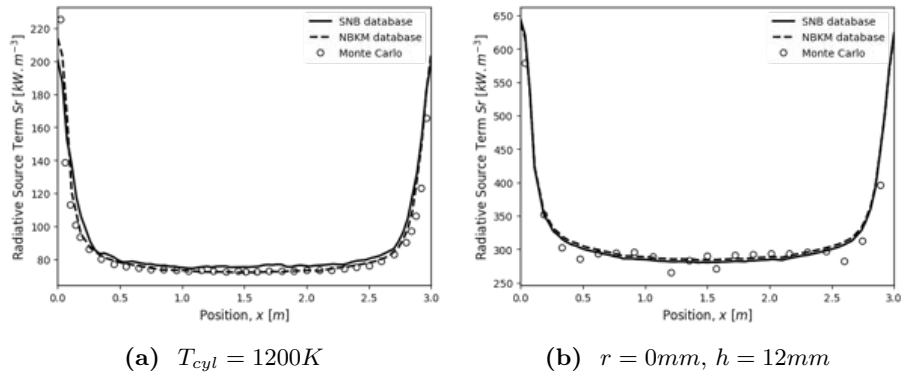


Figure B.1: RTC1: Comparison between SNB, new NBKM spectral database against the reference Monte-Carlo method using line-by-line model.

B. GAS SPECTRAL DATABASE

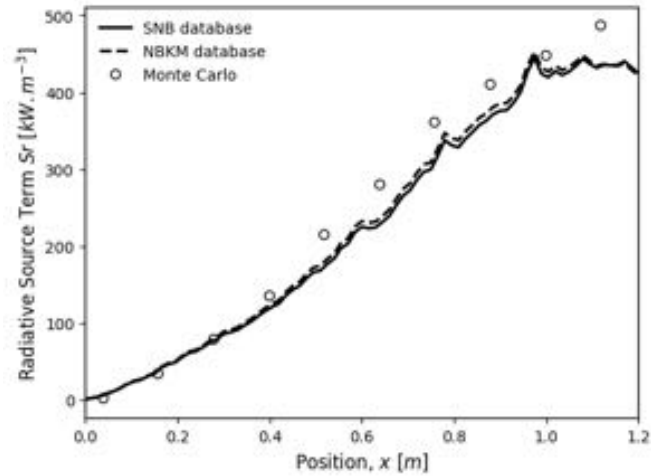


Figure B.2: RTC2: Comparison between SNB, new NBKM spectral database against the reference Monte-Carlo method using line-by-line model.

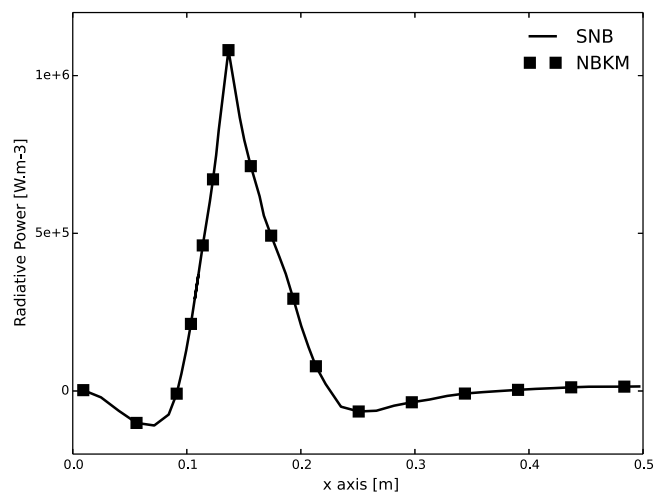


Figure B.3: RTC3: Comparison between SNB and new NBKM spectral database.

Appendix C

Coupling procedure AVBP-PRISSMA

C.1 Coupling libraries

Coupling is usually done with the open-source OpenPALM coupler [386] co-developed by CERFACS and ONERA. It has been developed to couple codes for multi-physics simulations. OpenPalm is composed of three parts: PALM, CWIPI and PrePALM.

- **PALM library:** The PALM library handles the parallel communications and the launching/exit of the different coupled applications. Each code sends its data of interest to PALM which then dispatches the associated information.
- **CWIPI library:** Coupling With Interpolation Parallel Interface (CWIPI) library handles the parallel interpolation of data in case of different meshes used by the applications [387]. A minimization of the global cost of the parallel communications is done through the optimization of the communication graph created by CWIPI.
- **PrePALM application:** It is a graphical user interface (GUI) enabling to create easily a coupling between different codes. Links and communications between the different codes are created through this interface which then creates the coupled applications using the PALM library and if necessary the CWIPI library.

In this work the coupling procedure has been reduced to the use of CWIPI library. The functions of the CWIPI library have been implemented directly in AVBP and PRISSMA.

C.2 Coupling communications

The coupling communications between the combustion solver (AVBP) and the radiation solver (PRISSMA) are schematized in Fig. C.1. After each coupling time step δt_{cpl} , the two solvers exchange information:

- AVBP sends the gaseous fields of temperature T , pressure P , soot volume fraction f_v interpolated on the grid and species molar fractions X_k of absorbing species

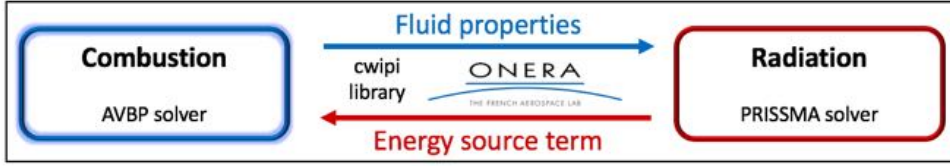


Figure C.1: Coupling procedure between AVBP and PRISSMA solvers.

- PRISSMA sends the field of radiative power P^R computed from the AVBP fields, to be used in the next time step in AVBP.

Thanks to CWIPI library, these communications are done at a low computational cost and the fields can be interpolated between the two different unstructured meshes used by the flow and radiation solvers. Indeed, PRISSMA does not need the same grid resolution of AVBP and then uses a coarser grid mesh.

C.3 Coupling time step

The coupling time step δt_{cpl} is proportional to the flow time step δt_f :

$$\delta t_{cpl} = n_{cpl} \delta t_f \quad (C.1)$$

For the coupling between radiation and fluid, the coupling frequency n_{cpl} between is determined to ensure that the chosen value is the optimum trade-off between accuracy and computing time, about $n_{cpl} = 100$ in this work.

Appendix D

Numerical set-up and FIRST flow validations

The numerical strategy used for the LES of FIRST configuration is briefly presented. All simulations are performed with the LES solver AVBP¹, an explicit cell-vertex massively parallel code solving the compressible reacting Navier-Stokes equations. A third-order accurate in space and time Taylor-Galerkin finite-element scheme with low-dissipation [388] is used for the discretization of the convective terms, while a second order Galerkin scheme is used for diffusion terms. The filtering operation of the filtered LES equations produces unclosed sub-grid scale (SGS) turbulent fluxes that must be modeled. The Reynolds SGS stress tensor is modeled using WALE approach [389], while the SGS diffusive heat and species fluxes are modeled by analogy with the filtered diffusive heat and species fluxes, assuming constant turbulent Prandtl and Schmidt numbers ($Pr^t = Sc_k^t = 0.6$). Turbulence-chemistry interactions are modeled by the DTFLES turbulent combustion model [390] using a generic sensor [350] (see Chapter 7).

Figure D.1 displays numerical axial, radial and tangential velocity profiles against experimental data at 4 axial positions of interest in the combustion chamber: $z = 15\text{ mm}$ and 18 mm are located in the primary combustion zone, $z = 95\text{ mm}$ is located near the secondary air injection while $z = 40\text{ mm}$ sits in between. Both RUN_HL_A4 and RUN_CPL_A4 have been compared to two different sets of velocity data: the Field of View (FoV) and the sum-of-correlation (SoC) (see [384] for definitions). Note that Geigle *et al.* [384] describe the FoV as being more reliable.

A very reasonable agreement is reached for both computations. The width and magnitude of the IRZ near the injector, in particular, is well captured by both cases.

¹<http://www.cerfacs.fr/avbp7x/>

D. NUMERICAL SET-UP AND FIRST FLOW VALIDATIONS

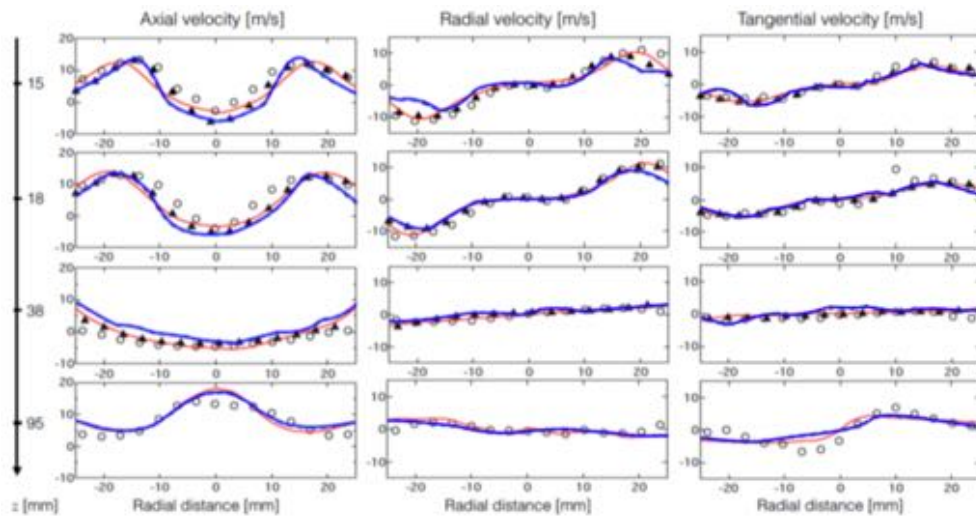


Figure D.1: FIRST configuration: Mean axial, radial and tangential velocity profiles for both chemical mechanisms extracted in mid-plane at $z = 15, 18, 40$ and 95 mm, RUN_HL_A4 (blue line), RUN_CPL_A4 (red line), experiment: FoV (\blacktriangle) and SoC (\circ).
